UNIVERSITY OF SOUTHAMPTON

FACULTY OF ENGINEERING, SCIENCE & MATHEMATICS

School of Engineering Sciences

Micromechanistic analysis of fatigue in aluminium silicon casting alloys

by

Andrew James Moffat

Thesis for the degree of Doctor of Philosophy

October 2007

UNIVERSITY OF SOUTHAMPTON

ABSTRACT

FACULTY OF ENGINEERING, SCIENCE & MATHEMATICS
SCHOOL OF ENGINEERING SCIENCES

Doctor of Philosophy

Micromechanistic analysis of fatigue in aluminium silicon casting alloys

by Andrew James Moffat

Due to increasingly stringent environmental legislation, there is a requirement for lower emissions and greater overall efficiency of light vehicle diesel (LVD) engines. This continues to be achieved through the optimisation of design and careful selection of the materials used in key LVD engine components, for example pistons, so that they are lighter and can operate at higher temperatures. Pistons are non-serviceable parts and so must be able to withstand the fatigue and high temperature environment of the car engine. It is therefore important to understand the mechanisms of fatigue in these alloys to help inform alloy development for the next generation of pistons.

Pistons are typically produced from multi-component Al-Si casting alloys. These alloys exhibit a complex, multiphase microstructure comprising α-aluminium as the matrix with silicon particles and several intermetallic phases. Previous research on Al-Si casting alloys has demonstrated that porosity is detrimental to fatigue life as cracks initiate freely at pores. However, with improved casting techniques porosity can be greatly reduced and other microstructural features influence fatigue life. In particular, Si particles have been shown to play an important role in the initiation and subsequent propagation of fatigue cracks. This study assesses the role of Si content and other microstructural features on fatigue behaviour by testing a set of well-characterised multi-component, Al-Si casting alloys with varying Si content.

Fatigue initiation behaviour was investigated at room temperature using S-N and short fatigue crack growth experiments. Pores, Si particles and intermetallic phases were shown to cause fatigue crack initiation. In a 0.67wt% Si containing alloy, large-scale porosity was observed and was the foremost reason for fatigue initiation. In two alloys the Al_9FeNi phase was observed to be the most detrimental hard particle causing fatigue crack initiation. Nanoindentation results showed that Al_9FeNi had a

lower hardness and higher modulus than Si and so Al_9FeNi may be expected to fracture preferentially, consistent with the fatigue results.

X-ray computed tomography demonstrated that all the alloys investigated contained a complex, interconnected, intermetallic sub-structure. As a result, the micromechanisms of fatigue are different to those in conventional particulate Al-Si alloys because particle fracture is required to ensure a level of crack continuity. At room temperature and 350˚C, and at low and high crack growth rates, the crack tip may be described as a diffuse region of micro-damage and intact ligaments. It is the extent of this damage in the alloys that controls the crack growth rates exhibited and simple trends between the Si content and roughness, reported for particulate systems, do not hold true in the alloys investigated in this study. The balance of the micromechanisms of fatigue was shown to be dependent on temperature. This highlights the importance of fatigue studies at temperatures that are characteristic of those experienced in service.

Contents

List of Figures

List of Tables

Nomenclature

a	crack length
a_0	critical crack length
c	bulk crack length
d	indent diagonal or diameter
da/dN	crack growth rate
h	indent depth
h_c	contact depth
h_f	final indent depth
h_s	sink-in depth
h_t	indent depth at maximum load
l_{max}	maximum particle length
l_f	feret length
m	Paris law exponent
m_1	constant
n	constant
r	distance from the crack tip
s	constant
A	projected indent area
A_A	area fraction
B	breadth
C	Paris law variable
C_1	constant
E	Young's modulus
E_r	reduced modulus
E_s	Young's modulus of the sample
E_i	Young's modulus of an indenter
G	strain energy release rate
G_{IC}	fracture toughness
H	hardness
H_v	Vickers hardness number
J	J integral
ΔK	range of stress intensity factor
ΔK_{app}	applied range of stress intensity factor
ΔK_{eff}	effective range of stress intensity factor
ΔK_{th}	threshold range of stress intensity factor
K	stress intensity factor
K_{Cl}	stress intensity factor at which the crack is closed
K_{1C}	fracture toughness
K_1	Mode I stress intensity factor
K_{max}	maximum stress intensity factor
K_{min}	minimum stress intensity factor
K_{th}	value of K at growth rate = 1x10-7

K_Q	value of K_{max} at fatigue failure
L_L	line fraction
L_3	mean intercept length
N	number of cycles
N_f	number of cycles to failure
N_i	number of cycles to initiation
N_L	number of intercepts per unit length
N_p	propagation lifetime
P	load
P_P	point fraction
P_T	number of points used in the grid for PFA
P_t	maximum load
Q	geometry correction factor
R	ratio of minimum to maximum load
S	initial gradient of indentation unloading curve
T_m	melting temperature
V_α	volume of α phase
V_f	volume fraction
V_T	test volume
W	width
Y	shape factor
δ	crack tip opening displacement
ε	strain
ε_1	indenter geometry parameter
ε_{fr}	fracture strain
ε_{max}	maximum strain
γ	surface energy
γ_e	elastic surface energy
γ_p	plastic surface energy
λ	mean free distance
σ	stress
σ	range of stress
σ_e	fatigue limit
σ_f	fracture stress
σ_{utx}	ultimate tensile strength
σ_y	0.2% proof strength
θ	angle
ν	Poisson's ratio
p.d.	potential difference
CCD	charge-coupled device
CMOS	complementary metal oxide semiconductor
CTOD	crack tip opening displacement
DAF	diamond area function
EBSD	electron back scattered diffraction
EDM	electrical discharge machining
EDX	energy dispersive X-rays
EPFM	elastic plastic fracture mechanics
ESRF	European Synchrotron Radiation Facility
DSC	differential scanning calorimetry

FBT	finite body tessellation
FEA	finite element analysis
FM	Federal Mogul
ICDD	International centre for diffraction data
LEFM	linear elastic fracture mechanics
LFA	line fraction analysis
LVD	light vehicle diesel
MMC	metal matrix composite
PFA	point fraction analysis
PICC	plasticity induced crack closure
RICC	roughness induced crack closure
RT	room temperature
S.D.	standard deviation
SDAS	secondary dendrite arm spacing
S.E.	standard error
SEM	scanning electron microscope
SENB	single-edge notched bend
UTS	ultimate tensile strength
X-ray CT	X-ray computed tomography
2-D	two-dimensional
3-D	three-dimensional

Declaration of Authorship

I, Andrew James Moffat declare that the thesis entitled:

Micromechanistic analysis of fatigue in aluminium silicon casting alloys

and the work presented in it are both my own, and have been generated by me as the result of my own original research. I confirm that:

- this work was done wholly or mainly while in candidature for a research degree at this University;
- where any part of this thesis has previously been submitted for a degree or any other qualification at this University or any other institution, this has been clearly stated;
- where I have consulted the published work of others, this is always clearly attributed;
- where I have quoted from the work of others, the source is always given. With the exception of such quotations, this thesis is entirely my own work;
- I have acknowledged all main sources of help;
- where the thesis is based on work done by myself jointly with others, I have made clear exactly what was done by others and what I have contributed myself;
- parts of this work have been published prior to submission and a list of journal publications is given in Appendix A.

Signed: …….

Date: ……

Acknowledgements

There are a great number of people to whom I will always be indebted for the help they have offered during the course of my research. My biggest thanks go to Philippa Reed and Brian Mellor for their support, guidance, ideas and supervision. They have contributed an enormous amount to my development, as well as my PhD, for which I will always be grateful. I would also like to thank Ian Sinclair who has been a great source of help and ideas and who I hold responsible for many sleepless nights at ESRF.

The work at ESRF could not have been performed without the ID19 beamline staff and in particular the kind help of Greg Johnson, Wolfgang Ludwig and Andy King. In addition I am especially grateful to Jean-Yves Buffière and Henry Proudon of INSA, Lyon who made working at ESRF a little more fun, and Airbus for sponsoring a year long project during which I was able to use a few hours of beam time for this research.

I would like to acknowledge the support of all the staff and students in the Engineering Materials Research Group at the University of Southampton who have aided me along the way. I am especially grateful to the people who have tolerated me in their office: Stewart, Toby, Thilo, Thomas, Nik, Pete, Sobia, Saleh, Hamdi, Leo, Fabien, Suresh and in particular Ian Stewart and Polly Sinnett Jones who have been (and continue to be) most excellent friends. The secretarial and technical staff (Gwyneth, Dave, Bob, Chris, Erik, Eric, Clive and James) have also been invaluable and helped me enormously. I would also like to acknowledge the help of Nong Gao and Marco Starink with the DSC experiments and analysis carried out as part of this research. For their assistance with phase mapping, and for hosting me at Loughborough University during the course of this research, I would like to thank Rachel Thomson and Chun-Liang Chen.

I am grateful to the School of Engineering Sciences for their financial support and also Federal Mogul and Simon Barnes for materials and useful discussions in addition to high temperature tensile testing and cyclic stress-strain testing. I would also like to acknowledge the Royal Academy of Engineering, the Worshipful Company of Armourers and Brasiers, the Institute of Physics, and the Institute of Materials Minerals and Mining for their financial support in the form of conference attendance awards.

On a personal note, my final thanks go to my wife Jodie (the first Dr. in the Moffat family) whose love and support have helped me everyday and whom I can always depend upon.

Finally, a small ditty:

No more fatigue testing for me
Forget the Instron, I'm drinking tea
I'll leave this to Stewart, Philippa and Dave
Whilst I sit by the CT and wave

Chapter 1

Introduction

1.1 Background

Automobiles play an important role in today's society; in the UK alone there are approximately thirty million licensed 'light vehicles' (cars and vans) (DVLA, 2007), which equates to one for every two people. Engineers such as Benz, Daimler and Maybach are generally regarded as the pioneers of the car with Benz receiving a patent (German patent number: 37435) for his *Motorwagen* in 1886 (Mercedes-Benz, 2007). The first cars used gasoline engines with the diesel engine being developed by Rudolph Diesel in 1895 (German patent number: 86633) and both fuel types are still in use today. Whilst cars have many benefits, there are also negative implications of car use, particularly the emission of gases (for example CO_2) through the combustion of fuels, which are thought to be related to climate change. The issue of climate change is high on the international agenda and this was highlighted by the award of the 2007 Nobel peace prize to the Intergovernmental Panel on Climate Change and Al Gore "for their efforts to build up and disseminate greater knowledge about man-made climate change" (Nobel Foundation, 2007). As a result of environmental concerns, efforts are being made to reduce harmful emissions. The key legislation driving this reduction is the 1997 Kyoto protocol amendment to the United Nations (UN) convention on climate change (UN, 1998).

The target set in the Kyoto protocol for the European Union (EU) is for an 8% reduction in 'greenhouse' gas emissions from 1990 levels by 2012. Whilst most areas of industry in the EU have reduced their emissions, those from transportation have risen by 26% from 1990 levels (EEA, 2007) and automobiles account for 24% of all CO_2 emissions in the EU. This is partially attributed to the increased number of cars,

for example in the UK there has been a 10% increase in light vehicles since 2000 (DVLA, 2007). To fulfil the Kyoto targets the EU has proposed a series of guidelines and these can be broadly split into two areas: 1) reduction in car usage and 2) reduction in car emissions (EEA, 2007). Development of road and alternative transport networks are seen as an important way in which car usage may be reduced whilst legislation is seen as the primary mechanism for reducing emissions. For example, the conclusions of a recent report (Smokers *et al.*, 2006) to reduce average CO_2 emissions to 120g CO_2/km by 2012 (the average level in 2004 was 163g CO_2/km) are likely to be adopted as EU policy (EU, 2007).

It is the increasingly stringent environmental legislation and the accompanying drive for efficiency in the automotive industry that has led to improvements in the design of key engine components, for example pistons. Recent piston developments have largely concentrated on two key aims: reducing weight and increasing operating temperatures. These aims continue to be met by careful optimisation of the piston design (for example, improved cooling), and by alloy development. Pistons are required to operate in an aggressive environment at temperatures up to 440˚C and are both mechanically and thermally cycled. Engine components such as pistons are non-serviceable parts and are therefore expected to last the lifetime of the engine, thus requiring 'excellent' reliability (lifetimes greater than $1x10^9$ cycles).

Figure 1-1 is a photograph of two pistons from the Federal Mogul (2005) website; the main parts of the piston have been labelled. A piston can be divided into two sections: the crown and the skirt. The piston crown forms one side of the combustion chamber in the engine, and because of this the top surface experiences the highest temperatures of the component. A combustion bowl is usually placed in the top of the crown. Due to the shape of the combustion bowl and the high temperatures that it experiences (up to 440˚C), fatigue cracks are often seen to initiate in this area (Myers and Hurd, 1990). Because of the susceptibility of this region to fatigue it is a key variable in piston design and individual car producers have their own (closely guarded) proprietary designs. There is therefore little research published in the open literature on the design of the piston bowl region but recent patents (for example Barnes and Barnes, 2002) suggest that research is on-going in this area; in this case the patent

covers the production of the piston bowl by a friction process, which also modifies the microstructure in this region.

There are a series of grooves around the edge of the crown and these contain the piston rings and form the ring belt (Figure 1-1). There are two categories of piston rings in diesel engines: 1) the compression rings and 2) the oil control ring and these are identified in Figure 1-1. The function of the compression rings is to seal the piston against the cylinder wall thus providing a tight seal for the combustion chamber, to prevent fuel and exhaust gases escaping. The compression rings also transfer heat from the piston to the cylinder. The oil control rings control the amount of oil between the cylinder and the piston. The oil control ring must ensure that a sufficient amount of oil reaches the compression rings but not so much that it enters the combustion chamber. Piston rings usually comprise a steel substrate with a wear resistant coating (Wellington and Asmus, 1995).

The piston crown transfers the energy produced by combustion to the connecting rod (and the rest of the engine) via the piston skirt and a pin, which is held secure in the gudgeon pin boss (Figure 1-1). The shape and function of the gudgeon pin boss region means that it experiences the highest stresses in the piston assembly and so it is therefore also a region that is particularly susceptible to fatigue crack initiation. The operating temperatures in this region are not as high as at the combustion bowl edge at approximately 200˚C (Joyce *et al.*, 2002). The remainder of the piston skirt ensures that the piston moves smoothly in the cylinder and prevents the piston from tilting under the high pressures of combustion. It is designed to be close fitting to the cylinder but so that a layer of oil separates the two. This ensures that heat can be dissipated and that the piston operates quietly. The piston crown is usually produced so that it is smaller in diameter than the piston skirt to allow for the different levels of expansion in the two regions when at the usual operating temperatures.

The material from which pistons are produced plays an important role in their performance. Properties that are desirable in light vehicle diesel (LVD) piston materials are good thermal conductivity, so as to reduce thermal gradients across the piston, and a low coefficient of thermal expansion, so that they do not expand too much as the engine heats up. The material needs to be lightweight, for improved efficiency, and inexpensive. The materials must be able to withstand the operating

environment and so be fatigue resistant (diesel engines operate at between 15Hz and 70Hz and are highly cycled through their lifetime). Furthermore the pistons must not wear easily. The materials are required to operate at high temperatures (up to 440˚C) and therefore require 'good' mechanical properties at their operating temperatures.

Pistons used in LVD engines are usually manufactured from multi-component Al-Si alloys (Haque and Maleque, 1998). The Si content of the alloys can vary from 6 wt% to 17 wt%. These Al-Si alloys are described as multi-component because of the additional alloying elements that are used, for example Cu, Ni and Mg. The use of additional alloying elements is an important method by which the previously mentioned properties of the alloy may be improved, ultimately to reduce the weight of the component and increase the operating temperature. Multi-component Al-Si pistons may be forged or cast. Forging is the more expensive technique but produces pistons that have a greater density with fewer defects. Forged pistons conduct heat more effectively than cast pistons and therefore allow the engine to operate at higher temperatures (Federal Mogul, 2007). In the automotive industry, however, minimisation of cost is of paramount importance and so cast pistons are more commonly used in 'everyday' cars with forged pistons being used in niche markets such as motor racing. In this project the alloys investigated will therefore be described as 'Al-Si casting alloys', with 'multi-component' being omitted for brevity throughout the thesis.

1.2 Aims and objectives

The aim of this project is to gain an in-depth understanding of the micromechanisms of fatigue that occur during all stages of fatigue life in Al-Si casting alloys at both room temperature and a characteristic in-service temperature of a piston. In particular, the role of Si content will be assessed to determine how Si quantity and morphology affect fatigue performance and to establish the effect of other microstructural features in the absence of Si.

Three alloy compositions will be investigated; the principal difference between the compositions is the Si content:

LVD25 – a near-eutectic alloy, containing 12.45 wt% Si.

LVD26 – a mid Si alloy, containing 6.90 wt% Si. There are two variants of this alloy: LVD26mod, which contains Sr, and LVD26unmod, which does not.

LVD27 – a low Si alloy, containing 0.67 wt% Si. Si is present as a result of impurities in the casting process (and so is strictly speaking not an Al-Si alloy).

The following objectives are key to fulfilling the aim of this project:

- Characterise the microstructural constituents using a series of experimental techniques including X-ray computed tomography (X-ray CT) analysis, 2-D image analysis and nanoindentation.
- Investigate fatigue crack initiation and subsequent propagation behaviour using a series of fatigue tests.
- Perform *in-situ* and post failure analysis to allow for qualitative and quantitative assessment of fatigue micromechanisms and hence establish the link between the microstructural constituents and fatigue performance.

1.3 Thesis structure

This thesis contains nine chapters, of which this is the first. Chapter two contains the literature review and is divided into three main sections: a review of the microstructure of Al-Si casting alloys, a general background to fatigue and the specific fatigue micromechanisms and performance in Al-Si casting alloys. Chapter three contains the details of all the experimental methods used in the course of this project. Background information on the less standard experimental techniques, such as nanoindentation and X-ray CT, is given in this chapter. The micro and macro scale properties of the alloys studied were characterised and these results are presented in chapter four. The results of the fatigue testing are contained in chapter five. S-N and short fatigue crack propagation tests were performed at room temperature, whilst long fatigue propagation tests were performed at both room and elevated temperature (350˚C). The discussion (chapter six) is divided into two sections. The micromechanisms of fatigue crack initiation and the effect of porosity and hard particles are discussed first. In the second section of this chapter, fatigue crack

propagation behaviour is discussed. The aim of this section is to demonstrate the link between the microstructural constituents (presented in chapter four) and their effect on fatigue crack propagation behaviour. The conclusions and future directions are in chapters seven and eight respectively. To aid the reader summaries are given at the end of the literature review chapter (two) and the results chapters (four and five) to highlight the key points in these chapters.

Figure 1-1 Photograph of pistons from the Federal Mogul (2005) website.

Chapter 2

Literature review

2.1 Introduction

Al-Si casting alloys are used widely in the automotive industry because they have a range of suitable properties. In particular, pistons are often made from Al-Si casting alloys and so these alloys must be able to withstand the high temperatures and cyclic loads that occur in car engines. As a result of alloy development over the last 20 years to improve, amongst other properties, their fatigue performance, Al-Si casting alloys contain many alloying additions and so exhibit complex multiphase microstructures. The first section of this chapter will therefore describe the many phases that form in these alloys. The second section will contain a general background to fatigue and the final section will provide the link between the previous two sections and in particular explore the effect of the microstructures of Al-Si casting alloy on all stages of fatigue life.

2.2 Microstructural constituents

Al is a lightweight metal and so is ideal for applications, such as automotive pistons, where lower weight components contribute to improvements in car engine efficiency. However, Al alone does not have all of the properties required of a piston material. Si and other alloying elements are therefore added to Al to give the required balance of important properties. In particular Si is added in large quantities and this improves the castability (Elliot, 1983), the wear and corrosion resistance (Harun *et al.*, 1996), the coefficient of thermal expansion (Polmear, 1999) and the mechanical properties (Elliot, 1983). Other alloying elements are added to improve the grain structure (Wang *et al.*, 2003), improve high temperature properties (Ye, 2003) and influence

the formation of other phases (Caceres *et al.*, 1999). As a result of the many alloying elements, Al-Si casting alloys exhibit a complex microstructure (Daykin, 1998; Edwards, 2002; Chen, 2006).

The two principal phases present in Al-Si casting alloys are primary, aluminium based α-Al which, as the phase with the largest volume fraction, acts as the matrix for the alloy, and the silicon phase, which is found largely in two forms: primary 'blocky' silicon and 'plate like' eutectic silicon. To fully assess the role of Si, an alloy containing a low quantity of Si has also been investigated in this work; this alloy is not strictly speaking an Al-Si casting alloy and so the microstructural constituents may be expected to be different, for example: it may contain few or no Si particles. Edwards (2002) identified thirteen intermetallic phases to be present in Al-Si alloys with similar alloying additions to those studied in this project. This section contains a brief description of the phases found in these alloy systems.

2.2.1 α-aluminium phase

Aluminium comprises 80-90 wt% in each of the alloys studied in this project and hence Al-based solid solution strengthened α-Al phase acts as the matrix for the alloys. This phase usually has a dendritic structure (Daykin, 1998) but this is known to be dependent on the solidification conditions of the casting (Wang *et al.*, 2001a); for example the temperature gradient across the sample and the thickness of the sample. A high temperature gradient is known to give elongated or columnar aluminium dendrites (Edwards, 2002; Elliot, 1983), with a small secondary dendrite arm spacing (SDAS) (Wang *et al.*, 2001b). The dendrites grow along the direction of the heat flow. More equiaxed dendrites form when the temperature gradient is lower e.g. in the centre of thicker sections of a casting.

Grain size is similarly affected by the cooling conditions, but may also be influenced by the addition of alloying elements (Wang *et al.*, 2003). Common grain refiners are Ti, B, Zr and V and these are all present in the alloys investigated in this study. The mechanism by which these elements work as grain refiners is not certain (Edwards, 2002). However, grain refiners are generally thought to provide inoculant particles, which do not dissolve in the melt, so that when the melt cools they provide sites for heterogeneous nucleation and therefore promote the growth of grains (Greer *et al.*,

2003). In Al-Si casting alloys fatigue cracks have been observed to be retarded at grain boundaries (Ludwig *et al.*, 2003). This retardation is usually attributed to the difference in the crystallographic orientation between grains, which inhibits the movements of dislocations ahead of the crack tip (Li and Edwards, 1996; Buffière *et al.*, 2001). If grains are large compared with other microstructural features (for example: dendrite or particle size) then their effect on crack propagation is less pronounced (Han *et al.*, 2002).

Al-Si casting alloys can be age hardened because the α-Al phase is a solid solution, which contains Cu and Mg. Under the correct aging conditions, these elements precipitate out of the α-Al, forming precipitates such as Al_2Cu (Lopez *et al.*, 2007) and Mg_2Si (Liao *et al.*, 2002; Zhang *et al.*, 2002). The peak aging time for Al-Si casting alloys is approximately thirty minutes at a temperature of 230°C (Barnes, 2005).

Etching of the aluminium phase in a 0.5% HF in water solution gives the matrix a characteristic yellow colour (Edwards, 2002). The shape of the aluminium dendrites formed is usually identifiable because the intermetallic and Si phases form at the tips of the dendrites and between the dendrite arms. The dendrites in eutectic alloys are less obvious because the primary and secondary phases are distributed more evenly throughout the matrix.

2.2.2 Silicon phases

The amount of silicon that is present in the alloys investigated in this study varies from 0.67 wt% to 12.45 wt%. In eutectic Al-Si casting alloys (which contain approximately 12 wt% Si), two types of silicon may be found: primary silicon and secondary, eutectic silicon (Daykin, 1998; Edwards, 2002; Chen, 2006). Primary silicon is known to have a blocky morphology (Gupta and Ling, 1999) but should not form in hypoeutectic alloys. Eutectic silicon usually has a plate or flake like morphology but this can be modified to have a much finer structure. Upon etching with a 0.5% HF in water solution, silicon has a grey colour. The size, volume fraction and morphology of the silicon phase are determined by the casting conditions, the chemistry of the alloy (for example the amount of Si and the other alloying additions)

and the heat treatment (Wang *et al.*, 2001b). The size of Si particles can vary from 2 μm (Lee *et al.*, 1995)) to greater than 100 μm (Stolarz *et al.*, 2001).

Increasing the Si content up to the eutectic level (approximately 12 wt %) improves the castability of the alloy by reducing the melting temperature and the temperature range of the 'mushy' zone (Polmear, 1993). As a result of a more fluid cast, smaller interdendritic pores form, which can improve the fatigue life of the alloys (Conley *et al.*, 2000). The addition of Si to Al also reduces the coefficient of thermal expansion (Polmear, 1989), this is important for a piston because it limits expansion in the engine and ensures the smooth movement of the piston when the engine warms up from resting temperature to the operating temperature. The more the material expands, the smaller the part must be produced so that it can expand in the cylinder, and then the greater the possibility of piston slap. This has been understood since the early part of the 20th century (Pacz, 1921; Bamberry, 1932).

Silicon is a relatively hard, brittle phase and so improves the wear resistance of the resulting alloy (Harun *et al.*, 1996; Ye, 2003). However, this does make the alloy more difficult to machine and so can increase production costs. Si is also added to improve the strength and elastic modulus of these materials (Elliott, 1983) and these properties are dependent on the morphology and size of the silicon phases (Kim *et al.*, 2002). It has been demonstrated that a finer eutectic silicon structure with a spherical morphology improves both the tensile strength and the percentage elongation of the alloy, whilst coarser particles are more detrimental to these properties (Suarez-Pena and Asensio-Lozano, 2006). Si particle shape and size may be altered through heat treatments such as hot isostatic pressing (HIPping) and solutionizing (Zhang *et al.*, 2002; Lee *et al.*, 2003), which produces a spherodised Si morphology (in a 2-D cross-section), or by the addition of alloying elements (Pacz, 1921).

Sr (Liao *et al.*, 2002) and Na (Verdu, 1996) are typical alloying elements added to Al-Si alloys to alter the morphology of eutectic Si from large plates to finer particles (Conley *et al.* 2000), which may form part of an interconnected fibrous network of Si particles (Lasagni *et al.*, 2006). Additions of Sr and Na are thought to produce finer Si particles because they lower the eutectic temperature and therefore restrict the growth of Si nuclei (Haque and Maleque, 1998). In this project the alloys have also been modified using P, and this is known to form the AlP phase (Edwards, 2002). The

modification mechanism for P is different to that of Na and Sr in that it encourages the growth of Si. The AlP phase acts as a nucleus on which primary 'blocky' Si grows. P and Sr or Na can be used together (Polmear, 1989) to give small, blocky Si particles. It should be noted that primary Si is only expected in near-eutectic and hypereutectic alloys and so P will have a limited effect on hypoeutectic alloys. As will be discussed in greater detail in section 2.4, the size, shape and distribution of Si plays an important role in the fatigue life of Al-Si alloys, for example initiation may occur at Si particles and Si particles may also affect crack propagation (Joyce *et al.*, 2002b; Gall *et al.*, 1999).

As well as the large phases mentioned, Si is also known to form as precipitates (Warmuzek, 2004). Much of the information about Si precipitates is found in work on 2XXX and 6XXX series alloys, which have low Si content (comparable with the lowest Si alloy in this work). The precipitates are reported to form on the {110} and {100} planes (Mondolfo, 1976) (similarly Al_2Cu and Mg_2Si precipitates also form on these planes) and can exhibit a size of approximately 1μm when the materials are in the overaged condition (Eskin *et al.*, 1999).

2.2.3 AlCuNi phases

Ni and Cu are both added to Al-Si casting alloys to increase their high temperature strength (Ye, 2003). The mechanism by which they do this is unclear but work by Joyce *et al.* (2002) indicates that Al-Si alloys containing higher quantities of these elements are more resistant to stress relaxation at 350˚C. This may be attributed to a greater number of large particles, which can both inhibit the movement of dislocations and increase load transfer (Eshelby, 1957), which shields the matrix phase.

Ni and Cu combine with Al to form three different phases (Edwards, 2002); these are the Al_3Ni, $Al_3(NiCu)_2$ and the Al_7Cu_4Ni phases. Whilst the name of the Al_3Ni phase suggests that it contains no Cu it actually contains approximately 10 wt% Cu and 29 wt% Ni. The Al_7Cu_4Ni contains 37 wt% Cu and 18 wt% Ni and so the principal difference between the alloys is the Ni:Cu ratio. The phases cannot be easily differentiated by a characteristic morphology. However, with etching in a solution of 0.5% HF in water solution the phases can be separated by colour which is generally related to the Ni:Cu ratio: a dark brown/grey colour indicates a phase with a high

Ni:Cu ratio and a lighter grey colour signifies a low Ni:Cu ratio. These three phases often form adjacent to one another and are usually interconnected (Chen *et al.*, 2006).

2.2.4 Fe containing phases

Fe is present as an impurity due to the steel equipment used in the casting process (Kearney and Rooy, 1990) and as a result Fe-containing phases are commonly found in Al-Si casting alloys. Several Fe containing phases have been observed in these alloys including the β(AlFeSi), Al_9FeNi, π($Al_8FeMg_3Si_6$) and α(AlFeMnSi) phases (Daykin, 1998; Edwards, 2002). The β phase is thought to be the most detrimental of the Fe-containing phases to the mechanical properties (Ravi *et al.*, 2002) and is also detrimental to the fatigue properties (Stolarz *et al.*, 2001). It forms large flakes and is reported (Roy *et al.*, 1996) to provide a good 'nucleation site' for pores as it restricts the flow of the cast. To limit the effect of the β-phase, alloying additions such as Mg and Mn (Roy *et al.*, 1996) are added to promote the growth of the other Fe-containing phases. The π and α phases have a 'Chinese script' morphology and are often smaller than the β-phase (Daykin, 1998) although Caceres *et al.* (1999) indicates that the improved properties obtained by the addition of Mg may be due to the formation of Mg_2Si precipitates and not because the π-phase is less deleterious. The Al_9FeNi phase is not often mentioned in the literature since Al-Si casting alloys (for example A356 and A357) do not contain large quantities of Ni. However, the Al_9FeNi phase was previously observed by Edwards (2002) and Joyce *et al.* (2002b). Al_9FeNi does not exhibit a 'Chinese script' or flake morphology like the other Fe-phases and so it is not yet established whether this phase is preferable in terms of mechanical and fatigue properties. The Fe-containing phases have a grey/brown appearance after etching in 0.5% HF in water solution.

2.2.5 Other phases

The AlP and Al_3Ti phases have been mentioned in previous sections because they have a indirect effect on the material properties, by altering the principal microstructural features: P is added to these alloys so that the AlP phase forms which acts as a nucleation site for primary 'blocky' Si particles (Edwards, 2002) inhibiting the formation of large Si plates. In micrographs this phase appears as a small black

dot (approximately 1 μm^2) in the centre of a primary Si particle. Ti is added to Al-Si alloys to act as a nucleant for the α-Al phase and encourage small, regular grains to form (Edwards, 2002).

Similarly the Mg_2Si and Al_2Cu phases have been previously mentioned. In Al-Si casting alloys, containing the required levels of Mg or Cu and under the correct aging conditions, these phases can be precipitated out of the α-Al matrix (Liao *et al.*, 2002; Zhang *et al.*, 2002; Lopez *et al.*, 2007). The state of these precipitates is known to play an important role in the strength of Al alloys (Polmear, 1989) and so depending on the aging conditions these precipitates are likely to have a direct effect on the material properties. However, these phases may also form during the cooling period of the casting process and form larger secondary phases that have a 'Chinese script' or lacy appearance (Daykin, 1998; Edwards, 2002). The effect of these larger phases on the mechanical or other properties of Al-Si casting alloys was not found in a review of the literature.

2.3 Fatigue

2.3.1 Characterising fatigue behaviour

The cyclic loading of a material to failure is referred to as fatigue. Many in-service components are subject to cyclic stresses and so knowledge of the mechanisms of fatigue may be necessary for the lifing of a component. Failure by fatigue can occur at stress levels that are below the yield strength of a material and fatigue is a complicated process that is dependent upon environmental factors, loading conditions, microstructure, stress state and the geometry of the crack and the component/sample.

A convenient way to represent the fatigue life of a sample is with an S-N curve (Wöhler, 1860; cited by: Suresh, 1998), which is illustrated in Figure 2-1; this is a plot of the maximum value (or amplitude) of stress or strain in the cycle to the number of cycles to failure. Many textbooks (for example Callister, 2000; John, 2003) report that some materials have a fatigue limit below which fatigue will not occur. However, most non-ferrous alloys do not exhibit this behaviour and so an endurance (or fatigue) limit is specified as the stress level giving a nominal life of $1x10^7$ cycles.

At low stress levels, where the S-N curve tends to the endurance limit, the deformation is elastic (in a global sense) and so the fatigue life is dominated by the stress amplitude. At high stress levels, where the S-N curve tends to the UTS, the deformation is largely plastic and the fatigue life is dominated by the strain amplitude. As the value of applied stress increases, initiation of a fatigue crack becomes increasingly 'easy' and so at low cyclic stresses the majority of the fatigue life is the time taken for the crack to initiate. When the stress level is high the majority of the fatigue life is taken up in propagation of the crack.

Fatigue cracks usually have a quasi-brittle appearance with little sign of overall plastic deformation, even in ductile materials. A characteristic indication of a fatigue failure is beach marks on the macro-scale and in some materials striations on the fracture surface. These indicate the position of the crack front at a particular time and usually radiate from the initiation point. Several stages are usually associated with the life of a fatigue crack. Firstly the crack must initiate forming a 'small' crack; this crack increases in length and becomes a 'long' crack, which grows incrementally with each cycle until final fracture. These stages are discussed in more detail in section 2.3.3, but first some of the fundamental theory used to describe fatigue failures will be discussed in more detail.

2.3.2 Application of fracture mechanics to fatigue

Fracture mechanics may be employed to analyse the relationship between cracks and stresses in materials or structures and can be applied to the process of fatigue to give an understanding of the way the fatigue crack interacts with the surrounding material, through which it propagates, by defining a crack tip driving force.

2.3.2.1 Linear elastic fracture mechanics

Linear elastic fracture mechanics (LEFM) is commonly used to assess fatigue crack growth. Early work was conducted by Griffiths (1921) who used a global energy balance approach. Griffiths considered the case of an infinitely wide plate (i.e. $W>>2a$) subjected to a constant tensile stress, σ, containing a through thickness crack of length $2a$. For a crack to grow, the rate of stored strain energy in the plate released by crack growth must be at least equal to the surface energy of the new crack surface.

This approach was used to link the fracture stress (σ_f), Young's modulus (E), the crack length (a) and the surface energy (γ):

$$\sigma_f = \sqrt{\frac{2E\gamma}{\pi a}} \tag{2-1}$$

There are limitations to the Griffiths approach, in that it only considers global energies and is only valid for brittle materials where plastic deformation does not occur. The Griffiths approach may be modified to accommodate limited plastic deformation ahead of the crack tip (i.e. small scale yielding) by considering an additional plastic work term γ_p (Orowan, 1952) thus:

$$\sigma_f = \sqrt{\frac{2\,E\left(\gamma_e + \gamma_p\right)}{\pi\, a}} \tag{2-2}$$

Since the individual surface energy terms are, experimentally, hard to measure, Irwin (1956) showed that it was possible to replace the surface energy term with the strain energy release rate, G. G is a measure of the stored strain energy released for an increment of crack growth. Crack extension occurs when G reaches a critical value (G_C) and this value represented the fracture toughness of the material. Equation (2-2) can therefore be rewritten such that in plane stress:

$$\frac{{\sigma_f}^2 \pi\, a}{E} = 2(\gamma_e + \gamma_p) = G_{IC} \tag{2-3}$$

In analysis of metals it is more usual to describe this critical level in terms of the stress intensity factor, K, instead of using the energy approach of G. Equation (2-2) can again be rearranged to define fracture toughness in terms of K:

$$\sigma_f \sqrt{\pi\, a} = \sqrt{2E(\gamma_e + \gamma_p)} = K_{IC} \tag{2-4}$$

where K_{IC} is the critical value of K and hence the fracture toughness. The two parameters (G and K) are clearly related, but this is dependent on the stress state of the material. In plane stress they are linked by equation (2-5) and in plane strain they are linked by (2-6) where ν is Poisson's ratio.

$$K^2 = GE \tag{2-5}$$

$$K^2 = \frac{GE}{(1-\nu^2)} \tag{2-6}$$

For K_{IC} to be valid, small scale yielding conditions must hold, i.e. the region of plasticity ahead of the crack must be smaller than the region of K dominance; this is an important approximation of LEFM conditions. A definition of this approximation is that the crack length (a), the thickness of the specimen (B), and the uncracked ligament (W-a) are each not less than a value related to K_{IC} and σ_y as defined by BS EN ISO 12737:1999:

$$a, B, W - a \geq 2.5\left(\frac{K_{IC}}{\sigma_y}\right)^2 \tag{2-7}$$

In equation (2-7) the surrounding elastic material (a, B, W-a) is approximately 50 plastic zone sizes (plastic zone size calculations are considered in more detail in section 2.3.2.2). For a given environment and a material under plane strain conditions, K_{IC} is a material constant. When the material is under mixed stress state conditions (i.e. when B does not obey equation (2-7)) then K_Q is dependent on B and so is no longer purely a material property (i.e. K_{IC}).

The Griffiths approach does not define the near tip-stress field, this was first quantified by Irwin (1957). Irwin proposed that the stress field near the crack tip was a function of geometry and loading conditions. When considering the stress field around a crack tip it is necessary to define the mode of loading. There are three basic modes: tensile opening (Mode I), in-plane sliding (Mode II) and tearing (Mode III) as illustrated in Figure 2-2. For Mode I loading the stress field can be represented using:

$$\sigma_{ij} = \frac{K}{\sqrt{2\pi r}} f_{ij}(\theta) + \textit{higher order terms} \tag{2-8}$$

where r and θ are polar co-ordinates and are used to describe a location in the stress field, σ_{ij} is the stress tensor and K is the stress intensity factor, which describes the magnitude of the local crack tip stress field. Thus K is the common factor linking the stress field near the crack tip proposed by Irwin, and defined by equation (2-8), and

the global energy approach of Griffiths (where K can be defined in a similar way to K_{IC} in equation (2-4)):

$$K = Y\sigma\sqrt{(\pi a)} \tag{2-9}$$

Y is a shape factor that describes the geometry of the sample.

The stress intensity factor is therefore a useful parameter since if the loading conditions and geometry of the specimen are known, i.e. using the global stress approach of Griffiths in equation (2-9), it is possible to evaluate the stress conditions near the crack tip. An important consequence of this is that for a given material and environment and the same loading history, K may be used to calculate the stress field in different size specimens with different crack geometries; this is the concept of similitude.

In fatigue tests a sample is cycled between different values of stress. From equation (2-9) it can be shown that the value of K will vary over the cycle as σ changes. If the stress amplitude ($\Delta\sigma$) of the waveform used is constant then the range of K (ΔK) can be expressed as:

$$\Delta K = K_{\max} - K_{\min} = Y\Delta\sigma\sqrt{\pi a} \tag{2-10}$$

Equation (2-10) indicates that ΔK is proportional to a and so for a given set of loading conditions ΔK will generally increase as a fatigue crack grows. Paris and Erdogan (1963) demonstrated that under cyclic loading the rate of crack growth (da/dN) was also proportional to ΔK and for a certain range of crack growth rates exhibited a log-log linear relationship such that:

$$\frac{da}{dN} = C\Delta K^m \tag{2-11}$$

where C and m are empirical factors that are material and environment dependent. ΔK is commonly plotted against da/dN on a log-log plot to present fatigue crack propagation data.

The fracture toughness of a material (K_{IC}) can be estimated from fatigue information, as it is approximately the same as the K_{max} value at final fracture in a fatigue test (K_Q).

If ΔK at failure and the ratio of minimum to maximum stress (R) are known then K_Q can be calculated using:

$$K_{IC} \approx K_Q = \frac{\Delta K_{\max}}{1-R} \tag{2-12}$$

However, in fracture toughness tests (as defined in BS EN ISO 12737:1999) the plastic zone size from the fatigue pre-cracking must be small compared with the plastic zone size at K_{IC}. In a fatigue test this will obviously not be the case and so this may be the cause of discrepancies between K_{IC} and K_Q.

2.3.2.2 Plastic zone

LEFM analysis of Irwin (1957) (i.e. equation (2-8)) predicts that for sharp cracks the stresses at the crack tip will be infinite. In reality, inelastic deformation (i.e. plastic yielding) occurs and as a result of this the calculated stress field will not be fully represented by equation (2-8). In the case of a mode I singular field on the crack plane where $\theta = 0$, equation (2-8) can be rewritten to calculate the stresses in the x and y direction:

$$\sigma_{xx} = \sigma_{yy} = \frac{K_I}{\sqrt{2\pi r}} \tag{2-13}$$

If σ_y is substituted into (2-13) and rearranged to make r the subject then:

$$r_y = \frac{1}{2\pi}\left(\frac{K_1}{\sigma_y}\right)^2 \tag{2-14}$$

where r_y is the calculated radius of the plastic zone to a first order approximation in plane stress; this is the light grey zone plotted in Figure 2-3. Assuming that strain hardening does not occur, the stress cannot exceed the yield stress and so at values smaller than r_y the stress is constant (and can be drawn as a horizontal line in Figure 2-3). The stress represented by the hatched area must therefore be redistributed to maintain equilibrium. To accommodate this stress, the plastic zone size will increase. This larger plastic zone (r_p) can be calculated by integration of equation (2-13) between 0 and r_y and results in a plastic zone twice the size of r_y:

$$r_p = \frac{1}{\pi}\left(\frac{K_1}{\sigma_y}\right)^2 \tag{2-15}$$

In plane strain a triaxial stress state exists because strain is constrained in the thickness direction. The resultant plastic zone can therefore to calculated to be approximately three times smaller because of the greater level of constraint around the crack tip. The plane strain plastic zone size can be estimated using:

$$r_p = \frac{1}{3\pi}\left(\frac{K_1}{\sigma_y}\right)^2 \tag{2-16}$$

The Irwin approach is thought to be a good plastic zone size approximation and will be used to calculate the plastic zone size in this work. It should be noted, however, that this is only a first order approximation and only considers the crack plane where θ=0. For mode I crack growth it can be shown that the plastic zone actually has a bean or figure of eight shape (Anderson, 1994), this has been confirmed using FE modelling (for example Dodds *et al*., 1991). A more detailed description of plastic zone size and shape can be found in Suresh (1998) and Uguz and Martin (1996) provide a useful review of the experimental methods typically used to investigate the plastic zone size.

2.3.2.3 Alternatives to LEFM

LEFM is useful for describing local crack tip stresses but is limited to situations where the plastic zone around the crack tip is well constrained by surrounding elastic material and where the plastic zone is smaller than the crack as defined by the small scale yielding criteria in equation (2-7). When LEFM conditions do not hold it is necessary to consider other methods to describe the stress field at the crack tip, and elastic-plastic fracture mechanics can be used. Crack tip opening displacement (CTOD) (Wells, 1963) and the *J* contour integral (Rice, 1968) are two alternative parameters.

Wells (1963) stated that as the yield stress at the crack tip is exceeded, plastic deformation occurs, causing blunting. It was observed that the degree of blunting was proportional to the toughness of the material and so it was concluded that this plastic deformation controlled fracture. As a result of crack tip blunting the distance between

the two flanks of the crack increases, this increase in distance is known as the crack tip opening displacement (CTOD or δ). The plasticity/blunting at the crack tip can be thought of as making the crack 'act' longer than it is (Irwin, 1961, cited in Anderson, 1994) and so the effective crack length may be described by $a+r_y$. It can be shown that δ and K are related by:

$$\delta = \frac{K_I^{\,2}}{m_1 \sigma_y E} \tag{2-17}$$

where m_1 is a constant that is approximately 1 for plane stress and 2 for plane strain (Anderson, 1994). Thus for materials with similar E, CTOD can be thought of as a normalisation of K by the yield strength of the material. In a fatigue situation, equation (2-17) can be altered to accommodate the alternating stresses thus:

$$\Delta\delta = \frac{\Delta K_1^{\,2}}{2m\sigma_y E} \tag{2-18}$$

The J contour integral is defined as a path-independent line integral, it represents the strain energy release rate of nonlinear elastic materials and may therefore be used as a parameter to characterise the crack tip conditions in nonlinear elastic materials. The J contour integral idealises elastic-plastic deformation as effectively non-linear elastic behaviour, i.e. it is assumed that the unloading curve is the same as the loading curve as illustrated in Figure 2-4. This is not the usual stress-strain relationship of a metal and so does not accurately model the unloading of a material. Suresh (1998) notes that the use of the J integral for cyclic loading violates the basic assumptions of the J integral but that experimental results give a reasonably good characterisation of fatigue crack growth, which is the main justification for the use of the J integral in fatigue. J will not be used in this work due to instrument limitations at high temperatures.

2.3.3 Stages of fatigue

2.3.3.1 Crack nucleation/initiation

Fatigue crack nucleation often occurs at areas of high local stress in a material. Microstructural, manufacturing, and environmental factors can cause high local

stresses and therefore act as initiation sites. Typical microstructural factors in Al-Si alloys include brittle phases, for example primary Si particles (Joyce *et al.*, 2003), pores (Yi *et al.*, 2003) and oxides (Gall *et al.*, 2000). Si particles have been shown to crack (Joyce *et al*., 2003) and decohere at the particle/matrix interface (Stolarz *et al.*, 2001) under cyclic loading and so act as initiation sites. Pores and other inclusions also act as stress raisers and are common artefacts of the casting process which reduce fatigue life (Wang *et al.*, 2001a)

Manufacturing features include sharp edges, notches and scratches. Component design usually necessitates that complex shapes with sharp edges and notches are produced, for example the combustion bowl edge and the gudgeon pinhole boss of a piston illustrated in Figure 2-5. Scratches are often the result of poor surface finish of a product. Manufacturing processes like extrusion can leave scratches in the direction that the material was drawn (Qamar *et al.*, 2004); these act as geometric stress raisers in a similar way as notches. The environment in which a material operates can be critical in determining crack initiation. Corrosive conditions can cause pitting (Vasudevan *et al*., 2001) or oxidation (Suresh, 1998). Corrosion sites can act as stress raisers and inhibit reverse slip upon unloading therefore giving a rough surface. Chemically aggressive environments can also cause grain boundary embrittlement.

Suresh (1998) notes that several micromechanical models have been developed to estimate the number of cycles for the nucleation of a fatigue crack to occur. When the material is defect free nucleation generally occurs where slip bands intersect a free surface (Tanaka and Mura, 1981) but in commercial alloys the models either regard defects as stress raisers which reduce the fatigue strength (Tanaka and Mura, 1982) or use analyses of dislocations around inclusions and non-shearable particles which cause the cracking or debonding of the particle (Morris and James, 1980).

2.3.3.2 Crack Propagation

Fatigue crack growth is usually split into three regimes; these can be seen in Figure 2-6, which is a log-log plot of the stress intensity factor and the crack growth rate. Regime I represents the low crack growth rates at low values of ΔK, and is called the near threshold region. In this region the crack growth rate decreases rapidly with a decrease in ΔK. Typically such data is collected by gradual load-shedding techniques

to determine the ΔK at which no further crack propagation is observed, ΔK_{th} (practically this is the ΔK value when $da/dN = 1\text{x}10^{-7}$ mm/cycle). At low values of ΔK crack propagation mechanisms may be similar to the early stages of crack growth after initiation. Regime I crack growth is often microstructurally dependent and cracks may grow along slip planes (Forsyth, 1962) experiencing the maximum resolved shear stress, which is 45˚ to the principal applied load; slip planes are along the {111} set of planes in Al alloys (Polmear, 1989). Non-shearable precipitates and grain boundaries can hinder the movement of dislocations along slip planes inhibiting slip band crack growth and so redirect the crack. In many metals the fracture surface is often characterised by smooth, transgranular facets giving it a quasi-brittle appearance.

Regime II crack growth occurs at mid ΔK levels and is often referred to as the Paris region. The crack growth rate in this regime is linear with ΔK on a log-log plot and so can be related by a power law as proposed by Paris and Erdogan (1963):

$$\frac{da}{dN} = C(\Delta K)^m \tag{2-19}$$

where C and m are material and environment dependent variables that may be fitted from a log-log plot of da/dN against ΔK. Crack growth in the Paris region is generally thought to be microstructurally insensitive. The fracture surfaces of this region are sometimes characterised by striations. Forsyth (1962), and Laird and Smith (1962) both proposed models for the formation of striations. In Forsyth's model the striations are thought of as ripples, whereas in the model of Laird and Smith they are considered troughs. However, both papers agree that each striation is caused by a single fatigue cycle and so show a particular point in the fatigue life of the material. Therefore striation spacing may be used to estimate da/dN in failure analysis.

When crack growth is in regime III, failure is imminent. The crack growth rate accelerates rapidly as K_{max} approaches K_Q. In this regime crack growth is sensitive to the microstructure (Suresh, 1998); for example in metal matrix composites (MMC's) static loading effects occur in the reinforcing particles i.e. they fracture in the plastic zone ahead of the crack tip (Srivatsan and Vasudevan, 1998). In Al-Si alloys static failure modes also occur and the crack is attracted to Si particles that fail ahead of the

crack tip (Kobayashi, 2002; Gall *et al*, 1999); these regions of damage form a weak path by which the crack may propagate and the crack therefore accelerates. Due to the high level of plasticity at the crack tip in stage III crack growth, LEFM assumptions may not be valid and so may not accurately describe the stress field at the crack tip (Lados, 2004).

Although fatigue life is often modelled using the three stages of fatigue growth corresponding to the three regimes shown in Figure 2-6, this behaviour is only associated with long cracks. The transition from a short crack to a long crack is not easily defined. Short cracks will be discussed and defined in more detail in the next section.

2.3.3.3 Short Cracks

Fan *et al* (2003) note that after the nucleation of a crack a microstructurally small crack forms and grows into a physically small crack. Suresh and Ritchie (1984) proposed four definitions for short cracks:

1. Fatigue cracks for which size is comparable to the scale of the microstructural features, for example the grain size or interparticle spacing, these are microstructurally small cracks.

2. Cracks where the near-tip plasticity is comparable to the crack size or when the crack is engulfed by the plastic strain field of a notch, these are mechanically small cracks.

3. Cracks that are larger than the local plasticity and the microstructure, but are smaller in length than 1 to 2 mm, these are physically small cracks.

4. Cracks that fulfil LEFM assumptions but which exhibit anomalies in propagation rates because of length dependence on environmental conditions, these are called chemically short cracks.

Short crack growth shows several anomalies when compared with typical near threshold propagation behaviour (shown schematically in Figure 2-7). The growth rates are typically higher than expected (Joyce *et al.*, 2003). Cracks can grow below the calculated ΔK_{th} value and there are fluctuations in the growth rate. The anomalies

are usually attributed to microstructural effects and the absence of crack closure as well as the invalidity of ΔK when applied to the short crack case (Suresh, 1998).

Grain boundaries can act as barriers to small fatigue cracks (Ludwig *et al.*, 2003) which retard and even arrest fatigue crack growth. The scale of the retardation is related to the relative mismatch in the crystallographic orientation of the grains; a larger mismatch generally equates to a more effective barrier (Han *et al*., 2002). This mechanism is associated with a change in the crack tip driving force due to crack deflection as the crack propagates into the new grain (Suresh, 1983) in addition to the restriction of dislocation movement between grains which inhibits slip band crack growth.

Many alloys contain hard phases in a soft matrix (e.g. Al-Si alloys and MMCs) and in such systems hard particles may also hinder fatigue crack growth (Shiozawa *et al.*, 1997). Consider a crack propagating through a soft phase, as it interacts with a hard phase: it must either crack the phase and propagate through it or deflect around the hard phase (Gall *et al.*, 1999). The deflection around the hard phase may change the crack tip driving force (Padkin *et al.*, 1987), forcing it out of the favoured Mode I direction. The deflection produces a more tortuous crack path thereby increasing the possibility of RICC.

The effect of crack closure (i.e. premature contact of the crack flanks behind the crack tip) is more important as the crack length increases (Singh *et al.*, 2006). For microstructurally small cracks the crack length may not be large enough to produce sufficient surface roughness usually associated with asperity crack closure. This can account for the higher crack growth rates associated with short cracks on a graph of *da/dN* versus $\Delta K_{applied}$, as the short crack data may be closure free.

The LEFM conditions of small scale yielding are described by equation (2-7); the condition states that the crack length must be greater than a value related to the yield strength and K_{IC}, short cracks may not obey this condition. Another basic assumption of LEFM is that continuum behaviour occurs (Suresh, 1998). Again short cracks may violate this condition because of the relative scale of the microstructure compared with the crack front: i.e. the retardation effect of grain boundaries and hard particles previously mentioned.

2.3.4 High temperature behaviour

Material properties are known to vary with temperature, for example in Al-Si casting alloys the 0.2% proof strength and UTS both decrease (Joyce *et al.*, 2003) as the test temperature increases above room temperature; this is typical of many alloy systems. The change in mechanical properties is often attributed to the increased mobility of atoms and dislocations as temperature increases (Dieter, 1988). Failure mechanisms may therefore vary with test temperature and at temperatures greater than 0.3-0.4 of the melting temperature (T_m) time-dependent processes may occur (Callister, 2000). Creep may be defined as the progressive deformation of a material under an applied load; it is therefore dependent on the load and also the temperature and length of time for which it is applied. Typically, creep is assessed by applying a constant load to a sample and measuring the change in its length (strain) as a function of time (BS EN 10291:2000). At different temperatures a different response may be expected.

Creep behaviour is usually split into three regimes (da C. Andrade and Chalmers, 1932), which can be seen in Figure 2-8; the slope of the curve is referred to as the creep rate. The primary creep region signifies a period of decreasing creep rate. The initial mobility of dislocations along slip planes is increasingly counteracted by an increase in strain hardening. Secondary creep is a linear region where creep is said to be in a steady state. Recovery processes, like climb, which increase dislocation mobility, are balanced (Mott, 1953) by strain hardening processes, which reduce dislocation mobility. Tertiary creep signifies a rapid increase in the strain rate until failure occurs; mechanisms that occur in tertiary creep include grain boundary sliding (Beere and Rutter, 1978) and cavitation (Zabler *et al.*, 2006). Grain boundaries slide because of the large shear stresses acting on them, this movement causes voids to form, which coalesce leading to fracture. Creep is discussed in greater detail in Evans and Wilshire (1993).

At high temperatures creep may affect fatigue crack growth, and in general this results in faster crack propagation rates (Klesnil *et al.,* 1993). The interaction between creep and fatigue may therefore be critical in materials that operate at high temperatures, for example gas turbines (Zabler *et al.*, 2006) and some car engine components (Chen and Daehn, 1991). The dominance of the each process is dependent on the

temperature. At very high temperatures creep can dominate and so the fatigue mechanism will be time dependent but at lower temperatures fatigue will be the most important mechanism and will be cycle dependent. Similar to fatigue, the creep mechanism produces a process zone in front of the crack (Carlson, 1996), these zones are superimposed on each other in creep fatigue. The use of LEFM and ΔK is still possible in some cases (Bensussan, 1990) but at high temperatures the plastic zone size may be large and so may not fulfil LEFM conditions (i.e. crack tip not constrained) in addition to containing a time dependent element contributed by the creep process.

Assessing the individual contributions of creep and fatigue in high temperature fatigue tests is difficult. Creep tests may be performed to ascertain a materials resistance to creep deformation (Chen and Daehn, 1991; Jaglinski and Lakes, 2004) and these studies suggest that Al-Si alloys can be susceptible to creep above 220˚C. However, this data does not reveal at what temperature time dependent processes would become the dominant mechanism in a fatigue test and how it may contribute to the evolution of damage. In the work of Joyce *et al.* (2003) the time dependent processes were assessed using different test frequencies under the premise that time dependent mechanisms would lead to differences in the fatigue crack propagation curves. The materials were investigated between the frequencies of interest in a car engine (15 – 50 Hz or 900 – 3000 rpm) and this demonstrated that Al-Si alloys, containing relatively high quantities of Cu and Ni, did not exhibit a frequency effect.

2.4 Micromechanisms of fatigue in Al-Si casting alloys

2.4.1 Fatigue crack initiation

It was identified in the previous section (2.3.3.1) that in commercial alloys fatigue cracks can initiate from microstructural stress raisers; in this section the relevant stress raisers in Al-Si casting alloys will be further explored. In Al-Si casting alloys fatigue cracks have been reported to initiate from four different microstructural features:

1. Pores (Shiozawa *et al.*, 1997; Zhang *et al.*, 1999; Seniw *et al.*, 2000; Buffiere *et al.*, 2001; Wang *et al.*, 2001a; Han *et al.*, 2002; Lee *et al.*, 2003; Yi *et al.*, 2003; Gao *et al.*, 2004; Yi *et al.*, 2006)

2. Oxides (Zhang *et al.*, 1999; Gall *et al.*, 2000; Wang *et al.*, 2001a)

3. Si particles (Shiozawa *et al.*, 1997; Zhang *et al.*, 1999; Stolarz *et al.*, 2001; Wang *et al.*, 2001a; Han *et al.*, 2002; Lee *et al.*, 2003; Joyce *et al.*, 2003)

4. Intermetallic particles (Caton *et al.*, 1999; Stolarz *et al.*, 2001; Joyce *et al.*, 2003)

Research by Wang *et al.* (2001a) indicates that pores are the most detrimental feature to the fatigue life of Al-Si alloys. Wang *et al.* (2001a) performed S-N tests on a series of mid Si containing, A356 alloys. Some of the alloys were hot isostatically pressed (HIPped) to reduce the level of porosity. By identifying the cause of failure in each S-N test Wang *et al.* (2001a) were able to use Weibull statistics to demonstrate that pores were more detrimental to fatigue life than oxides which were in turn more detrimental than eutectic Si particles and slip bands (Figure 2-9). Their work showed that in the absence of pores and oxides the fatigue life could be improved by an order of magnitude (at a maximum stress of 110 MPa). This is consistent with the work of Lee *et al.* (2003) who also demonstrated for a similar A356 alloy, over a stress range from 80 MPa – 180 MPa, HIPping could increase fatigue life by an order of magnitude. This was attributed to the reduction in the volume fraction of pores and their size. It should be noted that HIPping also causes modification of the Si phase (Caceres *et al.*, 1999) and so some of the improvement in fatigue lifetimes observed by Lee *et al.* (2003) may be attributed to this.

The work of Zhang *et al.* (1999) indicates that there is a critical pore size, 100 μm, below which other microstructural features are likely to cause fatigue crack initiation. This is contrary to the work of Wang *et al.* (2001a) who propose a smaller critical pore size of approximately 25 μm. The reason for the discrepancy in these results is not clear. In the work of Zhang *et al.* (1999) the maximum oxide size was larger, ~1000 μm, than in the work of Wang *et al.* (2001a) ~250 μm. It is therefore possible that oxides played a greater role in fatigue crack initiation in the alloys of Zhang *et al.*

(1999) and this may influence (or mask) the critical pore size for fatigue crack initiation. By careful optimisation of casting techniques, for example careful runner design to reduced the velocity and turbulent flow of the melt at the ingate, the oxide levels (Dai *et al.*, 2003) and therefore their effect on fatigue life can be reduced.

Several researchers (Zhang *et al.*, 1999; Seniw *et al.*, 2000; Gao *et al.*, 2002) agree that it is not just the size of the pore but its location relative to the sample surface that is important in determining if a crack will initiate from a particular pore. Using radiography Seniw *et al.* (2000) were able to locate large pores and produce fatigue samples with those pores in the sample gauge length. Large pores in the centre of the casting were observed to have little effect on fatigue life, whilst samples often failed from fatigue cracks, which initiated at smaller pores nearer the sample surface causing failure. The work of Zhang *et al.* (1999) indicated that pores (from which fatigue cracks initiated) were located within 30% of their maximum dimension from the free surface. However, these results were obtained using bend bar specimens and so the location of the initiating pores may be affected by the stress gradient in the samples, which is likely to promote initiation near the region of highest stress i.e. the tensile surface. Using finite element analysis (FEA) methods, Gao *et al.* (2004) were able to demonstrate that for a pore located near to the sample surface, the region between the pore and the surface exhibited a higher stress than at other locations around the pore. And in the research of Yi *et al.* (2003), it was shown that the maximum stress around a pore decreased the further it was from the free surface. These FEA results therefore confirm the observations of Seniw *et al.* (2000).

Finite element analysis of different pore shapes (Gall *et al.*, 2001; Gao *et al.*, 2004) suggests that the shape of the pore has little effect on the maximum stress concentration of the pore. The size and the location of the pore are the important parameters, which determine its effect on fatigue life (Yi *et al.*, 2006). However, modelling work of Gao *et al.* (2004) indicates that the highest stresses are found at the convex tips of pores and so fatigue cracks may be expected to form in these regions. The experimental work of Buffière *et al.* (2001) confirms this result showing that fatigue cracks do initiate in the high stress region at the convex tips of shrinkage pores (Figure 2-10).

All of the alloys discussed hitherto in this section are mid Si, A356 type alloys. It is known (Elliot, 1983) that adding Si to the eutectic level (~12 wt%) can improve the castibility of the alloy and reduce porosity levels. Shiozawa *et al.* (1997) tested mid and eutectic Si alloys. Over the stress range of 130 MPa to 180 MPa, the eutectic alloy exhibited an order of magnitude improvement in fatigue life compared with the mid Si alloy. In the mid Si alloy fatigue cracks initiated from pores but in the eutectic alloy initiation occurred at Si particles. It is therefore important to understand the mechanisms of fatigue crack initiation in the absence of pores.

Two micromechanisms are associated with initiation at Si particles: debonding of the particle/matrix interface (Shiozawa *et al.*, 1997; Zhang *et al.*, 1999; Han *et al.*, 2002) and particle failure (Stolarz *et al.*, 2001; Joyce *et al.*, 2003). In work on an A356 type alloy Zhang *et al.* (1999) were able to identify debonded eutectic particles at initiation sites on the fracture surfaces by their shape; some of the particles had a layer of the Al-matrix on their surface (identified by EDX). Zhang *et al.* (1999) use a load transfer (Eshelby, 1957) argument to explain why debonding occurred in the eutectic region: Si particles are stiffer than the matrix and so Si rich regions (i.e. eutectic regions) bear more load than the rest of the matrix. The stress concentration at the clustered Si particles in the eutectic region is sufficient to cause debonding to occur. In dense regions of Si particles multiple initiation events may occur (Han *et al.*, 2002; Stolarz *et al.*, 2001)

In general, debonding of the particle/matrix interface is observed in alloys that contain small Si particles, i.e. hypoeutectic alloys and the eutectic alloy of Shiozawa *et al.* (1997) that had undergone a solutionizing treatment and so had refined Si particles. Alloys containing primary Si particles were investigated by Joyce *et al.* (2003) and Stolarz *et al.* (2001) and particle fracture was observed in these alloys. Joyce *et al.* (2003) studied two near eutectic Si alloys (compositions given in Table 2-1), which contained different quantities of alloying additions (principally Cu and Ni). In room temperature tests, initiation occurred exclusively by the fracture of hard particles. In the alloy containing low quantities of Cu and Ni, initiation was only observed at fractured Si particles. Fractured Si particles also caused initiation in the alloy containing higher quantities of Cu and Ni. However, two of the eleven cracks observed were at intermetallic (AlNi containing) particles. Fracture at intermetallics

was also observed by Caton *et al.* (1999); in their study it was the AlFeMnSi phase that caused initiation and this was attributed to large size and complex 'Chinese script' morphology relative to the Si particles.

Han *et al.* (2002) made a qualitative observation that initiation occurred at larger Si particles. Joyce *et al.* (2003) quantitatively assessed the size of the Si particles that caused initiation and found that they were larger than the average Si particle size in each alloy. Joyce *et al.* (2003) commented that this may be attributed to a 'size effect' i.e. large particles contain more flaws and re-entrant angles and so there is a higher probability they will fail. A size effect in Si particles during tensile tests was also observed by Kobayashi (2002). Using the Eshelby inclusion method (Eshelby, 1957; Mori and Tanaka, 1973) Kobayashi (2002) estimated the strength of Si particles by performing tensile tests and observing when Si particles fractured. Smaller, eutectic particles (in a hypoeutectic alloy) were shown to exhibit higher fracture strength than the larger primary Si particles (in a hypereutectic alloy). Kobayashi offers no reason for this difference in properties but analysis of the method used to calculate the fracture strength provides a possible explanation. The Eshelby method assumes that particles are spheroids so that the stress inside the particle is constant; corners produce a stress concentration in the particle (Qin *et al.*, 1999). The shape of the eutectic particles may be well represented by a spheroid but primary Si particles were shown to exhibit a cuboid shape. Therefore the Eshelby inclusion method is likely to underestimate the maximum stress in primary Si particles because it does not account for the stress concentration produced by the corners of the particles. This may account for the difference in fracture strength between eutectic and primary Si particles. Small spherical particles are therefore thought to be beneficial in terms of fatigue life, as they require a greater far-field stress for fracture (Kobayashi, 2002).

2.4.2 Small fatigue crack propagation

Once initiation has occurred a fatigue crack may propagate away from the initiation site. The initial crack is described as a short crack and this term was defined in section 2.3.3.3. Short fatigue cracks are often microstructurally sensitive and the early stages of crack growth may be dependent on the initiation event. Joyce *et al.* (2003) observed that whilst many initiation sites may form (in their research many primary Si

particles were observed to fracture), not all become fatigue cracks. An effect of Si particle clustering at the initiation site was reported by Han *et al.* (2002) and Stolarz *et al.* (2001). It was observed that in dense clusters of Si particles, e.g. eutectic regions (Han *et al.*, 2002), many initiation events occurred and so the earliest stages of crack growth were dominated by linkage/coalescence of microcracks. Stolarz *et al.* (2001) quantified the clustering effect using the ratio of the maximum particle dimension to the mean distance between particles. When the Si particles were clustered (experimentally observed to be below a ratio of 7) multiple cracks were likely to form and crack coalescence was the dominant mechanism of growth. However, above this ratio the particles were sufficiently separated and a single, dominant fatigue crack formed. Cracks that initiate from pores also appear to form a single dominant crack (Shiozawa *et al.*, 1997; Han *et al.*, 2002; Ludwig *et al.*, 2003).

Classic short crack behaviour has been observed in Al-Si casting alloys. For example grain boundaries (Buffiere *et al.*, 2001; Ludwig *et al.*, 2003), and hard particles (Shiozawa *et al.*, 1997; Joyce *et al.*, 2003) act as 'barriers' to fatigue cracks and retard, or even arrest, fatigue crack growth. In addition crack growth rates are faster than in the equivalent long fatigue crack propagation tests (Caton *et al.*, 1999; Joyce *et al.*, 2003). Caton *et al.* (1999) showed that even when short fatigue crack growth data are compared with closure corrected ΔK_{eff} long fatigue crack growth data there may be a disparity between the curves. In a low yield strength Al-Si alloy the short and long fatigue crack growth curves did not converge. This was attributed to the violation of small scale yielding conditions thereby rendering the use of K invalid for short fatigue cracks in such low yield strength materials. In a higher strength Al-Si alloy investigated by Caton *et al.* (1999) and the alloys investigated by Joyce *et al.* (2003) the curves did converge. This highlights that the validity of K must be assessed on an individual alloy basis.

Gall *et al.* (1999) note that because of the 3-D nature of dendrites it is inevitable that a crack must propagate through inter-dendritic regions and therefore encounter Si particles. It has been reported by several researchers (Gall *et al.*, 1999; Shiozawa *et al.*, 1997; Joyce *et al.*, 2003) that when fatigue cracks are small (and so crack driving forces are also small) and encounter Si particles, they are deflected around the particle causing debonding of the particle/matrix interface (although Si fracture was observed,

but to a much lower extent). Si particles are stiffer than the matrix and so deflection around the particle is favourable in terms of the crack driving force (Padkin *et al.*, 1987). In addition, crack deflections increase the roughness of the crack (which may increase closure levels) and so debonding is a preferred crack propagation mechanism in terms of fatigue crack resistance (Shiozawa *et al.*, 1997). The exact nature of the debonding process is unclear, for example Zhang *et al.* (1999) report that some of the debonded particles had a layer of Al-matrix on them (whilst some presumably did not), and Gall *et al.* (1999) report that debonding is evident from the "smooth and rounded surface of the exposed Si particles" which suggest that no layer of Al-matrix is present.

Shiozawa *et al.* (1997) report that below a crack length of 1 mm the likelihood of a crack encountering a eutectic Si cluster was independent of the crack length. Above a crack length of 1 mm the preferentiality for eutectic regions was shown to increase as the crack length increased; this signified a change in the crack growth mechanism as the crack path became increasingly interdendritic. A change in crack growth mechanism was observed by Gall *et al.* (1999) and Verdu *et al.* (1996). Gall *et al.* (1999) made a qualitative assertion, from analysis of fracture surfaces, that the crack avoided Si particles at ΔK values less than 7 MPa$\sqrt{m}$. Above this value of ΔK crack growth was increasingly interdendritic and as a result showed preferentiality for hard particles. Gall *et al.* (1999) also identified a change in the dominant mechanism of particle failure from debonding to fracture at this value of ΔK.

2.4.3 Long fatigue crack propagation

Near threshold behaviour in conventional Al-Si casting alloys is influenced by the size of the 'important' microstructural features in the alloy. Depending on the composition and production conditions of the alloys this may be the Si particle size (Lee *et al.*, 1995; Lados *et al.*, 2006) or the dendrite size (Lados *et al.*, 2006). Lee *et al.* (1995) investigated a series of eutectic (~12 wt% Si) alloys where the size of the Si particles was the primary difference between the alloys. The mechanisms of debonding of the particle/matrix interface and particle fracture were observed. Debonding principally occurred in the alloy with the smallest Si particles (max. dimension 2.5 μm). In the alloys containing the intermediate and coarse Si particles

(max. dimension 5.5 μm and 8.9 μm respectively) fracture was the principal particle failure mechanism.

It was reported by Lee *et al.* (1995) that debonding caused deflections of the crack, which increased crack roughness. From qualitative observations the deflections caused by fractured particles were smaller than the deflections caused by debonding. The alloy containing fine Si particles exhibited a higher level of closure and therefore a higher ΔK_{th}, which was accounted for by the larger deflections. Lee *et al.* (1995) state that the fracture strength of Si particles is inversely proportional to their size, which is why fracture occurs in larger particles. This is consistent with the size effect observed for short crack initiation at particles; Joyce *et al.* (2003) suggested that the size effect could be attributed to the probability of particles containing flaws being proportional to the particle size. Lados *et al.* (2006) make no differentiation between the mechanisms of debonding or particle fracture and contrary to Lee *et al.* (1995) report that coarser Si particles increase the level of roughness and therefore RICC. Since Lados *et al.* (2006) make no mention of the particle failure mechanism it is possible that this may be the difference between the two studies. For example Joyce *et al.* (2002), (investigating eutectic alloys) and Chan *et al.* (2003) (investigating mid Si alloys) report that the likelihood of each mechanism is related to the stress intensity factor. Below a ΔK value of 6-8 MPa√m debonding was the principle particle failure mechanism but above this value of ΔK, particle fracture was more common; a similar observation was reported by Gall *et al.* (1999) who investigated naturally initiating fatigue cracks. It may be that debonding was the primary failure mechanism of the Si particles in the study of Lados *et al.* (2006) and so it follows that if particles do not fracture, larger particles will result in larger deflections that will lead to increased roughness and therefore high ΔK_{th} values.

The dendrite size was reported to be an important microstructural feature by Lados *et al.* (2006); a schematic diagram detailing the micromechanisms of crack growth is presented in Figure 2-11. A low Si alloy (~1 wt% Si) was shown to exhibit a rougher crack than a mid Si alloy, which in turn was rougher than the eutectic alloy. The dendrites in mid Si alloys were elongated and the secondary dendrite arm spacing was reported to be smaller than the diameter of the dendrites in the low Si alloy. The larger dendrite size in the low Si alloys allows for larger deflections and therefore a

rougher crack. The controlling feature in the eutectic alloy was the distribution and size of Si particles; in the alloys studied by Lados *et al.* (2006) the deflections caused by Si particles were smaller than those in the low and mid Si alloys. The roughness of the cracks affected the threshold value: the low Si containing alloy had the highest level of RICC and therefore the highest ΔK_{th} value and the eutectic alloy had the lowest level of RICC and therefore the lowest ΔK_{th} value.

In the Paris region there is little effect of particle size on fatigue crack growth: Lee *et al.* (1995) report similar crack growth rates for alloys containing fine, medium and coarse Si particles. Additionally Lados *et al.* (2006) show that grain size has no appreciable effect on crack growth rates during all stages of long fatigue crack propagation. However, both Joyce *et al.* (2002) and Lados *et al.* (2006) report that the crack growth rate is dependent on the amount of non-Al additions in the alloy; a greater quantity of non-Al elements results in faster crack growth rates. It is in the Paris region that the change in the dominant particle failure mechanism changes from debonding of the particle/matrix interface to particle fracture (Gall *et al.*, 1999; Joyce *et al.*, 2002; Chan *et al.*, 2003).

Several authors agree that Si particles are preferentially sought out in the latter stages of fatigue crack propagation (Lee *et al.*, 1995, Verdu *et al.*, 1996; Gall *et al.*, 1999; Joyce *et al.*, 2002; Chan *et al.*, 2003; Lados *et al.*, 2004). In alloys with a dendritic structure this results in characteristic inter-dendritic crack growth. This mechanism was experimentally observed, during interrupted fatigue tests, by both Lee *et al.* (1995) and Chan *et al.* (2003) who report that damage formed at particles ahead of crack tip. In later observations the crack coalesced with the damage. Qualitatively the number of failed particles increased with the value of ΔK. Lee *et al.* (1995) observed that both the debonding and particle fracture mechanisms occurred; this was again associated with the particle size. Whereas in the final stages of fatigue crack growth Chan *et al.* (2003) reports that particle fracture was the principal particle failure mechanism. The coalescence of the main fatigue crack with the failed particles ahead of it results in faster crack growth rates (Lee *et al.*, 1995).

Joyce *et al.* (2002) and Lados *et al.* (2004) both report that 1) the K_Q value is lower and 2) the crack growth rate before final failure is higher in alloys containing the greatest quantity of non-Al additions. This is attributed to the greater volume fraction

of hard particles in these alloys and therefore the greater number of static failures (particle fracture or debonding) that are likely to occur ahead of the crack tip. In the later stages of fatigue crack growth it may therefore be surmised that a high Si (or intermetallic) content leads to a reduction in fatigue resistance. Therefore, whilst Si particles retard crack growth and therefore improve fatigue performance near threshold they are detrimental to fatigue crack performance at high values of ΔK.

2.4.4 High temperature fatigue mechanisms

Little research has been published regarding the effect of high temperature on the fatigue behaviour of Al-Si casting alloys. Al-Si casting alloys are widely used in car engines (Ye, 2003) for applications such as the cylinder head (Fischersworring-Bunk *et al.* 2006) and pistons (Haque and Maleque, 1998). Therefore an understanding of the fatigue behaviour up to a temperature of 400˚C is important to ensure the alloys are 'fit for service' and to allow for alloy development. As previously mentioned in section 2.3.4, time dependent processes may be expected to occur above $0.4T_m$ (Callister, 2000) and so may be significant in Al-Si alloys which operate at temperatures up to approximately $0.8T_m$.

Myers and Hurd (1990) investigated the fatigue performance of eutectic Al-Si alloys at 300˚C. Some of the samples were preloaded at the test temperature and a maximum stress of 40 MPa for 70% of the lifetime to rupture. Other samples were aged for the same amount of time but not under load. In addition, pistons composed of the same materials were engine tested, during these tests the materials were thermally and mechanically loaded over a range of temperatures, loads and frequencies. S-N tests were performed on the pre-creep and no-creep samples: at high strains (where lifetimes were shorter than 100,000 cycles) the materials gave equivalent lifetime results, at lower strains the pre-creep samples exhibited shorter lifetimes. Analysis of the no-creep samples showed that the damage (particle fracture and debonding) was confined to a region near the crack. However, in the pre-creep samples damage occurred throughout the specimens and took the form of interdendritic voids and fractured particles; this damage was similar to that observed in the engine test samples around the combustion bowl (this is the maximum stress and temperature region in a piston). Analysis of the initiation sites indicated that the same features caused

initiation in both the pre-creep and no-creep samples and that these features were oxides, pores and Si particles approximately 100-150 μm in size. It was concluded that the damage caused by creep did not affect initiation in Al-Si alloys. Creep damage was thought to provide a weak path for short fatigue cracks in their early stages (where they are most microstructurally sensitive), which resulted in a reduction of fatigue life compared with the no-creep samples.

Joyce *et al.* (2002; 2003) also investigated the high temperature fatigue performance of two eutectic Al-Si alloys; the compositions are given in Table 2-1. Fatigue tests were performed at 200˚C and 350˚C; these temperatures were identified as being characteristic of those experienced at the gudgeon pin boss and the combustion bowl (identified in Figure 2-5). At elevated temperature the initiation of fatigue cracks was associated with the fracture and debonding of primary Si particles and so was similar to that observed at room temperature. Long fatigue crack propagation tests showed that at a test temperature of 200˚C both alloys exhibited improved fatigue resistance compared with their RT performance. From post-failure analysis it was identified that the critical value of ΔK at which the dominant failure mechanism changes from debonding of the particle/matrix interface to particle fracture (Gall *et al.*, 1999; Joyce *et al.*, 2002; Chan *et al.*, 2003) was higher at elevated temperature. The improvement in performance at 200˚C was attributed to the increased level of debonding which is the preferable particle failure mode. At 350˚C the low Cu and Ni containing alloy exhibited a frequency effect on fatigue performance, crack propagation rates were faster at 50 Hz compared with those at 15 Hz. This was not observed in the tests on the high Cu and Ni containing alloy. This indicates that the phases formed by the addition of Cu and Ni do make the material more resistant to time-dependent processes, but the exact mechanism(s) by which this occurs is unknown.

2.5 Summary

To optimise the various properties of Al-Si casting alloys, many alloying elements are added and as a result the alloys exhibit complex multiphase microstructures. With improvements in casting techniques it is possible to reduce the levels of porosity and oxides, which are detrimental to fatigue life, it is therefore important to understand how other microstructural features, for example: Si and intermetallic particles (hard

particles), affect fatigue crack initiation and subsequent propagation. Fatigue cracks have been reported to initiate as a result of particle failure and this may be via the mechanism of particle fracture or debonding of the particle/matrix interface. Classic short crack behaviour has been observed in Al-Si alloys and grain boundaries and Si particles retard crack growth. At low values of ΔK and when Si particles are small (~2.5 μm) a fatigue crack is likely to be deflect around intact particles and cause debonding at the particle matrix interface. Due to a size effect, large particles may fracture especially at (relatively) high values of ΔK (>6-8 MPa√m at RT) causing static failure modes ahead of the crack tip and therefore an acceleration in the crack growth rate.

Given their high temperature applications in car engines, few studies were found in the available literature on the high temperature fatigue properties of Al-Si alloys. Initiation appears to occur at the same microstructural features as at RT. Creep causes damage in the interdendritic regions, which can accelerate short fatigue crack growth. At high temperature there are increased levels of debonding, instead of particle fracture, during fatigue propagation and so at 200˚C the alloys exhibited improved fatigue performance. Additions of Cu and Ni resulted in an improved resistance to time dependent mechanisms during fatigue crack propagation at 350˚C.

Alloy	Si (wt.%)	Cu (wt.%)	Ni (wt.%)	Mg (wt.%)	Fe (wt.%)	Mn (wt.%)	Ti (wt.%)	Zr (wt.%)	V (wt.%)	P (ppm)
AE160	11.22	3.1	2.27	1.05	0.3	0.08	0.17	0.15	0.06	53
AE413	11.15	0.94	0.96	0.88	0.49		0.07	-	-	35

Table 2-1 Composition of the alloys studied by Joyce *et al.* (2002; 2003).

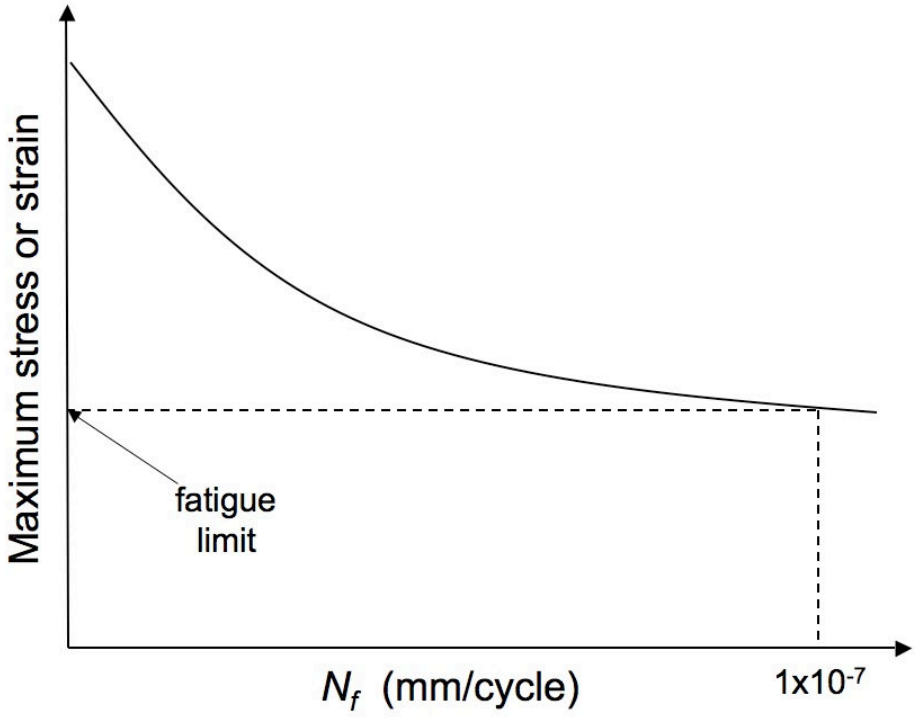

Figure 2-1 S-N curve for a material exhibiting no fatigue limit.

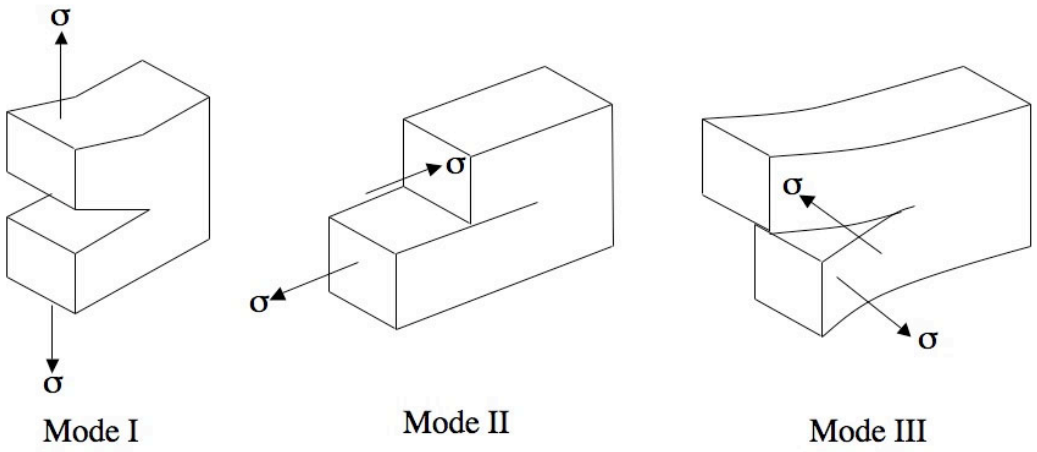

Figure 2-2 The three basic modes of loading.

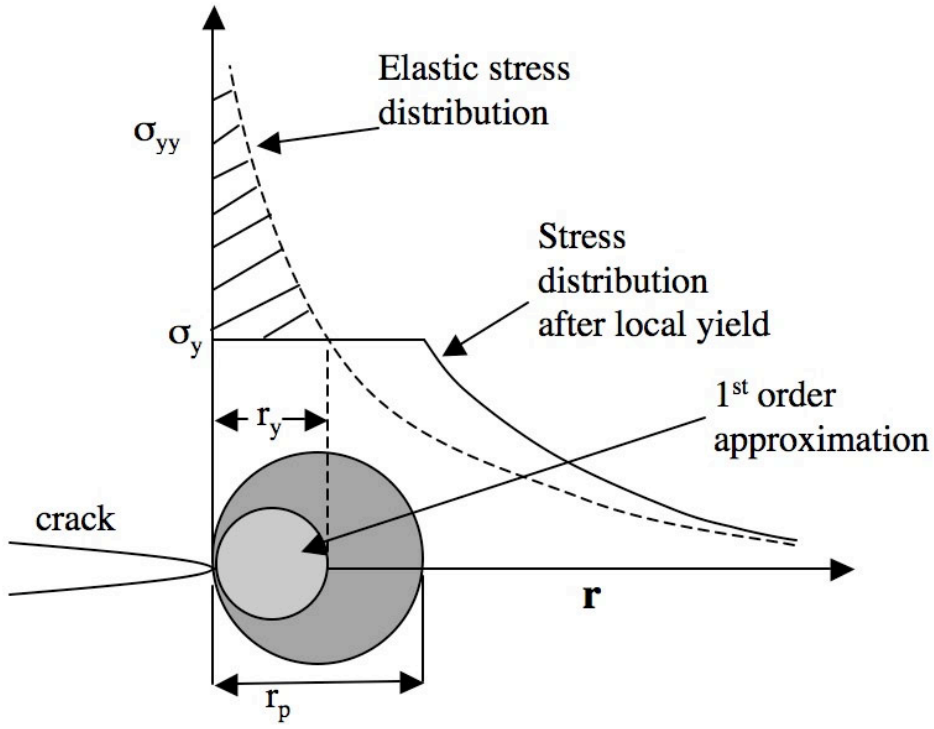

Figure 2-3 Schematic diagram showing the estimated plastic zone sizes at a crack tip on a graph of stress versus distance from the crack tip when θ=0. After Anderson (1994).

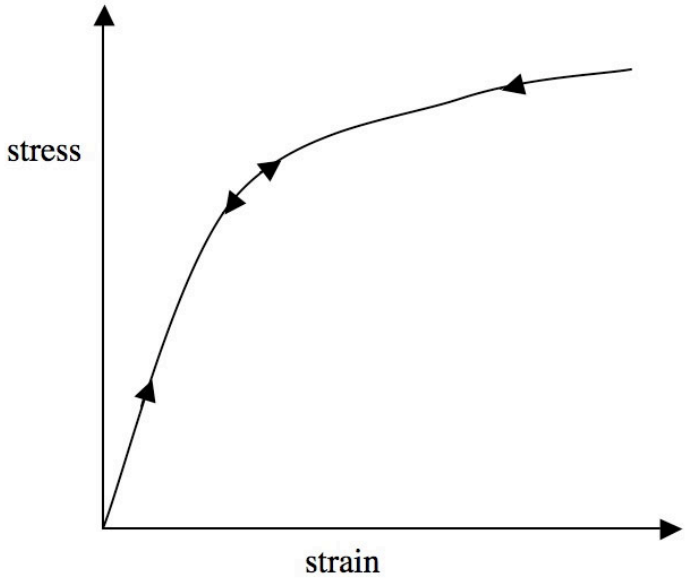

Figure 2-4 Schematic of the stress strain curve assumed for the *J* integral.

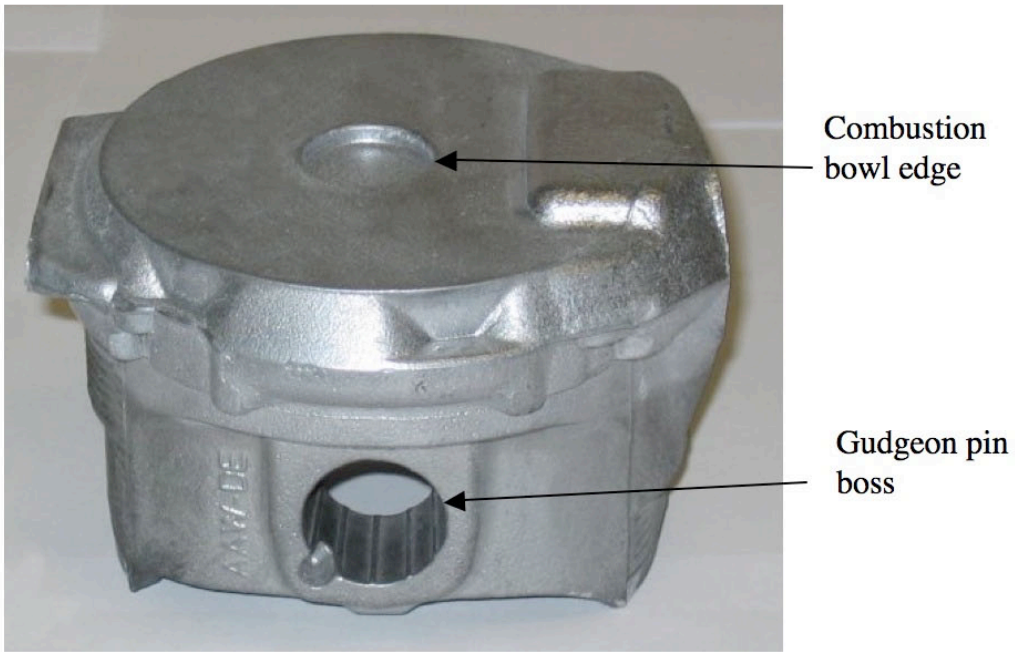

Figure 2-5 Photograph of a light vehicle diesel engine piston from the die prior to shaping and polishing.

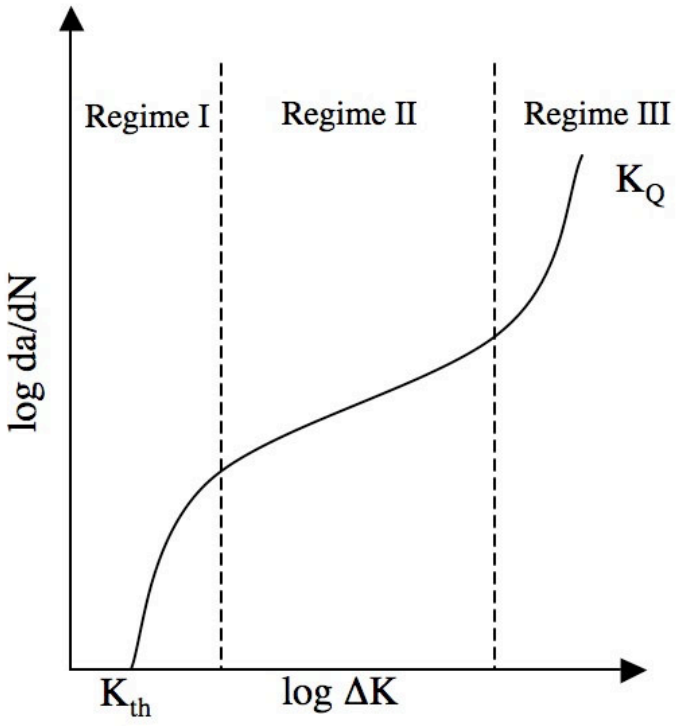

Figure 2-6 Stages of fatigue crack growth.

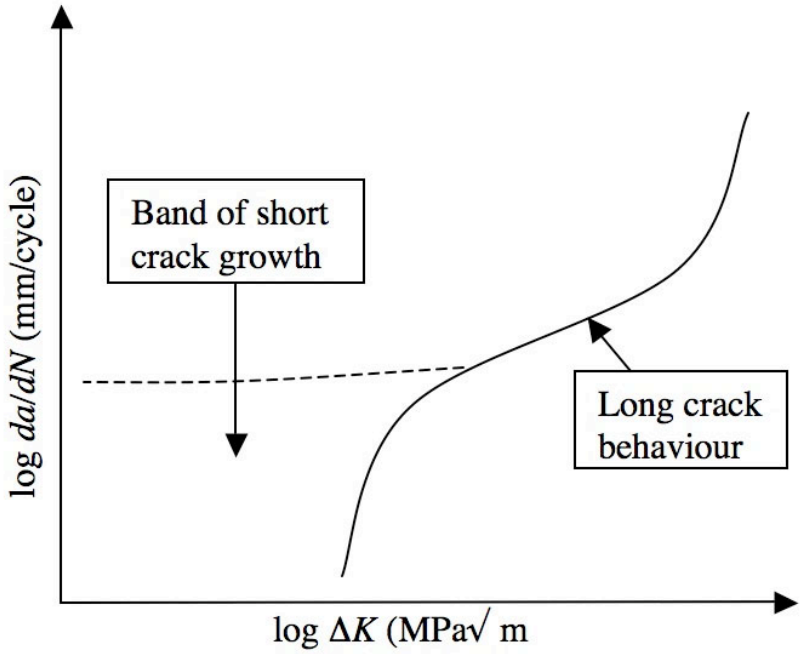

Figure 2-7 Schematic diagram showing crack propagation behaviour for short and long cracks.

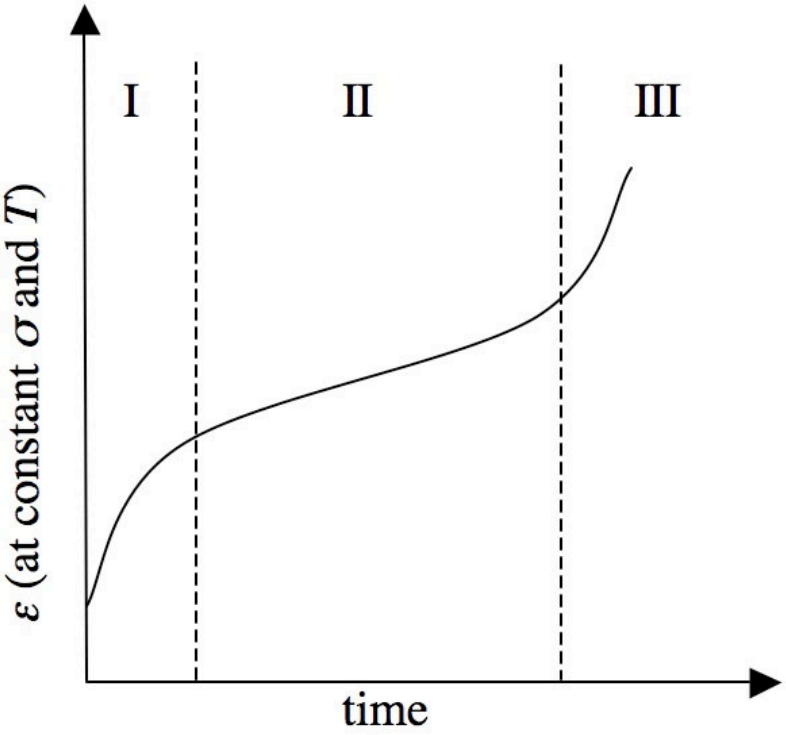

Figure 2-8 Schematic diagram of typical creep data where strain is plotted against time.

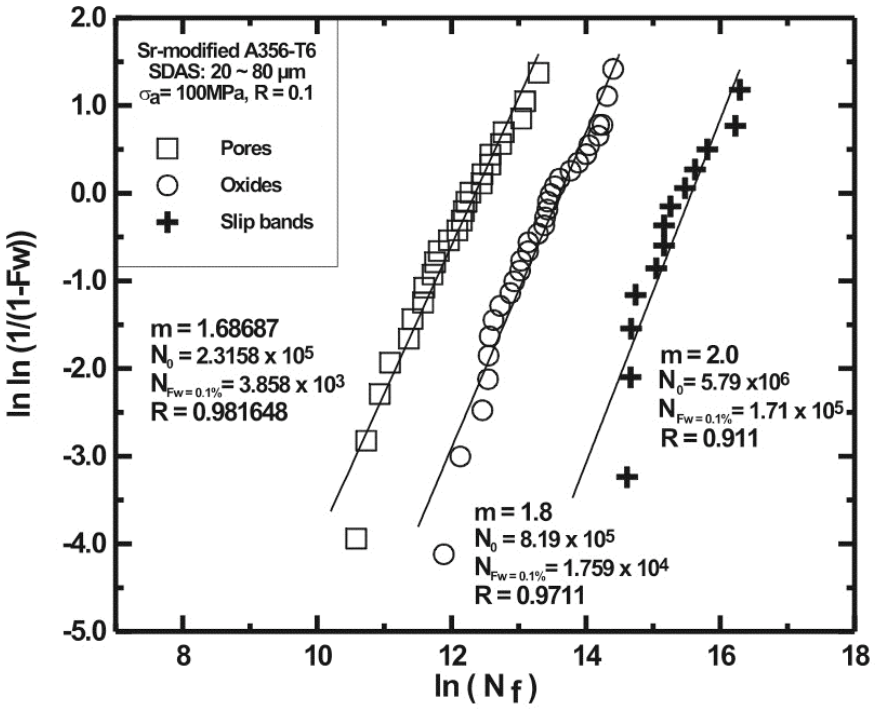

Figure 2-9 Weibull statistics plot showing the effect of pores, oxides and slip bands and Si particles on fatigue life from Wang *et al.* (2001a).

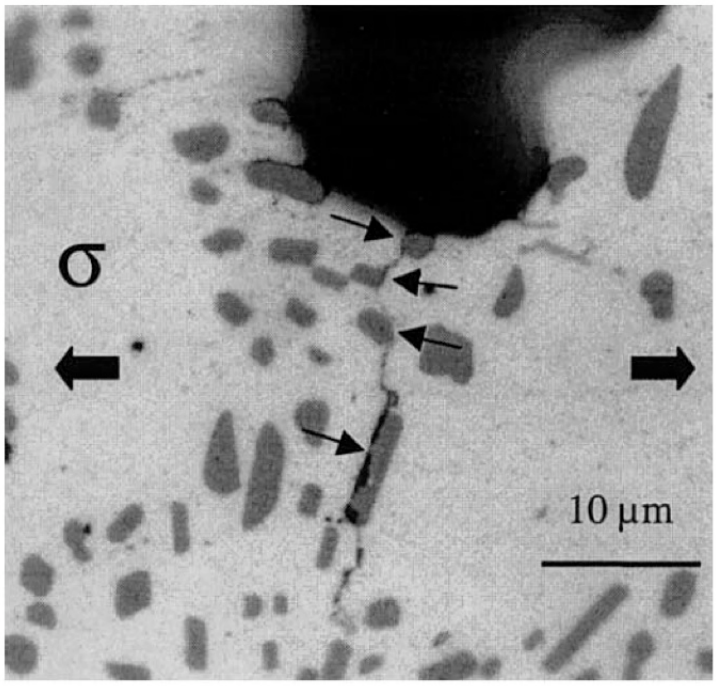

Figure 2-10 Debonded Si particles causing fatigue crack initiation at the high stress region near the concave tip of a shrinkage pore from Buffière *et al.* (2001).

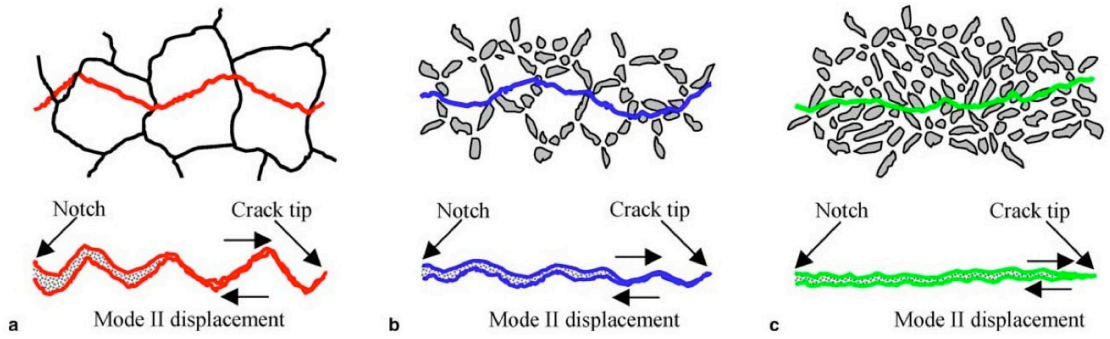

Figure 2-11 Schematic diagram from Lados *et al.* (2006) showing the micromechanisms of fatigue near threshold in (a) a low Si alloy (b) a mid Si alloy and (c) a eutectic alloy.

Chapter 3

Materials and Methods

3.1 Introduction

This chapter introduces the materials studied and the experimental methods used during the course of this work. The experimental methods were chosen for their suitability to investigate the link between microstructural features and fatigue in order to gain an understanding of the micromechanisms of fatigue in these alloys. As well as providing the detailed experimental parameters used, short descriptions of the background theory will also be presented for some of the more novel techniques used in this study.

3.2 Materials

Four development cast aluminium alloys have been investigated in this project. The materials were supplied by Federal Mogul (FM) and are being considered for use in the pistons of light vehicle diesel engines. The compositions of the alloys may be found in Table 3-1; the composition levels were obtained using optical emission spectroscopy by the manufacturer. The principal difference between the alloys is the Si content:

- LVD25 - the Si is at a 'near' eutectic level
- LVD26 – the Si is at an intermediate level (similar to that of an A356 alloy)
- LVD27 – the Si is present as an impurity

There are two variations of LVD26: one that contains Sr and another that does not. The alloy that contains Sr will be referred to as LVD26 mod (for modified as Sr

modifies the Si morphology) and the alloy without Sr will be referred to as LVD26 unmod. The differences between the remaining alloy additions are minimal and within the manufacturer alloy specification tolerances.

The materials were supplied as unfinished pistons, which had been cast on their side and quenched in water from the die (the feeder and the riser are identified in Figure 3-1). The standard FM aging (or stabilising) treatment for these alloys is 8 hours at 230˚C after which the pistons are air-cooled; this is the as-received condition. The peak aging time for these alloys is typically of the order of thirty minutes and so they are considerably over aged to dimensionally stabilise the pistons, and so minimise shape change 'in-service'. Figure 3-1 shows a whole piston with a sectioned piston crown placed on the top of the piston; all the test samples used in this study have been taken from piston crowns. All fatigue and tensile test samples were extracted from the crown, perpendicular to the feed direction. Unless stated otherwise (e.g. in the cyclic stress-strain data presented later) the alloys have been further aged at 260˚C for 100 hours to simulate in-service thermal exposures prior to testing.

3.3 Metallography

Metallography samples were hot mounted in Struers Polyfast resin (Bakelite). The mounting press applies a 3kN load at a temperature of 170˚C (below the aging temperature of the alloys) for 7 minutes. The samples were ground and polished to an OPS finish using the route described in Table 3-2. To aid identification of the many phases present in the alloys, the samples were etched in a solution of 0.5%HF in water. The etch gives several of the intermetallic phases a characteristic colour and is the same as that used by Edwards (2002) and so aids phase identification.

Two microscope systems have been used in this project to capture micrographs. The first system used a black and white DVC 1310M camera attached to an Olympus BH2 stereomicroscope; the software used was XCAP (EPIX Inc, USA). The second system used a colour Prosilica GC1350 camera also attached to an Olympus BH2 stereomicroscope, the software used was the Prosilica GigE sample viewer (Prosilica Inc, Canada). Most SEM analysis (except the phase mapping) was performed on a JEOL JSM 6500F. This system is fitted with an Oxford Inca 300 energy dispersive X-ray suite. A typical accelerating voltage of 15 kV was used.

3.4 Image analysis

Quantitative image analysis was used to characterise the microstructures of the alloys studied. The main text used to inform this analysis is that of Underwood (1970) which is a useful guide to the background theory and practical use of quantitative stereology. The point fraction analysis (PFA) and line fraction analysis (LFA) techniques described by Underwood were performed on two-dimensional micrographs. Finite body tessellation (Boselli *et al.,* 1998), which is a thresholding technique, was also attempted but this method is not well suited to the materials in this study since the grey levels are not sufficiently distinguishable.

Point fraction analysis uses a grid of points placed on a random but representative image of the microstructure. If a point falls on a phase of interest this counts as a positive score (1) and if it hits the matrix, for example, it counts as a 0. Each point in the grid is assessed and the score added up. This score is divided by the number of points used in the grid (P_T) and gives a value for the point fraction (P_P) of the phase of interest. This process is repeated several times (in this study 10 times) on other random samples of the microstructure and the average value of P_P calculated.

Although this method is simple it is very useful because it can be used to estimate the volume fraction (V_f) of the phase of interest in the alloy. If a test point is placed at random in a test volume (V_T) containing a volume of α (V_α) the probability of the point hitting the α phase ($P(\alpha)$) is:

$$P(\alpha) = V_\alpha / V_T \tag{3-1}$$

For many randomly placed points (P_T) the expected number of points lying within the α phase (P_α) will be:

$$P_\alpha = P_T . P(\alpha) = P_T . (V_\alpha / V_T) \tag{3-2}$$

and so we can see that:

$$P_\alpha / P_T = V_\alpha / V_T \tag{3-3}$$

hence:

$$P_P = V_f \tag{3-4}$$

A similar derivation can be performed for the lineal (or line) fraction (L_L) and the area fraction (A_A) and so it can be shown (Underwood, 1970) that V_f is related to these easier-to-measure quantities:

$$V_f = A_A = L_L = P_P \tag{3-5}$$

The micrographs used in this study were taken at a magnification of x500. Lower magnification images did not provide sufficient resolution to differentiate between some of the smaller microstructural features, particularly the Si particles in the LVD26 mod alloy. All the results of point fraction analysis presented in this study are the average of at least 10 measurements.

The number of random points that should be used in the grid for point fraction analysis was investigated using the LVD26 mod alloy. In this study all phases except the Al-matrix were counted as particles; the results are presented in Figure 3-2. The point fraction seems reasonably insensitive to the number of points used. Using 99 points or greater (i.e. the final 4 columns in Figure 3-2) the range of the standard error values are similar and all the mean P_P values are within similar bounds. Using less than 99 points (i.e. the first 3 columns) the standard error range is larger, also the mean P_P is greater and outside the bounds of the standard error of the final 4 columns. From these results it was determined that the minimum number of points that should be used is 99, since the standard error is small and the mean P_P is within acceptable bounds. However, because of the similar the P_P of the final 3 columns, 120 points were used.

Lineal fraction analysis should give the same average result as point fraction analysis (according to equation (3-5)). Lineal fraction analysis was used in the investigation of the fatigue samples to quantify the fraction of particles along the fatigue fracture profiles. In order to ensure that LFA could be used for this investigation it was necessary to check the method on a sample of random microstructure. LFA was performed using a straight line, and also a representative section of crack profile (which is made up of lots of smaller straight lines) to ensure both methods gave similar values for L_L and compared with the equivalent P_P from PFA.

In lineal fraction analysis a line of known length is placed on the micrograph (at a random angle). When the line intercepts a particle, the intercept distance is measured. The distance of the individual particle intercepts are summed and divided by the total line length to give the lineal fraction. This is repeated 10 times (on random sections of the microstructure) to give an average value. It can be seen in Figure 3-3 that the results of the PFA, LFA using a straight line and LFA using a representative length of the crack profile gave the same fraction of particles (within the standard error) for the LVD25 alloy. This confirms that this method may be used to quantify the particles found on the fatigue crack profiles. ImageJ software (National Institutes of Health, USA) and x500 magnification micrographs were used for this analysis.

LFA is a more time consuming technique to perform than PFA, however, it can be used to give extra information about the microstructure. Using LFA it is possible to obtain the mean intercept length (L_3) and the mean free distance (λ). The mean intercept length can be used as a measure of space-filling cell size (*i.e.* grain or dendrite size), equation (3-6), or particle size, equation (3-7).

$$L_3 = 1/N_L \tag{3-6}$$

$$L_3 = (V_f)_\alpha / N_L \tag{3-7}$$

$$\lambda = 1 - (V_f)_\alpha / N_L \tag{3-8}$$

where N_L is the number of intercepts (of the phase of interest) per unit length of test line. The mean free distance is a measure of the mean edge-to-edge distance for the microstructural constituent of interest and is calculated using (3-8). λ is sometimes referred to as the inter-particle distance (Zhang *et al.,* 2002). L_3 and λ require no assumptions to be made about the microstructure and so are very general measures.

Several other properties have been used to describe the microstructures of similar materials to those studied in this project: secondary dendrite arm spacing (*SDAS*) (Kalka and Adamiec, 2006; Lados, 2004; Shyam *et al.,* 2005; Stolarz *et al.,* 2001; Wang *et al.,* 2001b; Zhang *et al.,* 1999), equivalent circle diameter (Han *et al.,* 2002; Lados, 2004; Yi, 2004; Zhang *et al.,* 2002), maximum particle length (Stolarz *et al.,* 2001) and Feret length (Yi, 2004; Underwood, 1970). The *SDAS* is essentially the L_3 for a space-filling cell (3-6), but the lines are not placed on the microstructure at

random; they are placed down the length of the dendrite, hence ensuring that undesirable regions of the microstructure (large interdendritic clusters for example) do not affect the result. The equivalent circle area can be used to describe equiaxed dendrites, eutectic Si particles and pores. It uses the area of the feature but assumes the feature is spherical so that the diameter may be calculated. Both these features can reflect aspects of the microstructure well, but require assumptions to be made about the feature they represent unlike L_3 and λ.

The maximum particle length (l_{max}) and Feret length (l_f see Figure 3-4) are suitable measures to describe individual particles (e.g. eutectic Si particles). However, these measures are not suited to microstructures where there are large networks of interconnected particles, this is illustrated in Figure 3-4. When the particles are separate, as in the top two images, Feret length and maximum particle length can be easily measured. When the microstructure is interconnected it is not possible to perform these measurements on all the particles.

Thresholding image analysis techniques were investigated as part of this study. ImageJ and the Tesselation Analysis Program (TAP) designed by Boselli *et al.* (1998, 1999, 2004) can be used. The thresholding technique uses micrographs or tracings of the micrographs. Pixels in a specified greyscale range are selected as object pixels and given a value of 1. The remainder of the pixels are assigned a value of 0. Object pixels may be counted to give an estimate of the V_f, or further analysed to provide stereological information. A requirement of the technique is that the features stand out from the background matrix, in terms of greyscale differentiation, and in the tessellation program the particles cannot be interconnected. Unfortunately the microstructures of the materials studied do not fulfil these requirements adequately and so this method was not pursued.

3.5 Aging study

The samples for the aging study were taken from the central section of the piston crowns. The samples used were of size 5 mm x 5 mm x 2 mm and were in the as-received state (and so they had already undergone the manufacturer's standard heat treatment of 8 hours at 230˚C). The aging study was performed at a temperature of 260˚C (±2˚C) in a well-characterised oven. This temperature was chosen because it

simulates the typical in-service exposures of a piston; although regions such as the top surface do experience higher temperatures. 260˚C is also the temperature that the mechanical testing samples are aged at for 100 hours prior to testing. The samples were soaked for the following lengths of time: 1, 2, 4, 8, 16, 32, 64, 128, 256, 512, and 1024 hours. Based on an annual mileage of 10000 miles, at an average speed of 35 miles per hour, the longest aging time represents approximately 3.5 years of engine use.

The change in material properties as a result of the aging process was assessed using Vickers hardness tests. The tests were performed on a calibrated Vickers testing machine following the method outlined in BS EN ISO 6507-1 1998. A load of 10 kg and a dwell time at maximum load of 10 seconds was used. An average of five indents made on each sample was used to give the mean hardness value.

Differential scanning calorimetry (DSC) was performed on the as-received samples and samples aged at 260˚C for 100 hours. The samples were made from small disks approximately 1mm deep with a diameter of 3 mm. The samples were ground to a 4000 grit finish to remove surface oxides. DSC was performed using a Perkin Elmer Pyris 1 machine. The tests were carried out at a heating rate of 10 ˚C/min. Baseline testing was performed on pure Al and heat capacity effects (from the difference between the heat capacities of the reference sample and aged sample) were corrected for by applying a polynomial at temperatures where no reaction was expected (approximately 200˚C and just before melting at ~470˚C).

3.6 Tensile Tests

Tensile tests were carried out at room temperature (RT), 200°C (the typical temperature of the gudgeon pin boss) and 350°C (the typical temperature of the combustion bowl edge). All the samples were soaked at 260°C prior to testing to simulate in-service thermal exposures. The sample geometry may be seen in Figure 3-5 and complies with the ASTM E8M standard. The samples were extracted from the piston crown and their longest dimension was parallel to the feed direction. The room temperature tensile tests were performed on a 50 kN Instron 5569 and the tensile tests at 200°C and 350°C were carried out by Federal Mogul using a Zwick Z050 machine fitted with a three stage oven which controls the temperature to within

±2°C. All tests were carried out using a loading rate of 1 mm/min. The load information was obtained from the calibrated load cells on the tensile test machines and the extension information was obtained by attaching an extensometer to the sample.

3.7 Strain gauge tests

Strain gauge tests were carried out on four point bend bar specimens at RT to obtain the applied stress on the tensile surface of the samples. Kyowa strain gauges with a gauge length of 5 mm were used. The materials were aged at 260˚C for 100 hours prior to testing. The samples tested were size 12 mm x 12 mm x 80 mm. The experimental setup was similar to that used in the short fatigue crack tests and can be seen in Figure 3-6. The samples were ground to a 4000 grit finish and the surface was prepared using a conditioner and a neutraliser. Strain gauges were attached to the tensile surface, between the inner two rollers. Wires were soldered to the outputs of the strain gauges and attached to a strain gauge amplifier and reader where they could be monitored. The load was applied to the sample using an Instron 8502 servo-hydraulic testing machine.

3.8 Cyclic stress-strain tests

The cyclic stress-strain tests were carried out by Federal Mogul on the LVD25 alloy only. The samples underwent the standard aging treatment of 8 hours at 230˚C and were then further aged at their test temperature for 100 hours. The sample geometry was the same as that used in the tensile tests (Figure 3-5) but the ends were threaded. The experiments were performed using a Zwick Z050 machine fitted with a three-stage oven and an extensometer was attached to the sample to measure the strain. The tests were performed at 0.5 Hz and 50 Hz. The hysteresis loops were allowed to stabilise for 1000 cycles before the samples were tested.

3.9 Instrumented hardness testing

Instrumented hardness testing differs from conventional hardness tests (such as Vickers and Brinell tests) in that the loading and unloading cycle are continuously

monitored. This allows for additional information to be obtained, for example the Young's modulus. Such information can be used to characterise the local microstructural properties and so it is possible to obtain the Young's modulus of the different phases that may be present in the microstructure.

3.9.1 Description of Nanoindenter

A Micromaterials Nanotest machine was used for nanoindentation and a schematic diagram of the nanoindenter is presented in Figure 3-7. The main moving part of the nanoindenter is the pendulum. The pendulum is attached to the supporting stage via a frictionless pivot. Attached to the top of the pendulum is a coil, adjacent to this is a permanent magnet attached to the supporting stage. When a current is applied to the coil it forms an electromagnet, which attracts the coil towards the permanent magnet. This provides the movement of the pendulum. It is the current that is supplied to the coil that controls the load at which an indent is performed. A third of the way down the pendulum is a limit stop so that the coil and magnet do not touch.

Below the pivot is the indenter. There is a small housing into which different indenter tips may be located. All the work presented in this report has been carried out using a Berkovich indenter. In line with the indenter is a parallel plate; a second plate is attached to the supporting stage. The two plates act as a capacitor, and when the indenter moves the change in distance between the two plates changes the capacitance, which is monitored to give depth information during indentation. The whole system is maintained in a temperature-controlled cabinet. Over 24 hours the temperature in the cabinet is accurate to ±0.4°C.

3.9.2 Calibration

The nanoindenter essentially monitors two electrical signals: one for the load information and one for the depth information. It is therefore important that these signals are correctly calibrated so that the nanoindenter gives accurate data. Because of the sensitive nature of the indenter the calibrations must be performed regularly to ensure the machine remains accurate. There are five main calibrations, namely the load calibration, depth calibration, compliance calibration, bridge box calibration, and the diamond area function (DAF) calibration.

The load calibration ensures that the current applied to the coil corresponds to a known load. During this calibration, weights are hung on the balance weight and a current is applied to the coil until the pendulum is moved to its equilibrium position. This is done for a series of weights. It is then possible to use the law of moments to calculate the current that should be applied to give a certain load at the indenter tip. This calibration is performed every four months.

The depth calibration may be performed with a steel ball tip or a Berkovich tip. During the procedure an indenter is bought into contact with a fused silica sample. The sample stage moves a known distance and the change in capacitance is measured. This is performed several times and so the change in capacitance may be related to the distance moved. This calibration is also performed every four months.

The compliance calibration is performed each week. This test comprises six indents at loads between 150-200 mN on a fused silica reference sample. Since the sample properties are known, the compliance value may be fixed to give the correct values of hardness and modulus for the reference sample. This test is also a useful check for the load calibration.

The bridge box calibration must be performed daily. This ensures that the range of movement over which the capacitor plate measures is equal to the full range of voltage that the nanoindenter hardware can measure. The trace of this test is also used to check that the operation of the pendulum is smooth, for example bent springs in the pivot will show as a ‘bump’ on the trace.

The DAF calibration is performed once the previous calibrations are complete. The purpose of the calibration is to ensure that the indenter tip is properly calibrated so that correct values may be obtained at all indent depths; this is especially important at low penetration depths where the effect of the indenter tip being imperfect is most noticeable. The procedure comprises a series of experiments over the depth range of the machine. The experiments are analysed and the values of hardness and modulus are fitted to a polynomial, which is then used to correct future results. For depths greater than 200 nm the general equation for indenter area is accurate. In depth details of all the calibration procedures may be found in the Micromaterials Nanotest Handbook (Beake *et al.,* 2003).

3.9.3 Background theory

A schematic representation of a typical loading-unloading curve is presented in Figure 3-8a. The sample is loaded until it reaches the maximum depth (h_t) at a corresponding maximum load (P_t). The indenter is allowed to dwell for the specified period of time and then unloads leaving a residual indent of depth h_f. The difference between h_t and h_f shows that there has been some (but not total) elastic recovery. Sneddon (1965) proposed that during the initial part of the unloading stage (where the curve is linear) the contact area between the sample material and the indenter remains constant and so exhibits elastic, 'Hertzian' behaviour. It is this part of the loading curve that may therefore be used to calculate the elastic modulus for the indented material. Pharr *et al.* (1992) showed that a power law could be fitted to the unloading curve in the form:

$$P = \alpha(h - h_f)^m \tag{3-9}$$

where h is a point on the unloading curve. By differentiating for the point at the start of the unloading curve (i.e. h_t) it is possible to calculate the gradient, S.

To calculate the modulus and hardness it is necessary to know the contact area between the indenter and the material at the point of maximum load. An assumption of the original work by Sneddon (1965) and Pharr *et al.* (1992), which is also a limiting factor in the applicability of the method (Oliver and Pharr, 2004), is that sink-in occurs. Sink-in is the result of the displacement of material downwards during the indentation process and is illustrated in Figure 3-9. Sink-in results in the reduction of the area of contact between the indenter and the material, and so it is necessary to calculate the reduction of the indent depth due to sink-in (h_s) in order to calculate the contact depth (h_c) and therefore contact area (A). h_s may be calculated using the gradient of the unloading curve with the following relationship:

$$h_s = \varepsilon_1 \frac{P_t}{S} \tag{3-10}$$

where ε_1 depends on the indenter geometry and is 0.75 for a Berkovich indenter. In Figure 3-8b it can be seen that $h_c = h_t - h_s$ and so the contact depth can be calculated using:

$$h_c = h_t - \varepsilon \frac{P_t}{S} \tag{3-11}$$

For a Berkovich indenter the contact area (A) can be calculated using:

$$A = 24.50\, h_c^2 \tag{3-12}$$

It is possible to calculate the reduced modulus (E_r) using:

$$E_r = \frac{\sqrt{\pi}\, S}{2\sqrt{A}} \tag{3-13}$$

E_r is actually a function of the sample and the indenter material properties as shown in equation (3-14) and so may be used to calculate the modulus of the sample (E_s) if the indenter modulus (E_i) and the Poisson ratio (ν) for the sample and the indenter are known. For Al $\nu_s = 0.33$ (Deiter, 1988) and for a diamond indenter $\nu_i = 0.07$ and $E_i =$ 1141 GPa (Beake *et al.,* 2003).

$$\frac{1}{E_r} = \frac{\left(1 - \nu_s^2\right)}{E_s} + \frac{\left(1 - \nu_i^2\right)}{E_i} \tag{3-14}$$

The hardness value (H) can be simply calculated by dividing the maximum load by the contact area calculated in equation (3-12):

$$H = \frac{P_t}{A} \tag{3-15}$$

As has previously been mentioned, an assumption that sink-in occurs is made in the analysis of Sneddon (1965) and Pharr *et al.* (1992). This limits the applicability of the Pharr *et al.* (1992) method for calculating the modulus and hardness because this is not always the case. Tabor (1951) notes that pile-up may also occur and describes sink-in and pile-up as the displacement of metal during the indentation process; these mechanisms are illustrated in Figure 3-9. Sink-in is the displacement of the material downwards and pile-up is the displacement of the material upwards. If a material does not sink-in (as the theory predicts) then the contact depth (and so contact area) will be underestimated. Bolshakov and Pharr (1998) note that the contact area can be underestimated by as much as 60%, which can lead to a large over-estimation of the material hardness using the Pharr *et al.* (1992) method.

The degree of pile-up has been shown to be dependent on the amount a material work hardens (Oliver and Pharr, 2004). Materials which work harden, for example annealed metals, are less prone to pile-up as the material on the sample surface next to the indenter hardens during deformation thus constraining the flow of the material underneath, this inhibits pile-up. However in materials which do not work harden (for example soft metals which have been cold worked) the surface material is unable to constrain the flow from underneath. Bolshakov and Pharr (1998) also identified that in materials where elastic recovery is low ($h_f/h_t > 0.7$) pile-up may occur.

The Pharr *et al.* (1992) method of calculating modulus and hardness is the method recommended in the British Standard BS EN ISO 14577-1:2002. No approach is currently suggested for correcting for pile-up when using a Berkovich indenter and so instrumented hardness results need to be carefully assessed and the required caveats made when pile-up may occur.

3.9.4 Samples

Nanoindentation samples are typically of size 10x10x10 mm although they can be smaller than this. The samples were taken from the central section of the piston crown. The samples were aged at 260°C for 100 hours so that they were consistent with the mechanical testing samples. The samples were mounted in Bakelite and one face of the sample was polished to a 1μm finish using the polishing route described in Table 3-2. The opposite face of the embedded sample was ground to a 600 grit finish so that the non polished face of the sample was visible. An automatic polisher was used to ensure that the faces remained parallel. Both sides of the sample were exposed so that the only compliance not accounted for by the calibration procedure was that of the sample. The samples were mounted on an aluminium sample stub, which in turn was attached to the positioning stage during indentation. A schematic diagram of the nanoindenter is presented in Figure 3-7 and this shows the position of the sample stub during indentation.

3.9.5 Test procedure

The sample stage is used to bring the sample into contact with the indenter. The sample is then retracted 15 μm away from the indenter and displaced in the Z or Y

direction to a virgin piece of material. The experimental details, for example the maximum load or maximum depth, loading rate and number of indents are set in the Nanotest software (Micromaterials, UK). Once the experiment details are input, the indentation procedure is automatic.

The minimum indent depth and load possible should be set with a knowledge of the noise in the nanoindenter system; it is important that the noise has little effect on the results. It was found experimentally that the noise in the depth dimension was ~4 nm and in the load dimension 0.03 mN. To ensure that the error in the results due to noise was less than 2% it was determined that the minimum load should be 1.5 mN and with a minimum h_t of 200 nm. An indent depth of 750 nm (which corresponds to a load of ~9 mN in Al i.e. well above the recommended minimum parameters) was used, the dwell time was 15 seconds and the loading and unloading rate was 0.1 mN/second.

The data analysis (i.e. calculation of hardness and modulus using the Pharr *et al.* (1992) method) is automated and performed by the Nanotest software. The software simply requires the user to review the loading-unloading curves and remove any incorrect data (*e.g.* data that does not start at zero depth and load) and then run the analysis program. The data is output as text files which can be used in Microsoft Excel (Microsoft Corporation, USA) or Matlab (The Mathworks Inc. USA).

3.10 Long fatigue crack growth tests

3.10.1 Samples

Long fatigue crack growth tests were performed on SENB tests of size 12x12x80 mm. One sample was extracted from the centre of each piston crown, perpendicular to the feed direction. A slit of approximately 0.25 *a/W* (where *a* is the slit/crack length and W is the width of the sample) was placed in the top surface of the sample using an electro discharge machine (EDM). The ends of the sample were tapped and drilled to allow current wires to be connected easily to the sample using bolts. The samples were aged at 260˚C for 100 hours prior to testing to simulate in-service thermal exposures.

3.10.2 Test procedure

Long fatigue crack growth tests were carried out using an Instron 8501 equipped with a high temperature furnace. The tests were conducted at room temperature (as a baseline test) and at 350˚C (the typical temperature of the combustion bowl edge). The temperature of the 350˚C tests was controlled using a thermocouple spot-welded to the sample; the temperature was controlled to within ±1˚C. All the tests were carried out in four-point bend with a span of 10 mm. To ensure that the load was evenly spread between the loading rollers a self-aligning rig was used; this corrects for any tilt in the loading chain or inaccuracies in the specimen geometry. In all the tests, an *R-ratio* = 0.1 and a sinusoidal waveform with a frequency of 15 Hz was used (15 Hz simulates the engine idle speed).

To monitor crack growth a two-point probe direct current potential difference (DCPD) method was used. A constant current source was connected to the sample via the tapped holes in either end. Two wires were spot welded at opposite ends and on opposite sides of the slit (as shown in Figure 3-10) to measure the potential difference (p.d.) as the crack grew. Because the measured voltage was small an amplifier with a gain of x10000 was utilised. The voltage was recorded using a data logger. As a result of the current used the baseline tests were not, strictly speaking, performed at RT but slightly above (at 40˚C). With hindsight it may have been better to perform the baseline testing at 70˚C so that the temperature could have been more accurately controlled with an oven.

In the RT tests the crack was grown away from the EDM slit for 0.5 mm at ΔK = 5.5 MPa$\sqrt{m}$. For the RT samples it was possible to use a load shedding technique to obtain a threshold ΔK value. The load shedding technique is outlined in BS ISO 12108:2002. The crack is grown through four plastic zones and the ΔK is then reduced by 10%; this is repeated until the threshold value is obtained. Threshold is defined as the ΔK where the crack growth rate (*da/dN*) is less than 1×10^{-7} mm/cycle which, with the resolution of the system used, equates to ~7.5 hours with no change in p.d. Once at threshold the samples were left to grow out at constant load (increasing ΔK) until failure.

In the 350˚C samples the crack was grown at RT away from the EDM slit for 0.5 mm at ΔK=5.5 MPa√m. The samples were then heated to test temperature. The theoretical, monotonic plastic zone ahead of the crack tip is large at 350˚C and so it was not possible to use the load shedding technique at this temperature. Instead the crack was grown at constant ΔK (decreasing load) to an estimated crack length of a/W = 0.425 (approximately 4 plastic zones). The cracks were then left to grow out at the same load (P_{max}=1.4 kN) so that regardless of LEFM validity the curves may be compared.

3.10.3 Data analysis

The number of cycles and the p.d. were recorded throughout each experiment. A reading was taken every second and so a lot of data was produced. An automated method to reduce the data was investigated but manually reading the points off the graph of p.d. versus cycles was found to be the most convenient method. The p.d. is related to the crack length; the relationship was initially modelled using finite element methods by Joyce *et al.* (2002b). This relationship was used to estimate the crack length during the experiment but was not always exact (since the p.d. wires were not always in exactly the same place). Post-failure the final and initial crack length could be measured on the fracture surfaces and the data adjusted accordingly. ΔK was determined using the method described in BS ISO 12108:2002 and da/dN was calculated using the secant method (also described in BS ISO 12108:2002).

3.10.4 Fractography

One fracture surface was sectioned for image analysis. To protect the fracture surface it was cold mounted prior to sectioning. A schematic diagram of the fracture surface is presented in Figure 3-11, the dashed lines show where the sample was sectioned. The line e-f was at a low crack growth rate (~ $3\text{x}10^{-7}$ mm/cycle at RT and ~ $3\text{x}10^{-6}$ mm/cycle at 350˚C) and the line g-h was at a high crack growth rate just before failure (~ $5\text{x}10^{-4}$ mm/cycle at RT and ~ $3\text{x}10^{-4}$ mm/cycle at 350˚C). The sections were polished using the route in Table 3-2 and several micrographs were taken for each section to give a total length of ~3 mm of the fracture profile. LFA (see section 3.4) was used to assess the fraction of hard particles along the fracture profiles. It was not possible to differentiate sufficiently between the different phases and so any phase

that was not the α-Al matrix was counted as a hard particle. The remaining fracture surface was used for SEM analysis.

3.11 Small fatigue crack tests

3.11.1 Samples

Small fatigue crack tests were performed on bend bar specimens of size 12x12x80 mm. One sample was extracted from the centre of each piston crown, perpendicular to the feed direction. The top surface of each specimen was polished to a 1μm finish and the corners were rounded off to minimise the possibility of initiation from machining marks on the corners of the samples. The samples were aged at 260˚C for 100 hours prior to testing to simulate in-service thermal exposures.

3.11.2 Test procedure

Short fatigue crack tests were carried out using an Instron 8501 at room temperature. It was not possible to perform the tests at 350˚C because the materials are too ductile at this temperature, and the samples just bend (without failing). The loads used were determined experimentally for each material and temperature to try to ensure that the tests would fail at equivalent lifetimes; a lifetime of 80,000 cycles was the target. A dummy sample was tested at an initial load corresponding to 90% σ_y, after 100,000 cycles with no failure the load was increased by 10% σ_y and the test continued for another 100,000 cycles. This process was repeated until the sample failed thus identifying the loading conditions that would produce fatigue failure. The stresses that the samples were tested at are given in Table 3-3.

All the tests were carried out in four-point bend with a span of 20 mm using the self-aligning rig described in section 3.10.2. In all the tests, an *R-ratio* = 0.1 and a sinusoidal waveform with a frequency of 15 Hz was used. The tests were interrupted periodically and acetate replicas of the tensile surface between the two inner rollers (i.e. the region of maximum stress) were made to record an image of the top surface and any cracks within it.

3.11.3 Data analysis

The final acetate replica was examined and several cracks identified; micrographs of the cracks were taken. Working back through acetates a record of crack growth and the point of fatigue crack initiation (or the point when the crack became visible at the surface) could be obtained. Micrographs and SEM images of the selected cracks were obtained. SEM analysis was also used to examine the fracture surfaces for sub-surface defects. Phase mapping (see section 3.12) was performed on several initiation sites to give a thorough analysis of the phases associated with the initiation of fatigue cracks. Synchrotron X-ray tomography (see section 3.14) was also performed on several of the samples to give a detailed analysis of the region underneath the initiation site and along the fatigue crack.

In all cases the loads used corresponded to a stress greater than the 0.2% proof stress. At these loads simple beam theory (which is linear elastic) does not apply. In the RT samples the strain gauge test results allowed for the calculation of the strain on the tensile surface which could be cross referenced against the tensile test curves to estimate the stress. The method of Scott and Thorpe (1981) was used to calculate ΔK values; *da/dN* was obtained using the secant method and so crack propagation curves could be obtained.

3.12 S-N fatigue tests

3.12.1 Samples

S-N tests were conducted on samples of size 6x6x60 mm. Eight samples were extracted from the centre of a piston. The top surface of each specimen was polished to a 1μm finish and the corners were rounded off to minimise the possibility of initiation from machining marks on the corners of the samples. The samples were aged at 260˚C for 100 hours prior to testing to simulate in-service thermal exposures.

3.12.2 Test procedure

All the tests were carried out at RT in four-point bend with a span of 10 mm using the self-aligning rig described in section 3.10.2. In all the tests, an *R-ratio* = 0.1 and a

sinusoidal waveform with a frequency of 15 Hz was used. The tests were interrupted after 10,000 cycles and acetate replicas of the tensile surface between the two inner rollers (i.e. the region of maximum stress) were made to record an image of the top surface and any cracks within it. The tests were carried out at different load levels and the stress was calculated using the strain gauge and tensile test data. The fracture surfaces were assessed using an SEM

3.13 Phase mapping

The phase mapping was performed in conjunction with Prof. Rachel Thomson and Dr. Chun-Liang Chen at Loughborough University. Using the results of simultaneous electron backscatter diffraction (EBSD) and energy dispersive X-ray (EDX) analysis, it is possible to produce maps of the phases present in a specified region of the microstructure. By combining the results of the two techniques, phase identification is enhanced compared with the individual methods and this is especially useful in complex multiphase microstructures. In this work phase mapping has been used to map the regions around fatigue crack initiation sites and along the fatigue cracks.

Phase mapping was performed on several short fatigue crack test samples. The samples were polished using the route presented in Table 3-2 before the fatigue tests were performed. Ideally the samples should undergo a final polish using a vibration polisher or an ion beam mill to ensure excellent surface (and near surface) preparation (Chen 2006). However, this was not possible on these samples and so the fifth polishing stage was repeated after the fatigue tests for an extended period (in the order of 15 minutes) to ensure the best finish possible.

The phase mapping work was performed in collaboration with Loughborough University and simultaneous EBSD and EDX were carried out using their LEO 1530VP FEGSEM. The data was collected using Delphi software (EDAX, USA) and analysed using TSL OIM 4 software (EDAX, USA). This software uses the International centre for diffraction data (ICDD) database to analyse the EBSD data. The EDX data is analysed by setting chemical bounds for the phases that are likely to be present. Loughborough University has expertise in this area and have built up over several years a database of the chemical compositions of the phases present in these

alloys. The EBSD and EDX data is compiled by OIM software, which produces the phase maps.

3.14 X-ray computed tomography

3.14.1 Background

X-ray computed tomography (X-ray CT) is a 3-D imaging technique. It is one of the non-invasive imaging techniques routinely used in hospitals for the imaging of surface and deep structures within the human body. X-ray CT is also a useful tool in the field of materials research and is an attractive imaging technique for characterising the microstructures of materials (Salvo *et al.*, 2003). X-ray CT may be used to identify microstructural features such as pores (Buffiere *et al.,* 2001; Hamilton *et al.* 2003), and secondary phases (Khor *et al.,* 2004). It may also be used to monitor fatigue crack growth (Ferrie *et al.,* 2005) or other damage evolution (Horstemeyer *et al.,* 2003) in materials providing an otherwise difficult to obtain insight into the interaction between damage mechanisms and the microstructure. Furthermore, in metals, X-ray CT is a non-destructive method.

X-ray CT uses the principles of radiography: X-rays are directed at the sample and the transmitted beam is recorded on the opposite side of the sample (typically using a CCD detector). As the X-ray beam passes through the sample it is attenuated via interactions such as the photoelectric effect and Compton scattering. The effectiveness of a material in attenuating X-rays is defined by its attenuation coefficient which is a function its density, atomic number and the energy of the X-ray. The 2-D X-ray image produced contains the superimposed information of the volume. The basic principles of X-ray CT image capture and reconstruction are presented in Figure 3-12. By rotating the sample around an axis perpendicular to the X-ray beam, it is possible to acquire radiographs at many angles (through 180˚ or 360˚ depending on the system). The images may then be reconstructed using a back projection algorithm (ASTM E 1441-00); this is schematically shown in Figure 3-13. In Figure 3-13a the incident X-ray passes through the sphere and is detected. Back projection consists of projecting each view back along a line corresponding to the direction it

was collected; this is schematically shown in (with projections from only 4 angles) Figure 3-13b, the reconstructed image forms where the lines converge.

3.14.2 Microfocus computed tomography

Compared with the synchrotron radiation system, discussed in the next section, microfocus CT systems are less expensive and smaller. They can typically fit in a small room, which makes them a suitable laboratory tool. Electrons are produced by an electron gun and accelerated towards a target (which is typically made of tungsten or molybdenum). Upon hitting the target, one of the reactions that occur is the emission of X-rays; these are filtered to produce a conical beam of X-rays. The sample is placed on a rotating stage between the target and the detector (in the Southampton system this is a CMOS flat panel detector); the system is shown schematically in Figure 3-14.

Because of the conical nature of the X-ray beam the projected image is naturally magnified, the closer the sample is to the target the greater the magnification. For small samples (< 6 mm) the maximum resolution is limited by the spot size of the electron beam; in the Southampton system this is ~5 μm. In addition whilst high magnification images can be obtained for small samples (giving a voxel size smaller than 5 μm^3) the inherent resolution of the images is still 5 μm. In large samples (> 6 mm in diameter) the maximum resolution is limited by number of pixels in the CCD detector array (1200x1200 pixels in the Southampton system). For example, the minimum voxel size when a 20 mm^3 volume is scanned is 16.7 μm^3.

In conventional microfocus CT systems the X-ray beam is polychromatic. Because of this the resulting reconstructed volumes can suffer from ‘beam hardening’. This occurs when the energy spectrum of the X-rays change; this is attributed to the greater attenuation of lower energy X-rays. Fewer low energy X-rays will be transmitted through the thickest part (e.g. the centre) of the sample compared with the edge of the sample and so the average energy of the transmitted beams will vary between these two sections. This ultimately affects the greyscale value recorded by the detector and results in a gradient of the grey level between the centre and the edge of the reconstructed volume. This can be seen to occur along the line AB in Figure 3-15.

The beam hardening effect may be reduced by using filters in the beam line, or corrected later in the post-processing,.

Cylindrical samples with a diameter of 4 mm were utilised in this study. A molybdenum target was used to produce the X-rays and suitable parameters for the electron gun were found to be a filament current ~ 70 μA and an accelerating voltage ~ 45 kV. No filters were used in the X-ray beam. Approximately 1800 images were taken throughout a 360˚ rotation. The CMOS detector used a digital gain of 4 and a frame rate of 1 fps. Two images were taken at each point and averaged to reduce noise in the images. White and black reference images were also obtained to correct for inconsistencies in the detector. The images were reconstructed using Inspect-X CT Client (X-Tek Systems Ltd., UK) software, and the images analysed in VG Studio Max (Volume Graphics GmbH, Germany).

3.14.3 Synchrotron computed tomography

Synchrotron radiation is produced in a different way to that previously described for microfocus CT, and necessitates the use of much larger facilities; for example the circumference of the storage ring at the European Synchrotron Radiation Facility (ESRF) is 844 m. Synchrotron radiation benefits from having a bright and parallel beam and the beamline at ESRF used in this project (ID19) is specially designed to ensure that the beam is also highly coherent for CT imaging.

A schematic diagram showing the basic design of a synchrotron facility is presented in Figure 3-16. Electrons are produced in an electron gun and initially accelerated in a linear accelerator. They are then transmitted into a circular accelerator (the booster synchrotron) where they are accelerated to the required energy (typically 6 GeV). The electrons are then injected into the storage ring in discrete bursts. Electrons travel in straight lines and so magnets are required to ‘bend’ the electrons around the storage ring. There are three types of magnets in the beamline (ESRF, 2007):

1. Focusing magnets – These are found in straight sections of the storage ring and are used to ensure the electron beam remains focused.

2. Bending magnets – These are used to direct the electron beam around the storage ring. It is the change in direction that causes synchrotron radiation to be produced and so the beam lines start at these magnets.

3. Undulators – These are used by some beamlines to produce a higher intensity beam. The undulator forces the electrons to follow a 'wavy' trajectory. The radiation caused by this movement constructively interferes hence increasing the intensity of the beam.

An advantage of the ID19 setup is that the X-ray beam may be either polychromatic (as in the microfocus CT system) or monochromatic. Using a monochromatic X-ray beam prevents beam hardening from occurring (Salvo *et al.,* 2003). Due to the very small cross-sectional area of the electron beam used to create the X-ray beam, the X-ray beam is parallel (i.e. diverges very little) (Cloetens *et al.,* 2001) and so the magnification effect that occurs in microfocus CT systems does not occur in synchrotron systems. As a result, the X-ray beam may also be used for phase contrast imaging in addition to the conventional absorption imaging, which is an important tool in identifying the edges of defects.

When the X-ray beam is transmitted through the sample a phase change is imposed in addition to the attenuation of the beam. At interfaces (phase-phase or phase-air) there is a sharp difference in the phase retardation. Phase contrast forms when these neighbouring sections of the beam interfere as they propagate away from the sample. On beamline ID19 phase contrast imaging is easily performed. In practise all that is required is that the X-ray detector is placed a certain distance, approximately a tenth of a metre, from the sample (Cloetens *et al,*. 2001); this is in the near-field Fresnel region.

Synchrotron CT was performed on samples cut from the short crack fatigue test pieces. These samples encompassed a fatigue crack and were 1x1x12 mm in size. Samples were also taken from long fatigue crack growth test piece for the LVD25 alloy at 350˚C. Several tests were performed, one was stopped at a low crack growth rate (~$3x10^{-6}$ mm/cycle) and another were stopped at a high crack growth rate (just before final failure, ~ $2x10^{-4}$ mm/cycle). The samples were of size 1x1x12 mm and 2x2x12 mm and were sectioned so that they would encompass the crack tip region.

In this work a monochromatic X-ray beam with an energy of 20 keV was used. The X-rays were captured using a scintillator coupled to a fast readout low noise (FRELON) 14 bit dynamic range CCD camera with an array of 2048x2048 pixels. A pixel size of 0.7 μm and 1.4 μm was obtained in the 1x1x12 mm and 2x2x12 mm samples respectively. An exposure time of 1 second was used and 1500 images were taken over a 180˚ rotation. The detector was placed 60 mm behind samples and so some absorption and phase contrast imaging was expected. Flat field and dark-current corrections were performed to account for error/inconsistencies in the beamline setup. A detailed description of the ID19 optics setup can be found at the ESRF website (ESRF, 2007)

The images were reconstructed using the filtered back projection method (Kak and Slaney, 1988). The software used for this is in-house software produced at ESRF. The reconstructed volumes are 32 bit files and these were reduced to 8 bit files to minimise the file size. However, each scan still produces 8GB files even after this process. The images were analysed in VG Studio Max and ImageJ software.

Alloy	Si (wt.%)	Cu (wt.%)	Ni (wt.%)	Mg (wt.%)	Fe (wt.%)	Mn (wt.%)	Ti (wt.%)	Zr (wt.%)	V (wt.%)	P (ppm)	Sr (ppm)
LVD25	12.45	3.93	2.78	0.67	0.44	0.03	0.01	0.05	0.04	55	0
LVD26 unmod	6.90	3.89	3.00	0.62	0.22	0.03	0.01	0.05	0.04	45-50	0
LVD26 mod	6.90	3.89	3.00	0.62	0.22	0.03	0.01	0.05	0.04	45-50	150-155
LVD27	0.67	3.91	2.99	0.80	0.21	0.05	0.01	0.01	0.01	45	0

Table 3-1 Compositions of the alloys studied.

Stage	grinding	grinding	2nd Polish	3rd Polish	4th Polish	5th Polish
Abrasive	600 Grit	1200 Grit	6μm Diamond	3μm Diamond	1μm Diamond	OPS
Force (lbf)	17	17	20	17	17	5
Speed (rpm)	300	300	150	150	150	150
Time (min)	Till plane	3	4	3	3	~15

Table 3-2 Metallography polishing route.

Alloy	Temperature	theoretical stress (%YS)	strain (%)	extrapolated stress (MPa)	extrapolated stress (%YS)
LVD25	RT	213	0.76	172	158
LVD26 unmod	RT	210	1	160	151
LVD26 mod	RT	215	1.1	170	159
LVD27	RT	175	0.54	132	105

Table 3-3 Stresses and strains at which short crack tests were performed.

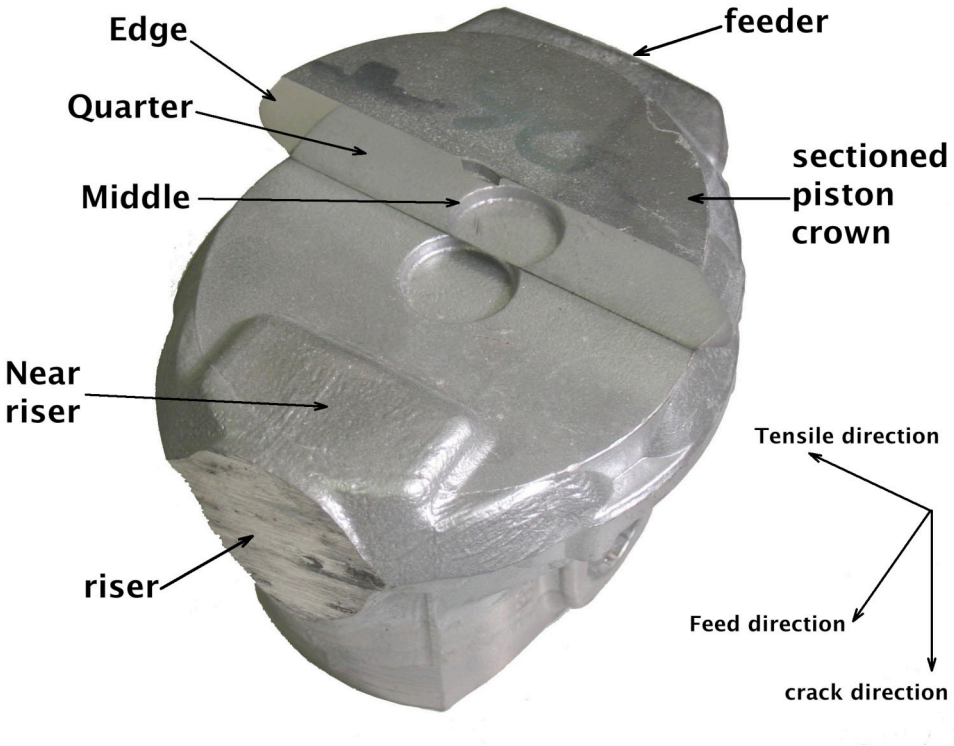

Figure 3-1 A photograph of a piston supplied by Federal Mogul and a sectioned piston crown placed on it.

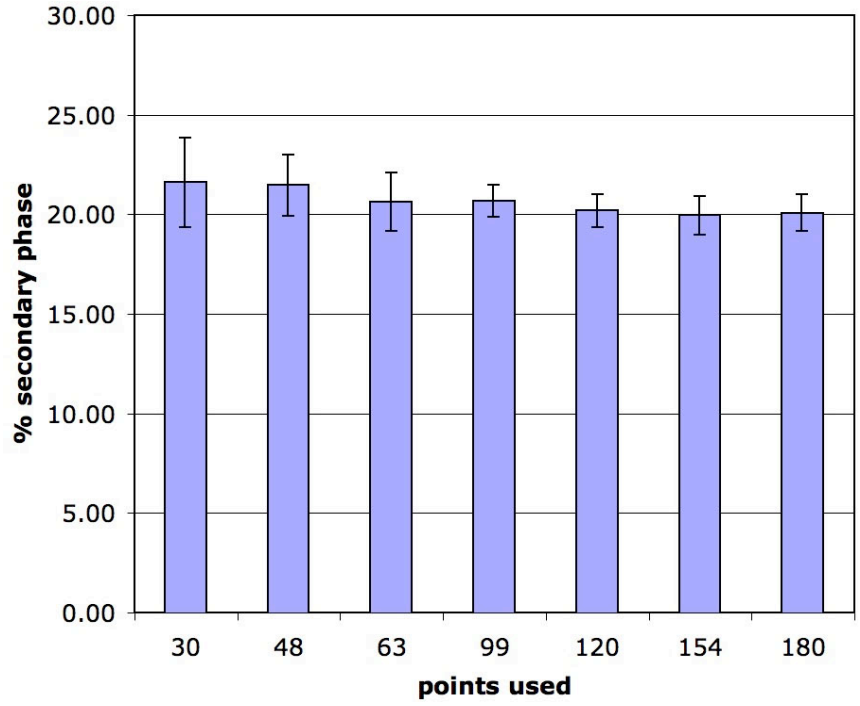

Figure 3-2 Analysis on the effect of the number of points used for the point fraction analysis.

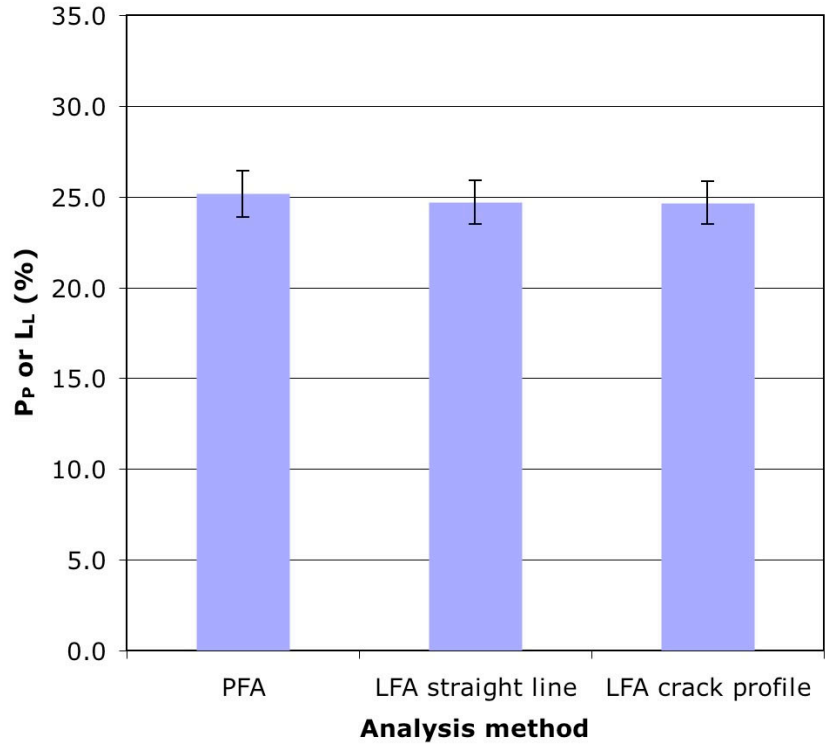

Figure 3-3 LFA and PFA results for LVD25.

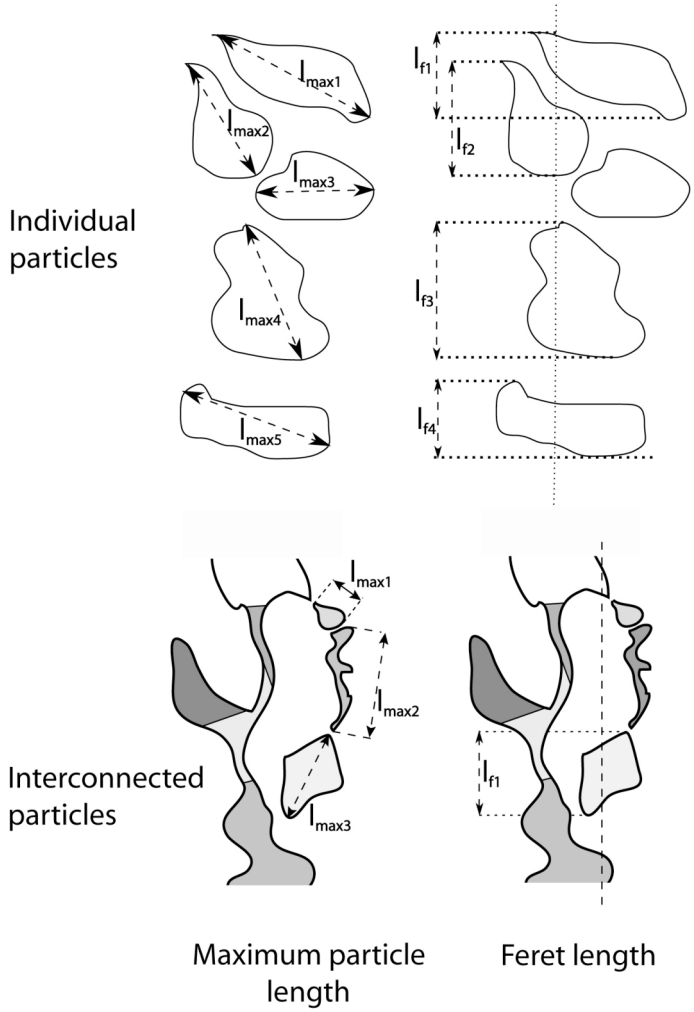

Figure 3-4 Particle lengths for an individual particle network and an interconnected network.

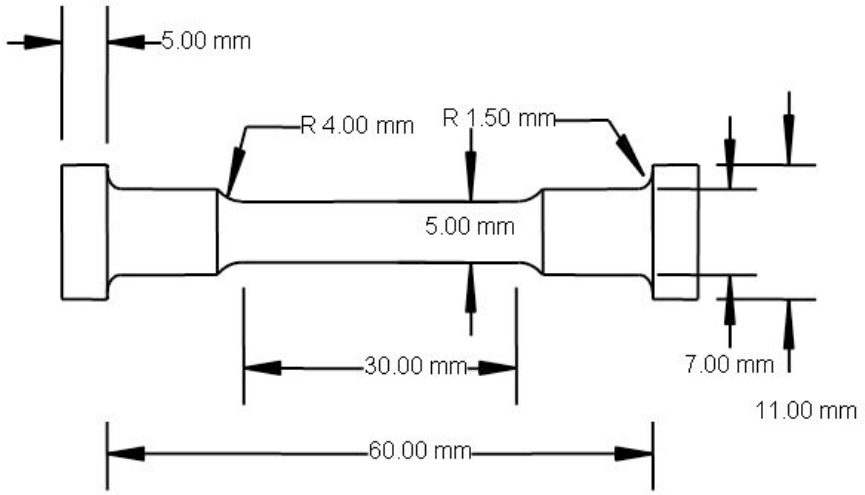

Figure 3-5 Tensile test piece specimen geometry conforming to ASTM E8M standard.

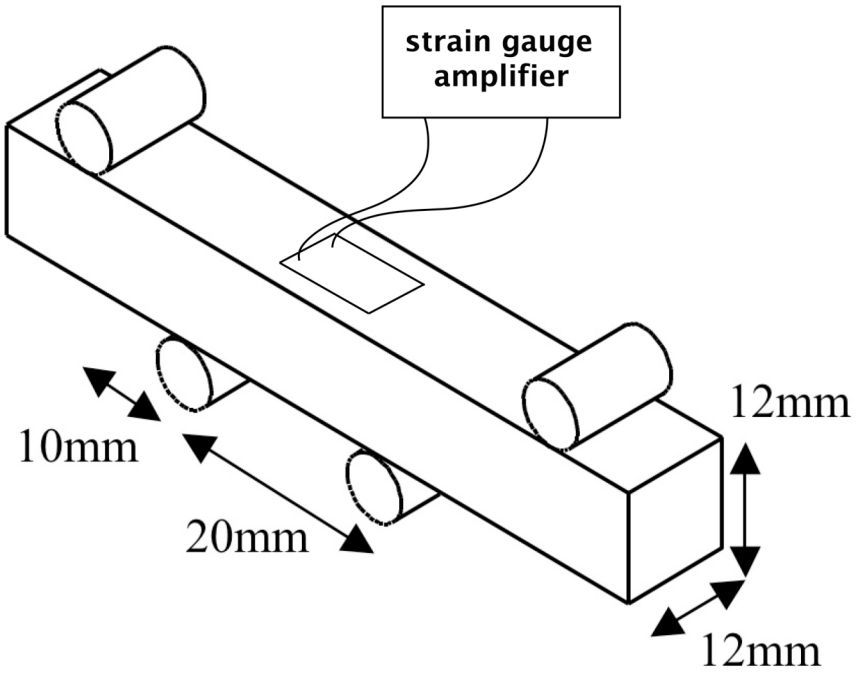

Figure 3-6 Strain gauge setup.

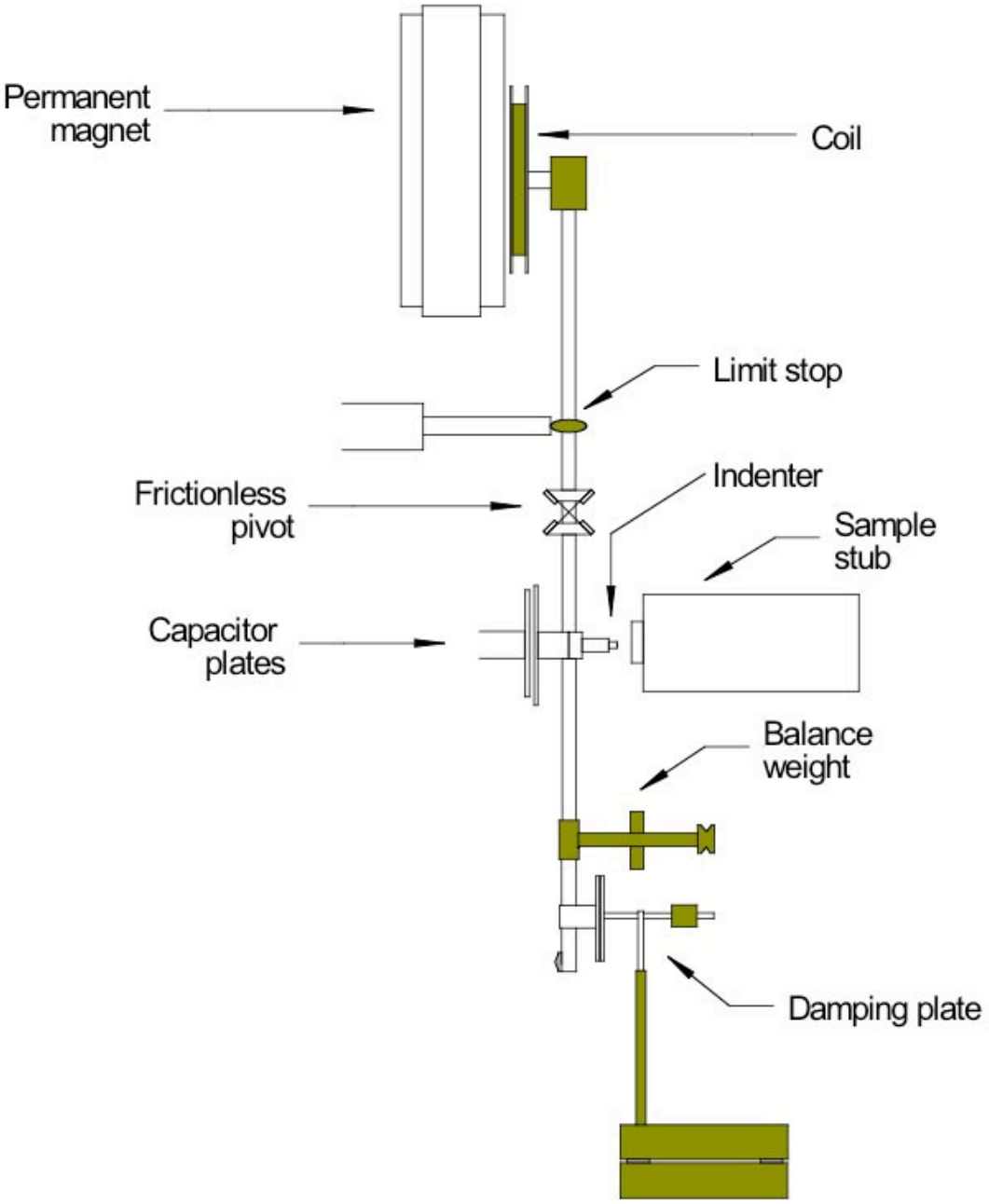

Figure 3-7 Schematic diagram of the Nanoindenter from Beake *et al.* (2003).

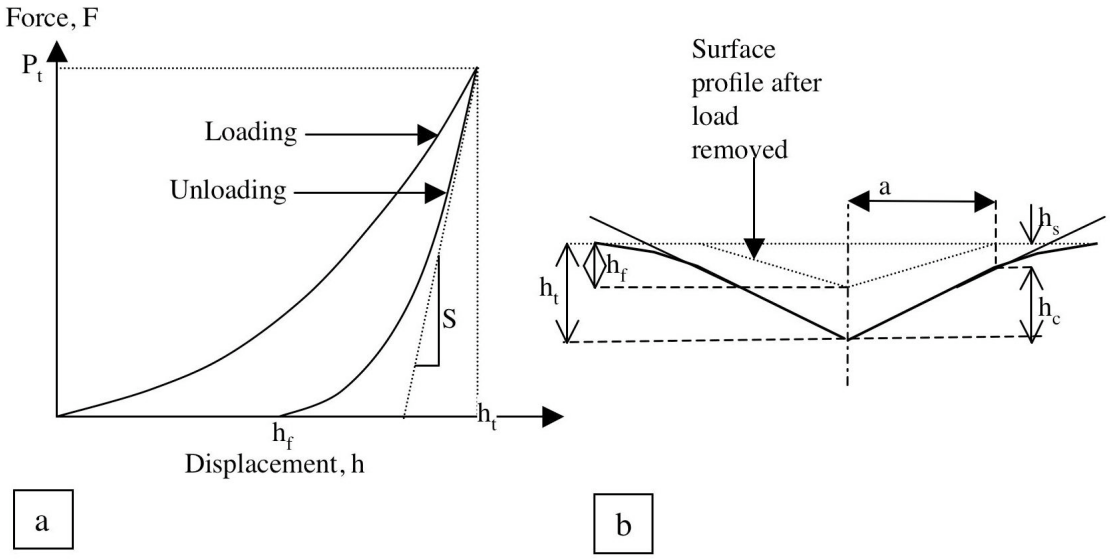

Figure 3-8 a) typical force displacement curve for an indent and b) is a schematic showing the displacement during loading and unloading (after Pharr *et al.* 1992).

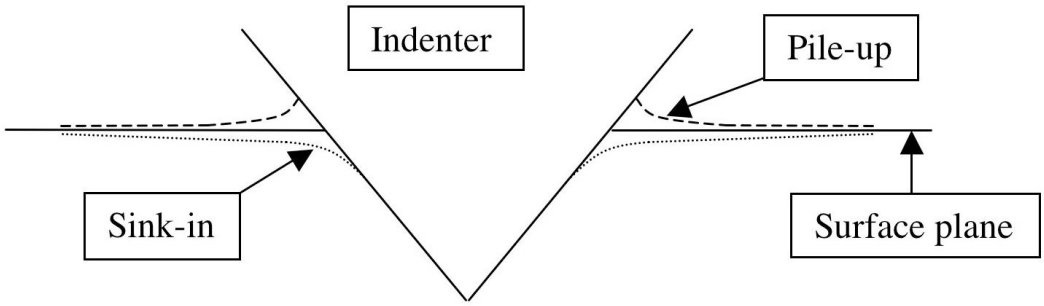

Figure 3-9 Schematic diagram of sink-in and pile-up.

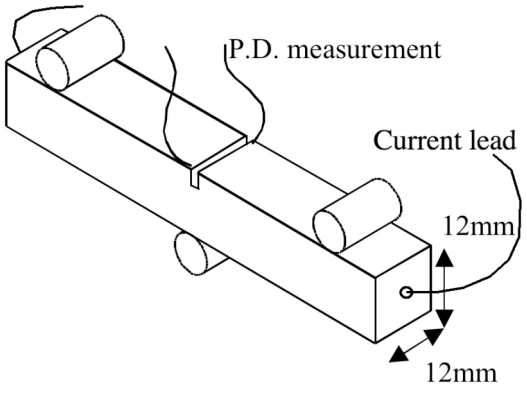

Figure 3-10 Long fatigue crack growth test setup.

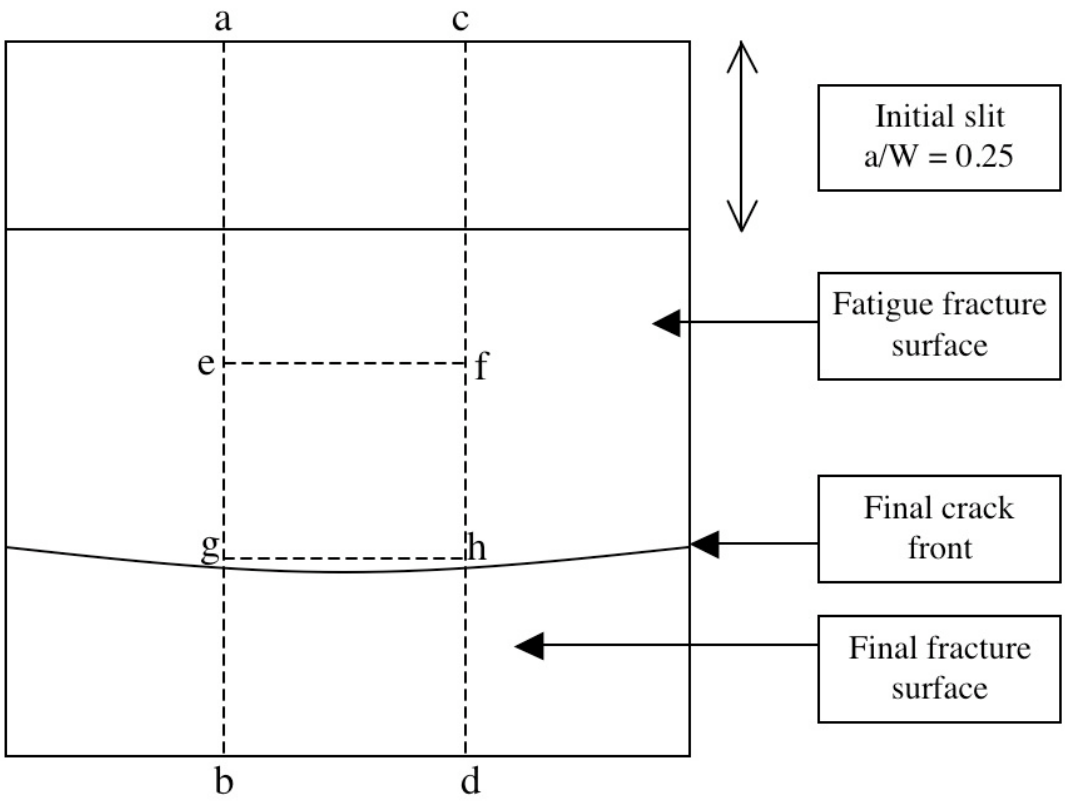

Figure 3-11 A schematic diagram of the fracture surface of a long fatigue crack growth test sample, the dashed lines show where the sample was sectioned.

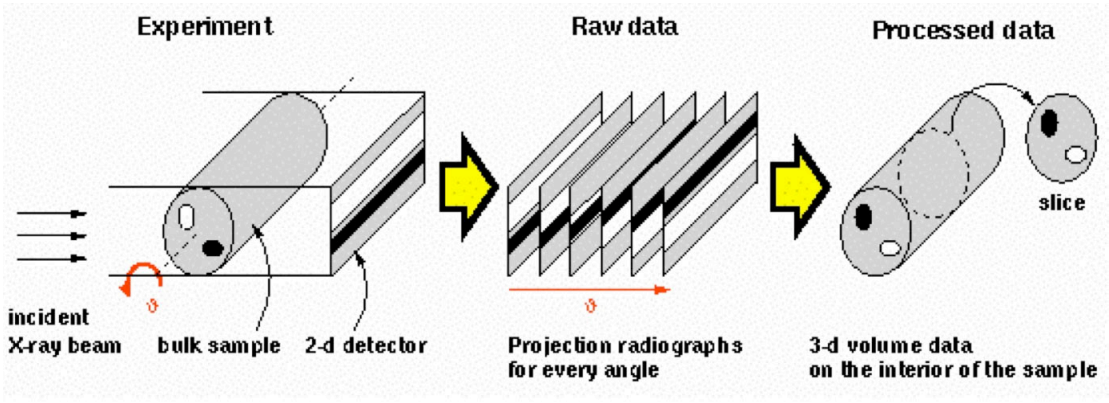

Figure 3-12 Basic principles of X-ray computer tomography (ESRF 2007).

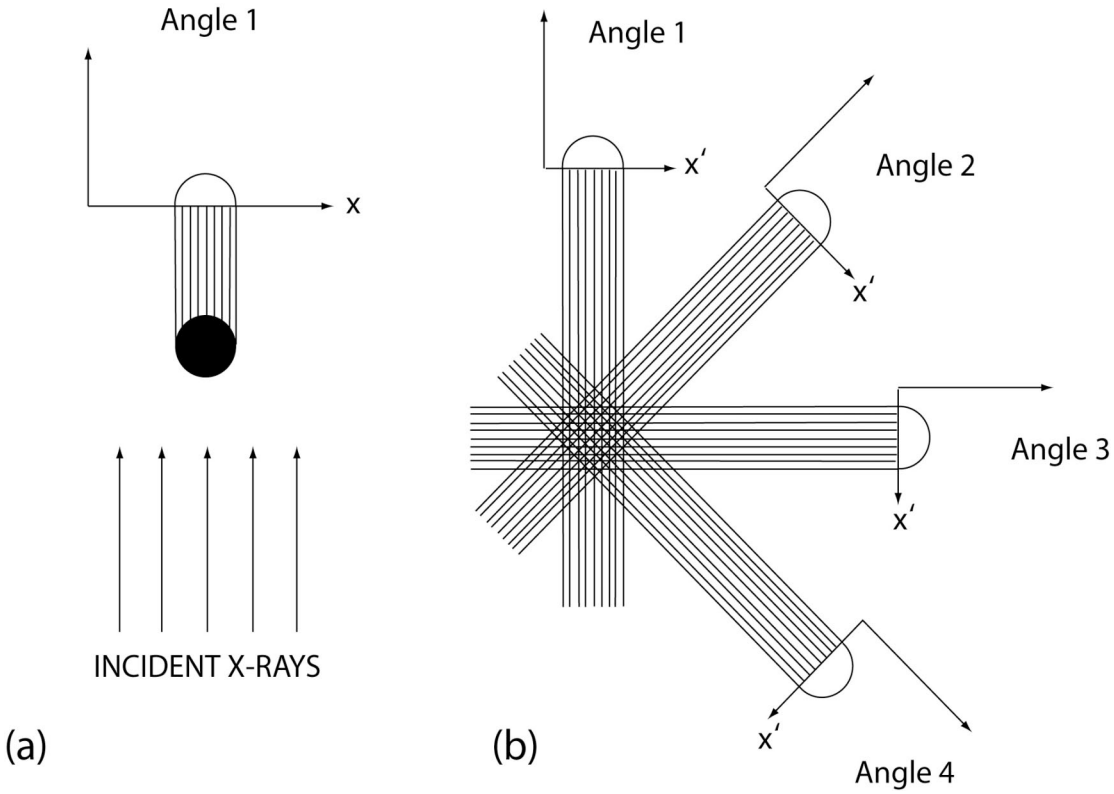

Figure 3-13 Schematic diagram of back projection.

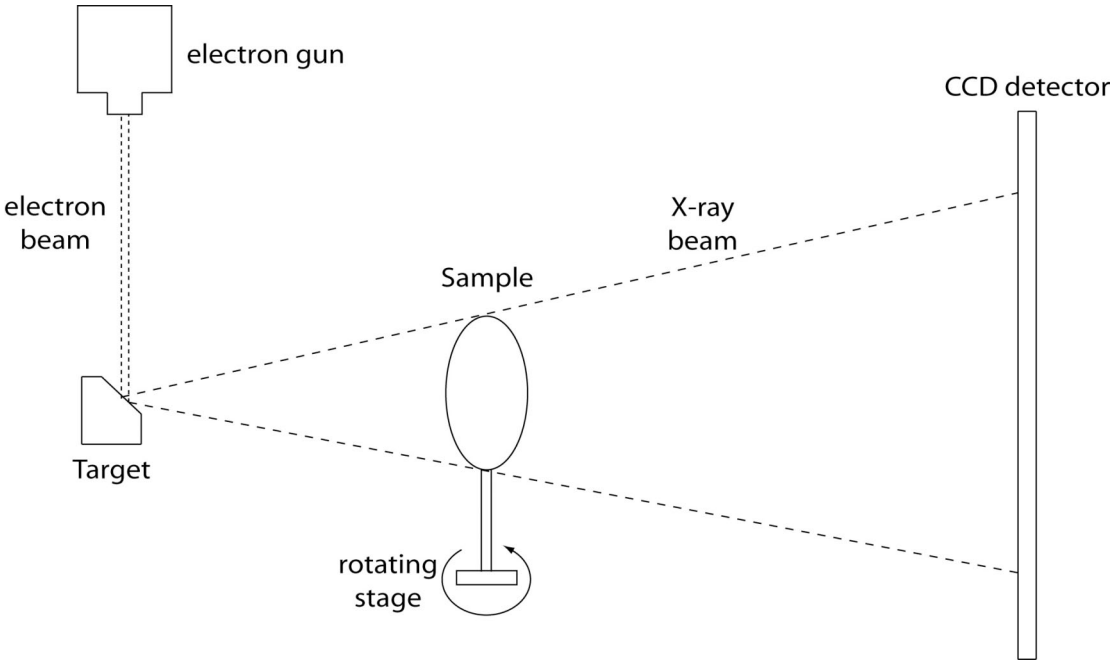

Figure 3-14 Microfocus CT setup.

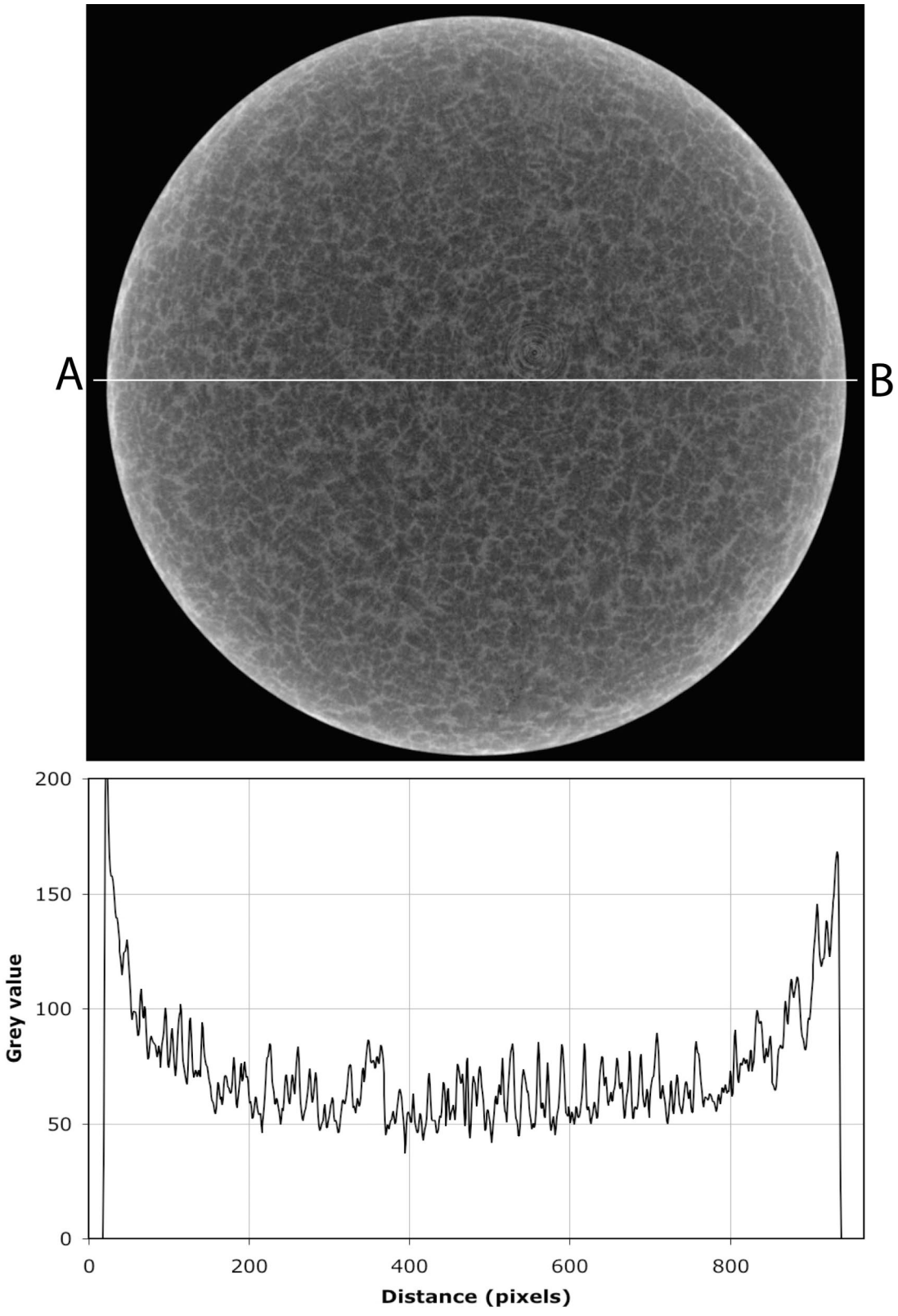

Figure 3-15 Change in grey scale across AB from beam hardening.

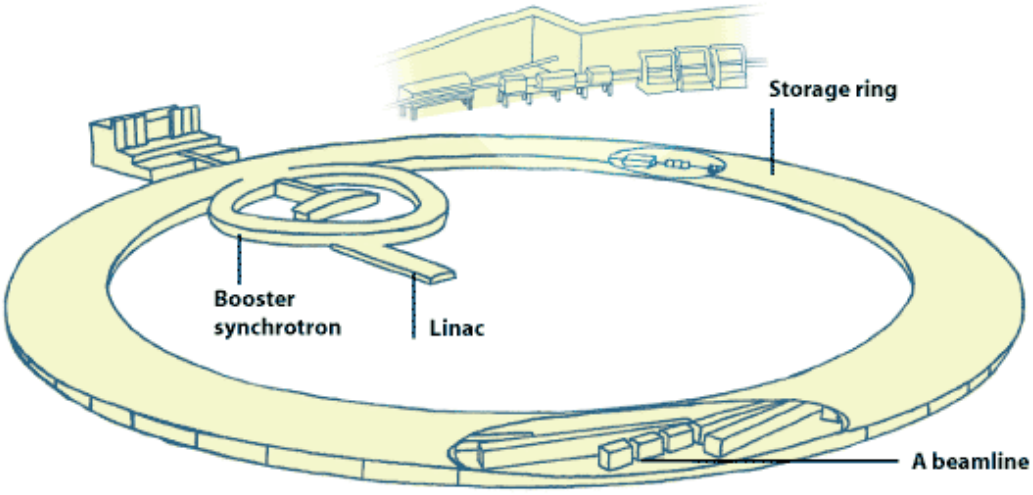

Figure 3-16 Schematic diagram of the basic design of a synchrotron facility (ESRF 2007).

Chapter 4

Materials Characterisation

4.1 Introduction

An aim of this project is to link the fatigue properties to the underlying microstructure of these alloys to inform further materials optimisation in terms of their fatigue performance. It is therefore important to thoroughly assess the alloy microstructures since the materials studied have many alloying additions and contain many different phases. The materials have been characterised in two dimensions using standard stereological methods and many of the phases present in the alloys have been identified. Using X-ray computed tomography (X-ray CT) it has been possible to further assess the microstructures of these alloys and their complex, three-dimensional structures. Nanoindentation has been used to ascertain some of the local mechanical properties for individual phases in these alloys. The macro-scale mechanical properties of these alloys have been assessed. Their monotonic behaviour at a range of temperatures will be presented in this chapter as well as the results of an ageing study to characterise the effect of in-service thermal exposures.

4.2 Two dimensional microstructural analysis

The materials studied contain many alloying elements, some of which (e.g. Cu and Ni) are at relatively high levels and as a result the materials exhibit a complex microstructure containing Si particles and many different intermetallics in a solid solution of α-Al matrix (Si particles and intermetallics will be referred to collectively as hard particles in these microstructures). In Figure 4-1 and Figure 4-2 some of the typical phases in LVD25 have been identified. It may be seen that these phases have a

range of morphologies and in many cases the phases are connected. Si has a dark grey appearance, the larger blocks of Si are primary Si and the smaller Si particles are eutectic Si. In Figure 4-2 the AlP phase has been identified, this phase acts as a nucleation site for primary Si (Polmear, 1989; Ye, 2003). Less common phases such as Mg_2Si and Al_2Cu have also been observed. These phases have similar Chinese script morphologies but can be differentiated after etching by colour since Mg_2Si is darker (Daykin, 1998).

As discussed in the literature review the AlCuNi phases can be differentiated by the ratio of Cu and Ni they contain. It can be difficult to differentiate between the AlCuNi phases by optical microscopy alone as their morphologies are not sufficiently different from each other. However, the phases have a brown/grey colour and in general the darker the phase the lower the Cu content (Edwards, 2002). It can also be difficult to differentiate the Al_9FeNi phase from the AlCuNi phases as the colour and morphology are similar.

In Figure 4-3 the AlCuNi phases and eutectic Si phases that form in LVD26 mod have been identified. The intermetallics that form are similar to those in LVD25 but the Si is different. Primary Si is not present in this alloy and because of the Sr modification the Si has a fine morphology and forms in clusters. In many cases the Si particles seem interconnected. This appearance of the Si can be contrasted to that of LVD26 unmod in Figure 4-4, where the Si particles have a coarser morphology. The intermetallics in both LVD26 variants are again similar to those in LVD25 but in LVD26 unmod there are occasionally some irregular phases where the phase has a 'patchy' appearance (Figure 4-4).

Phase mapping (which combines EDSD and EDX information and so unambiguously identifies the phases present) was primarily performed to carefully characterise the microstructure around the fatigue initiation sites. However, it is worth noting some of the interesting microstructural features identified from these results, in this chapter. A phase map of the irregular/patchy phase that occurs in LVD26 unmod (presented in Figure 4-5) identifies that this particle consists of the Al_9FeNi phase and the $Al(CuNi)_2$ phase. The intricate way in which different intermetallics and Si particles are connected may also be observed in Figure 4-5. A phase map for a primary Si particle is presented in Figure 4-6a, and the corresponding inverse pole figure is

presented in Figure 4-6b. Two twin boundaries were identified; these are of interest because previous work by Edwards (2002) indicated that these boundaries may provide a preferential crack path if they are aligned perpendicular to the direction of applied stress.

LVD27 contains the AlCuNi phases previously identified in the other alloys (Figure 4-7) but contains no (or very little) individual Si phase; this is in agreement with the thermodynamic equilibrium models of Chen (2006). In Figure 4-7 interdendritic porosity can also be observed (porosity will be discussed in more detail, in section 4.3). As with the other three alloys, many of the phases are interconnected.

Microstructure 3-D cubes have been produced from 2-D images to show the typical alloy microstructures (at a lower magnification to the micrographs previously presented) and these may be seen in Figure 4-8 to Figure 4-11. In all the alloys a solid solution of α-Al acts as the matrix and has a dendritic form. In the micrographs the matrix has a yellow/orange colour, and is the major phase. In both LVD26 alloys the dendrites are generally elongated but have no particular alignment. In LVD27 the dendrites have a more equiaxed appearance i.e. are more spherical in shape. The dendritic structure is less obvious in LVD25 although both elongated and equiaxed dendrites can be observed.

No particular alignment is observed in any of the alloys; dendrites do not tend to form preferentially in any particular direction. Whilst the general population of hard particles is found in the inter-dendritic regions, the individual hard phases are not evenly distributed throughout the alloy in these regions. An example of this is the distribution of primary Si in LVD25 (this will be discussed in more detail later in this section). Furthermore, hard particles may form distinct clusters, this is observed in all the alloys and a dense region of secondary phases, characteristic of those that form in LVD27, is identified in Figure 4-11.

Qualitatively, the microstructures of the alloys appear similar throughout the piston crowns. Three micrographs showing the microstructure near the edge of the crown (<5 mm), approximately 25 mm from the edge of the crown and in the middle of the crown for LVD26mod, are presented in Figure 4-12 (the locations are also shown in

Figure 4-13). Eutectic Si, intermetallics and α-Al dendrites are present and appear to be similar in size and morphology in all the micrographs.

To assess quantitatively the microstructure throughout the pistons the volume fraction (V_f) of hard particles (Si and intermetallics) at different locations has been obtained using point fraction analysis. The locations at which these measurements were taken are given in Figure 4-13. The results of this assessment are in Figure 4-14, in which the error bars represent one standard deviation (S.D.), and Figure 4-15, in which the error bars represent the standard error (S.E.). The standard deviation gives an indication of the level of scatter that might be expected if the V_f analysis was repeated once. The standard error indicates the range of values in which the mean value would be expected if the experiment were repeated several times.

In LVD25 and both LVD26 alloys the mean V_f of hard particles for each region falls within the corresponding standard errors of the other regions. In LVD27 the V_f of hard particles at the quarter and edge locations are outside the standard error bounds of the opposite location, but both values lie within the expected bounds when compared with the measurements taken at the middle and near riser locations. Therefore the results seem to indicate that the distribution of hard particles, at this macro level, is uniform throughout the piston crowns.

Whilst on this larger scale the average microstructure is relatively uniform, at a more local microstructural level there is considerable variation (as has previously been indicated). If, for example, one considers the distribution of primary Si particles in LVD25 (Figure 4-16), then it can be seen that the distribution of this phase is relatively heterogeneous. In Figure 4-16 the micrograph has been split into two halves: in the bottom section the V_f of primary Si is observably greater (V_f ~ 19.2%) than in the top section (V_f ~ 6.7%). Using point fraction analysis it has been determined that the average V_f of Si in LVD25 is 14% (with S.D. = 4%), and so the values obtained within Figure 4-16 are not within ±1 S.D. of the expected mean V_f of Si. This example illustrates the large variation in the distribution of Si that may be expected in LVD25 at the more local microstructural level. The colour and morphology of the Si phase allow automated image analysis approaches to be used for this type of analysis but it has not been possible to perform similar analyses on other phases because they are more difficult to differentiate between by greyscale and

morphology characteristics. However, qualitative assessment of the micrographs previously presented in this chapter indicate a heterogeneous distribution of these other phases as well.

All the alloy microstructures have been quantified using standard stereological methods, and these results can be found in Table 4-1; each result is presented with the corresponding S.D. The V_f of hard particles is the average result of all the measurements taken for each alloy (i.e. it takes into account the results from all regions of the piston crown). As might be expected the greater the quantity of alloying additions, the greater the V_f of hard particles in the alloys; LVD25 has the highest V_f of hard particles and LVD27 the lowest. The V_f of hard particles for LVD26 mod lies within the expected bounds of error of LVD26 unmod and *vice versa* and so this difference is not considered significant.

Two results have been presented for the mean free distance (λ) between hard particles for LVD26 mod. The italicised (smaller) value is obtained when any particle intercepts the line used for the measurement. The non-italicised (larger) value is the result when a eutectic region is treated as a single particle when the line used for measurement intercepts that eutectic region. When the eutectic Si regions are treated as single particles the λ is, in general, inversely proportional to the Si content. When eutectic Si particles are treated as individual particles, LVD26 mod does not follow this trend and λ for this alloy is approximately halved. Whilst the italicised value is statistically correct it may not reflect the microstructure accurately. LVD26 has a dendritic structure and the interdendritic regions contain intermetallics and eutectic Si so the alloy may be better described, for example, using two λ's: one for the dendrites and another for the eutectic Si regions. It is possible to perform a similar stereological analysis on the eutectic Si regions in LVD26 mod: $V_f \sim 36.3\%$, $\lambda \sim 2.4\mu m$ and the mean intercept length, $L_3 \sim 1.4\mu m$. Accurately reflecting hard phase distribution with a view to modelling these microstructures will be discussed in more detail in the chapter 6.

Two values for L_3 are presented for LVD26 for the reasons previously discussed. When the eutectic Si regions are treated as a single particle, L_3 is proportional to the Si content. When eutectic Si particles are counted individually (in LVD26 mod), L_3 is

reduced by a factor of 2. The dendrite arm size (in Table 4-1), is very similar to the L_3 of a space-filling cell (*n.b.* this is slightly different to the L_3 for a particle (Underwood, 1970)). In the case of alloys similar to LVD26 it is often referred to as the secondary dendrite arm spacing (SDAS). SDAS is not, however, obtained from lines taken at random (as for L_3) but from lines placed down the length of the dendrites. The SDAS of both LVD26 alloys is similar and they are both within the expected standard error bounds and so Sr modification does not appear to have altered this feature. The dendrite size for LVD27 is obtained in a similar way but the lines were placed so that they did not intercept dense regions of secondary phases. No dendrite arm size is presented for LVD25 because the dendrites are less obvious. Dendrite arm size differs from the mean free path (and L_3 of a space filling cell) in that it is a measure of a specific feature of the microstructure and not an average feature for the entire microstructure.

4.3 Three dimensional microstructural analysis

X-ray tomography has been performed on all the alloys and allows study of the microstructures in three dimensions. These alloys are not entirely suited to this analysis because X-ray attenuation of the Al and Si phases is very similar and so it is difficult to differentiate between the two. However, the intermetallic phases in these alloys do attenuate X-rays differently to Al and Si and so it is possible to segment these phases to reveal their three dimensional morphologies. In all the alloys, the intermetallics form a complex and largely interconnected microstructure.

Lower and higher magnification tomography images for LVD25 are presented in Figure 4-17 and Figure 4-18 respectively. The Al and Si phases have been removed to reveal the intermetallic structure. Because of the complex nature of the intermetallics only thin slices have been presented in an attempt to avoid the image being cluttered and confusing (*n.b.* representing 3-D images in a static 2-D form whilst maintaining the required level of detail is difficult). Every effort has been made to present clear and representative images. ‘Tricks’ employed include leaving a bounding box around the slice to maintain a level of context and also making the Al and Si phases ‘misty’

but so that the intermetallics remain visible; this has the effect of giving the images an element of depth which they might not otherwise have.

Fully describing the three dimensional morphology of the phases presented in Figure 4-17 is a challenging task but here the main features will be identified. In two dimensions it is possible to see that intermetallics (and Si particles) are often interconnected (see Figure 4-8 to Figure 4-11) and so they are likely to be interconnected in three dimensions; the tomography data confirms that this is the case and the interconnected intermetallic network is shown in Figure 4-17.

Many different particle morphologies have been observed in the two-dimensional images and can also be identified in three dimensions. Region one in Figure 4-17 contains a phase that in two dimensions would appear to be two flakes (1a and 1b). However it can be seen that the three-dimensional nature of this phase is more complex. The two flakes are connected and in fact part of a much larger phase that has several arms. In region 2 a phase has been identified that has circular features and several of these can be observed throughout the image. It seems likely that this phase may have formed around dendrites; it is again connected to other phases. The third region identified contains a larger phase. From the morphology this phase appears to be similar to the region 3 identified in Figure 4-1. It is large (>200 μm) and appears to be comprised of many 'arms'.

In Figure 4-18 several flake/plate like structures are visible. The alignment of the flakes is a local feature and not representative of the alloy. Although they are mostly interconnected it has been possible to carefully segment one of these flakes to reveal the three-dimensional structure in more detail, this is presented in Figure 4-19. The surrounding material has been withdrawn to reveal part of the flake. The flake is not continuous and several holes have been identified. The edges of the phase are rough and some very sharp angles may be observed. This may be of particular importance when considering stress concentration effects in the local microstructure; the more acute/sharp the corner, the greater the stress concentration in the particle (Qin *et al.,* 1999). The flake is large, the visible section is >150 μm in length and approximately 50 μm in width. However, the minimum dimension is the thickness, which is <10 μm in general.

Tomography images for the intermetallic networks in LVD26 unmod and LVD26 mod are presented in Figure 4-20 and Figure 4-21 respectively. In both cases the intermetallics have complex morphologies: they contain many arms and have a rough appearance with many acute angles. In Figure 4-20 several elongated flake-like structures have been identified and these are sections of a larger structure. It is not easy to appreciate the elongated dendrites that exist in this alloy from these three-dimensional images but a region has been identified in Figure 4-21 that shows the intermetallics around a likely dendrite. In general the intermetallics are finer in the LVD26 alloys compared with the LVD25 alloy and large plates, similar to those presented in Figure 4-19, were not observed. A larger cube of the intermetallic network in LVD26 unmod is presented in Figure 4-22. This image has been presented because it is the approximate volume of the plastic zone that would form at high *da/dN* (at RT) in these alloys, and illustrates the volume of intermetallics, which may be sampled in the plastic zone. It is important to remember that in LVD25 and the LVD26 alloys Si particles are also present (although not easily distinguished in the tomography structures) which makes the 'hard particle' network even more complex.

The tomography image of the intermetallic network for LVD27 is presented in Figure 4-23; once again the intermetallics are very interconnected. It has been identified that LVD27 contains equiaxed dendrites and large clusters of secondary phases (Figure 4-11) and these can also be observed in Figure 4-23. Several circular features (i.e. around the dendrite) may be observed and some of these have been identified. In addition a dense region of secondary phases has been indicated towards the bottom of the image. Different morphologies can be observed throughout the alloy, for example thin 'stick' phases, and flatter vertebrae type structures; these particles form many acute angles. The apparent alignment observed in Figure 4-23 is a 'sectioning' artefact; a cube of the intermetallic structure is presented in Figure 4-24 and demonstrates that such an alignment does not exist.

Porosity is present in all the alloys studied. The level of porosity is low and therefore difficult to characterise in two dimensions (because a very large number of micrographs would be required). An example of the porosity found in LVD25 is presented in Figure 4-25. The pore has formed around and in-between the intermetallics which is typical for this alloy (*n.b.* it is possible to see the Si particles in

this image, but it can be seen that their grey level is very similar to that of the Al matrix, hence the problem segmenting them). It is possible to segment the pore and view it in three dimensions; this is presented in Figure 4-26. The surrounding material has been partially withdrawn to reveal the pore shape but leave it in its microstructural context.

A similar example is presented in Figure 4-27 for LVD26 unmod. In this example the surrounding Al and Si have been withdrawn to reveal the intermetallics (yellow) and the pore (red). In the first image the pore is hardly visible as it is obscured by the intermetallics. As the intermetallics are drawn back the pore becomes visible. As with the pore presented for LVD25 (Figure 4-26), it has formed in between the intermetallic phases. The final image shows the pore without any of the surrounding material. In this image the pore is presented from the opposite side. The pore may be better described as a porous region as it actually comprises four different sized pores; this is quite typical and similar porosity is observed in all the alloys. An example of interdendritic porosity in LVD27 is presented in Figure 4-28; this is actually part of a large porous region. These pores are often associated with the dense clusters of intermetallics and it can be seen that this pore is on the edge of such a region. Pores form in these regions during the casting process because of the inability of the cast to flow through these regions to compensate for the volume shrinkage associated with solidification (Roy *et al.,* 1996).

The volume fraction of porosity has been estimated and the results are in Table 4-1. These results have been obtained from very limited data (the volume assessed for each alloy is ~600 μm^3) and so it is not possible to give an estimate of the scatter that may be expected. The maximum dimension of the porous region can be large (and pores in the region of 400 μm in length have been observed) but due to their interdendritic nature the minimum dimension is small; this is the limiting factor that precludes the use of the more readily available laboratory CT, as the resolution is insufficient (further analysis would ideally be performed at ESRF). LVD27 contained the highest volume fraction of porosity but for all the alloys the level was <0.1%. The largest porous region was also observed in LVD27 although large porous regions (>200 μm in length) were observed in all the alloys.

4.4 Nanoindentation

The nanoindenter at the University of Southampton does not have a microscope attachment and so indents cannot be purposefully placed in selected phases. A 'bombing raid' technique was therefore used; this entails hundreds of indents being performed in grids so that they indent the microstructure randomly. This method is very inefficient and only a few Si particles and secondary phases are indented such that the indent is three times the diameter from the side of the particle as required by BS EN ISO 14577-1:2002 (approximately 2% of indents hit a secondary phase or Si particle). So, only indentation results for the Al matrix, Si particles and the Al_9FeNi phase are presented (see Table 4-2).

Si had a higher hardness but a lower modulus than Al_9FeNi, Al had the lowest hardness and modulus. The modulus of the Al matrix is higher than 70 GPa, which is the modulus commonly quoted for Al in the literature (Callister, 2000; Polmear, 1989). The h_f/h_t ratio was lowest in Si and greatest in the Al-matrix and the h_f/h_t ratio is greater than 0.7 for both Al and Al_9FeNi. This indicates (Bolshakov and Pharr, 1998) that pile-up may occur in the Al matrix and Al_9FeNi. Pile-up is known to occur in Al (Bucaille *et al.,* 2004) and so it seems probable that this accounts for the higher than expected modulus of the Al-matrix, if this is the case the hardness of Al will also be an overestimate.

There is currently no correction (simply using indentation data) for the effects of pile-up on hardness and modulus for indents created with a Berkovich indenter. Oliver and Pharr (2004) note that a more representative (although still inaccurate) method of estimating these values is to optically measure the indents. By doing this, hardness and modulus values for the Al matrix are reduced by 20% and 10% respectively to a hardness of 0.59 GPa and a modulus of 82 GPa. The value for the modulus is still greater than expected which indicates that the contact height (because of pile-up) and contact area are underestimated using this method.

Values for the modulus and hardness of Si can be found in the literature, several have been listed in Table 4-3. The range of the values for both modulus and hardness are quite large: hardness ~ 9.6 – 12.5 and modulus 140 – 169. The values obtained in this study fit within these bounds. The only reported modulus and hardness data found in

the literature for the Al_9FeNi phase is that from the sister project at Loughborough University by Chen (2006) (see Table 4-3); the modulus results agree very well although the hardness value for Al_9FeNi obtained in this study is lower. This may be attributed to experimental differences: Chen performed his tests on samples slow cooled after DSC; this was done to ensure that the secondary phases and Si particles would grow to a much larger size compared with the as-received samples in this study, and so be easier to indent. EDX analysis of the Al_9FeNi phase by Chen shows that this changes the composition of the phase slightly, increasing the Fe and Ni content by 2 at.% and 1 at.% respectively, hence reducing the level of Al. The increase in harder elements may lead to the higher hardness in the slow cooled samples of Chen.

The full results from Chen (2006) are reprinted in Table 4-4 and shown graphically in Figure 4-29. They are discussed in detail in his thesis, but the trends of the data will be briefly mentioned here. At all temperatures the Al-matrix is the softest phase and has the lowest E_r; this is the justification for grouping all the secondary phases and Si particles together as 'hard particles' throughout this thesis. At all temperatures Si is the hardest phase although the E_r at elevated temperature is considerably lower than at room temperature. Apart from Al, the other phases do not exhibit such a large reduction in E_r when indented at higher temperature. In particular Al_3Ni_2, Al_7Cu_4Ni and Al_9FeNi exhibit good thermal stability in terms of their E_r value.

An increase in test temperature from RT to 200˚C corresponded to a reduction in the hardness of all the secondary phases of < 15%. In Si no reduction in hardness value was observed, but the Al-matrix hardness decreased by > 50%. The hardness of all the phases is lowest at 350˚C. The secondary phases with the highest Cu content (Al_2Cu and Al_7Cu_4Ni) exhibited the largest reduction in hardness when compared with their RT values. The other secondary phases showed good thermal stability with a reduction of less than 25% at 350˚C compared with the RT results. The hardness of the Al matrix dropped considerably at the highest temperature. This may affect the absolute hardness and modulus values of the other phases since the increase in compliance of the Al matrix cannot be accounted for in the experimental setup and so cannot be accounted for in the equations used to calculate hardness and modulus. In addition, creep at maximum load was observed to be greater in all phases test at

350˚C compared with the lower test temperatures and this may affect the calculated hardness and modulus values at this temperature. It is not clear if the creep observed is a genuine property of the individual phases or simply a testing artefact because of the high level of creep in the Al matrix.

4.5 Ageing study

As previously mentioned, the materials were aged by the manufacturer for 8 hours at 230˚C and so were already in an over aged condition when received. Before mechanical testing, the materials were further aged for 100 hours at 260˚C to simulate in-service thermal exposures and so an ageing study was performed on the as-received alloys (LVD25, LVD26 mod and LVD27) to assess the effect of this further heat treatment. The results of the Vickers hardness versus ageing time are presented in Figure 4-30. The as-received hardness and the hardness after 1 hour were the same for all the alloys investigated. The initial hardness value has therefore been omitted from the graph to allow a log time plot to be more easily plotted.

After one hour, LVD27 had a hardness value similar to that of LVD25, and LVD26 mod had the lowest hardness value. At the end of the ageing study the hardness value was proportional to the Si content (i.e. LVD25 was the hardest and LVD27 the softest). The trend of LVD26 mod is similar to that of LVD25 and is consistently ~10 H_V lower at each point. The reduction in hardness was approximately 24% for both alloys. The rate of change of hardness is initially higher in LVD27 and after 32 hours the alloy has gone from being the hardest alloy to the softest alloy, the hardness in LVD27 reduced by 44% over the duration of the ageing study. The hardness of LVD25 and LVD26 mod appears to plateau after 128 hours whereas in LVD27 the plateau occurs later at 512 hours. In general, however, the change in hardness occurs mostly within the first 100 hours with only minor reductions in hardness after this time.

SEM images of the polished samples after 1 hour of ageing and 1024 hours of aging are shown in Figure 4-31 and Figure 4-32 respectively, in each figure image (a) is LVD25, image (b) is LVD26mod and image (c) is LVD27. In all the alloys, after 1 hours ageing treatment, the precipitates were only observable near intermetallic and Si particles, in the centre of dendrites it was not possible to resolve the precipitates.

After 1024 hours ageing at 260˚C (Figure 4-32) the precipitates had coarsened considerably and were more evenly distributed through the matrix. The coarsening of precipitates accounts for the reduction in the hardness observed in all the alloys at longer ageing times.

The results of DSC analysis can be seen in Figure 4-33. On each graph the red line corresponds to the sample in the as-received condition (i.e. after ageing for 8 hours at 230°C) and the blue line corresponds to the sample which has undergone further ageing at 260°C for 100 hours. In all cases the endothermic reaction (dissolution) has negative heat flow. Baseline variability was accounted for by subtracting heat flow data for pure Al from the sample data and the curves were normalised to account for heat capacity effects using a polynomial with fixed points at two temperatures: 200°C (below the ageing temperature) and 460°C (just before melting) where no reactions were expected to occur.

It may be seen for all the graphs in Figure 4-33 that for the as-received samples, dissolution reactions occurred just above the temperature at which the alloys had been aged, at approximately 240°C. Similarly in the 260°C soaked samples, dissolution reactions did not occur until above the temperature at which the alloys had been substantially further aged, at approximately 270°C.

For both ageing conditions in LVD25 (Figure 4-33 (a)) only an endothermic reaction occurred signifying precipitate dissolution. The as-received sample has two overlapping endothermic peaks; this could signify the dissolution of two phases. However, TEM would be required to confirm this. In the 260°C soaked sample there is just one endothermic reaction over the temperature range 270°C to 460°C. LVD26 mod (Figure 4-33 (b)) showed a similar trend to LVD25, no precipitates appear to form during the DSC experiment. In both aged states an endothermic reaction over a large temperature range occurred; 240°C-460°C for the 230°C aged sample and 270°C-460°C for the 260°C aged sample. For both alloys more dissolution occurred in the further aged samples and there was only one peak, signifying that there is a greater volume of the final, stable precipitate in this condition.

The curve for the as-received sample of LVD27 (Figure 4-33 (c)) differs from those of LVD25 and LVD26 mod in that it contains an exothermic peak and therefore the

formation of a phase has occurred. It can be seen that just above the 230°C ageing temperature there is an endothermic peak signifying dissolution, but between 330°C and 400°C there is an exothermic peak. In the 260°C soaked sample, only dissolution occurs and this is between 270°C and 460°C. The melting reactions may be seen after 500°C. Using the ternary phase diagram for a Al-Cu-Mg alloy (Polmear, 1989 and Figure 4-34), θ (Al_2Cu) and S (Al_2CuMg) precipitates may be expected to form in LVD27. Al_2Cu precipitates have also been observed to form in high Si content alloys, for example an Al-1.3 at% Cu-19.1 at% Si alloy (Starink and Van Mourik, 1994) and so may be present in LVD25 and LVD26mod.

In the as-received sample it is possible that the first endothermic peak corresponds to the dissolution of (the metastable) θ′, followed by the exothermic peak corresponding to the formation of the final (stable) θ phase. After further ageing all the θ′ has dissolved leaving only θ. This sequence may only be fully established by TEM analysis but the presence of metastable precipitates in the as-received LVD27 alloy may account for its increased hardness when compared with LVD26 mod. The metastable precipitates in LVD27 are likely to be more finely dispersed than the stable precipitates in LVD26 mod (and LVD25). The number of dislocations formed by the Orowan (1952) looping mechanism will therefore be greater in LVD27 hence the higher hardness value.

4.6 Tensile test curves

Tensile test results are presented in Table 4-5 and Figure 4-35. It can be seen in Figure 4-35 that there is a difference between the results at the various temperatures and the results have been grouped in the figure to show this difference. At room temperature the alloys were very brittle: they exhibited low % elongation but they had the highest UTS. The samples that were tested at 200˚C had moderate UTS and elongation values whilst the samples tested at 350˚C had the highest elongation and the lowest UTS and 0.2% proof strength. In all cases the eutectic alloy, LVD25, was the most brittle. There is no general relationship between the mechanical properties presented in Table 4-5 and the Si content of the alloys. An increase in testing temperature from RT to 200˚C did not give a decrease in the 0.2% proof strength of

the LVD25 alloy. However, a 10% reduction was observed in LVD27 and a 14% reduction was observed in LVD26 unmod.

A section of the RT, tensile test graph for the LVD26 alloys is presented in Figure 4-36. This figure can be used to demonstrate the level of scatter in the experiments and also to show the similarity in the tensile properties between the two alloys at RT. This similarity is significant because the Si morphologies in these alloys are different: in LVD26 mod the Si is refined and in LVD26 unmod the Si is coarser. At room temperature the Si morphology does not appear to have a first order effect on the tensile properties. The similar tensile properties would suggest that a microstructural feature that is similar to both alloys controls the tensile properties. Such features might include: secondary phases, α-Al matrix and SDAS. Unfortunately a similar comparison cannot be made at the higher temperatures, as these tests were not carried out by Federal Mogul and the high temperature testing facilities required were not in place at the University of Southampton.

4.7 Strain gage tests on bend bar samples

Fatigue tests were performed at loads well above the 0.2% proof strength of the alloys and so the stress in the top surface could not be estimated using standard linear elastic equations. The strain gage tests provide a value for the strain on the top surface, which may be compared with the tensile test curves to estimate a value for the surface stress. A graph showing the results of the strain gage experiments on a bend bar sample is presented in Figure 4-37. The initial parts of the curves are linear, reflecting the fact that the samples are behaving elastically. After approximately 60% of the 0.2% proof strength the materials start to behave plastically. If this is compared with the tensile test curves in Figure 4-36 it can be seen that this is expected as this is the point at which these curves deviate from the linear elastic regime.

4.8 Cyclic stress strain

The results of the cyclic stress-strain tests performed by Federal Mogul using the LVD25 alloy are presented in Figure 4-38. As previously mentioned these alloys were aged slightly differently to those used in other mechanical tests. They were given the

standard heat treatment of 8 hours at 230˚C but then soaked at the test temperature for 100 hours not at 260˚C (*i.e.* the RT sample had no further ageing *etc*). This difference in the ageing of the samples can account for the maximum stress shown at RT (Figure 4-38a) and at 200˚C (Figure 4-38b) being higher than the UTS values of LVD25 presented in section 4.6.

At RT the difference in the stress at the two different frequencies is small: approximately 4%. At 200˚C (which it should remembered is ~0.6 T_m) the difference is also small, approximately 6%. These values are within the scatter that might be expected for such an experiment and so the materials seem frequency independent at these temperatures. At 350˚C (Figure 4-38c) the materials are at ~0.8 T_m and it may be seen that strengths obtained at 0.5 Hz are approximately 50% lower than those obtained at 50 Hz. At 350˚C the materials are clearly highly strain rate dependent.

4.9 Summary

Four Al casting alloys have been investigated in this project. The quantity of Si present in each alloy was the primary difference. However, a Sr modified version of LVD26 has also been assessed. The materials are all microstructurally complex and contain many different phases. Using work from the literature (Chen, 2006; Edwards, 2002; Daykin, 1998) it has been possible to identify many of the phases by optical microscopy from their morphology and colour (after etching). Si was identified in LVD25 and both LVD26 alloys but not in LVD27. Other phases identified include the AlCuNi phases (Al_3Ni, Al_3Ni_2 and Al_7Cu_4Ni), Al_9FeNi, Al_2Cu, Mg_2Si and AlP and the α-Al matrix. Sr had the effect of producing much finer eutectic Si in LVD26mod. This was expected and has been well reported in the literature (Pacz, 1921, Elliott, 1970).

It has been possible to characterise the microstructure using established stereological methods (Underwood, 1970) and the volume fraction of ‘hard’ phases is evenly distributed throughout the section of the piston crown investigated. However, there is considerable local microstructural variation and the distribution of Si has been presented as an example of how phases may cluster locally on a scale commensurate with expected fatigue processes. Both LVD26 alloys have similar SDAS but Sr

modification can have a large effect on statistical features such as the mean free path and mean particle intercept length.

Tomography allows for the observation of the intermetallics present in the alloys. Most importantly it can be seen that the intermetallics form a complex interconnected microstructure, which is not immediately obvious from two-dimensional analysis. The intermetallic network is akin to the reinforcement phase of an interpenetrating composite. Whilst the phases look complex in two dimensions, in three dimensions it is even more difficult to describe, quantitatively, their important features. Flakes, circular features and clusters may all be observed, but the phases are often irregular and contain holes and many arms; the arms often form acute angles. The LVD25 and LVD26 alloys contain Si particles and so a further level of complexity exists in these alloys.

Porosity is present in all the alloys; estimates, using tomography data, indicate that the volume fraction of porosity is < 0.1%, although further analysis would be required to give a more accurate range. The tomography data shows that pores are usually associated with hard particles and interdendritic regions. Pores were generally clustered in larger regions and the maximum pore dimension in LVD27 was ~400 μm.

Nanoindentation was used to obtain the Young's modulus and hardness of the Al matrix, Si and Al_9FeNi phases. Si and Al_9FeNi are both harder and have a higher modulus than Al. A more comprehensive study using nano-indentation to characterise the many phases found in these alloys was performed in a sister project at Loughborough University by Chen (2006) and the results have been reprinted here. The nanoindentation results will be used later in the thesis to investigate load transfer from the matrix to the stiffer/harder phases, which is of interest when considering fatigue crack initiation.

The metastable precipitate present in the as-received LVD27 alloy (and not in LVD25 or LVD26mod) gives it a hardness value similar to that of the as-received LVD25. After ageing for 100 hours the hardness is proportional to the volume fraction of hard particles in the alloy and only the final, stable precipitates are present. It is interesting to note that the as-received pistons have undergone the same heat treatment as those

supplied to car manufacturers and so a similar change in hardness (and so we may infer related mechanical properties) is expected over the first 100 hours (or approximately 3000 miles) of a cars life. This change in properties has not been explicitly investigated in this project but previous work by Joyce *et al.* (2002b) on lower Cu and Ni containing eutectic AlSi alloys shows that the 0.2% proof strength and the UTS were reduced by 35% and 20% respectively after 100 hours ageing at 260˚C.

At room temperature the alloys are all brittle, and increasing the test temperature gives increased ductility but lower UTS. Si morphology did not appear to have a first order effect on the tensile properties of the LVD26 alloys at room temperature. At all temperatures LVD25 was the most brittle alloy. The cyclic stress strain data shows that at RT and 200˚C LVD25 is not strain rate dependent but at 350˚C a dependency was observed.

	LVD25	LVD26 unmod	LVD26 mod	LVD27
Volume fraction of hard particles (%)	25.1 ± 3.5	19.0 ± 2.9	19.5 ± 2.4	12.1 ± 2.2
Mean free distance λ (µm)	16.9 ± 5	20.2 ± 4.2	*10.3 ± 2.5* or 21.4 ± 3.4	24.9 ± 6
Particle mean intercept distance L_3 (µm)	5.7 ± 1.6	4.8 ±1	*2.5 ± 0.6* or 5.2 ± 0.8	3.4 ± 0.8
Dendrite arm size (µm)	n/a	25.2 ± 3.7	25.8 ± 2.8	67.0 ± 13
Vol. fraction of porosity (%)	0.073	0.076	0.052	0.092
Maximum porous region size (µm)	241	210	364	400

Table 4-1 Stereological quantification of the microstructure for all the alloys (error=S.D.).

Phase	Hardness (GPa)		Er (GPa)		ν	E (GPa)	h_f/h_t	
	mean	S.E.	mean	S.E.			mean	S.E.
Si	9.99	0.35	140	4	0.25-0.30	145-150	0.61	0.04
Al_9FeNi	6.32	0.43	153	4	0.28-0.34	156-163	0.77	0.01
Al	0.74	0.01	94	3	0.33	91	0.95	0.01

Table 4-2 Nanoindentation results for Al matrix, Si and Al_9FeNi.

Phase	**Hardness (GPa)**	**Young's modulus (GPa)**	**Reference**
Si	9.6 – 10.4	145-150	This study
	11.5 – 12.5	160-165	Jang *et al.,* 2005
	9.6	169	Thurn and Cook, 2004
	11.1	155-159	Chen, 2006
		140	Smith and Zheng, 2000
Al_9FeNi	6.3	156-163	This study
	7.7	164-171	Chen, 2006

Table 4-3 Nanoindentation results from the literature and this study for Si and Al_9FeNi.

Phase	Hardness (GPa)			Reduced Modulus (GPa)		
	25˚C	200˚C	350˚C	25˚C	200˚C	350˚C
Si	11.1	11.1	9.2	148	111	100
AlFeMnSi	10.8	10.1	8.1	175	146	133
Al_3Ni_2	10.5	9.5	6.7	171	152	171
Al_7Cu_4Ni	9.3	8.2	5.0	164	140	151
Al_9FeNi	7.7	6.7	5.8	161	138	142
$Al_5Cu_2Mg_8Si_6$	6.5	5.9	5.1	118	113	99
Al_2Cu	5.8	5.3	2.5	110	101	
Al matrix	1.5	0.7	0.1	85	55	27

Table 4-4 Nanoindentation results at 25˚C, 200˚C and 350˚C from Chen (2006).

	RT			200˚C			350˚C		
Material	0.2% proof stress (MPa)	UTS (MPa)	% el	0.2% proof stress (MPa)	UTS (MPa)	% el	0.2% proof stress (MPa)	UTS (MPa)	% el
LVD25	109	186	0.94	108	141	2.7	55	75	4.0
LVD26 mod	107	186	1.49				46	64	16.8
LVD26 unmod	103	176	1.40	89	127	5.1			
LVD27	125	180	1.45	113	155	5.0	46	61	12.4

Table 4-5 Tensile test results.

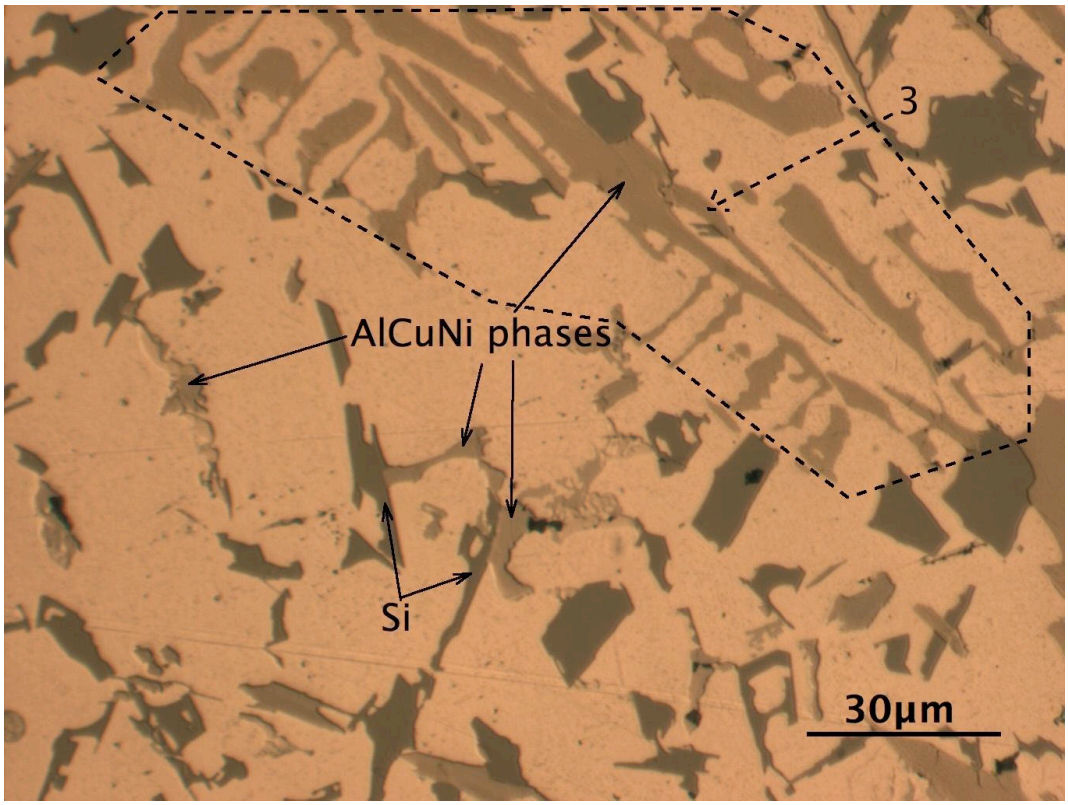

Figure 4-1 The AlCuNi and Si phases in LVD25.

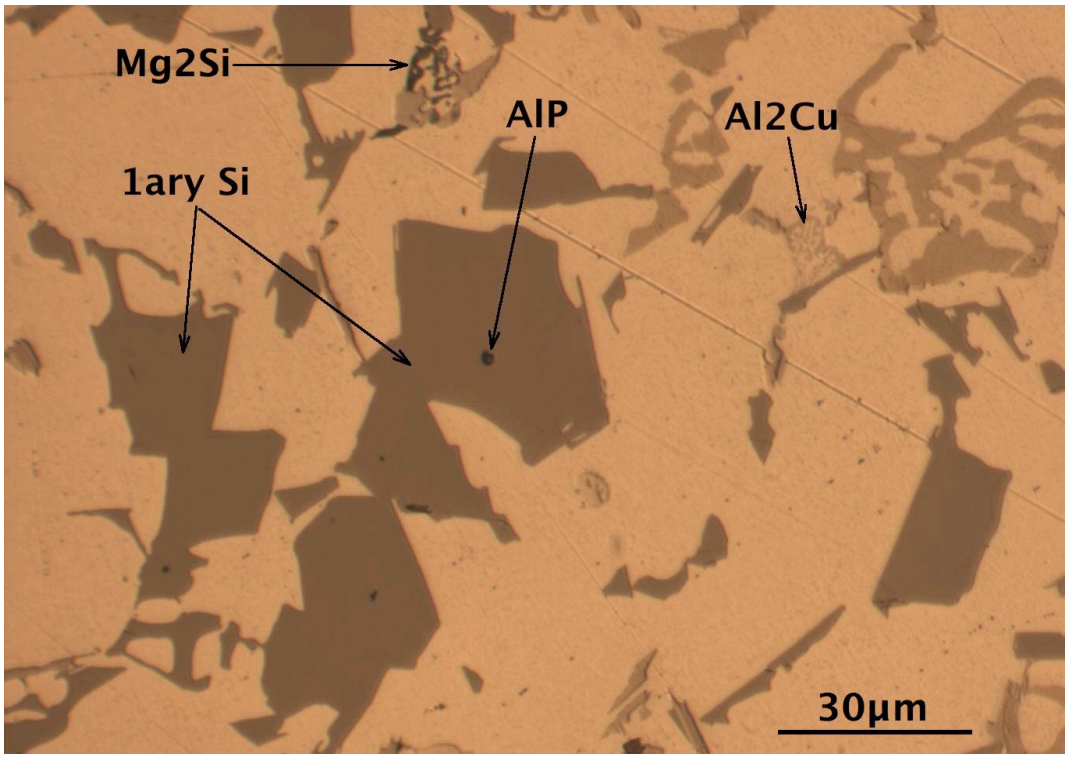

Figure 4-2 Primary Si and other phases in LVD25.

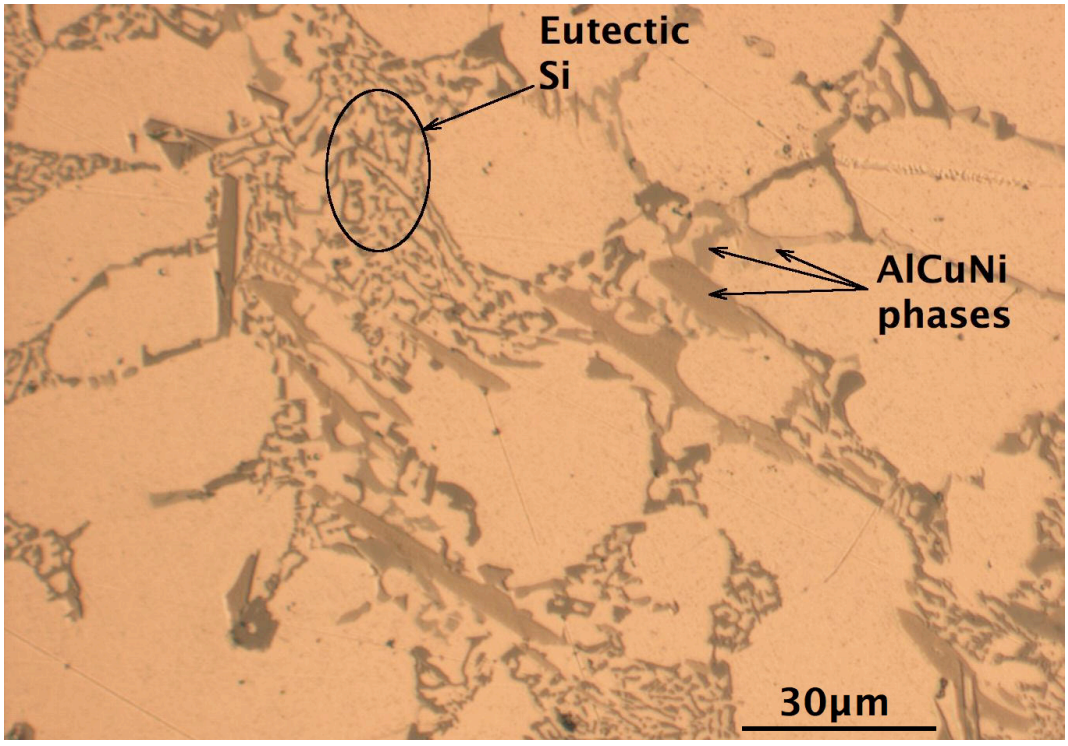

Figure 4-3 Eutectic Si and AlCuNi phases in LVD26 mod.

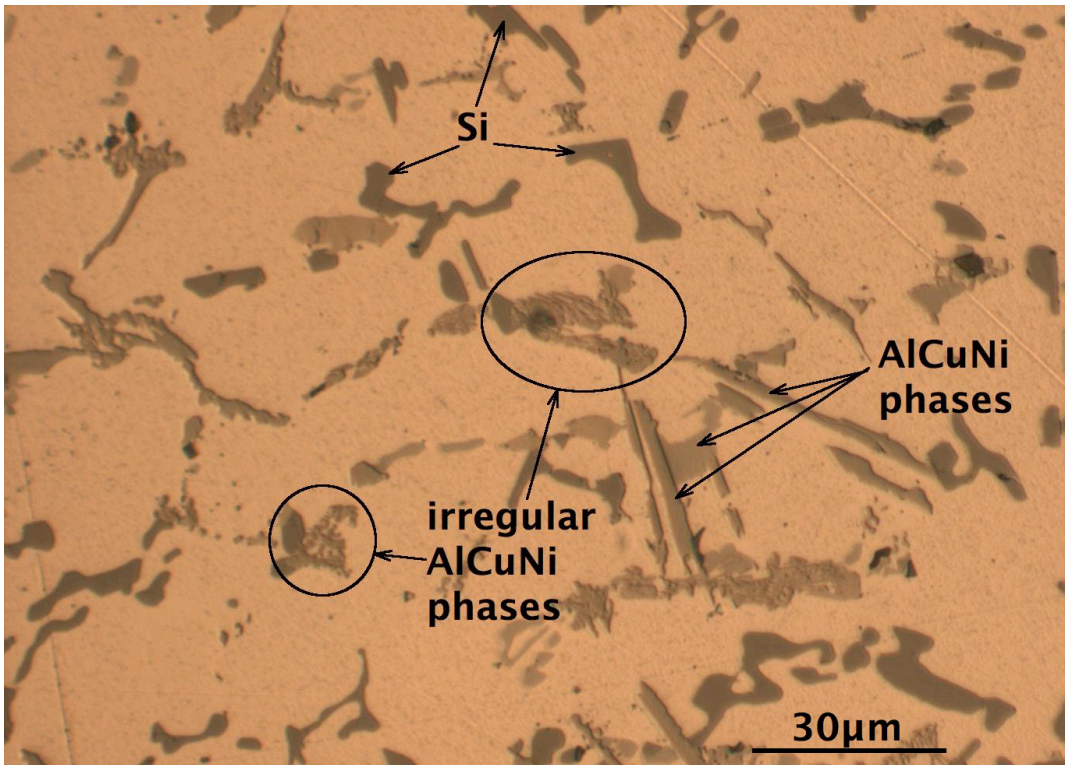

Figure 4-4 Si and AlCuNi phases in LVD26 unmod.

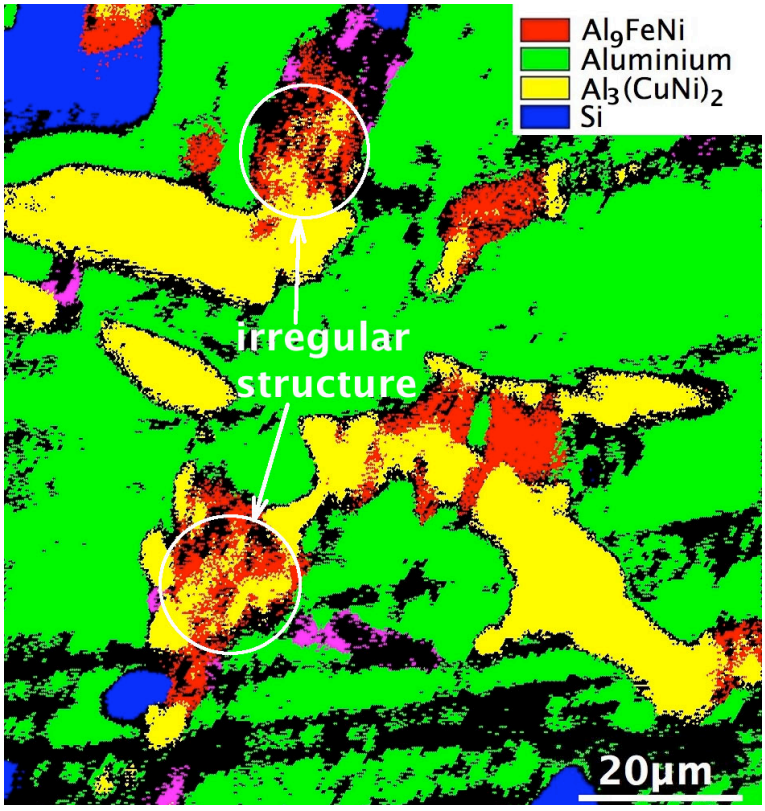

Figure 4-5 Phase map of LVD26 mod.

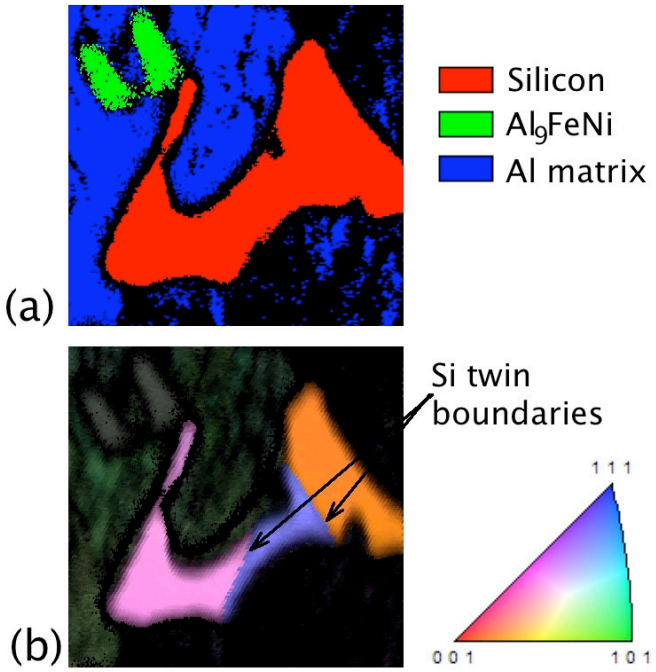

Figure 4-6 (a) phase map showing a primary Si particle in LVD25 and (b) the corresponding inverse pole figure.

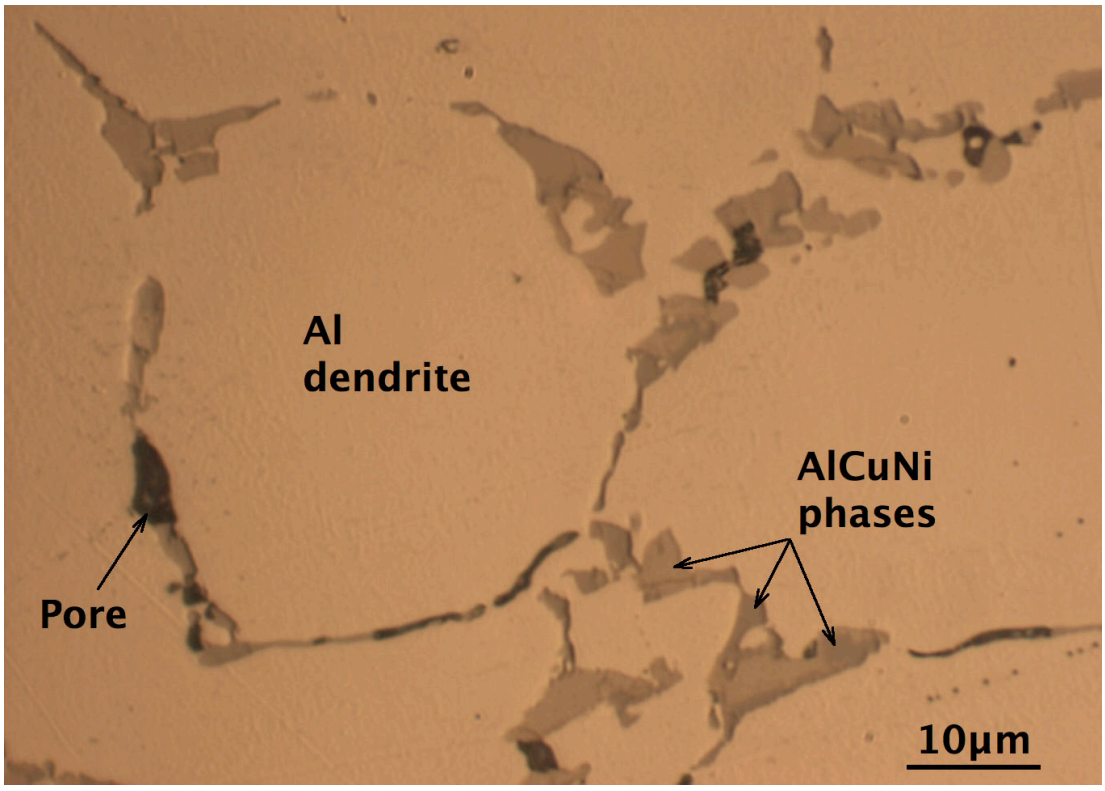

Figure 4-7 Typical microstructural features observed in LVD27.

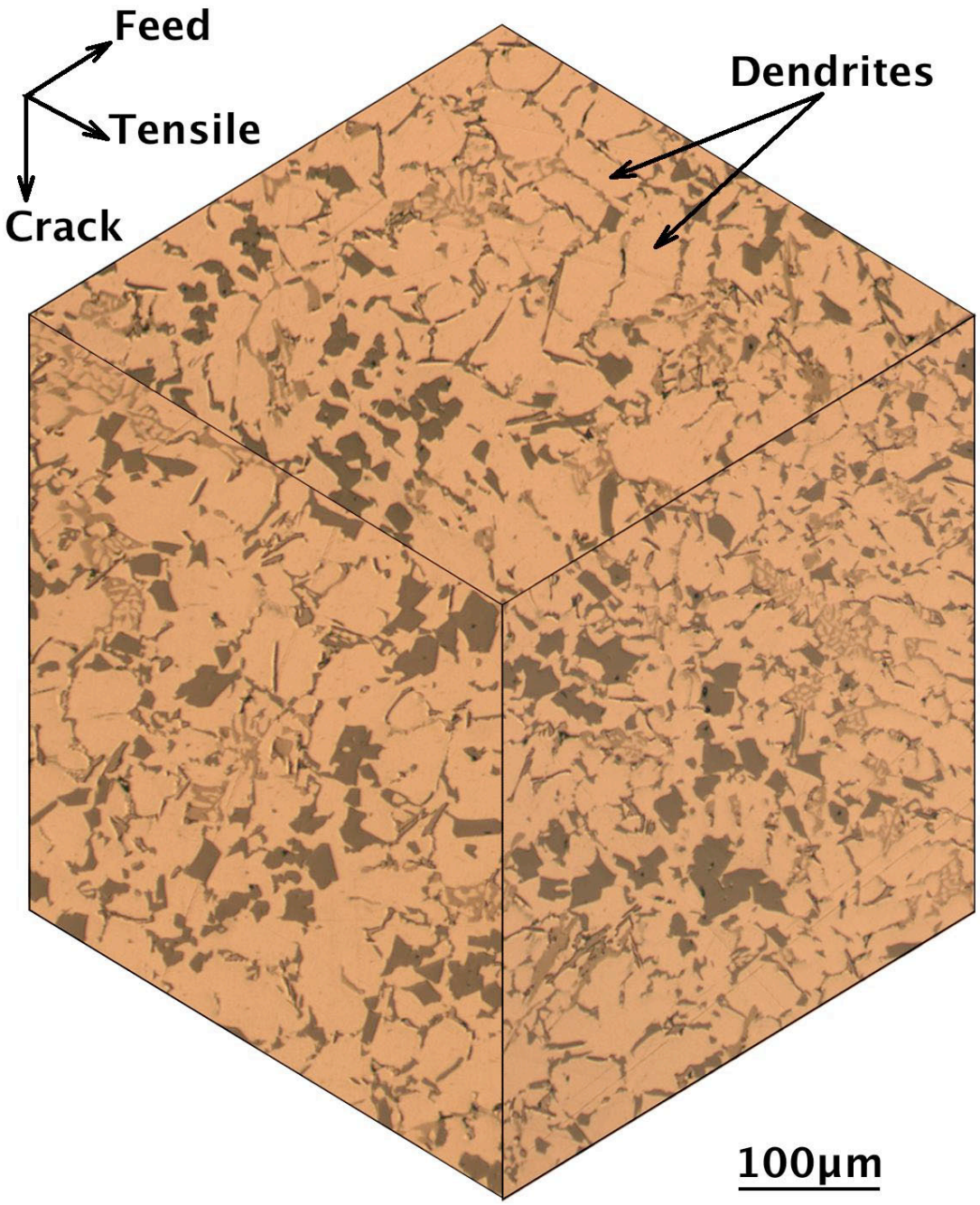

Figure 4-8 Microstructure cube for LVD25.

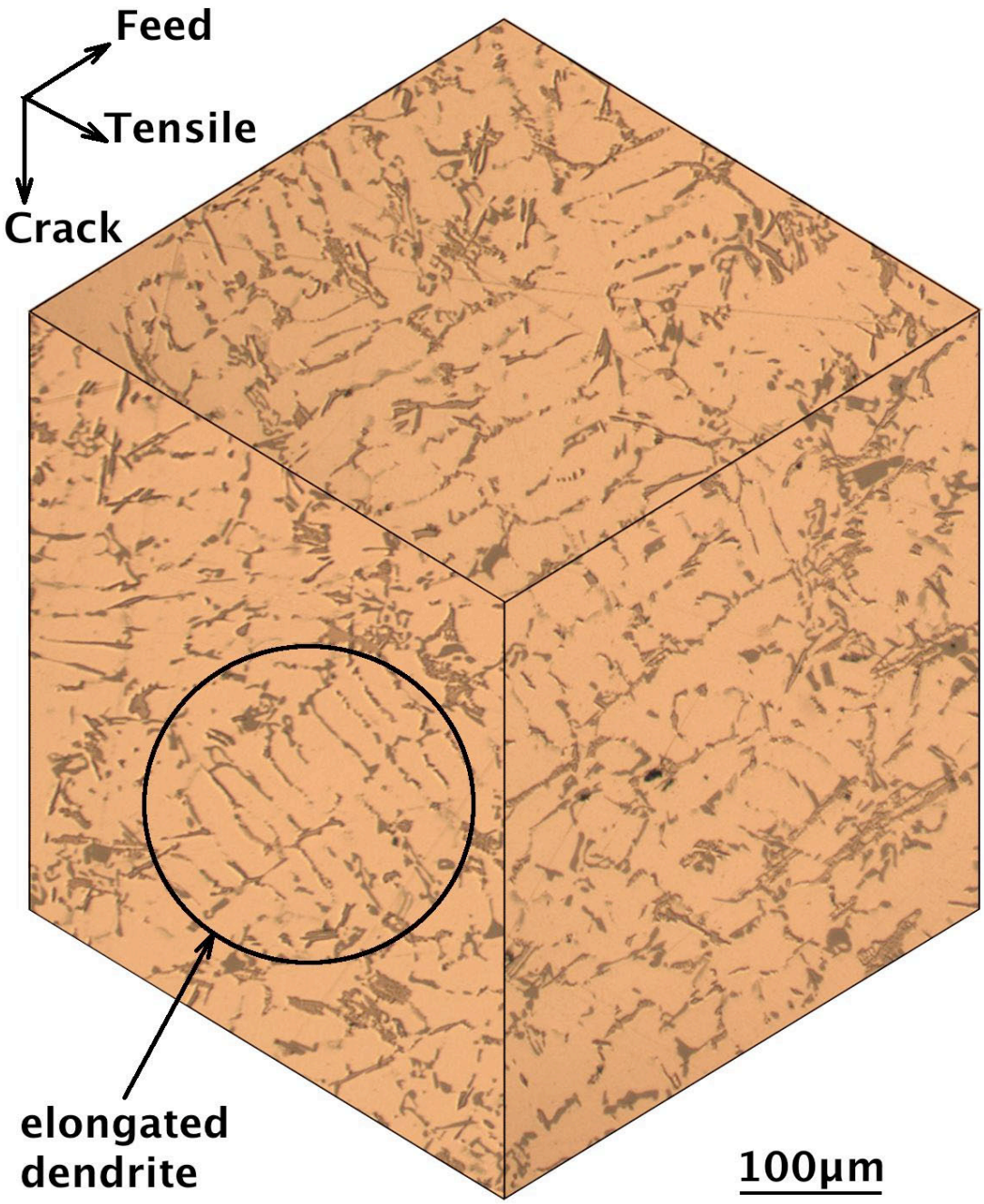

Figure 4-9 Microstructure cube for LVD26 unmod.

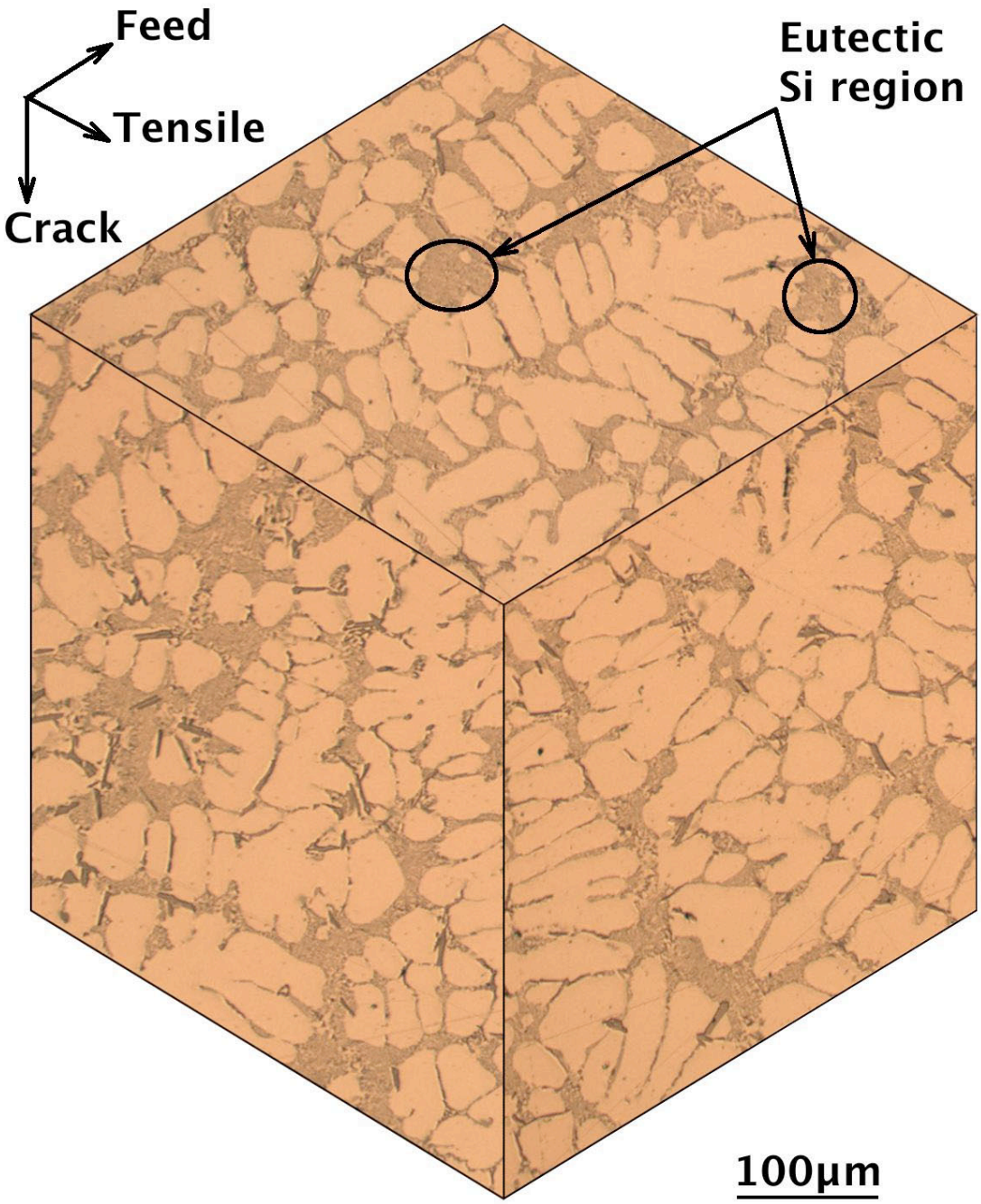

Figure 4-10 Microstructure cube for LVD26 mod.

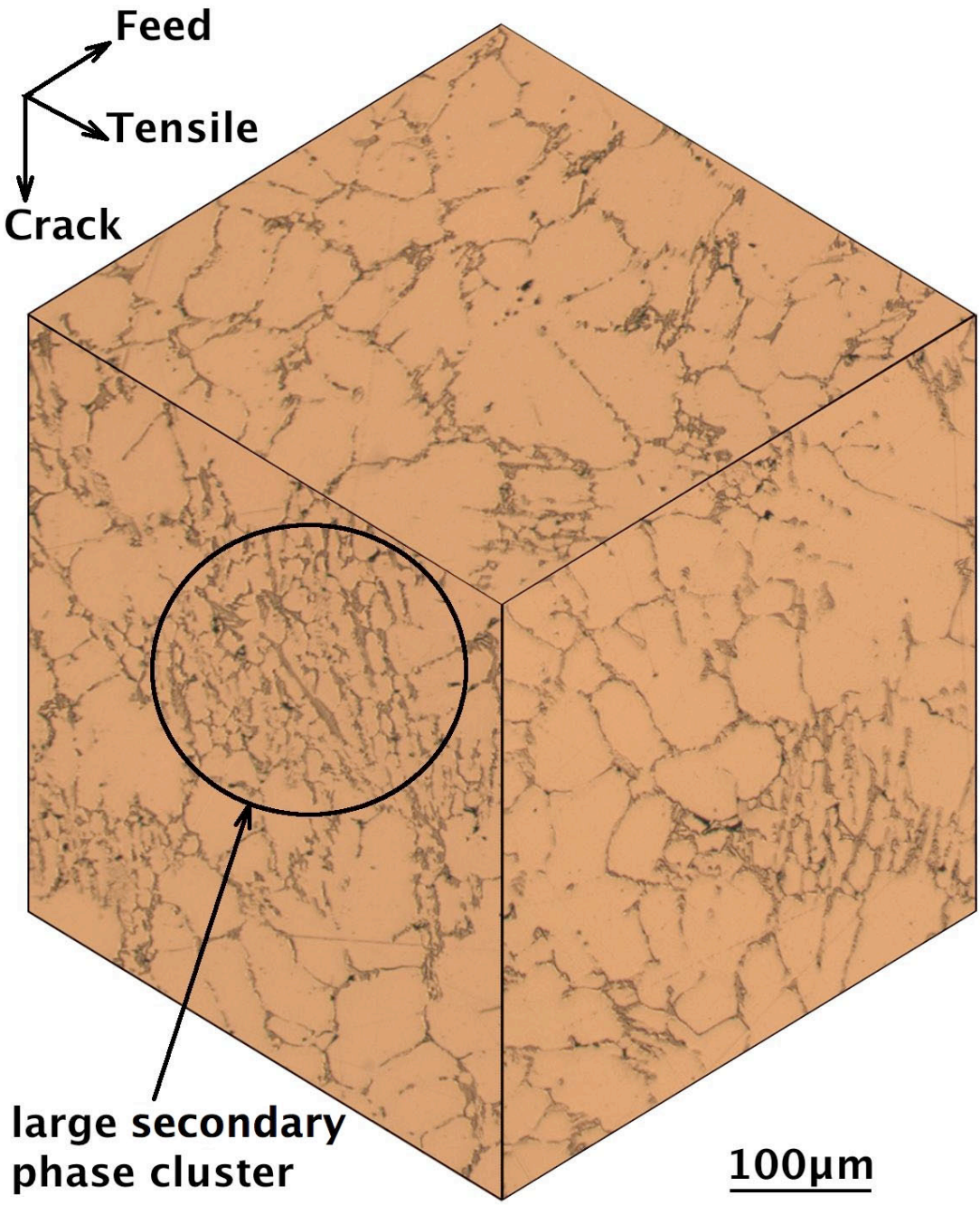

Figure 4-11 Microstructure cube for LVD27.

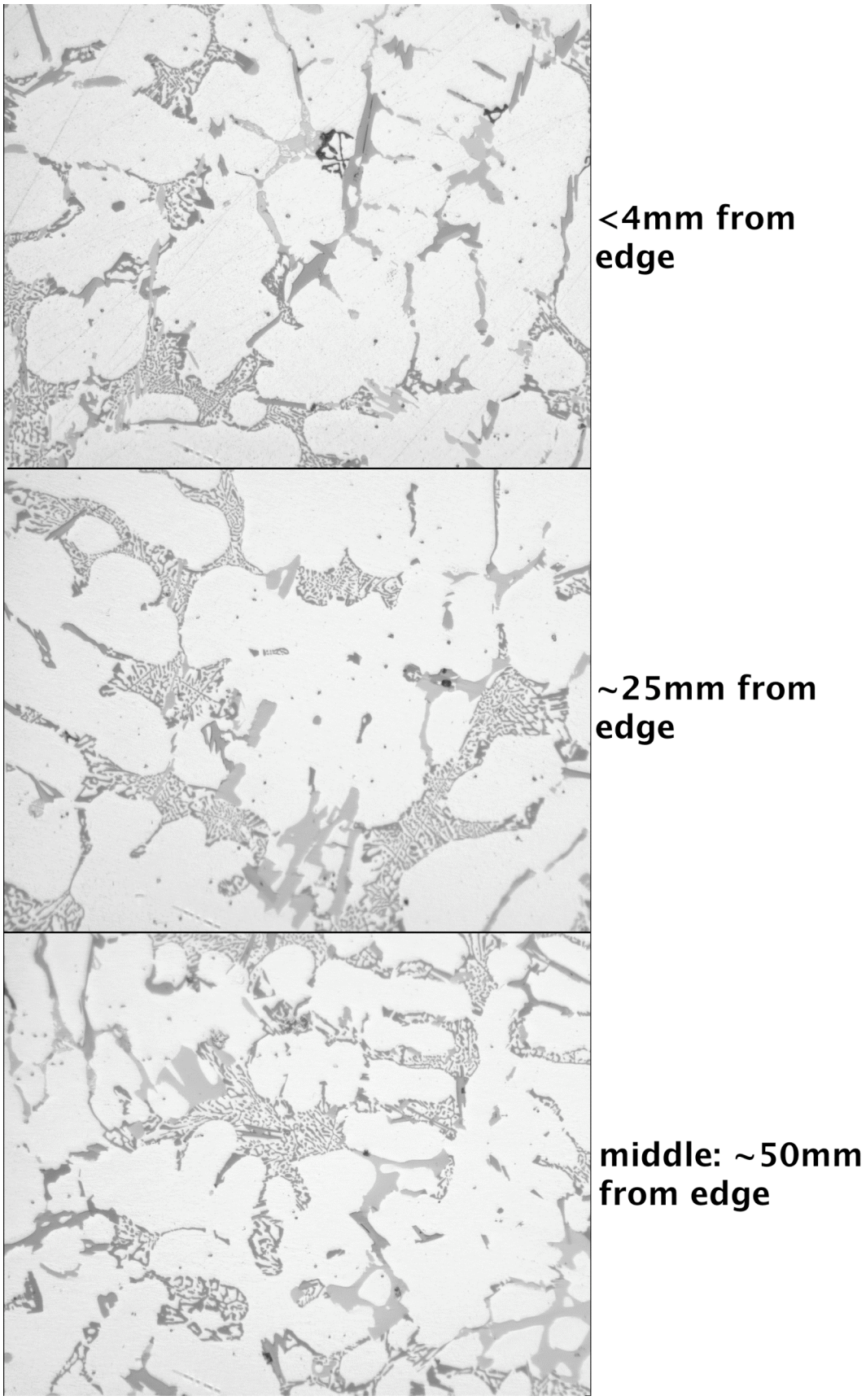

Figure 4-12 Microstructure of LVD26 mod at different location in the piston crown.

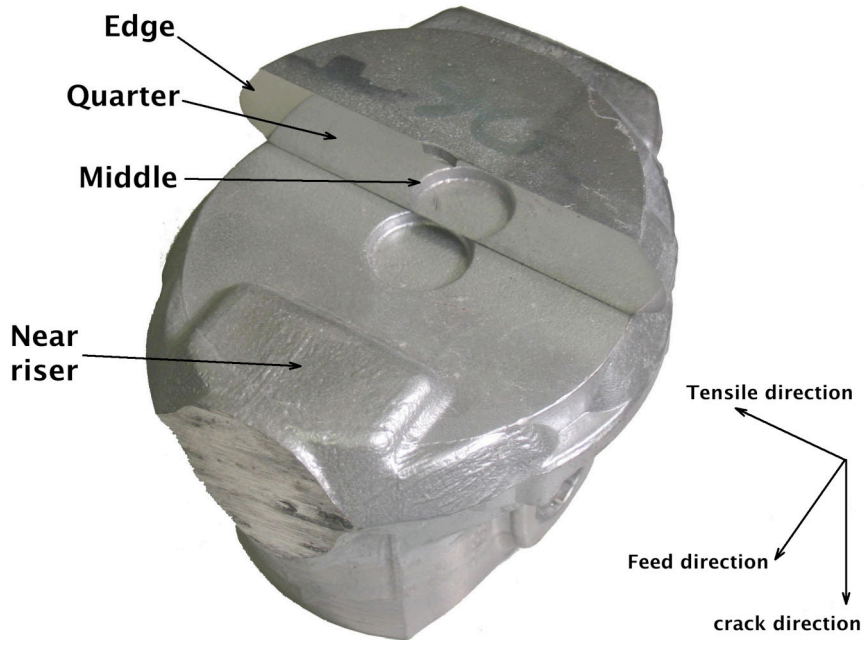

Figure 4-13 Photograph of a piston with a piston crown placed on its top.

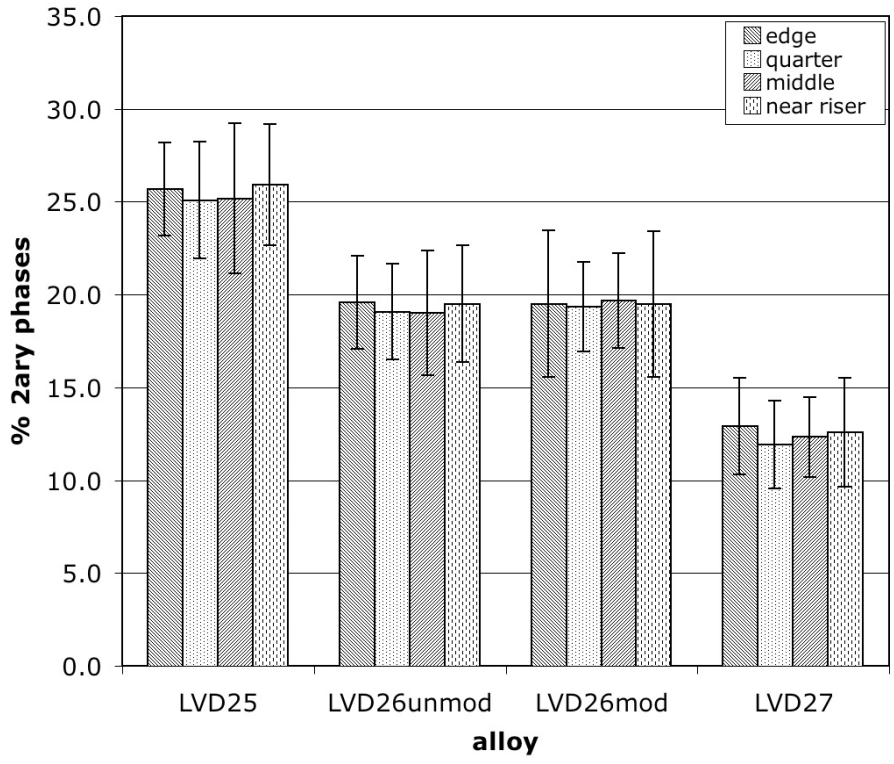

Figure 4-14 Volume fraction of hard particles at different locations in the piston crown, errors bars represent are the standard deviation.

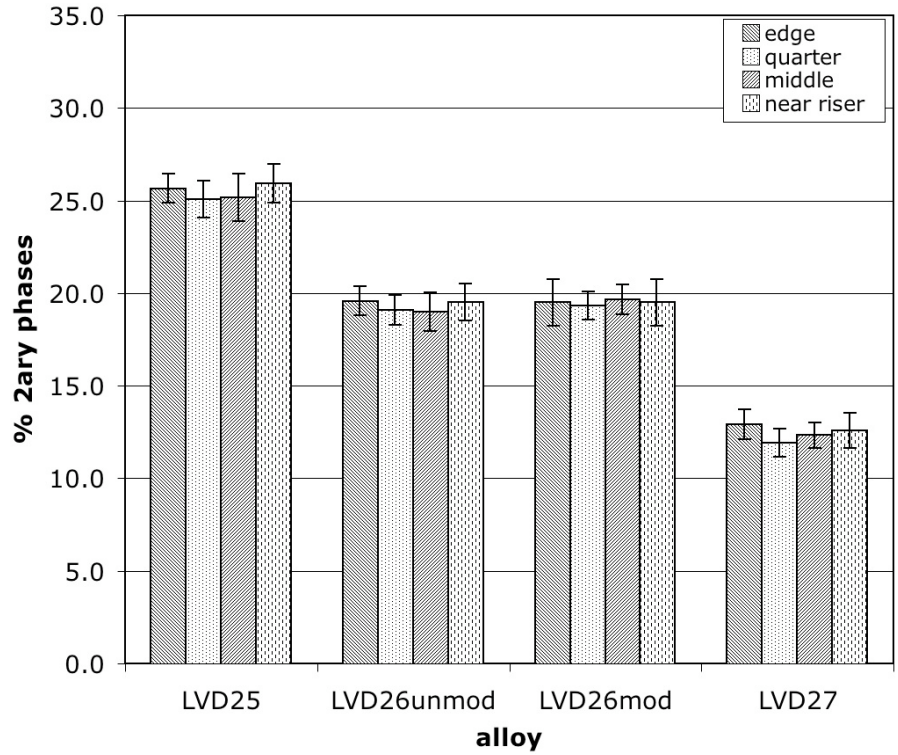

Figure 4-15 Volume fraction of hard particles at different locations in the piston crown, errors bars represent are the standard error.

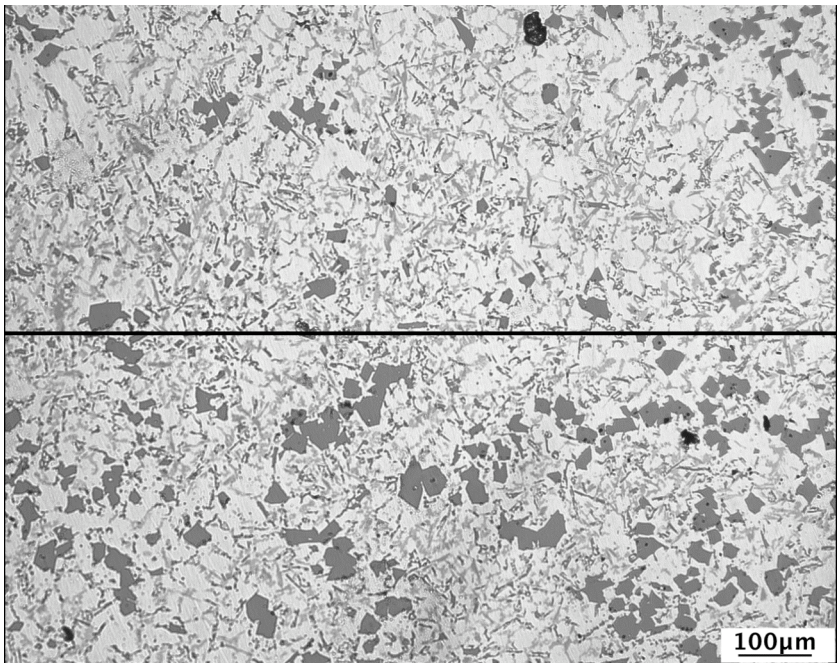

Figure 4-16 Micrograph showing a heterogeneous distribution of primary Si in LVD25.

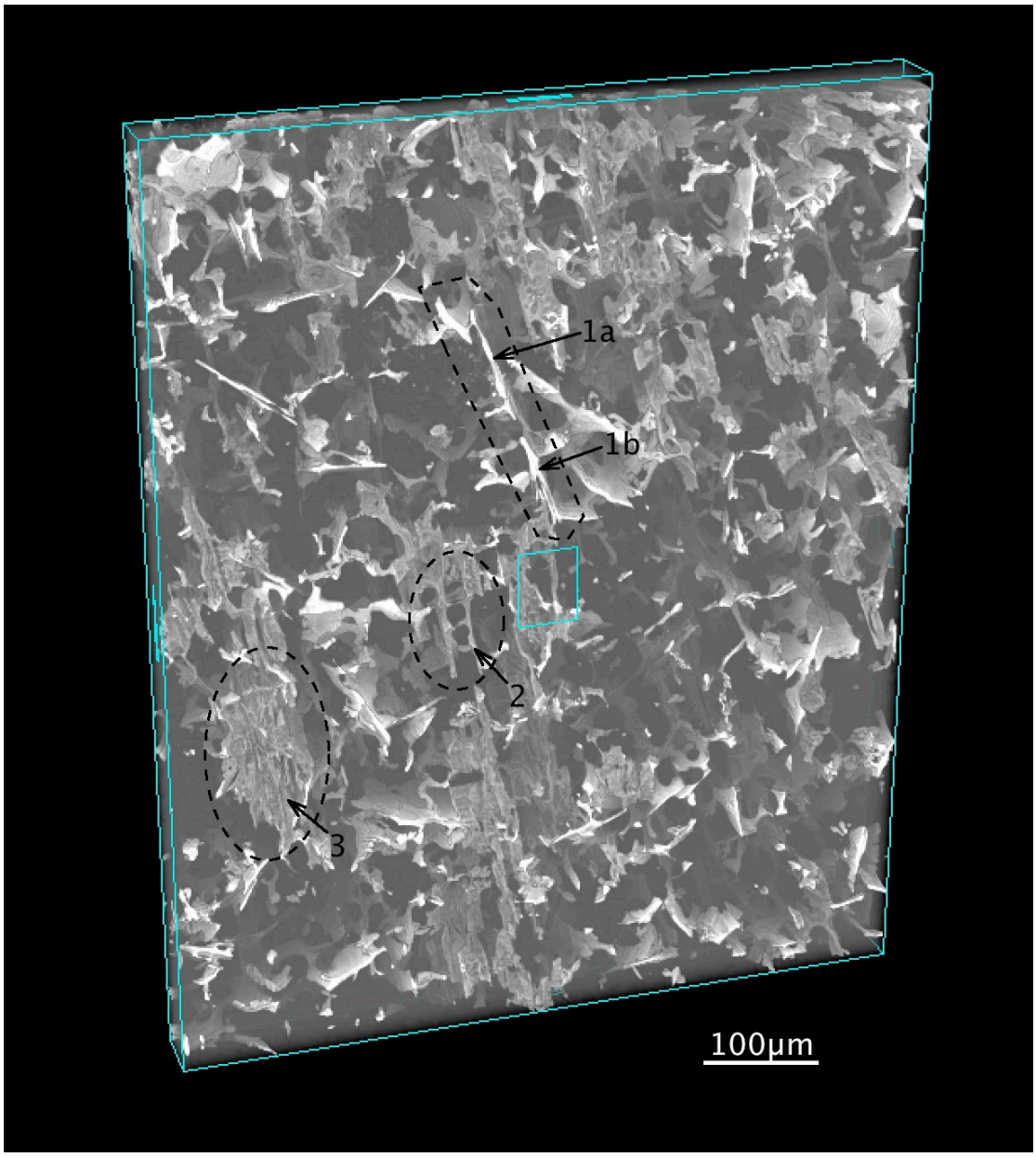

Figure 4-17 Lower magnification tomography image of LVD25.

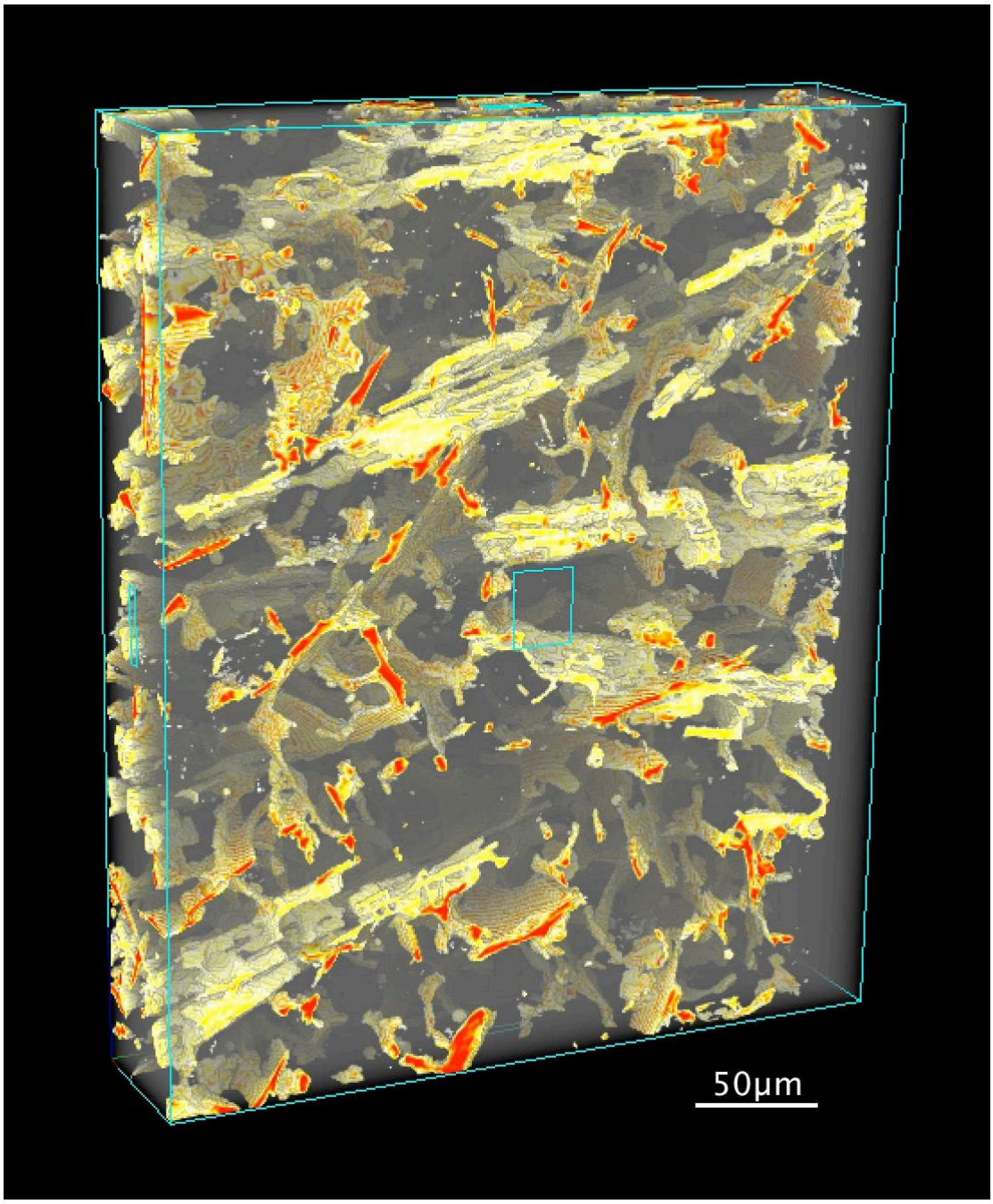

Figure 4-18 Higher magnification tomography image of LVD25.

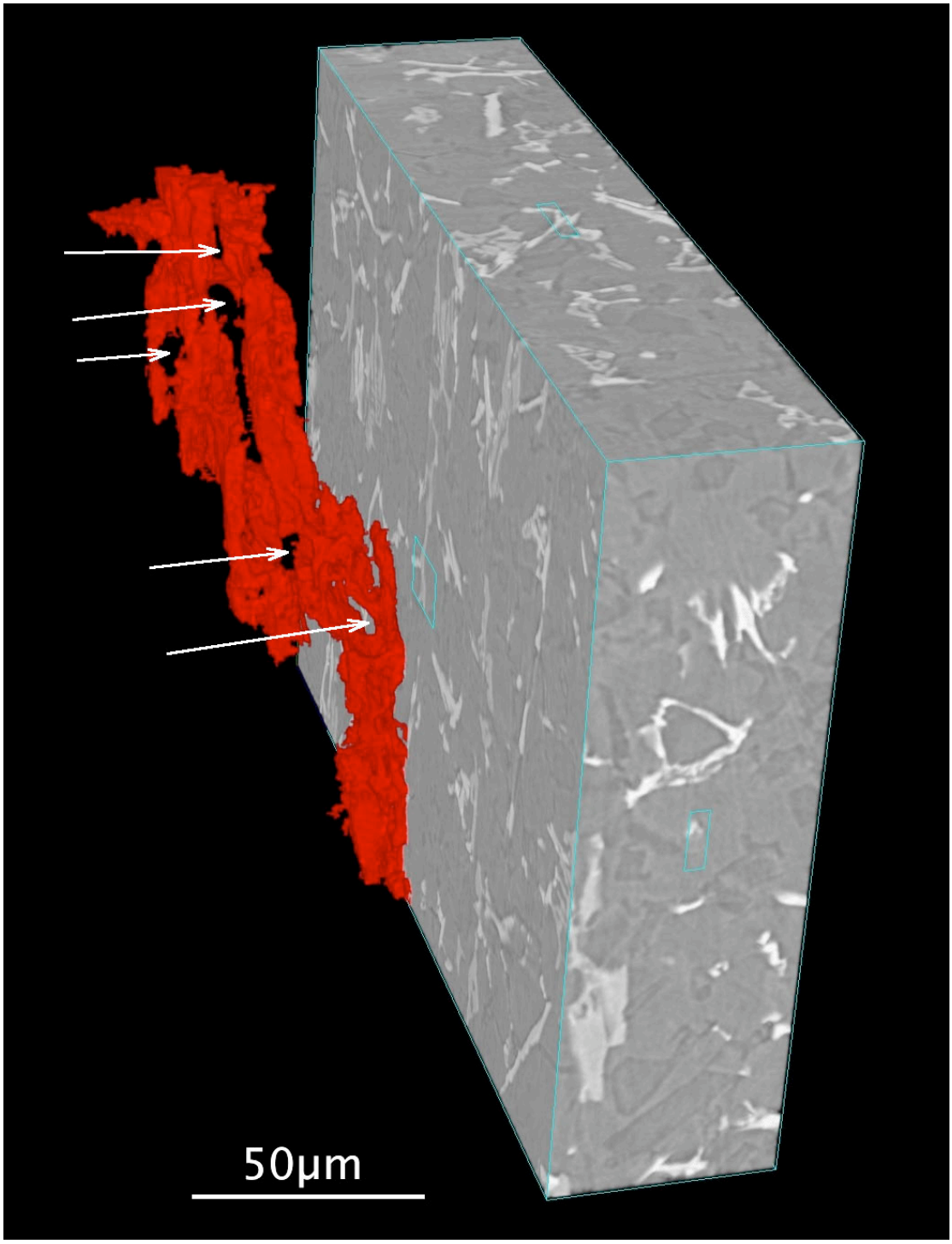

Figure 4-19 Segmented flake in an LVD25 alloy.

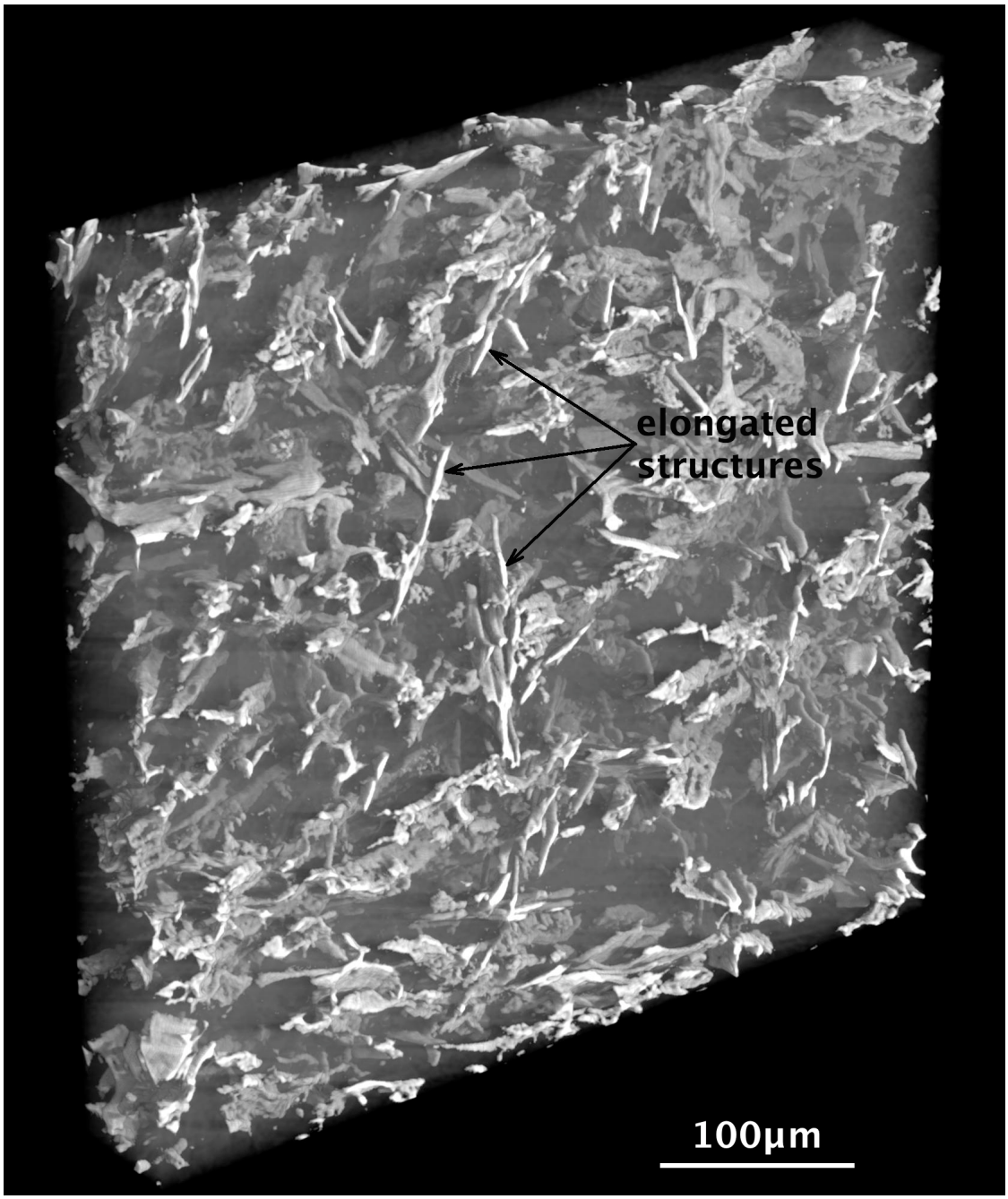

Figure 4-20 Tomography image of intermetallic network in LVD26 unmod.

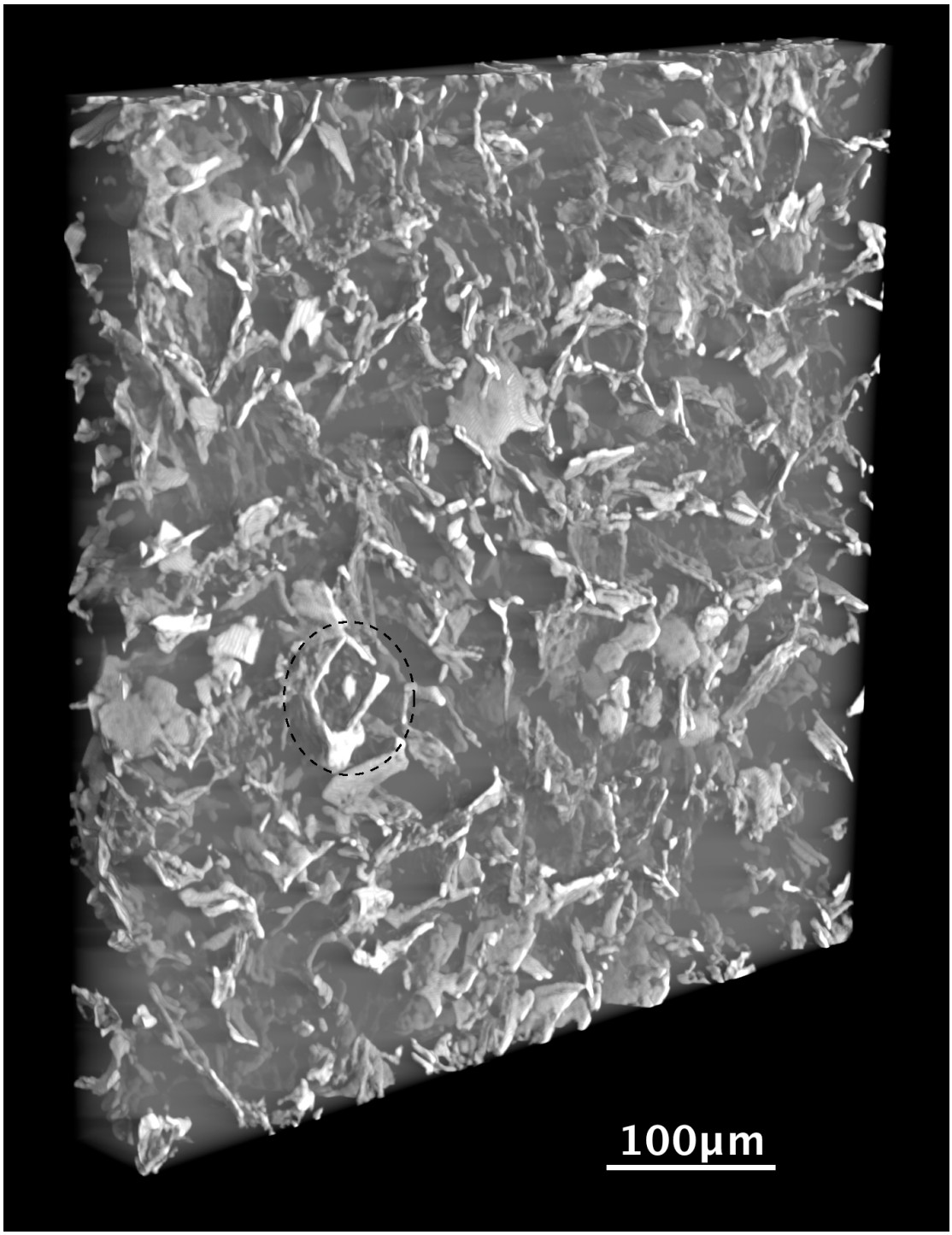

Figure 4-21 Tomography image of intermetallic network in LVD26 mod.

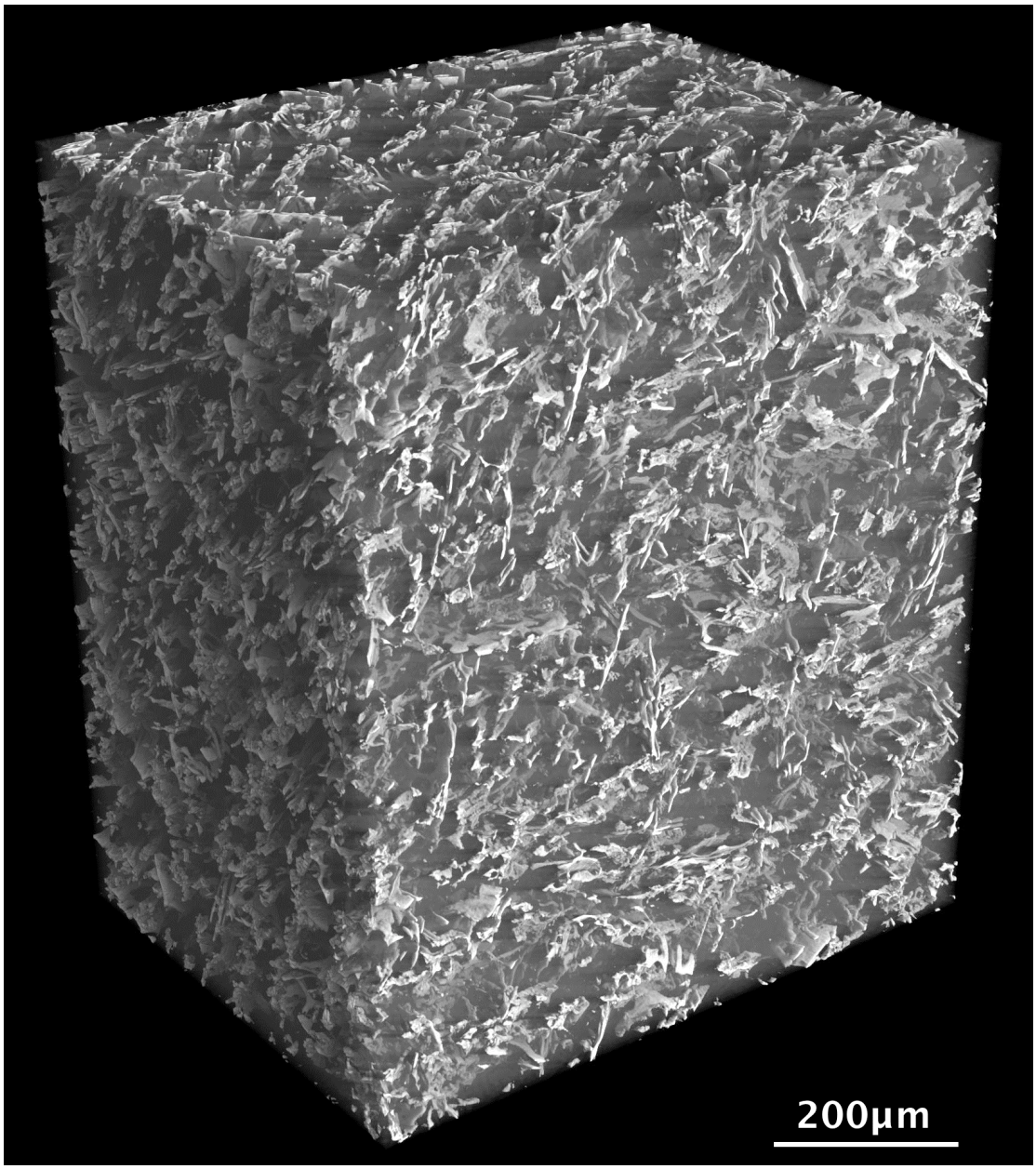

Figure 4-22 Tomography image showing a cube of the intermetallic network in LVD26 unmod.

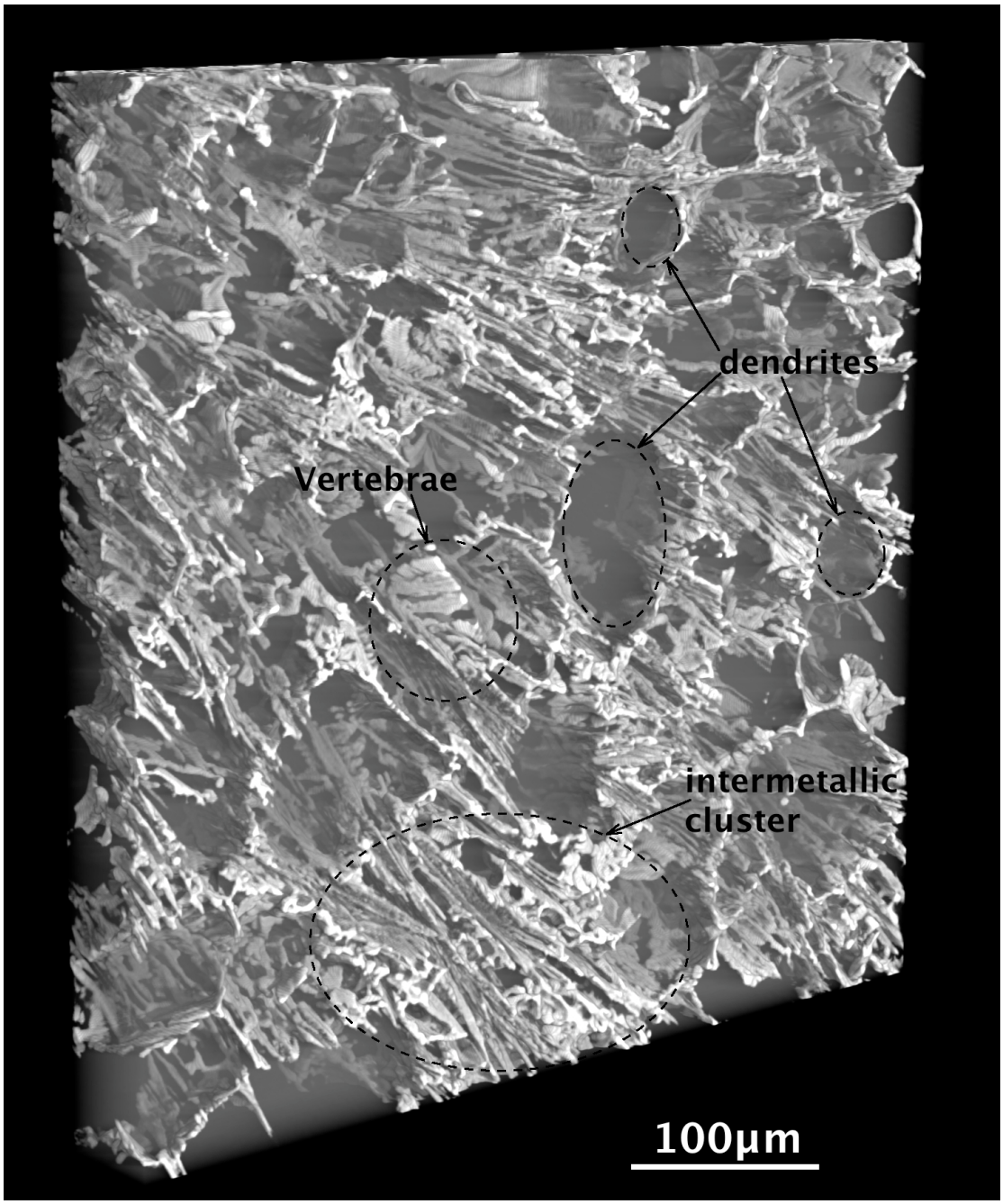

Figure 4-23 Tomography image of intermetallic network in LVD27.

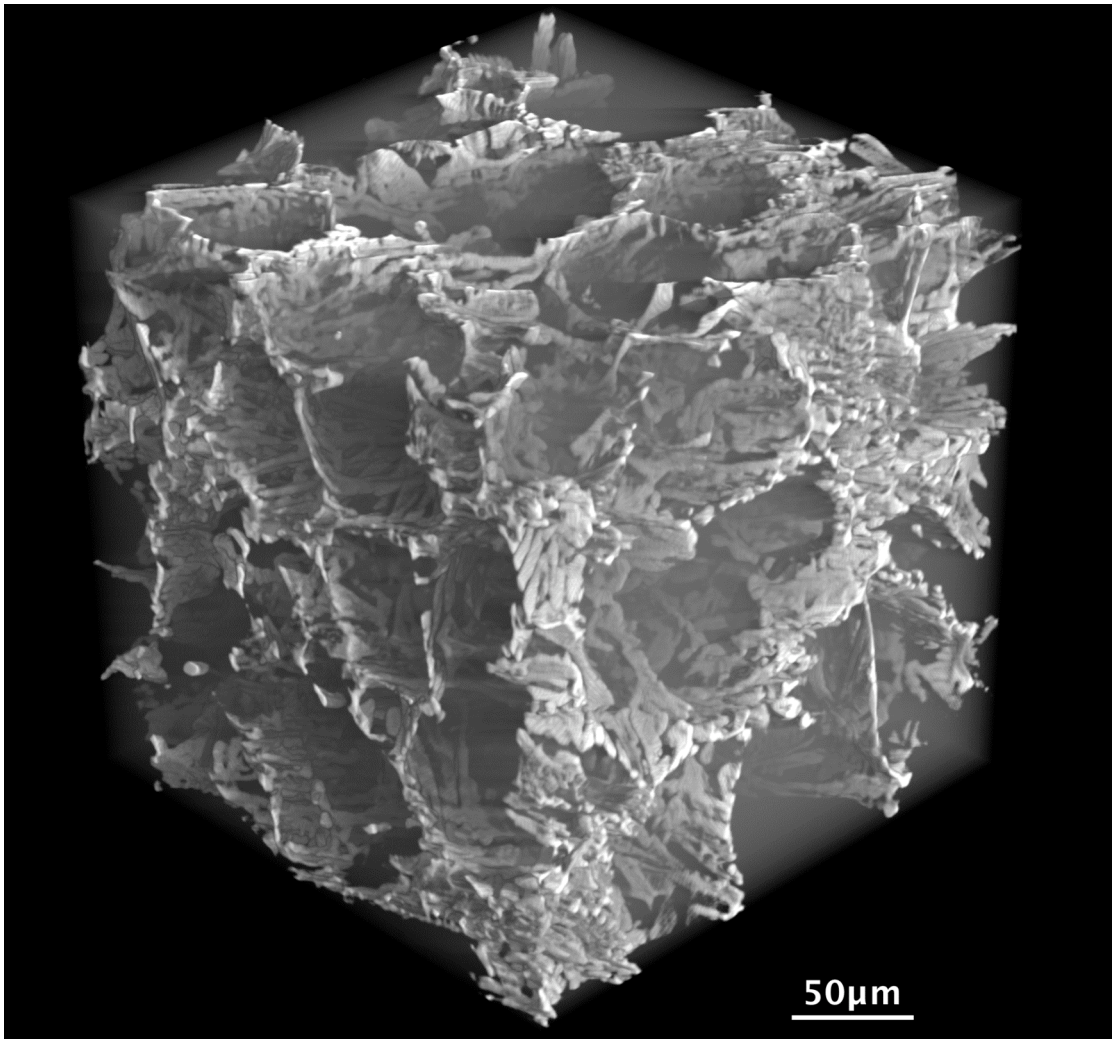

Figure 4-24 Tomography image showing a cube of the intermetallic network in LVD27.

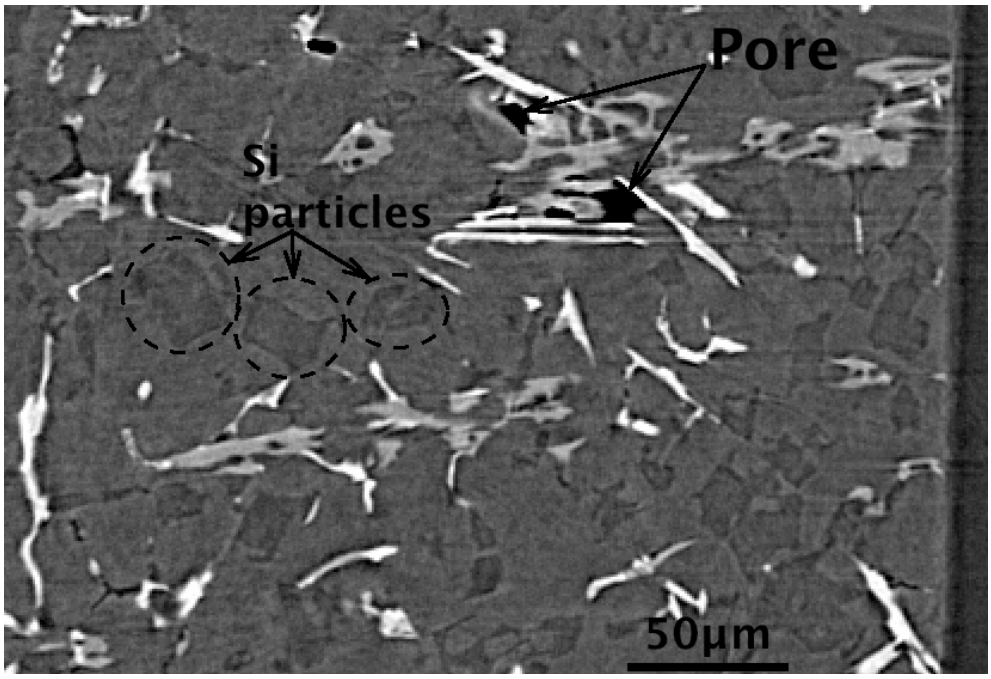

Figure 4-25 Two dimensional image of a pore in LVD25 from CT data.

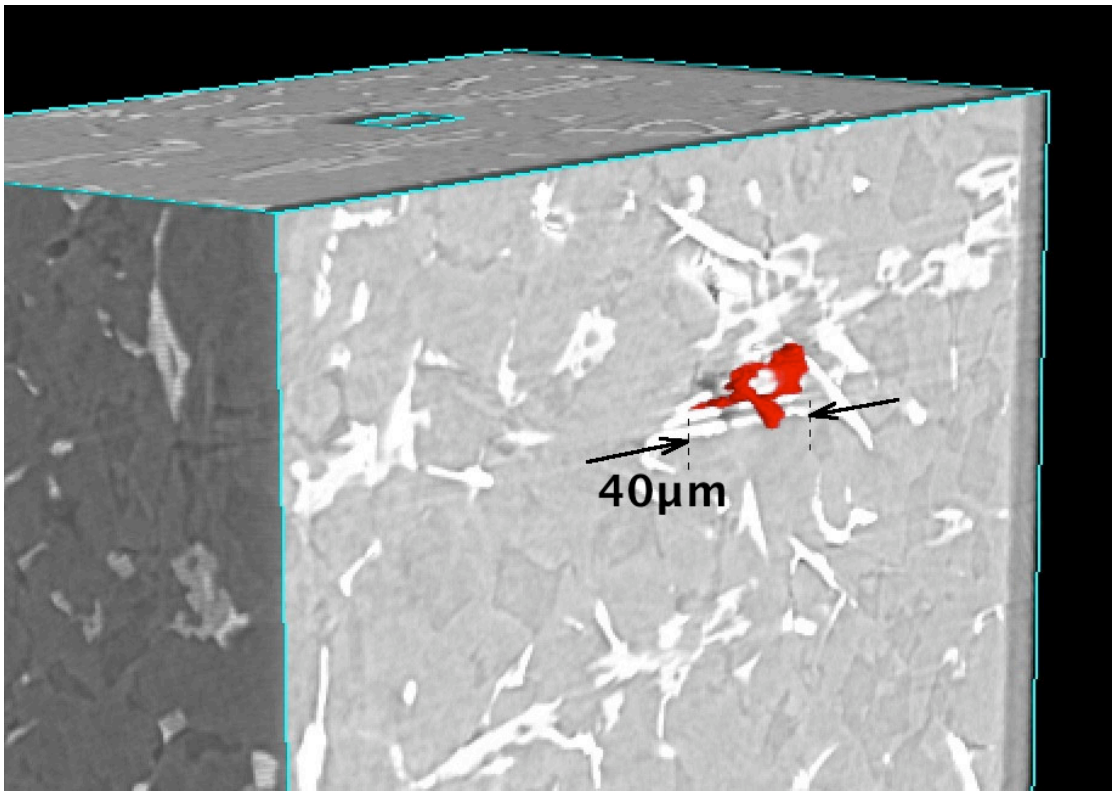

Figure 4-26 Three dimensional image of the pore (red) presented in Figure 4-25,

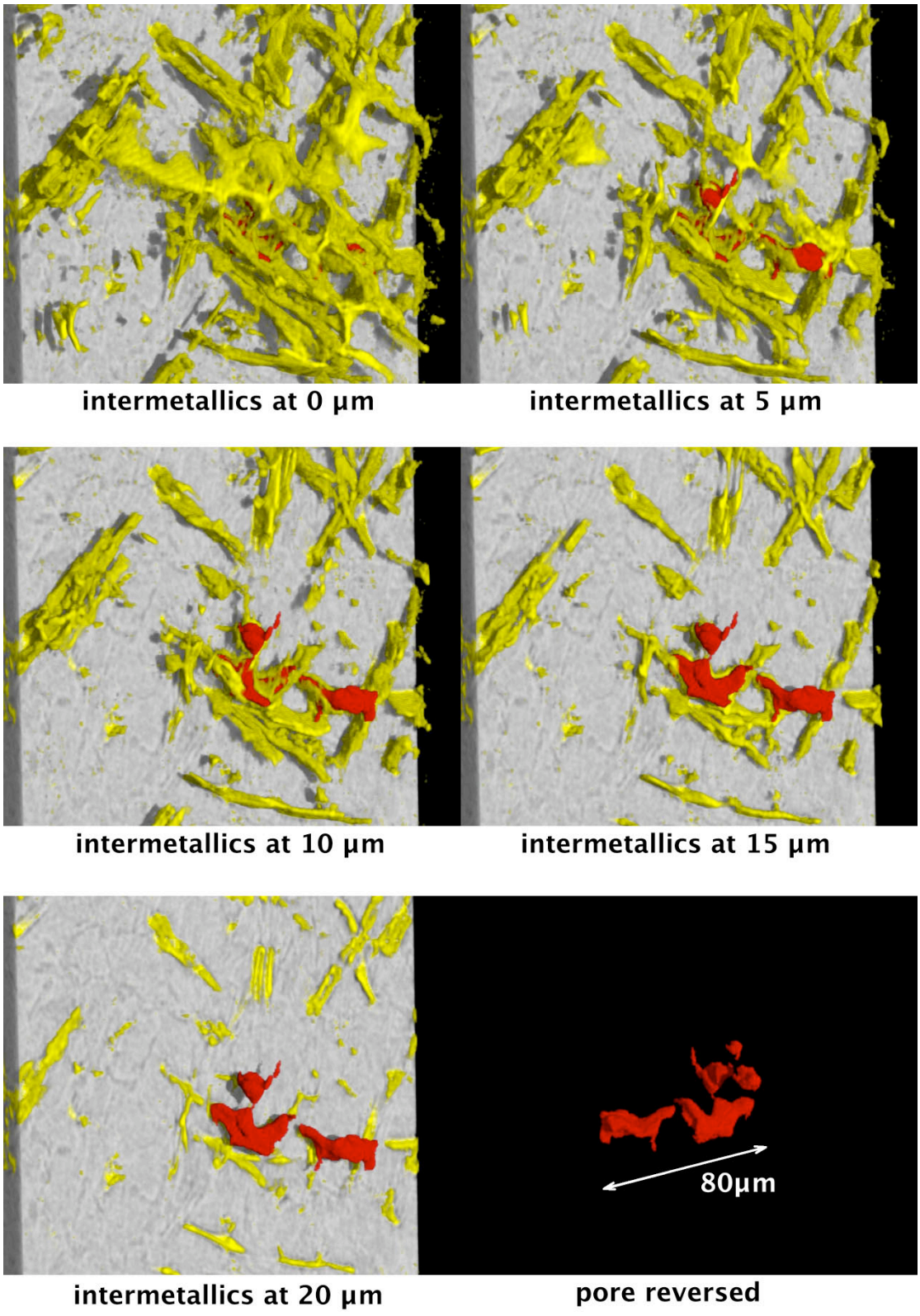

Figure 4-27 Interaction between the pore and the intermetallics. In successive images the intermetallic phase are withdrawn to real the pore. The final image shows the pore from the reverse direction.

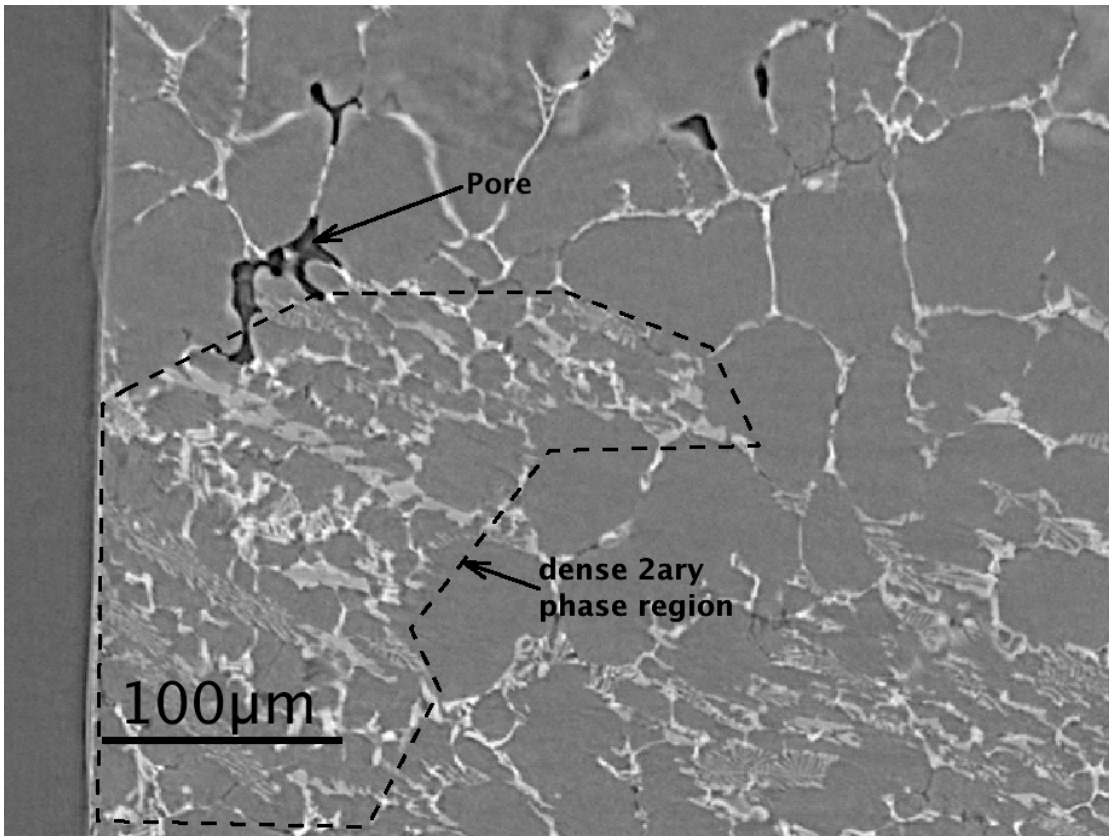

Figure 4-28 Interdendritic porosity in LVD27.

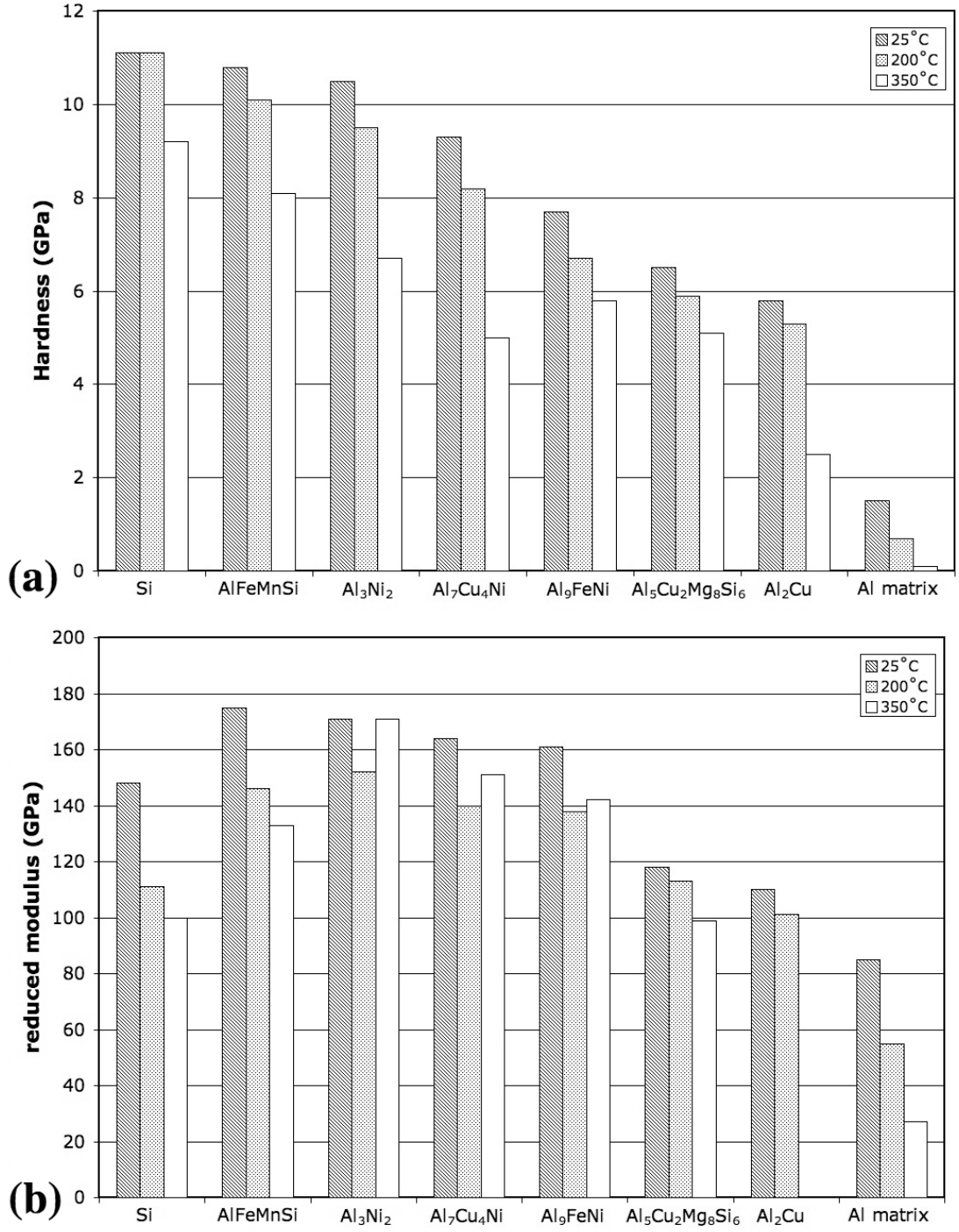

Figure 4-29 (a) hardness and (b) reduced modulus values from Chen (2006).

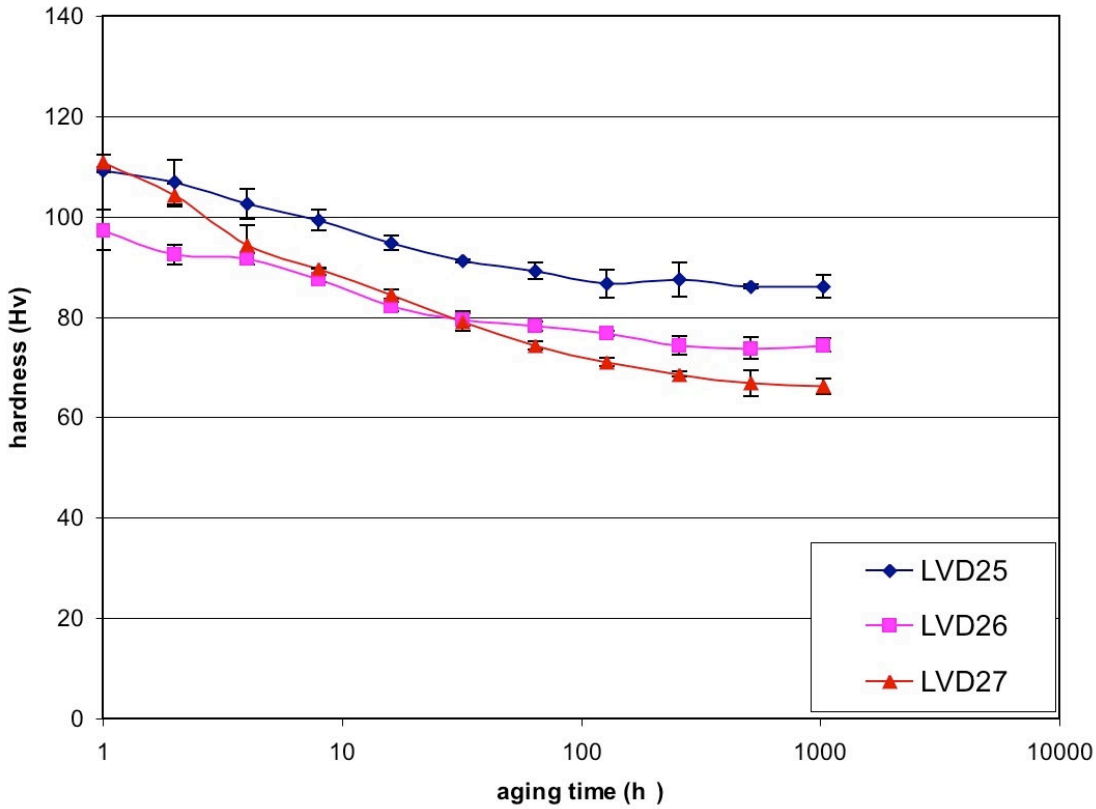

Figure 4-30 Vickers hardness as a function of ageing time

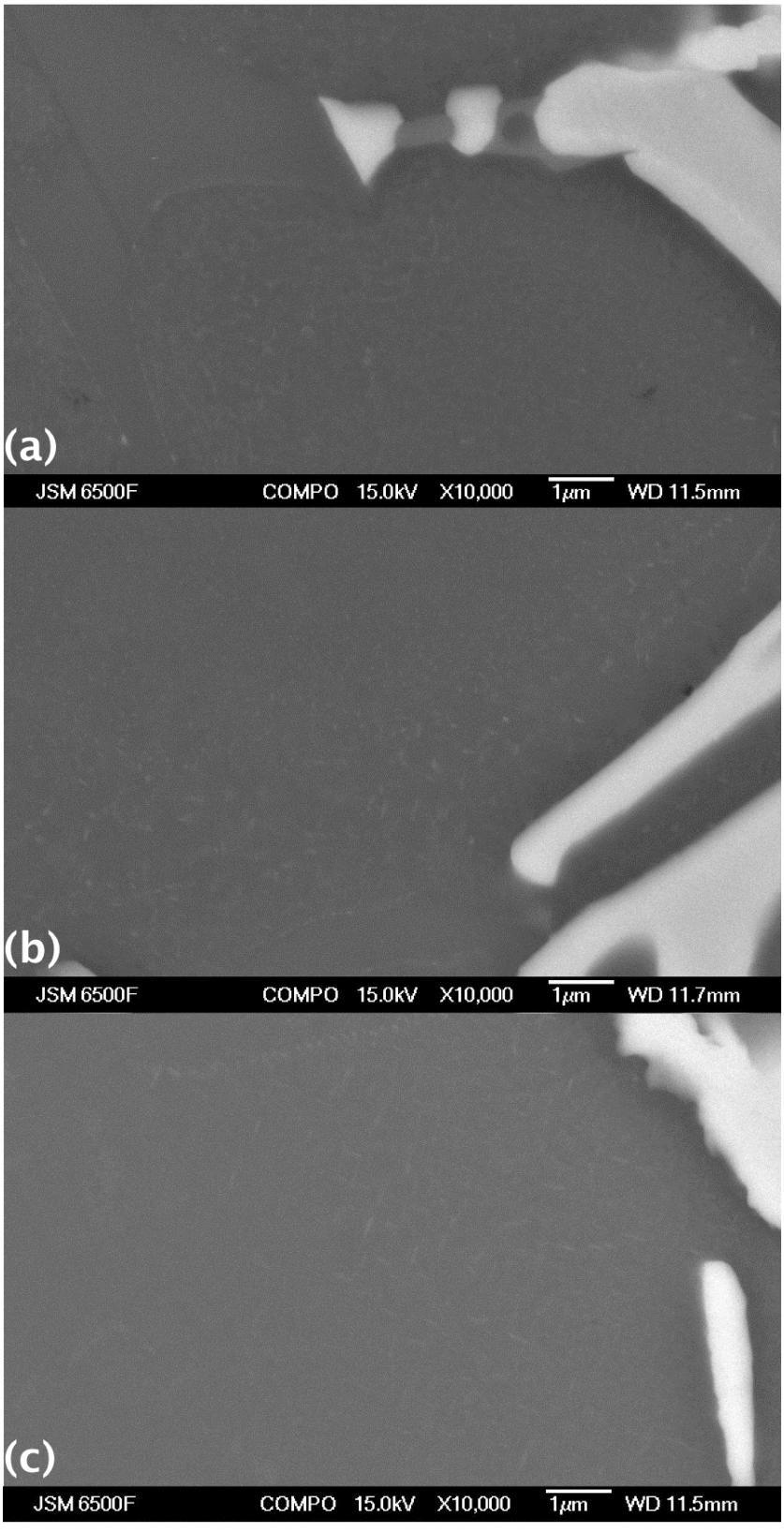

Figure 4-31 SEM images of (a) LVD25, (b) LVD26mod and (c) LVD27 after 1 hour aging at 260˚C.

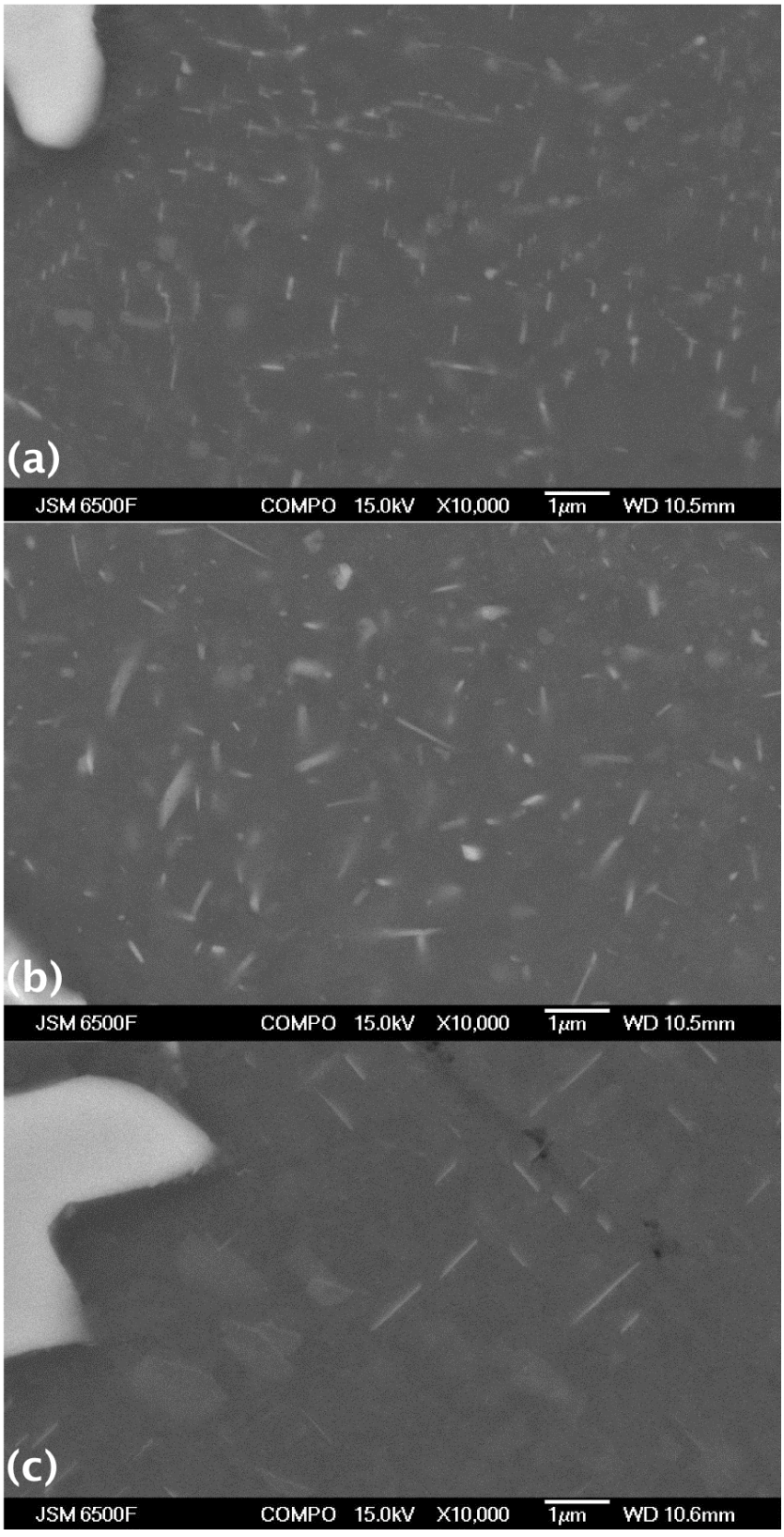

Figure 4-32 SEM images of (a) LVD25, (b) LVD26mod and (c) LVD27 after 1024 hours aging at 260˚C.

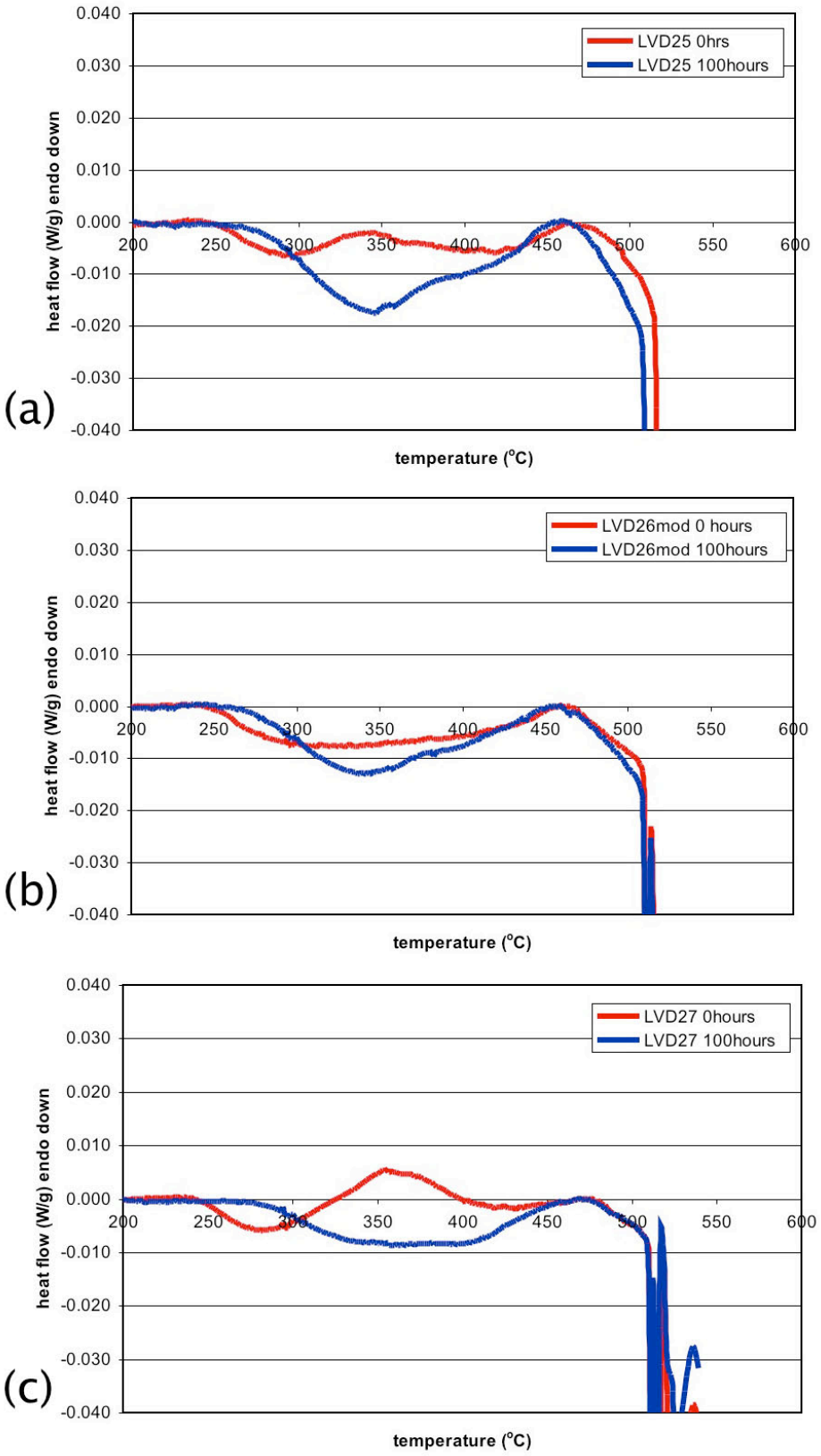

Figure 4-33 DSC results for alloys (a) LVD25, (b) LVD26 mod and (c) LVD27 after 0 and 100 hours.

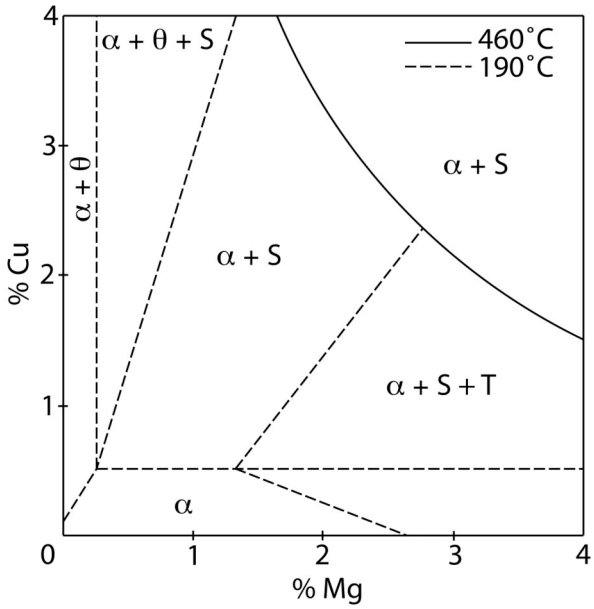

Figure 4-34 Section of the estimated ternary Al-Cu-Mg phase diagram at 460˚C and 190˚C from Polmear (1989), θ = Al_2Cu, S = Al_2CuMg and T = Al_6CuMg_4.

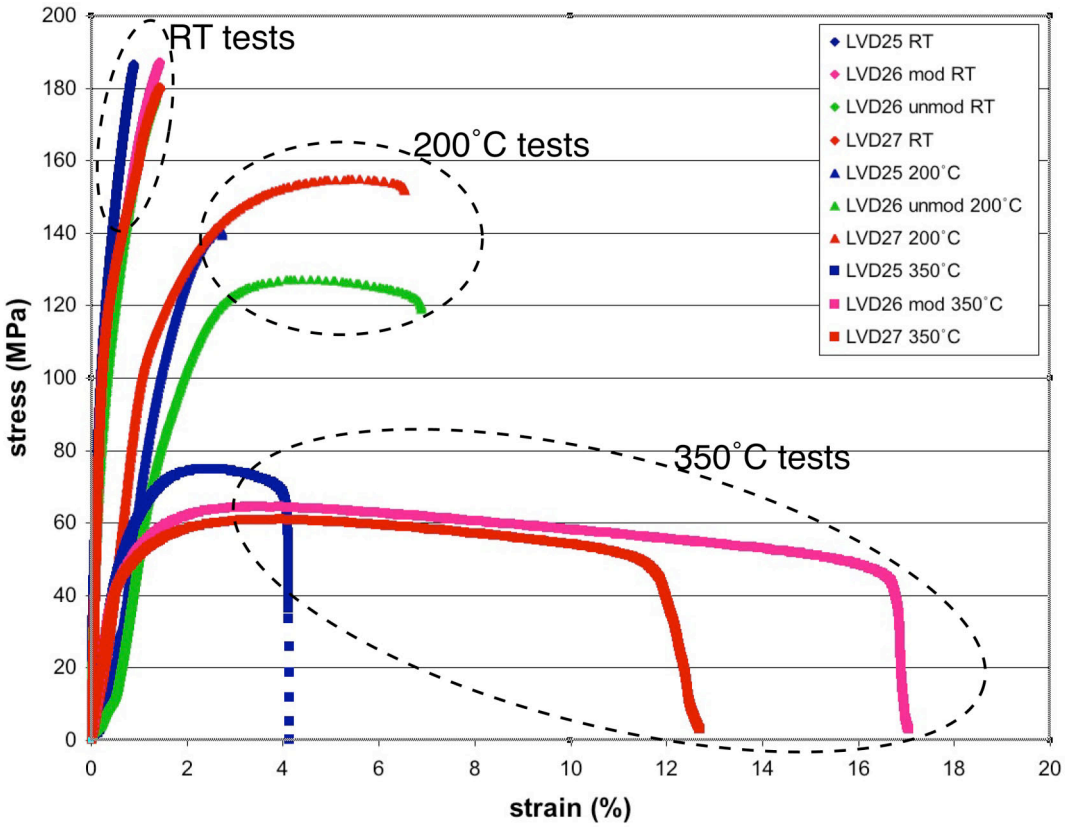

Figure 4-35 Tensile test stress-strain curves.

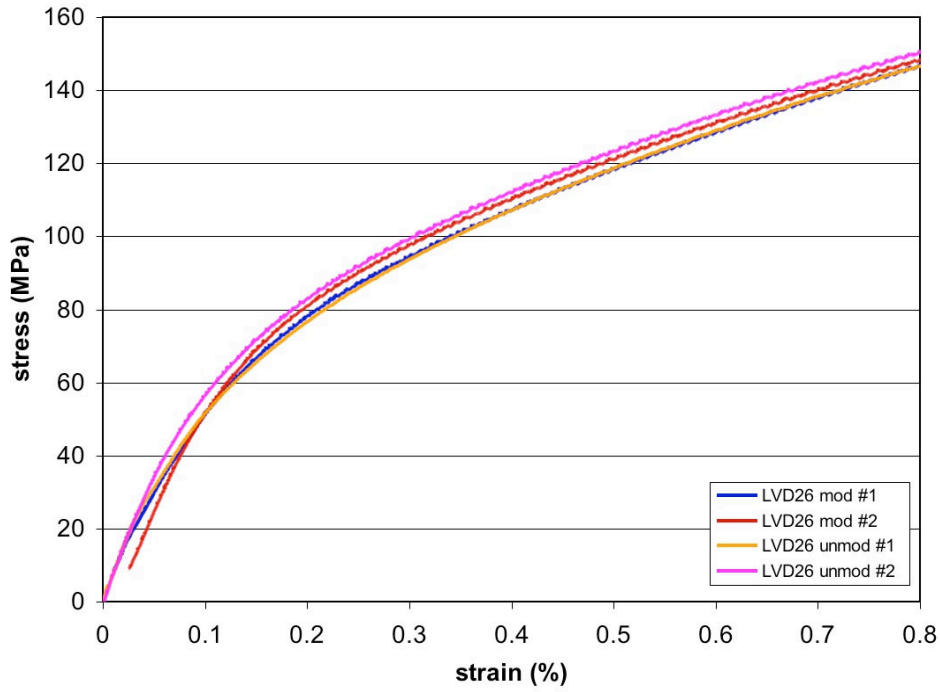

Figure 4-36 Tensile test curves for LVD26 alloys at RT.

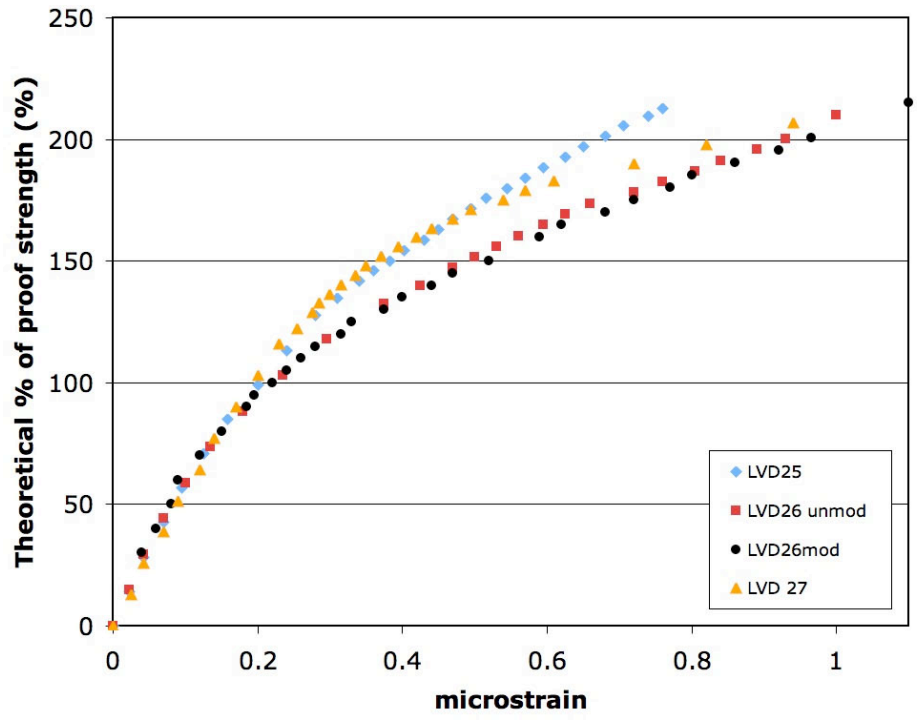

Figure 4-37 Strain gage tests on bend bar samples showing the % of theoretical (from beam theory) 0.2 % proof strength as a function of microstrain.

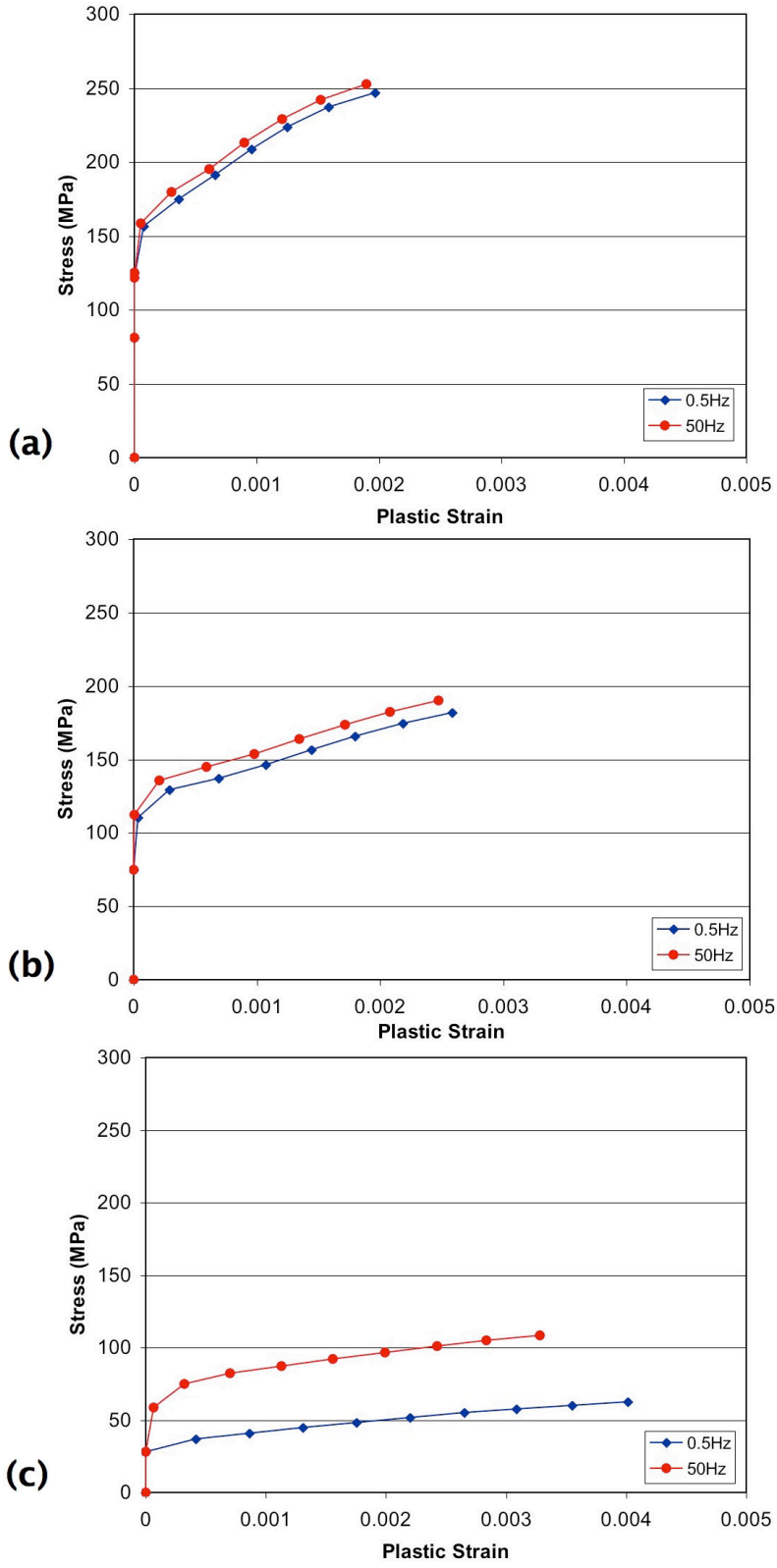

Figure 4-38 Cyclic stress-strain results in LVD25, (a) at RT, (b) at 200˚C and (c) at 350˚C.

Chapter 5

Fatigue Results

5.1 Introduction

Fatigue crack initiation and growth in Al-casting alloys is microstructurally dependent. Features such as intermetallic particles, Si particles and pores play an important role in the micromechanisms of fatigue. In order to gain a detailed understanding of these micromechanisms a systematic set of fatigue tests were performed to assess all stages of fatigue life in the alloys studied.

S-N tests allowed for an assessment of the baseline behaviour of the alloys, in addition the fracture surfaces were analysed using SEM to identify the causes of fatigue crack initiation. Initiation was further studied using interrupted, short fatigue crack growth tests where acetate replication was used to monitor initiation as well as subsequent small crack propagation. Short fatigue crack samples were analysed using novel techniques such as phase mapping and X-ray CT to gain a detailed insight into the influence of the microstructure on all stages of fatigue life.

Fatigue crack propagation was further studied using long fatigue crack growth tests; these were conducted at room temperature and 350˚C. The distribution of hard particles on the fracture surfaces at low and high crack growth rates was quantitatively assessed using line fraction analysis. To complement the X-ray CT performed on the short fatigue crack samples (which were tested at room temperature), X-ray CT was also used to image the crack tip at low and high crack growth rates in LVD25 samples tested at 350˚C.

5.2 S-N tests

The results of the S-N tests are presented as a function of the absolute stress (the stress values were obtained from the strain gage experiments, see 3.12) versus the number of cycles to failure (N_f) in Figure 5-1. The lowest Si alloy (LVD27) gave the worst performance; at the stress level (~132 MPa) at which the other alloys exhibited lifetimes greater than 10 million cycles, LVD27 failed at a lifetime two orders of magnitude lower. The unmodified version of LVD26 appears to give the best performance. At stresses between 140 MPa and 160 MPa the lifetime to failure of LVD26 unmod was, in general, an order of magnitude greater than the Sr modified version of the same alloy and the eutectic Si alloy (LVD25). The performances of LVD25 and LVD26 mod are similar and the results for these two alloys appear to be within the scatter of the experiment.

The S-N results are also presented as a percentage of the 0.2% proof strength versus the number of cycles to failure (N_f) in Figure 5-2 as an estimate of the level of yield or plastic strain. It may be seen in Figure 5-2 that in both LVD26 alloys and in LVD25 the fatigue limit (σ_e) (here defined as a lifetime greater than $1x10^7$ cycles) is well above the 0.2% proof strength of these alloys. In LVD27 the fatigue limit was 92% of the 0.2% proof strength. Because of the higher yield strength of LVD27, compared with the other alloys, the inferior performance of LVD27 is emphasised when the data are assessed in this manner. For completeness, the S-N data are also presented as a function of the maximum strain in the sample in Figure 5-3. LVD26 unmod again exhibits the best performance, followed by LVD26 mod. LVD25 has an inferior performance to LVD26 mod, and at strains greater than 0.5% is similar to that of LVD27. However, at strains between 0.4% - 0.5%, LVD25 exhibits better performance than LVD27.

Post failure analysis of the fracture surfaces showed that fatigue crack initiation occurred as a result of: 1) failure of hard particles (although it was not possible to say if this is debonding of the particle-matrix interface or particle fracture from fractography alone), 2) porosity and 3) the higher stresses at the edge of the bend bar sample due to the stress concentration effect of a sharp edge. The number of failures from each mechanism is presented in Table 5-1. Porosity was least prevalent in

LVD25 and was the primary cause of initiation in LVD27. In general the number of failures from porosity was inversely proportional to the Si content of the alloys. In LVD25 and both LVD26 alloys the Al_9FeNi, $Al_3(NiCu)_2$ and Si phases were observed at initiation sites. This range of initiation mechanisms accounts for the scatter in the results presented in Figure 5-1.

Two example micrographs of fracture surfaces for LVD25 are presented in Figure 5-4 and Figure 5-5. In Figure 5-4 two regions have been identified as probable initiation sites. EDX shows that Al_9FeNi and Si particles are at the centre of these regions. In the second example (Figure 5-5) a pore can be identified at the initiation point. The pore appears to be approximately 50 μm in size. Hard particles can be observed around the pore, the particles have a flat appearance and the Al is rougher. Using EDX analysis, Al_9FeNi and Si particles have been identified in this region.

Two examples of initiation sites in LVD26 unmod are presented in Figure 5-6 and Figure 5-7. A porous region can be observed at the initiation site in Figure 5-6, which is larger than the pore in LVD25 (Figure 5-5) at approximately 200 μm in size. A particle is identified in Figure 5-6, it was determined to be the $Al_3(NiCu)_2$ phase. The phase comprises three laths, and highlights the complex morphology of the secondary phases that form in these alloys, which may inhibit the flow of the cast during the casting process causing the porosity observed in Figure 5-6. An additional initiation site is presented in Figure 5-7. It is a large Si particle just below the tensile surface of the bend bar.

The first example of an initiation site in LVD26 mod is presented in Figure 5-8. Several large particles (which have a flat, cleaved appearance) can be seen in this region. Using EDX analysis these large particles have been determined to comprise the Al_9FeNi phase and the $Al_3(NiCu)_2$ phase. However a full phase map of this region was not obtained and so other phases may also be present. The second initiation site (Figure 5-9) is a large porous region, the maximum dimension of which is approximately 500 μm. This pore is larger than the maximum pore size identified from tomography in Table 4-1. Secondary phases with a cuboid structure have been identified in Figure 5-9, which were determined to be the Al_3Ni phase.

Porosity was identified at all the LVD27 fatigue initiation sites, two examples of these initiation sites are presented in Figure 5-10 and Figure 5-11. The maximum dimension of the pore in Figure 5-10 is ~400 μm and the maximum dimension of the pore in Figure 5-11 is ~175 μm. The shape of these pores (and the pores in the other alloys) indicates that they formed as a result of shrinkage and restriction of flow during the casting process.

Acetate replication was not used extensively throughout all the S-N tests due to time constraints, but in each test a replica of the polished surface was taken after 10,000 cycles. In LVD26 mod (at 136 MPa) and LVD27 (at 125 MPa) cracks were observed on the polished surface, signifying initiation, at less than 3% N_f. In LVD26 unmod and LVD25 (both at 149 MPa) cracks were observed at less than 6% N_f. The time to initiation in the samples that exhibited longer lifetimes (>400,000 cycles) were not determined because the initiation event was not observed on the acetates. The polished surfaces of the run out tests were assessed using optical microscopy. Initiation damage was only observed in LVD27 and this was in the form of particles apparently extracted from the sample surface.

5.3 Initiation and short fatigue crack growth

To further assess the initiation and early crack growth processes, more detailed results from a smaller subset of interrupted short crack growth tests will be presented in this section. The results are presented for each alloy and these sections are further divided into initiation and propagation observations.

5.3.1 LVD25

5.3.1.1 Initiation

Four initiation sites and subsequent cracks were analysed for LVD25. In this study the point of initiation (N_i) is defined as the earliest cycle at which a crack was observed using the acetate replica record. Initiation in LVD25 was first observed at 9000 cycles which was approximately 5% N_f (Table 5-2). The first initiation site is presented in Figure 5-12. As with all the initiation sites that will be presented in this chapter: image (a) is the post failure micrograph of the polished surface, and image (b) is the micrograph of the acetate replica. It can be seen in Figure 5-12b that a particle was

extracted from the sample during the replication process leaving a void. It is not possible to ascertain the phase of the extracted particle but using EDX Al_9FeNi, $Al_3(NiCu)_2$ and Al_4Cu_7Ni phases have been identified as being attached to the extracted particle. It may also be seen in Figure 5-12b that a small crack formed underneath the extracted particle; the void and the crack are not connected on the surface at the point the acetate was created.

The second initiation site is presented in Figure 5-13, the sample failed from the subsequent crack from this initiation site. Initiation occurred as a result of particle fracture; using EDX the initiating particle was identified as the Al_9FeNi phase. It was not possible to find the opposing section of the initiation site after failure and so the morphology and composition of that section could not be fully ascertained. It can be seen in Figure 5-13a that a bifurcation occurred in this region during the subsequent crack growth, though it is not clear from surface observation why the bifurcation occurred.

The third initiation site investigated in LVD25 is presented in Figure 5-14, the corresponding phase map and inverse pole figure for this region are presented in Figure 5-15. The acetate replica micrograph in Figure 5-14b suggests that initiation occurred as a result of particle failure. From the phase map presented in Figure 5-15a it is possible to identify the particle as the Al_9FeNi phase. Two other cracks have also been identified by arrows in Figure 5-14b, and if compared against Figure 5-14a, it can be seen that these cracks did not form part of the main fatigue crack. The phase map in Figure 5-15 shows that the right hand particle (arrow 2) is the Al_9FeNi phase (n.b. the crack did not occur at the nearby phase boundary) and the left hand particle (arrow 1) is Si.

The fourth initiation site, in Figure 5-16, had a similar appearance to the site in Figure 5-12. From the acetate replica in Figure 5-16b it can be seen that the replication technique has caused particles to be extracted from the surface. However, the adjacent particles remained attached to the sample. In this example there are three cracks that are unconnected on the surface and the initiation site was > 100 μm when first observed. Si particles remain around the upper void but the void was smaller at initiation (Figure 5-16b) signifying that a further section of the particle was extracted later in the test. The lower void was connected to the $Al_3(NiCu)_2$ phase.

There is ambiguity concerning the reason for fatigue initiation in the fourth example, since the initiation site was large when first observed. High resolution X-ray CT was therefore used to assess the three-dimensional nature of this region, the results are presented in Figure 5-17. Because of the difficulty of representing 3-D data in a static 2-D form, the images are presented as slices moving through the initiation site. This method may be described as a 'virtual sectioning' method, as it gives a similar effect to that which might be obtained from serial sectioning and polishing.

The top surface of the cubes, presented in Figure 5-17 a-f, is the polished tensile surface and Figure 5-17a is a section just below the upper void (the position of which is shown by the dashed line in Figure 5-16). The next section (Figure 5-17b), is taken 5 μm away from the first section in the direction of the upper void. There is 5 μm between each subsequent image thereby showing several sections through the upper void. It is evident in Figure 5-17a that the Si particle below the void is connected to a larger hard particle network and that there are several large intermetallic phases below this point. Looking at the subsequent slice in Figure 5-17b and Figure 5-17c it can be seen that where the two intermetallic phases form a right angle, a pore is present. In Figure 5-17d the image shows that the large pore under the surface is connected to the void and hence must have originally been connected to the particle before it was extracted by the replication process. The porous region continues past the void (Figure 5-17e and f), the maximum dimension of this pore is ~75 μm. The similarity in appearance between this initiation site and the first initiation site (presented in Figure 5-12) raises the possibility that porosity may also be present under the surface in the first initiation site although further analysis would be required to confirm this.

5.3.1.2 Crack propagation

The earliest stages of short fatigue crack growth in this alloy were observed to be microstructurally dependent. The crack propagated through the Al-matrix and caused hard particles to fail. There were three categories of hard particle failure:

1) Decohesion of the particle/particle interface

2) Decohesion of the particle/matrix interface

3) Particle fracture

The first two observations may be seen to occur at the Si particle above the void in Figure 5-12a. After initial growth through the matrix the crack was blocked by a Si particle and deflected by 65˚ along the interface of the Si particle and the matrix. Upon reaching the border between the Si particle and the $Al_3(NiCu)_2$ phase the crack then progressed via the interface between the two particles. A further example of particle/matrix decohesion may be observed at the large 'cartwheel' shaped Al_9FeNi phase in Figure 5-14a. The crack can be seen to grow via the edge of the particle.

The large Si particle (arrow 1) opposite the Al_9FeNi (Figure 5-14) is an example of the third mechanism of growth via fractured particles. From the phase map in Figure 5-15a it is possible to identify that the Si particle is fractured with a small section of the Si on the right side of the crack (attached to the Al_9FeNi) and the remainder on the left side of the crack. The inverse pole figure in Figure 5-15b shows that this Si particle contains at least three different crystal orientations (as denoted by the different colours: peach, light green and light blue). The angle between the adjacent regions (peach-light blue and light blue-light green) is ~60˚, this signifies a twin boundary in Si (Edwards, 2003). The Si particle did not fail at the twin boundaries, however, the twin boundary does appear to have had an effect on the way the particle cracked as it may be seen in Figure 5-14a that two cracks emanate from the position of the boundary.

The influence of twin boundaries on the way Si particles fracture was further assessed using EBSD. A larger Si cluster is presented in Figure 5-18, where (a) is the phase map (b) is the inverse pole figure and (c) is the micrograph of the region. The inverse pole figure shows that the first large Si particle on the left of the image has one crystal orientation (the whole particle is purple) and so particle failure was clearly not influenced by twin boundaries. The large Si cluster to the centre-right of the images in Figure 5-18 (number 2) is fractured in several different locations, and the fractures in this particle are irregular in shape (i.e. not straight or in the same direction). This particle contains many different crystal orientations (Figure 5-18b) but none of the cracks in the particle occur at twin boundaries. The white arrows in Figure 5-18b identify the principal fractures and the fracture mode at these locations is intra-crystallographic. When a crack did occur through a twin boundary (at the point

illustrated by the black arrow in Figure 5-18c) the crack was seemingly unaffected by the boundary.

A smaller Si particle was also investigated and the results are shown in Figure 5-19. This particle was chosen because of the irregular manner in which the particle fractured with two acute deflections. This particle has two crystal orientations (Figure 5-19b) and the yellow line in Figure 5-19b represents the position of the twin boundary. The main (irregular) crack through the particle does not pass through a twin boundary and so, as with the previous example, crystal orientation does not seem to account for the irregular fracture shape in Si. However, a secondary crack does appear to have occurred partially along the twin boundary.

As well as being used to image the region underneath the initiation sites, X-ray CT was also used to look at the mechanisms of fatigue crack growth. In the example studied for LVD25 the crack grew approximately 270 μm from the initiation site ($2a \approx 540$ μm), just before the end of the test $da/dN \approx 1\text{x}10^{-5}$ mm/cycle and using Scott and Thorpe (1981) to estimate: $\Delta K \approx 3.1$ MPa$\sqrt{\text{m}}$. By eye it was possible to see the crack in each slice of the reconstructed volume (Figure 5-20). However, automatic segmentation by greyscale was not possible as the crack was not sufficiently different (in greyscale) from other features in the microstructure.

The X-ray CT data showed that the crack tip may be better described as a diffuse region of micro-damage and uncracked, ligamented sections; this region is approximately 100 μm in depth in LVD25. The virtual sectioning method has again been used, in Figure 5-20, to show two sections through the crack tip region. In order to relate the cracked and ligamented sections to the microstructure; six interesting features have been identified in Figure 5-20.

1) A particle is debonded at the particle/matrix interface but has also been fractured.

2) The crack was deflected around a Si particle through the matrix and not around the particle matrix interface.

3) This ligamented section comprises both Al-matrix and hard particles. Damage can be seen ahead of this region (below this point in the image); damage

occurs as a result of particle fracture and failure of the particle/matrix interface.

4) The crack was deflected towards a Si particle and the crack passed through the fractured Si particle.

5) A secondary phase forms a ligamented section

6) A thin section of a secondary phase is fractured. Below this is further damage, in this case the damage appears to be as a result of debonding of the particle/matrix interface.

In Figure 5-21 the Al and Si phases have been removed to reveal a thin 3-D section of the crack (in red) and the secondary phase sub-structure. Towards the surface of the sample (the top of the image) is a region of micro-damage with ligamented sections. Secondary phases can be seen in this region (in addition to the Al or Si that is not shown). Towards the bottom of the image the crack interacts with a section of a large, intermetallic flake (identified by the arrow); the failure mechanisms of particle/matrix decohesion and particle fracture occur but sections of the flake remain intact. The crack was not deflected around this region and in fact appears to have been drawn towards it.

Because of the diffuse nature of the damage in the crack tip region, segmenting the entire crack is a time consuming task and would produce very large (unprocessable) image files. A projection method was therefore used to summarise and give a 2-D representation of the crack shape (see Figure 5-22). To produce this image the reconstructed volume is positioned so that the plane of the crack is parallel to the viewer. Each voxel has an X, Y and Z position and a projection is made at each X, Y position along the Z direction. The minimum greyscale value at each projection is then assigned as the grey value at that X, Y location, thereby producing a 2-D image. Air has a low greyscale value and so cracks can be identified using this method as the darkest areas of the image. The brightness and contrast of Figure 5-22 has been adjusted to give a clearer image of the crack, however, it is still ‘noisy’.

The ‘shorter’ dashed line in Figure 5-22 pinpoints a nominal position of the crack tip after which relatively little damage occurs; although as previously mentioned the

concept of a crack tip in this alloy is questionable. To the left of the crack there are several failed particles (enclosed by the 'longer' dashed line), and it is likely that this damage was produced as a result of fatigue crack growth but is far less contiguous than the damage in the 'main' crack. The crack is considerably longer in the bulk than at the surface and $a/c \approx 0.7$ (where a is the surface length and c is the bulk length perpendicular to a). The crack does not have a regular shape and 'bulges' in regions; there is no obvious microstructural reason for this observable, but it is likely to be due to the prior history of damage during crack evolution.

The short fatigue crack growth data for LVD25 are presented as a function of ΔK in Figure 5-23. ΔK was calculated using the method described in Scott and Thorpe (1981) for a 'thumbnail' crack and is the average ΔK along a semi-circular crack front. The method uses the measured surface crack length to calculate ΔK. The a/c value used in the calculation was 1, not 0.7 (obtained from the X-ray CT data) because analysis of the final fractures indicated that the a/c of the crack which caused failure was ~1 (using a value of a/c=0.7 increases the average ΔK by <5%). The crack exhibits typical short crack behaviour, da/dN is scattered (which indicates its microstructural dependence) and crack arrests are mostly attributed to the crack being blocked by hard particles. Only one exception to this was observed and this is identified by an arrow in Figure 5-23, the corresponding section of the crack shown in Figure 5-24. The point at which the crack arrested is identified by the arrow in Figure 5-24a, no particle can be observed on the surface. Using tomography data it is possible to view below the surface. Figure 5-24b shows that 2 μm below the surface there was also no particle but at 5 μm below the surface there is an intermetallic phase. It is likely that this particle locally arrested the crack until it fractured, allowing the crack to proceed. This indicates the importance of the 3-D local stress environment around the crack tip.

5.3.2 LVD26 unmod

5.3.2.1 Initiation

Two initiation sites were investigated for LVD26 unmod, no other cracks grew to a sufficient length to be monitored in this alloy. Fatigue initiation occurred after 60,000 cycles which was ~14% N_f (Table 5-2). The first initiation site is presented in Figure

5-25. The initiating particles were extracted from the sample surface as a result of the replication technique leaving two voids. An Al_9FeNi particle is adjacent to the left hand void but the phase of the extracted particles is unknown. Fractography shows that a pore, maximum dimension < 75 μm, was present under the surface.

The second initiation site is presented in Figure 5-26, and again a particle was extracted from the sample surface by the replication technique. The $Al_3(NiCu)_2$ phase and Al_9FeNi phase were attached to the extracted particle. Because the second initiation site is intact it is not possible to use conventional fractography to analyse below the sample surface and so X-ray CT was performed. The virtual sectioning method has been used to show sections through the initiation site (Figure 5-27). A pore was present below the initiation site and is the likely cause of fatigue crack initiation in this region. From the shape of the pore it appears to have formed as a result of shrinkage and restricted flow of the cast (by the particles surrounding the pore) during the casting process. The maximum pore dimension is approximately 50 μm.

5.3.2.2 Crack propagation

The same observations about hard particles on the crack path described for LVD25 (in section 5.3.1.2) were also observed in LVD26 unmod. Particle cracking and debonding of the particle/matrix interface may be observed in Figure 5-26. The 2-D images of the sample surface show that the crack often deviates from the mode 1 direction, though these deflections cannot always be linked to hard particles on the sample surface; an example of a deflected crack is identified in Figure 5-26. As the crack grows away from the initiation site it is deflected by 45˚. There is no particle on the surface and the crack does not appear to be attracted to a failed particle.

Using X-ray CT it was possible to image underneath the surface and ascertain the 3-D nature of the interaction between the fatigue crack and the microstructure. In Figure 5-28 the crack is red, the intermetallics are yellow, and the top 10 μm of Al and Si has been removed. Approximately 8 μm underneath the surface is an intermetallic, which is directly underneath the crack path. The particle/matrix interface was debonded and formed part of the crack. It is likely that this particle influenced the path of the fatigue crack at the surface. It is perhaps not surprising that particles underneath the sample

surface affect the crack path observed at the surface but this example emphasises the 3-D nature of fatigue crack growth through these alloys.

A combination of a narrow crack and less than optimum quality X-ray CT images meant that segmentation of the crack tip was not possible in this sample. Using the projection method it was also difficult to identify the crack, and this image may be seen in Figure 5-29. The dashed line is the nominal crack shape, which was obtained by recording the co-ordinates of the crack tip in every 10th slice of the X-ray CT volume (Figure 5-30). The nominal crack shape is the maximum position around these points. The crack tip is a diffuse region of damage with ligamented sections. A 2-D section of the crack tip is presented in Figure 5-31, two points of interest are identified:

1) marks the first point of damage ahead of a contiguous crack, it appears to be a debonded Si, and

2) is a debonded intermetallic and cracked Si particle.

In Figure 5-31, the Al matrix appears to form the ligament between these sections but intermetallics are also often observed in the ligamented regions. This damage is typical ahead of contiguous sections of crack in this alloy.

The length of the crack (analysed using X-ray CT) at the sample surface, was approximately two times that of the bulk crack length ($a/c \approx 1$) and a semi circle is a close approximation of the crack shape (Figure 5-30). Just before the test finished the average $\Delta K \approx 4$ MPa$\sqrt{m}$ and the da/dN was approximately 1×10^{-5} mm/cycle. The fatigue crack growth data for both cracks are plotted as a function of ΔK in Figure 5-32. Crack retardation and acceleration typical of surface monitored short crack growth was observed. All crack arrests were observed to occur at hard particles.

5.3.3 LVD26 mod

5.3.3.1 Initiation

The LVD26 mod short crack sample failed from an edge crack. However, two freely initiating cracks have been analysed. Initiation was observed to occur (in the first acetate replica taken) at 5000 cycles, which is approximately 11% N_f (Table 5-2). The

first initiation site is presented in Figure 5-33, two fractured particles can be observed in this region and arrows identify them. Besides particle fracture, partial decohesion of the particle/matrix interface occurred in the upper particle. Phase mapping has been used to identify the phases in this initiation site (Figure 5-34). The upper initiating particle was the Al_9FeNi phase, on its left hand side the particle is attached to a cluster of Si particles and on its right hand side it is connected to an Al_3Ni phase. The lower particle is comprised of the Al_9FeNi and Al_3Ni phases. This particle has a hole in its centre, which contains the Al-matrix. It is the Al_9FeNi sections of the particles that appear to have fractured, causing fatigue crack initiation.

The second initiation site is presented in Figure 5-35; in this figure image (a) is a secondary electron SEM image (not an optical micrograph) and image (b) is the acetate replica of this region. In the second LVD26 mod initiation site three particles appear to have fractured causing fatigue crack initiation; these are identified by arrows. The particles are located in the inter-dendritic region and form part of the larger hard particle network in these alloys. Using EDX analysis these particles were all determined as the Al_9FeNi phase.

X-ray CT analysis was performed on the second initiation site and the SEM image and the corresponding X-ray CT image are presented in Figure 5-36. During the preparation of the CT sample it appears that the crack slightly sheared so that the peaks and troughs do not align exactly. The initiating particles have been numbered 1-6. Using the virtual sectioning method the regions under the initiating particle can be observed (see Figure 5-37). All of the particles are connected to a large intermetallic particle (or network of particles). The intermetallic is fractured and debonded and this forms part of the fatigue crack. There is no evidence of porosity under the initiating particles or in this region.

5.3.3.2 Crack propagation

Crack growth mechanisms were similar in this alloy to those observed in LVD25 and LVD26 unmod. Fractured and debonded particles were present along the crack path and influenced the way in which the crack propagated. The deflections caused by the microstructural features produced a rough crack. In this alloy, 2-D micrographs reveal that the Si particles have a much finer size when compared with the Si in the

equivalent unmodified alloy. The crack was observed to propagate through the Si clusters (Figure 5-38a) and around the Si clusters (Figure 5-38b). On the micrographs of the sample surface, extensive damage to the Si particles in the clusters was not observed.

The crack tip region was comprised of diffuse damage and intact ligaments and was similar to that observed in LVD26 unmod and LVD25; two examples of X-ray CT sections of the crack tip are presented in Figure 5-39. From the top of Figure 5-39a to position 1 the crack is contiguous, but at position 1 there is a ligament between the contiguous crack and the damage ahead of it (position 2). The ligament comprises the Al-matrix and two intermetallic particles, it is also possible that Si particles are in this region, but this cannot be fully confirmed. The damage ahead of the contiguous crack at position 2 is at a large, fractured intermetallic particle. Position 3 (Figure 5-39b) marks the point of an uncracked ligament comprised of the Al-matrix, intermetallics and (given the size of the ligament and knowledge of the microstructure) probably Si. Cracked and debonded particles can be seen in the micro-damage below position 3. In Figure 5-39b, micro-damage can be observed over a distance greater than 200 μm.

A section of the crack was carefully segmented and is presented in Figure 5-40. The crack has been shown from six different angles to help give an impression of its three-dimensional nature. At the 0˚ position the crack front region has a rough appearance and micro-damage is present but in general the crack has a semi-circular shape. Dark regions in the crack represent the intact ligaments and these can be observed at a distance greater than 200 μm behind the forwardmost micro-damage; at 30˚ the uncracked ligaments are more apparent. As the crack is rotated to 75˚ it appears much less contiguous than at 0˚. Perpendicular to the plane of the crack, at 90˚, it can be seen that the spread in the damage is greater than 150 μm.

The projection method has been used to show the 2-D crack shape and is presented in Figure 5-41. The bottom of the crack is missing in the image (due to specimen size restrictions for X-ray CT imaging). The crack is slightly longer in the bulk than on the surface, but because the bottom of the crack is missing the exact a/c cannot be given. From the shape of the crack it is likely that $a/c \approx 0.9$. Just before the test finished, $da/dN \approx 1\text{x}10^{-4}$ mm/cycle and $\Delta K \approx 5.3$ MPa$\sqrt{\text{m}}$. The full da/dN versus ΔK curve is given in Figure 5-42; intervals between replica collection were initially too large and

so early crack growth was not fully captured and in particular crack arrests were not observed. Towards the end of the test, replicas were obtained at shorter intervals and so there is a larger scatter in the captured crack growth data consistent with surface analysed short cracks.

5.3.4 LVD27

5.3.4.1 Initiation

The LVD27 sample ultimately failed because of an edge crack, however, four freely initiating fatigue cracks have been analysed. Initiation occurred before the first replica was taken at 2000 cycles, which is 3% N_f. Considerably more damage was observed on the sample surface of this alloy compared to the other alloys; in particular many particles were extracted as a result of the acetate replica process. In Figure 5-43a large black voids can be observed where particles have been extracted by the acetate replicas. If the location of the voids is compared against the equivalent location on the acetate replica (Figure 5-43b) it can be seen that these voids occurred during the fatigue test and were not present beforehand. The acetate replication process was repeated ten times on an unloaded and un-fatigued sample, the damage that was observed in the fatigue sample did not occur in the unloaded sample. This indicates that particle extraction happens as a result of the loading of the sample.

The first initiation site analysed is presented in Figure 5-43. The initiation site was approximately 100 μm when first observed and other damage (which could be described as initiation events) are located near this site. Initiation occurred at the edge of a dense region of secondary phase particles. The second initiation site (Figure 5-44) has a similar appearance to the first: the crack was large (~ 200 μm) when first observed and is on the edge of a dense region of intermetallic particles. Voids signifying particle extraction are also present in this region (Figure 5-44a) and some of the voids are connected to the crack.

Similar observations were made at the third initiation site analysed: initiation occurred near a dense region of intermetallics and particle extraction was observed. Phase mapping was performed on this site (Figure 5-45) but the damage in this region meant that the results were poor. Nevertheless, the $Al_3(NiCu)_2$ and Al_9FeNi phases can be

identified in this region (Figure 5-45b) and the SEM image (Figure 5-45a) shows that several of these particles were fractured.

The fourth initiation site is very similar in appearance to the others already presented, and was further analysed using X-ray CT imaging. Figure 5-46 is an optical micrograph of the site and Figure 5-47 is a virtual section from the CT data, which cuts through the dashed white line in Figure 5-46. Large pores exist under the surface of the sample, and along with the crack they appear to form a very large network. It is not possible to differentiate between the crack and the pores but a thin section showing the crack/pore network under the initiation site (Figure 5-48) gives a good impression of the scale of porosity at this initiation site. A similar level of porosity occurs in the 100 μm in front of and behind this section. Because of the similarity between all the initiation sites it seems likely that similar porosity exists under the sample surface at these sites also.

5.3.4.2 Crack propagation

Short fatigue crack growth in LVD27 is microstructurally dependent; fractured and debonded intermetallics were observed on the crack path (Figure 5-49) and they influenced the way the crack propagated through the sample. In this alloy, coalescence of smaller cracks to create larger, dominant cracks was observed. In Figure 5-50a, three cracks can be identified, 4,000 cycles later (Figure 5-50b) the right hand and middle cracks have coalesced to form a dominant crack. After a further 20,000 cycles (Figure 5-50c) all three cracks were connected (on the surface) as a single fatigue crack. Small fatigue cracks propagated through both inter and intra-dendritic regions (Figure 5-52), the deviations around dendrites cause the crack path to have a rough appearance.

Figure 5-51 contains a series of X-ray CT ‘virtual’ sections at the initiation site and at three locations along the crack path. Below the surface, 100 μm away from the initiation site (Figure 5-51b), is a porous region; this is part of the same porous network that was at the initiation site. Smaller, less open, cracks can be seen emanating from the pore through the Al-matrix possibly signifying additional initiation sites. Below the pore is a region of dense intermetallic particles. The crack appears to have grown preferentially through the porous and intermetallic regions,

this causes large scale deflections along the crack path. 200 μm away from the initiation site (Figure 5-51c) the crack has propagated away from the porous region. However, it may be seen that the crack has formed a ligamented section between a shallow crack, which breaks the sample surface (from which crack growth was monitored during the fatigue experiment) and a sub-surface section, which passes through the intermetallic region (observed in Figure 5-51b). At this point the ligament is approximately 100 μm wide and comprises intermetallics and Al-matrix.

A further 100 μm away (Figure 5-51d) the crack is still ligamented although the width of the ligament has reduced. The larger section of crack remains 'hidden' below the sample surface. The intermetallic region can still be observed at the bottom of the section and pores are present in this region and connected to the crack. Because of the bright fringes around the crack, caused by phase contrast, it is difficult to fully determine if crack growth is inter or intra-dendritic because the intermetallics can be hidden by the fringes. Both inter and intra-dendritic crack growth occurs in LVD27 (Figure 5-52) Qualitatively, looking at the shape of the crack and the position of the visible intermetallics near it, it does seem that when the crack is away from large pores (as in Figure 5-51d) crack growth is preferentially intra-dendritic. However, since the pores form in inter-dendritic regions crack growth near pores appears preferentially inter-dendritic.

The crack tip region of the ligamented crack (in Figure 5-51) was segmented and is presented in Figure 5-53; the larger sub-surface crack is coloured red and the shallower surface crack is green in (a) and grey in (b). The crack remained ligamented until the test was stopped and showed no sign of recombining (Figure 5-53a). The two crack tips are reasonably contiguous; little micro-damage occurred ahead of the crack tips. The sub-surface crack was advanced at three main positions (identified by the arrows) and this was associated with micro-damage at clusters of intermetallic particles. To the left of the dotted line in Figure 5-53b, the two cracks appear to have an equilibrium state, the red crack has an average distance that it remains below the surface and the grey crack has an average depth. To the right of the dashed line (i.e. towards the crack tip) these average distances alter: the distance between the sample surface and the top of the red crack increases and the depth of the grey crack decreases.

The other side of the crack was also segmented and is shown from two angles in Figure 5-54. Much of the crack tip is contiguous (Figure 5-55a) but micro-damage does occur ahead of the crack tip (identified by the arrow in Figure 5-55b). However, the level of micro-damage ahead of the crack tip in LVD27 is lower than in the other alloys. The crack tip is non-planar and protrudes forwards in two regions in Figure 5-54; the upper region occurs at a sub-surface pore and the lower area is at a dense region of intermetallic particles. Failure of the intermetallic particles is by fracture of the particles and decohesion of the particle/matrix interface.

Unfortunately, due to a software error during the reconstruction of the X-ray CT images some of the volume was not reconstructed and therefore the overall shape of the crack cannot be determined (see Figure 5-56). Just before the test finished the $\Delta K \approx 3.9$ MPa$\sqrt{m}$ and the *da/dN* was $\approx 5 \times 10^{-5}$ mm/cycle. The full *da/dN* versus ΔK graph is presented in Figure 5-57. Each time cracks coalesced the new crack was given a different name, hence the reason so many crack data are plotted in Figure 5-57. Crack arrests were observed either just before, or just after cracks coalesced. The arrests could not be attributed to particles on the sample surface.

5.3.5 Summary

5.3.5.1 Summary - Initiation

Fatigue cracks initiated at fractured particles in LVD25 and LVD26 mod and at pores in LVD25, LVD26 unmod and LVD27. LVD26 mod and LVD27 ultimately failed from edge cracks. The Al_9FeNi phase was the principal phase associated with initiation of fatigue cracks at hard particles. These particles were shown to be connected to larger intermetallic networks under the sample surface. The maximum dimension of the pores observed under the initiation sites in LVD25 and LVD26 unmod was approximately 75 μm or less. The X-ray CT data shows that the pores in LVD27 were much larger and formed complex networks.

The replication technique was shown to extract particles from the sample during the fatigue test. However, X-ray CT images of these regions showed that where this occurred sub-surface porosity was present. This observation may therefore be used to identify sub-surface porosity at initiation sites in these alloys. The Si, $Al_3(NiCu)_2$, Al_7Cu_4Ni and Al_9FeNi phases were all found adjacent to the voids. Initiation occurred

latest in LVD26 unmod at 14% N_f. However, this sample lasted approximately an order of magnitude longer than the other samples and so the initiation period may be expected to contribute to more of the lifetime. Nevertheless, the majority of fatigue life for all the alloys studied was spent in the fatigue crack propagation stage.

5.3.5.2 Summary - Crack propagation

Fatigue crack propagation was microstructurally dependent in all the alloys studied. Hard particles were observed on the crack path and using the replication technique the following mechanisms were identified:

1) Crack growth through the matrix and deflected by intact particles.

2) Crack growth through the matrix until blocked by a hard particle.

3) Crack growth through the matrix and attracted to failed particles, particles were observed to fail in the following ways:

   - Decohesion of the particle/particle interface
   - Decohesion of the particle/matrix interface
   - Particle fracture

In LVD25 primary Si particles did not fail along twin boundaries and so this cannot account for the irregular fractures that were sometimes observed in primary Si.

Microstructural features 'hidden' below the surface affected crack growth observed on the sample surface. Using X-ray CT sub-surface particles were observed to cause deflections (Figure 5-28) and arrests (Figure 5-24). In LVD27 crack coalescence was observed and crack arrests occurred either just before or just after the cracks coalesced. The tomography data showed that porosity influenced fatigue crack propagation in LVD27, since the crack appeared to be attracted towards porous regions.

In LVD25 and both LVD26 alloys the crack tip is a region of diffuse micro-damage and intact ligamented sections. Micro-damage occurred at hard particles via particle fracture and decohesion of the particle interface. The crack tip was more contiguous

in LVD27, although damage ahead of the crack tip was observed at porous regions and clusters of intermetallics. The ligamented sections in the crack tip region comprised the Al-matrix, intermetallics and Si particles. Ligaments were observed at up to 200 μm behind the 'crack tip' region in LVD26 mod, approximately 150 μm in LVD26 unmod and approximately 100 μm behind the 'crack tip' region in LVD25. The size of the crack tip region does not scale with the monotonic plastic zone size but does appear to be proportional to ΔK.

The smallest crack analysed using X-ray CT was from LVD25. The 2-D projection showed that this crack had an irregular shape and $a/c \approx 0.7$. The cracks analysed in both LVD26 alloys were longer and more semicircular in shape than LVD25, and $a/c \approx 0.9$ in LVD26 unmod and $a/c \approx 1$ in LVD26 mod. The LVD27 crack imaged using X-ray CT was ligamented (Figure 5-53), a feature that was not apparent from observations of the sample surface. X-ray CT proved an excellent tool for determining the three-dimensional nature of fatigue cracks in these alloys.

Crack growth curves were presented for all the alloys and ΔK was calculated using the method described by Scott and Thorpe (1981). The upper bound of the *da/dN* observed in each alloy has been summarized in Figure 5-58. The upper bound of *da/dN* was slowest in LVD26 unmod but was similar in the other alloys, however, LVD27 exhibited the fastest *da/dN*.

5.4 Long fatigue crack growth

5.4.1 Room temperature

The room temperature (RT), long fatigue crack growth curves are presented in Figure 5-59. The threshold region of the curves occurs between 3-4 MPa√m. LVD27 had the lowest ΔK_{th} value (defined here as the ΔK when $da/dN = 1\text{x}10^{-7}$ mm/cycle), which was 3 MPa√m. LVD26 unmod had the highest ΔK_{th} value at 3.6 MPa√m, which was 20% higher than for LVD27. The ΔK_{th} for LVD25 and LVD26 mod were 3.3 MPa√m and 3.2 MPa√m respectively. This data (and the other crack growth parameters: K_Q, C and m) are summarised in Table 5-3.

Above a ΔK of 4 MPa√m the fatigue crack growth behaviour curves of both LVD26 alloys and LVD27 follow a similar trend and their ΔK values remain within 10% of each other. LVD25 exhibited the worst performance of the alloys above ΔK = 4 MPa√m with crack growth rates consistently higher than in the other alloys. Above the threshold region, *da/dN* and ΔK exhibited a log-log linear relationship until *da/dN* $\approx 1x10^{-4}$ mm/cycle, at which point there is an acceleration as the cracks approach final failure. The acceleration is small particularly in LVD25 and LVD26 unmod. The Paris law describes the curves well and the Paris law exponents (*C* and *m*) for the log-log linear region are given in Table 5-3. At final failure, LVD26 mod had the highest K_Q value but since repeat testing was not performed it is possible that the difference in K_Q between these three alloys is within the scatter expected in the experiment. The K_Q value of LVD25 was significantly lower than in the other alloys at 8.8 MPa√m.

For ease of comparison all the RT SEM fractographs are presented in Figure 5-60. The left hand column contains the fracture surfaces at the low *da/dN* ($3x10^{-7}$ mm/cycle) and the right hand column contains the fracture surfaces at high *da/dN* ($5x10^{-4}$ mm/cycle). At low *da/dN* brittle and ductile failure modes were observed. Hard particles can be seen on the fracture surfaces, they have a cleaved (brittle) appearance and are surrounded by the Al-matrix. The Al-matrix is ductile and has a 'dimpled' or 'feathered' appearance; these features are identified in the larger fractograph in Figure 5-61a. Qualitatively, at low *da/dN* fewer hard particles appear on the fracture surface than at high *da/dN* and so the low *da/dN* surfaces are less rough with fewer ridges between the flat particle regions.

At high *da/dN*, brittle and ductile failure modes were both observed, but in general the fracture surfaces appear more brittle than at low *da/dN* because a greater amount of hard particles are on the surface. The 'feathered' effect in the Al-matrix is still observable but is much finer than on the low *da/dN* surfaces; this can be seen in Figure 5-61b. The hard particles occur at different heights on the fracture surfaces, because the crack links between a greater number of hard particles, the fracture surfaces have a rougher appearance than at low *da/dN*.

It was not possible to quantify the level of hard particles on the fracture surfaces. Qualitatively LVD25 and LVD26 unmod appear to have a greater quantity of hard particles than LVD27 at low *da/dN* but at high *da/dN* a trend between the alloys could

not be identified. In order to quantitatively assess the relationship between hard particles and fatigue crack propagation the fracture surfaces were sectioned at low and high *da/dN* and line fraction analysis (LFA) was used to assess the hard particles along the crack path. Using this technique the line fraction of hard particles (L_L), the mean intercept distance between hard particles (λ), the mean particle intercept length (L_3) and the number of particle intercepts per unit length (N_L) (all defined in chapter 3.4) were obtained to describe the distribution of hard particles along the surface, the roughness of the crack profile was also determined.

Only one side of the crack can be analysed using this technique because it would be very difficult to section the corresponding fracture surface at exactly the same position. As a result of only having one side of the crack there will always be an ambiguity in determining whether a particle is fractured or debonded. Examples demonstrating this ambiguity are presented in Figure 5-62 and Figure 5-63. In the first example (Figure 5-62a) the Si particle in the centre of the image is partially debonded on the lower left side, a thin layer of Al (<1 μm) is attached to the particle. However, the bottom of the particle has no Al layer, and from the shape of this region it is not possible to report with certainty if that section of the particle is also debonded or actually cracked. Observations of short fatigue crack fracture paths presented earlier in this chapter showed that both mechanisms can occur in the same particle. In the second example (Figure 5-63a) several particles have been identified; there is a debonded particle to the left of the image, a very fine layer of Al is attached to this particle. There are two particles that appear to be fractured because they have a very flat edge, which is not characteristic of the shape of this phase. On the right of the image are two particles where the fracture modes are less obvious; neither particle has a layer of Al between them and the crack, but because of their shape and position on the crack profile, debonding is a possible failure mode.

Because of this ambiguity in determining the failure mode it was decided that all particles that were flush with the crack profile or had a fine layer (<1 μm) of Al between them and the crack profile would be used in the LFA as failed particles. In Figure 5-62b and Figure 5-63b the white lines represent the sections of the crack profile that would count as being a failed particle. Debonded particles with a fine

layer of Al between them and the crack were observed at low and high *da/dN* but it was not possible to confirm if debonding was more prevalent at low *da/dN*.

The L_L of hard particles on the fracture profile for each alloy at low and high *da/dN* is presented in the chart in Figure 5-64; the V_f of hard particles in the bulk (± 1 standard deviation) is also given in Figure 5-64 for comparison. At low *da/dN* the L_L of hard particles on the fracture profile was within one standard deviation of the V_f for each of the alloys; at low *da/dN* the crack path showed no preferentiality for hard particles. At the high *da/dN* the L_L of hard particles was significantly higher than the V_f in the respective alloys in all cases; at high *da/dN* the crack grew preferentially via hard particles. LVD25 and both LVD26 alloys had a similar L_L of hard particles on the fracture profile. The preferentiality ratio (L_L/V_f) is presented in Figure 5-65, LVD27 had the highest L_L/V_f and L_L/V_f was inversely proportional to the Si content (and therefore V_f of hard particles).

The mean free distance (λ) is a measure of the distance between particles and the mean particle intercept distance (L_3) is a measure of the size of the particles on the crack profile. Charts showing λ and L_3 for all the alloys at low and high *da/dN* are in Figure 5-66 and Figure 5-67 respectively. The corresponding values for λ and L_3 in the bulk alloy (i.e. for a line placed randomly in a section of the microstructure away from the crack) are also shown in these charts. In the LFA the Si particles in LVD26 mod were treated as individual particles and not as a cluster of particles.

At low *da/dN* in LVD25 and LVD26 mod, λ on the fracture profile ($\lambda_{(FP)}$) was within one standard deviation of the λ for the bulk alloy ($\lambda_{(B)}$), but in LVD26 unmod and LVD27 $\lambda_{(FP)}$ was greater than one standard deviation above $\lambda_{(B)}$. The L_3 of particles on the fracture profile ($L_{3(FP)}$) for LVD25 and both LVD26 alloys was within one standard deviation of the value of L_3 for the bulk ($L_{3(B)}$). In LVD27 $L_{3(FP)}$ was greater than one standard deviation above $L_{3(B)}$.

At high *da/dN,* $\lambda_{(FP)}$ was lower than the corresponding values of $\lambda_{(B)}$ in all cases, indicating that the distance between particles on the fracture profile is shorter than in the bulk. $L_{3(FP)}$ was greater than one standard deviation above $L_{3(B)}$ for all alloys. A larger value for $L_{3(FP)}$ indicates that the average size of the hard particles exposed on the fracture profile is larger than the average size in the bulk alloy.

It can be seen in Figure 5-68 that at low *da/dN* the number of particles intercepted per unit length along the fracture profile ($N_{L(FP)}$) was lower than the corresponding N_L for the bulk ($N_{L(B)}$), and at high *da/dN*, $N_{L(FP)}$ was higher than $N_{L(B)}$. However, with the exception of LVD27 at low *da/dN*, the $N_{L(FP)}$ was within one standard deviation of $N_{L(B)}$ in all cases. For LVD25 and both LVD26 alloys there is no significant difference between the number of particles intercepted along the fracture profile at both low and high *da/dN*.

The percentage difference between the crack length and the projected crack length are plotted in Figure 5-69, and this may be used as a measure of roughness (Underwood and Starke, 1979) of the fracture profile. In all alloys the high *da/dN* fracture profile was rougher than at low *da/dN*. There was no simple trend between the Si content and the roughness of the surface at either *da/dN* studied.

5.4.2 350˚C

Because of the low yield strength of the alloys at 350˚C the monotonic plastic zone size was large when compared with the specimen dimensions, and so LEFM conditions were not applicable. To ensure that the crack growth characteristics of the alloys could be compared, the samples were pre-cracked (at constant ΔK) to the same estimated length and then left to grow until failure at the same load; the long fatigue crack growth curves are presented as *da/dN* versus *a/W* in Figure 5-70.

Although the cracks were grown to the same estimated *a/W* it may be seen in Figure 5-70 that the crack growth curves start at different values of *a/W*. The position of the p.d. wires can affect the p.d. measurement recorded and is the likely cause of the inaccuracy in estimating the correct *a/W*. The crack growth data presented were corrected using distances measured on the fracture surfaces. Threshold *da/dN* was not reached in any of the alloys and although the cracks grew out to failure from different *a/W*'s the lowest *da/dN* obtained in each alloy was approximately $3\text{x}10^{-6}$ mm/cycle. After the initial crack growth (between $8\text{x}10^{-6}$ mm/cycle and $2\text{x}10^{-5}$ mm/cycle) the curves are similar but above $2\text{x}10^{-5}$ mm/cycle the curves diverge.

Near final failure LVD26 unmod gave the worst performance and failed with the largest uncracked ligament. The performance of LVD26 mod was marginally better

than LVD26 unmod. LVD25 and LVD27 exhibited similar crack growth rates near final failure and the length of the uncracked ligament was also similar at final failure, their performance being better than both LVD26 alloys. There was no trend between *da/dN* and the Si content of the alloys.

All the SEM fractographs are presented in Figure 5-71 for comparison; the left hand column contains the fracture surfaces at the low *da/dN* ($3x10^{-6}$ mm/cycle) and the right hand column contains the fracture surface at high *da/dN* ($3x10^{-4}$ mm/cycle). The fracture surfaces have a generally ductile appearance at both *da/dN*s. In all the alloys hard particles can be seen on the fracture surfaces and they have a cleaved appearance. Hard particles appear to be less prevalent in LVD27 than in the other alloys but this cannot be quantified. In all the alloys the Al-matrix has a 'dimpled' or 'feathered' effect which is similar in scale at both *da/dN*s, and this can be observed in Figure 5-72. Figure 5-72a is the low *da/dN* fracture surface and Figure 5-72b is the high *da/dN* fracture surface of the LVD26 unmod alloy.

To quantitatively assess the interactions between hard particles and fatigue crack propagation the fracture surfaces were sectioned at low and high *da/dN* positions. LFA was performed to analyse the distribution of hard particles along the crack profiles to determine the L_L, λ, L_3 and N_L for each alloy and *da/dN*. The L_L of hard particles on the fracture surface is presented in Figure 5-73, the V_f of hard particles in the bulk (±1 standard deviation) is also given in Figure 5-73 for comparison. At low *da/dN* the L_L of LVD25 and both LVD26 alloys is within one standard deviation of V_f. However, the L_L of LVD27 is below one standard deviation. At high *da/dN* the L_L is consistently below the V_f for all the alloys and so the crack showed a preferentiality for avoiding hard particles. There is no trend between the preferentiality ratio and the Si content of the alloys (see Figure 5-65); the LVD26 mod alloy had the lowest L_L/V_f and LVD25 the highest L_L/V_f.

Charts showing the values for $\lambda_{(FP)}$, $L_{3(FP)}$ and $N_{L(FP)}$ are presented in Figure 5-74, Figure 5-75 and Figure 5-76 respectively, the corresponding $\lambda_{(B)}$, $L_{3(B)}$ and $N_{L(B)}$ are also presented in these charts. At low *da/dN* the $\lambda_{(FP)}$ for all the alloys is greater than one standard deviation above the $\lambda_{(B)}$. In LVD25 and both LVD26 alloys the $L_{3(FP)}$ are greater than one standard deviation above $L_{3(B)}$ but in LVD27 $L_{3(FP)}$ falls within the

expected error of $L_{3(B)}$. Conversely LVD25 and both LVD26 alloys have $N_{L(FP)}$ values less than one standard deviation below $N_{L(B)}$ but in LVD27 the $N_{L(FP)}$ again lies within the expected level of scatter. The combination of a low $N_{L(FP)}$ but high $\lambda_{(FP)}$, and $L_{3(FP)}$ for LVD25 and both LVD26 alloys indicates that fewer particles were intercepted on the fracture profile and that the distance between them and their size on the fracture profile is larger than would be expected for a line placed in the bulk alloy.

At high *da/dN*, the trends in $\lambda_{(FP)}$, $L_{3(FP)}$ and $N_{L(FP)}$ for all the alloys are similar: $\lambda_{(FP)}$ is greater than one standard deviation above $\lambda_{(B)}$, $L_{3(FP)}$ is within the expected scatter of $L_{3(B)}$ and $N_{L(FP)}$ is lower than one standard deviation below $N_{L(B)}$. This indicates that at high *da/dN* and 350˚C the crack was attracted to fewer particles and that the distance between particle intercepts was longer but that the size of the particles on the fracture profiles were similar to the size that was obtained from analysis in the bulk alloys.

The percentage difference between the crack length and the projected crack length are plotted in Figure 5-77. In all the alloys the fracture profile was rougher at the higher *da/dN*. At both *da/dN*s a similar trend existed between the relative roughness of the alloys: LVD26 mod had the highest roughness followed by LVD26 unmod, LVD25 and LVD27.

For LVD25 only, long fatigue crack growth tests were interrupted at the low and high *da/dN*s so that synchrotron X-ray CT could be used to image the crack tip region. In Figure 5-78 two virtual sections of the crack tip at low *da/dN* are presented, the crack tip region is on the left of the images. Because constant *K* loading conditions were used to grow the crack to this position the entire crack length shown is at the same *da/dN*. Cracks and pores appear as the black regions in the images.

In Figure 5-78a the crack has an irregular (rough) shape, deflections can be observed along the crack. Such a deflection at a debonded and fractured hard particle is identified at position 1. Micro-damage can be seen above and below the more contiguous section of the crack in addition to the micro-damage in the crack tip region. At the crack tip region the damage appears to form at 45˚ to the crack direction. The scale of the damage in the crack tip region is larger than the damage around the contiguous section of the crack and a bifurcation has been captured.

Micro-damage in the crack tip region does occur at intermetallics and an example is identified at position 2. Damage also occurs in the Al or Si phases (position 3) but because of their similar X-ray attenuation it is not possible to fully determine which phase or the mode of failure. Bifurcations or cracks growing along different planes were observed in this alloy at low *da/dN* and an example is given in Figure 5-78b. The lower crack is more contiguous than the upper crack in which large ligaments (for example at position 4) can be observed between the regions of crack or damage.

In Figure 5-79 four different sections along the crack are presented, in these images the viewer is face on to the crack. Figure 5-79a is in the crack tip region and the successive images are sections from further behind this position. The images confirm that the crack tip region contains diffuse micro-damage and ligamented sections. In general the micro-damage initially forms perpendicular to the tensile direction. Further behind the crack tip it can be seen that these sections can extend along similar planes to form longer regions of damage and are eventually linked by vertical sections of damage (parallel to the tensile direction). The crack tip region of micro-damage and ligamented sections is in the region of 250 μm deep.

In Figure 5-80 virtual sections through the crack tip region at high *da/dN* and at two positions further behind this point are presented. The crack tip region (Figure 5-80a) is comprised of micro-damage aligned perpendicular to the tensile direction and between this damage are uncracked ligaments and so the crack is therefore non-contiguous. The crack has a rough shape and has a peak-to-peak height of greater than 600 μm. Further behind the crack tip region (Figure 5-80b) the crack comprises three main sections (circled), which are relatively contiguous. Micro-damage occurs in-between the three principal regions but there are many intact ligaments between the cracks.

430 μm behind the crack tip region (Figure 5-80c) the crack is fully contiguous, crack branching can be observed as well as other micro-damage around the crack. The crack shape is rough, there are small-scale deflections caused by micro-damage linking together as the crack propagates forward. There are also larger-scale deviations in the crack path (represented by the peak-to-peak height). Qualitatively, the amount of micro-damage is less at high *da/dN* (at 350˚C) than at low da/dN, which correlates with the lower L_L of particles on the crack path at high *da/dN*. The plastic zone size at

high *da/dN* is larger than at low *da/dN* and so the level of micro-damage around the crack tip does not scale with the increase in plastic zone size at high temperature.

5.4.3 Summary

Room temperature ΔK_{th} values of between 3-3.6 MPa√m were obtained, and LVD26 unmod had the highest ΔK_{th}. There was no clear trend between ΔK_{th} and Si content. Above 4 MPa√m in both LVD26 alloys and LVD27, crack growth performance was similar. LVD25 gave the worst performance and had the lowest K_Q. The Paris law described the majority of the crack growth curves well. The high *da/dN* fracture surfaces had a more brittle appearance than the low *da/dN* fracture surfaces and the LFA confirmed this was because hard particles were found preferentially on the fracture profile at high *da/dN*.

At low *da/dN* the values of $\lambda_{(FP)}$ $L_{3(FP)}$ and $N_{L(FP)}$ for LVD25 and both LVD26 alloys were within one standard deviation of the corresponding values for a line analysed in the bulk. However, in LVD27 $N_{L(FP)}$ was lower and $\lambda_{(FP)}$ and $L_{3(FP)}$ were both greater than one standard deviation of the corresponding bulk values. At high *da/dN*, $N_{L(FP)}$ was within than one standard deviation of $N_{L(B)}$ and so the higher L_L of particles on the fracture profile can be attributed to lower $\lambda_{(FP)}$ and larger $L_{3(FP)}$ values. The high *da/dN* fracture profiles were rougher than the low *da/dN* fracture profile.

LEFM conditions were not applicable in the 350˚C samples and so crack growth data were presented as a function of *a/W*. LVD25 and LVD27 gave the best performance failing with a similar sized uncracked ligament (which was smaller than in the LVD26 alloys). At both *da/dN* values the Al matrix had a ductile 'feathered' appearance and the scale of the effect was similar. Hard particles were observed on the fracture surfaces.

At 350˚C and low *da/dN*, L_L was within one standard deviation of V_f for LVD25 and both LVD26 alloys; $N_{L(FP)}$ was less than one standard deviation below $N_{L(B)}$ but $\lambda_{(FP)}$ and $L_{3(FP)}$ were greater than one standard deviation above their respective bulk values. In LVD27, L_L was greater than one standard deviation below V_f. $N_{L(FP)}$ and $L_{3(FP)}$ were both within one standard deviation of their respective bulk values but $\lambda_{(FP)}$ was greater. At high *da/dN* the L_L of particles on the fracture profiles was less than one

standard deviation below V_f for all the alloys, $L_{3(FP)}$ was within one standard deviation of $L_{3(B)}$, $\lambda_{(FP)}$ was greater and $N_{L(FP)}$ was lower than one standard deviation of their respective bulk values.

At 350˚C and both *da/dN*s, X-ray CT data show that the crack tip is actually a diffuse region of micro-damage with many intact ligaments. The micro-damage at the front of the crack tip region is generally aligned perpendicular to the tensile direction. The cracks have a rough appearance: there are small-scale deflections possibly due to micro-damage linkage and larger-scale deflections in terms of the peak-to-peak distance. Qualitatively the amount of micro-damage is lower at high *da/dN* than at low *da/dN* and so does not scale simply with plastic zone size.

Alloy	Particle	Pore	Edge	Run-out	Total	σ_e (MPa)
LVD25	4	2	1	1	8	135
LVD26 unmod	2	4	1	1	8	136
LVD26 mod	3	4	1	1	9	132
LVD27	0	6	0	1	7	115

Table 5-1 Initiation sites for S-N tests at RT and the fatigue limits for each alloy.

Alloy	Stress (MPa)	Strain (%)	N_i	N_f	N_i/N_f (%)
LVD25	172	0.71	9000	166900	5.4
LVD26 unmod	160	1.03	60000	438849	13.7
LVD26 mod	170	1.10	5000	45252	11.0
LVD27	132	0.55	2000	67580	3

Table 5-2 Short fatigue crack growth loading conditions and results.

Alloy	ΔK_{th} (MPa$\sqrt{m}$)	K_Q (MPa$\sqrt{m}$)	C (mm/cycle)	m
LVD25	3.3	8.8	$1.5x10^{-10}$	7.2
LVD26 unmod	3.6	11.2	$2.7x10^{-9}$	4.9
LVD26 mod	3.2	12.8	$4x10^{-9}$	4.7
LVD27	3.0	11.9	$3.4x10^{-9}$	4.8

Table 5-3 Room temperature crack growth parameters.

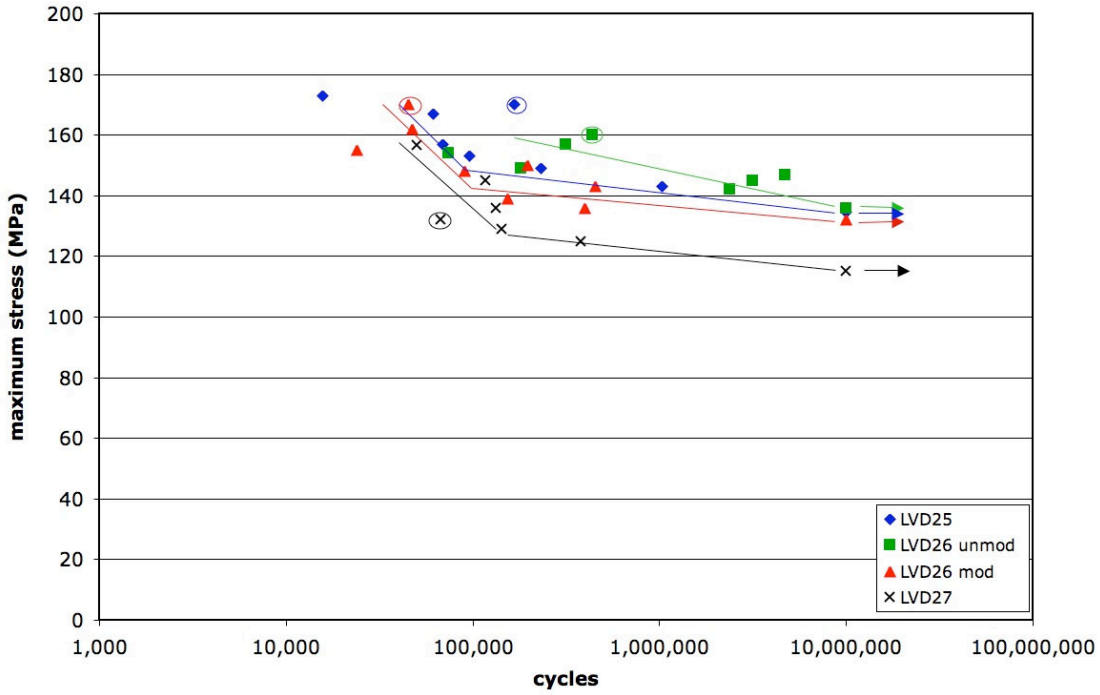

Figure 5-1 S-N results where stress is presented as a function of absolute stress at RT, the short fatigue crack growth sample are highlighted by a circle, the trend lines are just a guide.

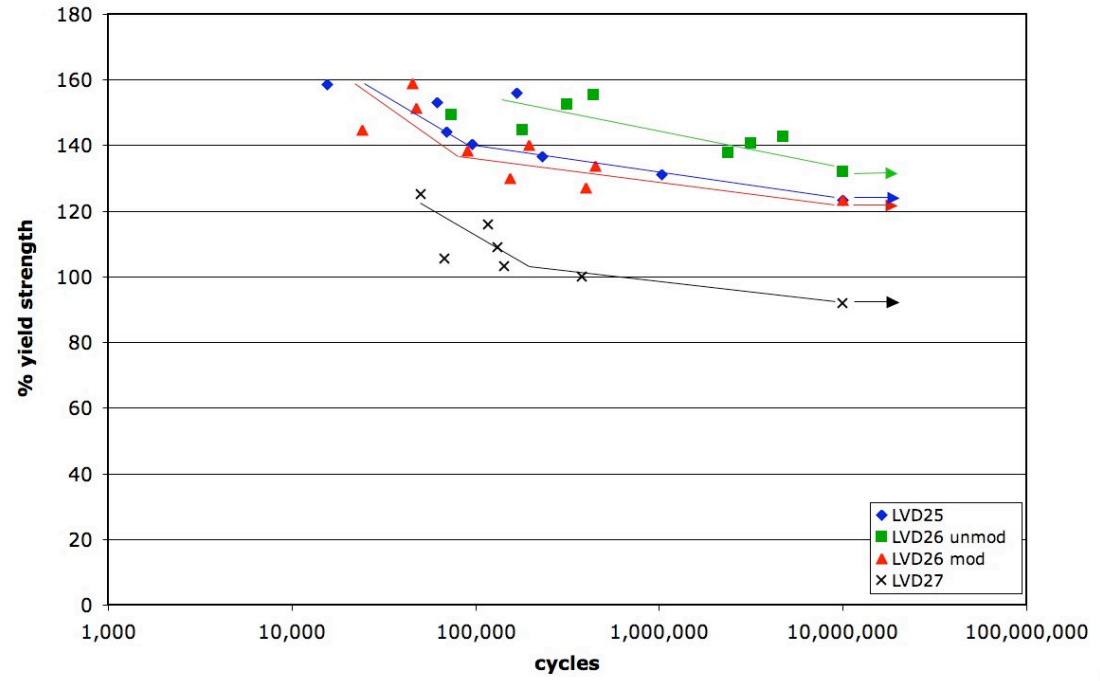

Figure 5-2 S-N results where stress is presented as a % of the 0.2% proof stress at RT, the short fatigue crack growth sample are highlighted by a circle, the trend lines are just a guide.

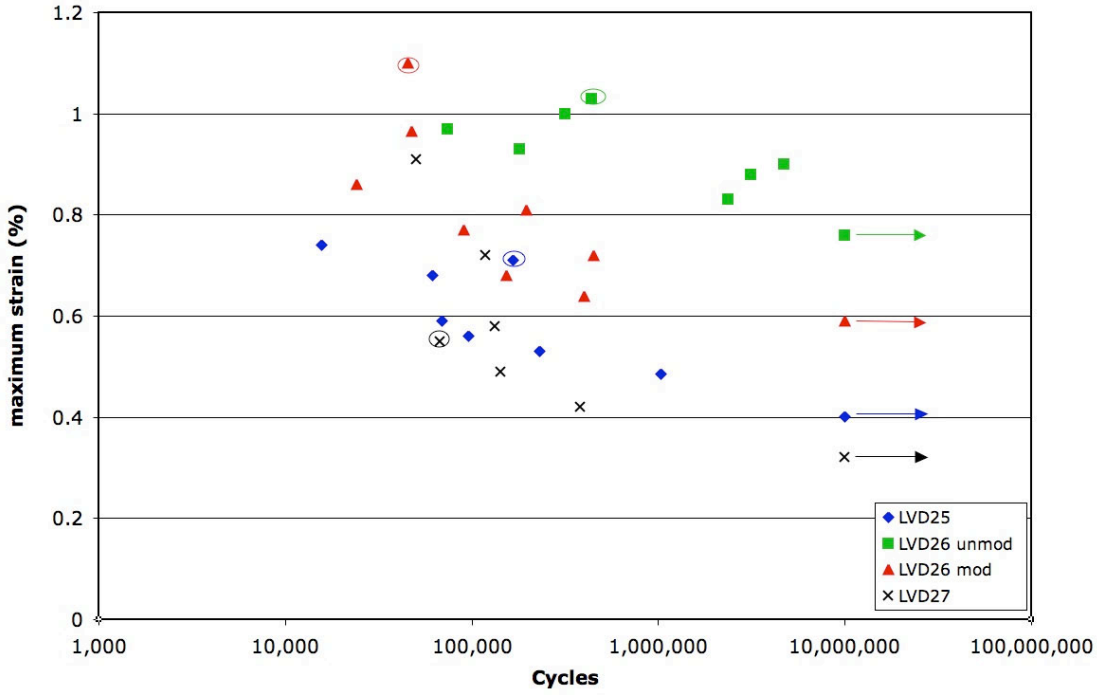

Figure 5-3 S-N results of strain versus the number of cycles to failure at RT, the short fatigue crack growth sample are highlighted by a circle.

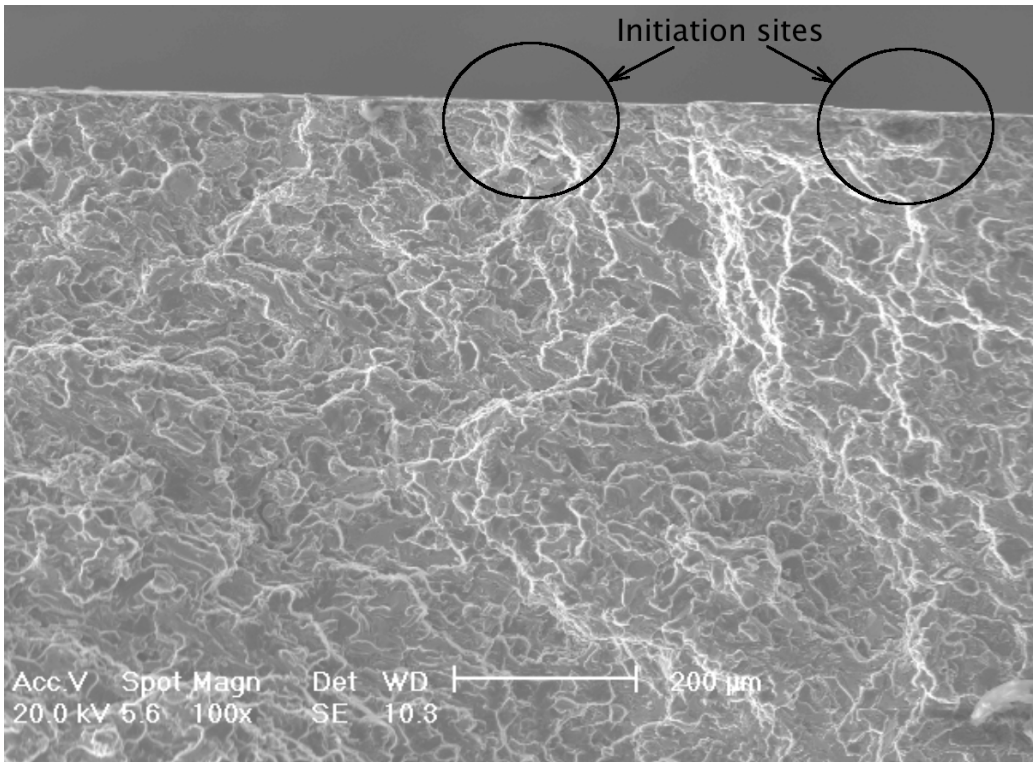

Figure 5-4 First fracture surface and initiation site in LVD25.

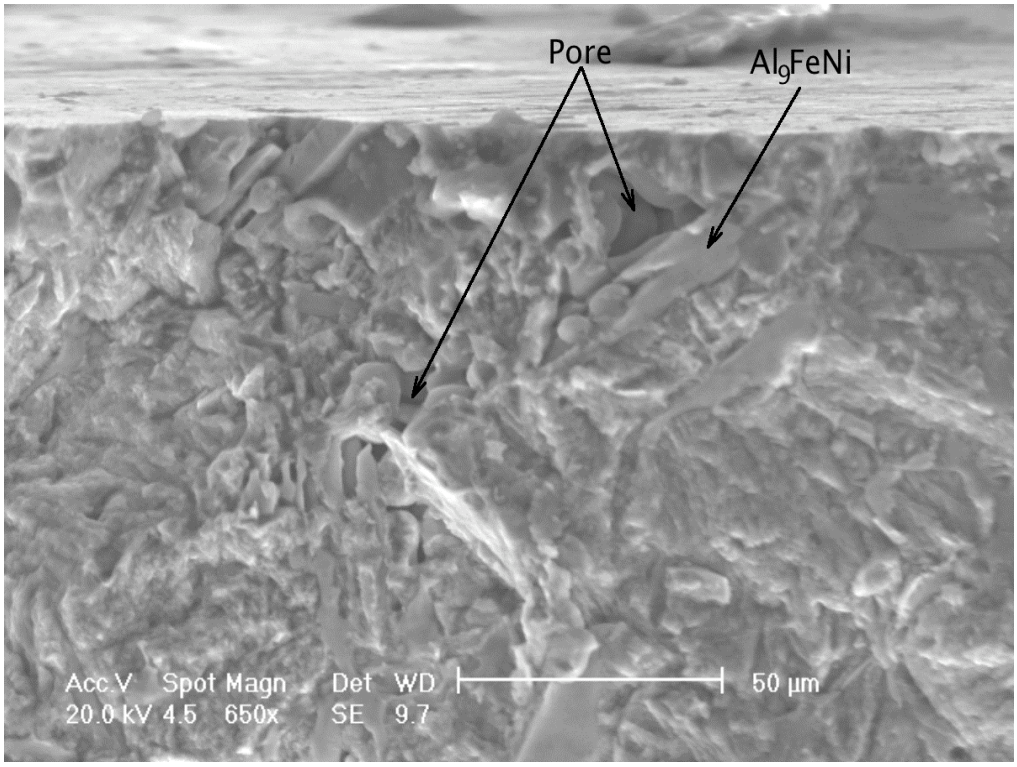

Figure 5-5 Pore at initiation site in LVD25.

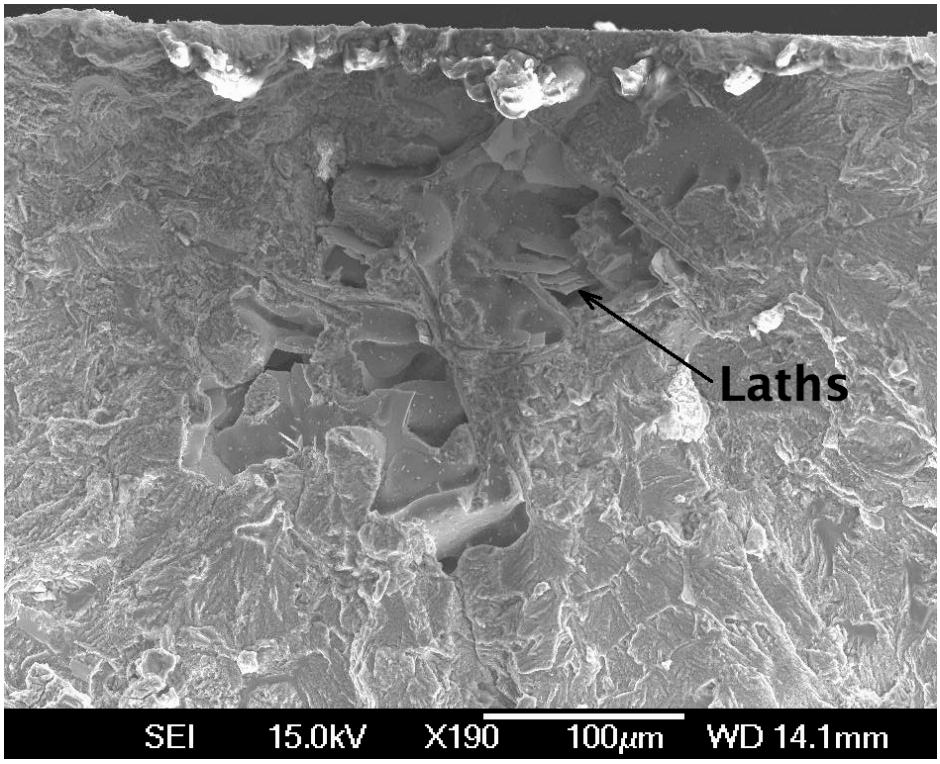

Figure 5-6 Pore at initiation site in LVD26 unmod.

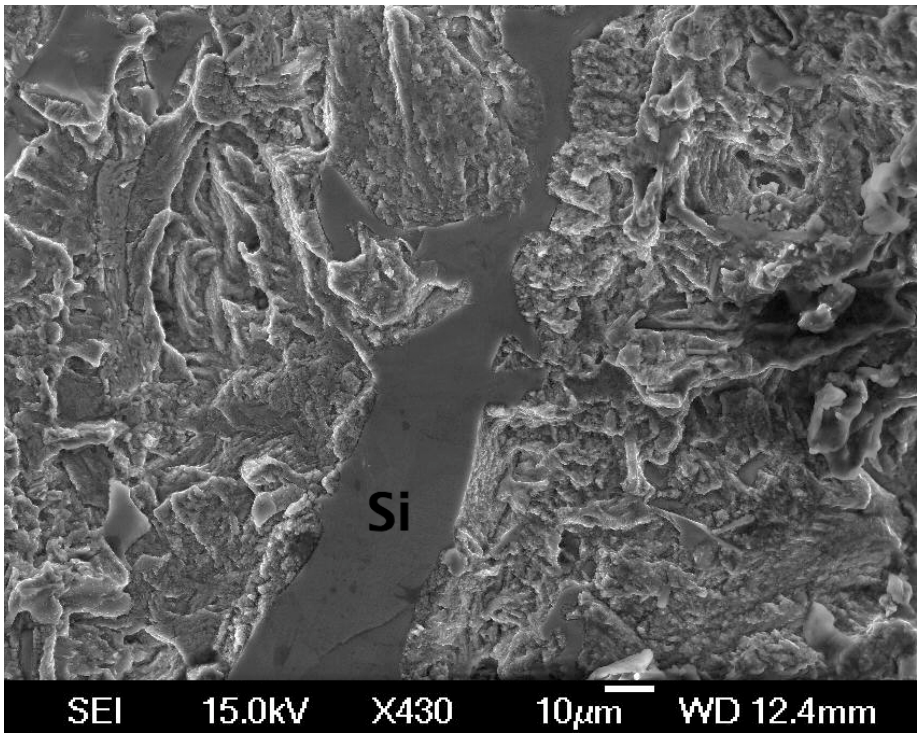

Figure 5-7 Si particles at initiation site in LVD26 unmod.

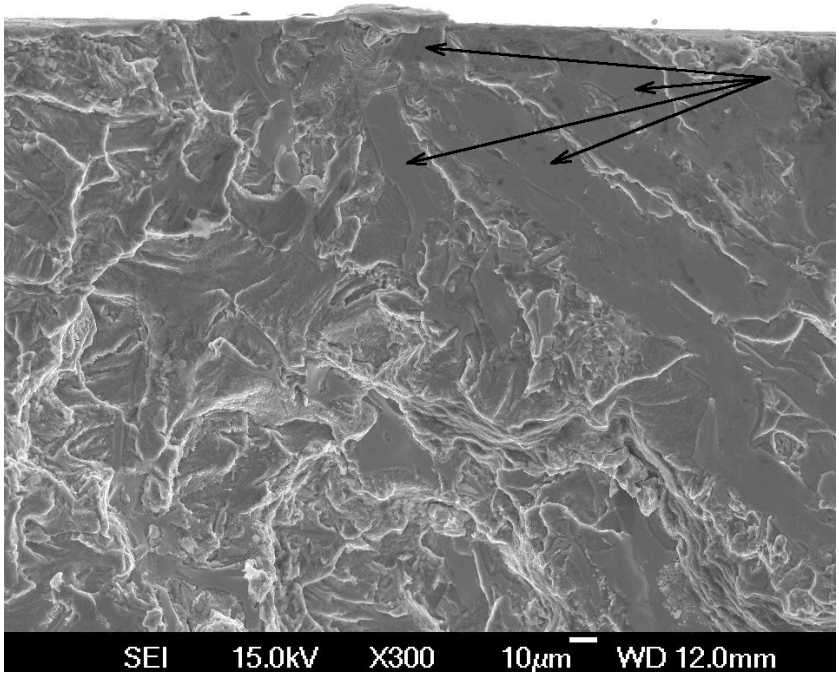

Figure 5-8 Al_9FeNi particle at initiation site in LVD26 mod, the arrows show where EDX analysis was performed and indicated that the particles were Al_9FeNi and Al_3Ni_2 type.

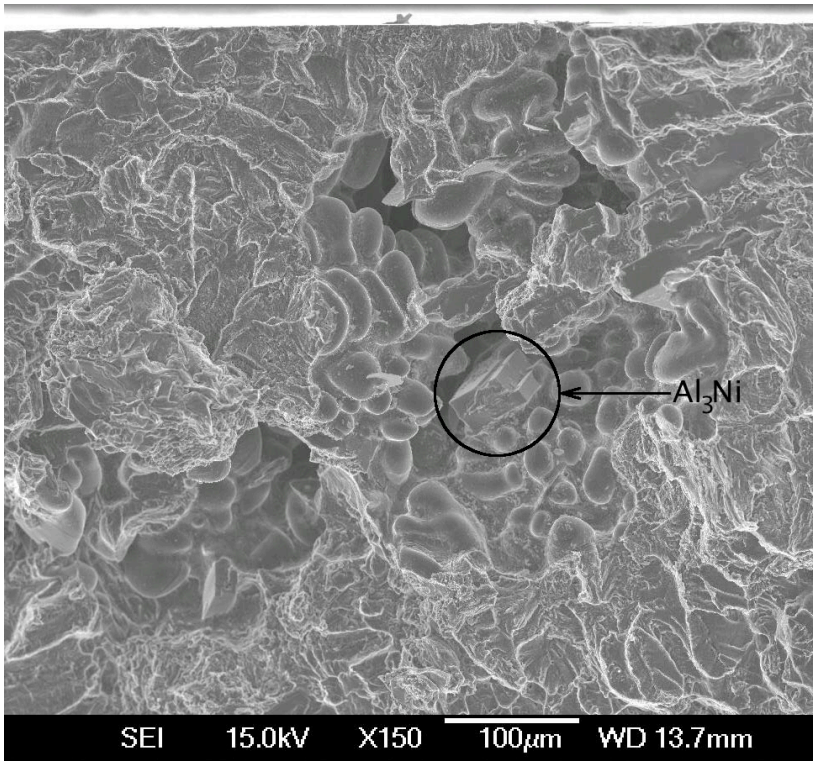

Figure 5-9 Pore at initiation site in LVD26 mod.

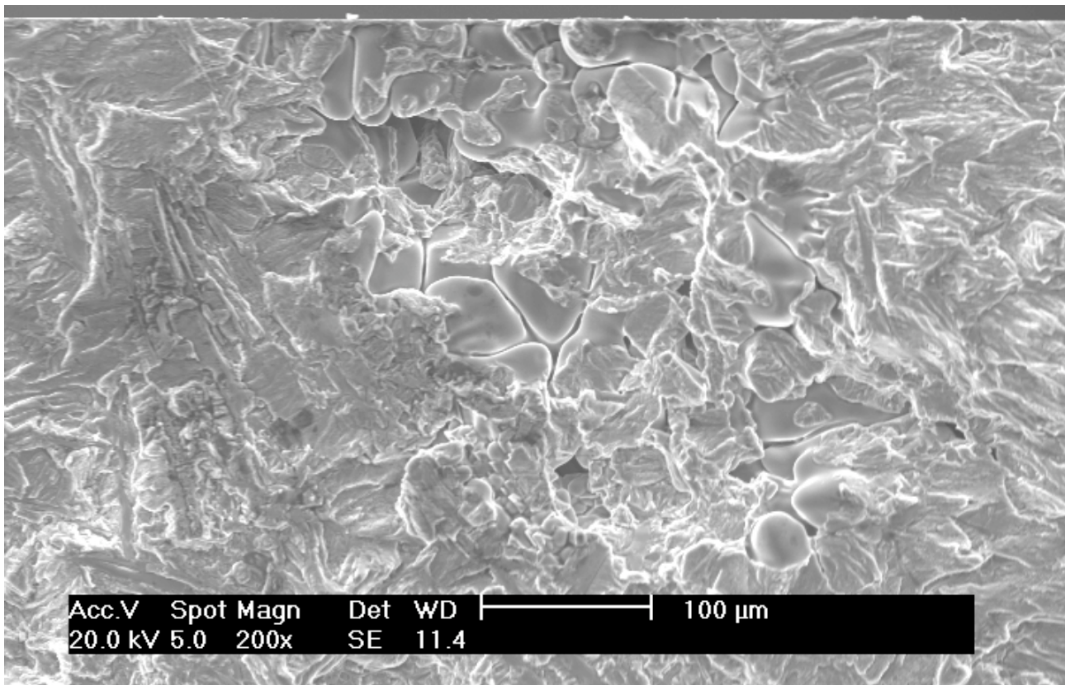

Figure 5-10 Porous region 1 at initiation site in LVD27.

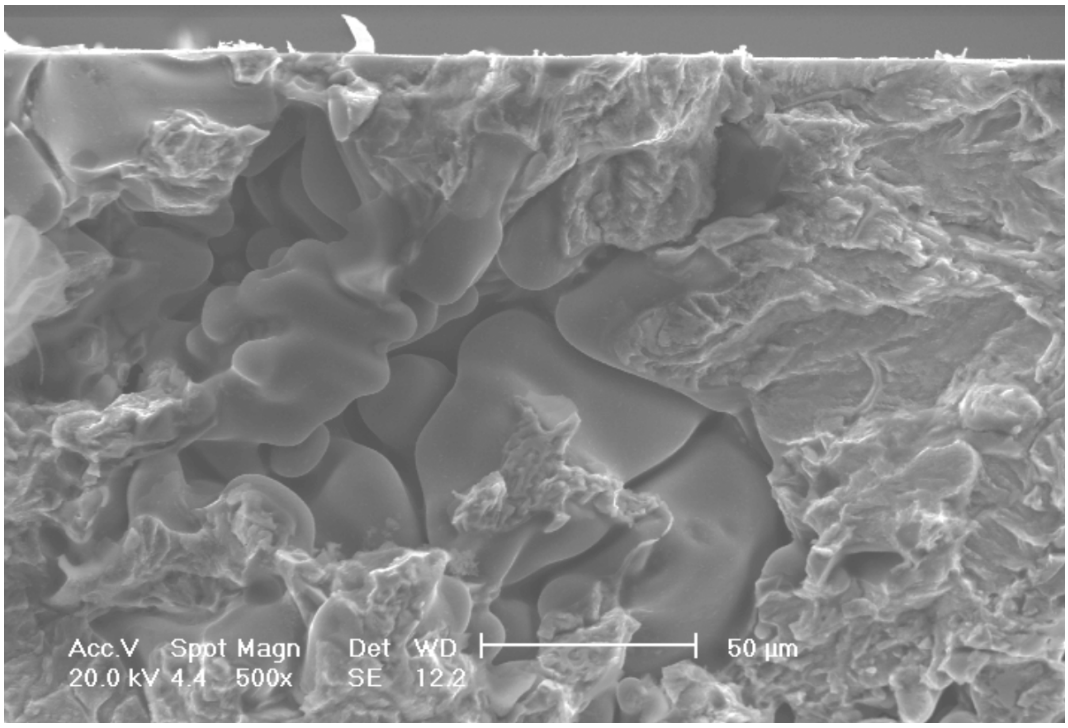

Figure 5-11 Porous region 2 at initiation site in LVD27.

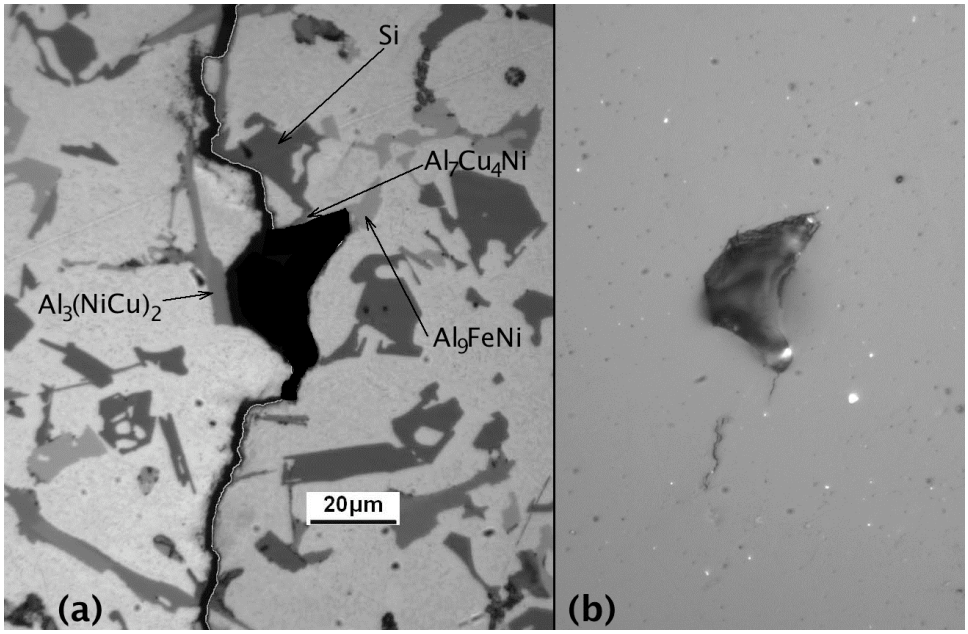

Figure 5-12 First initiation site in LVD25, (a) is the optical micrograph and (b) is the acetate replica showing initiation.

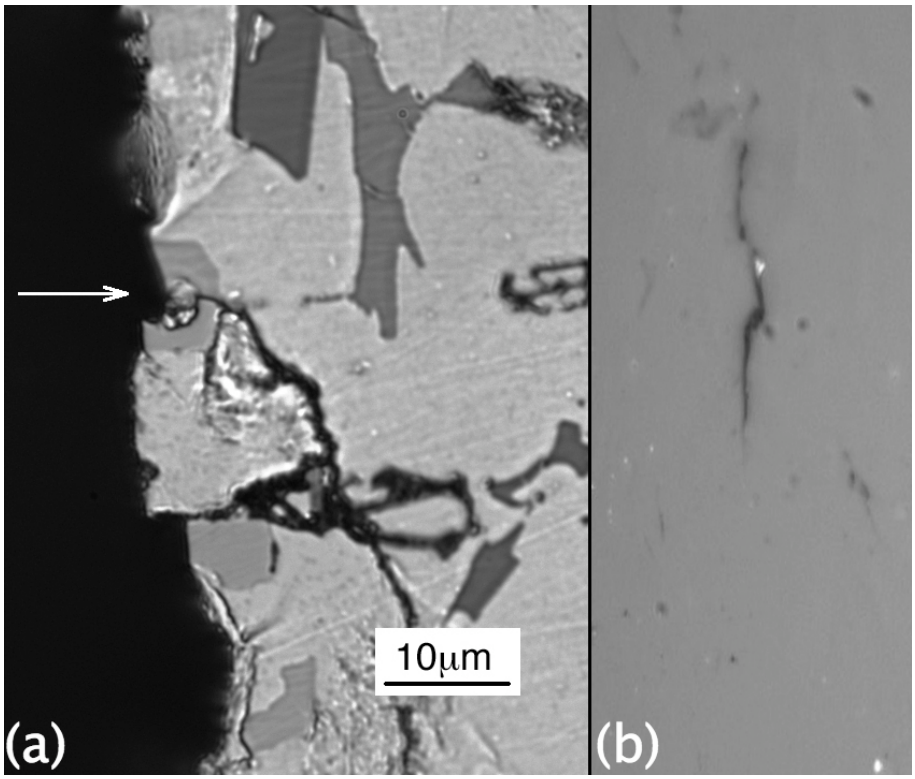

Figure 5-13 Second initiation site in LVD25, (a) is the optical micrograph and (b) is the acetate replica showing initiation.

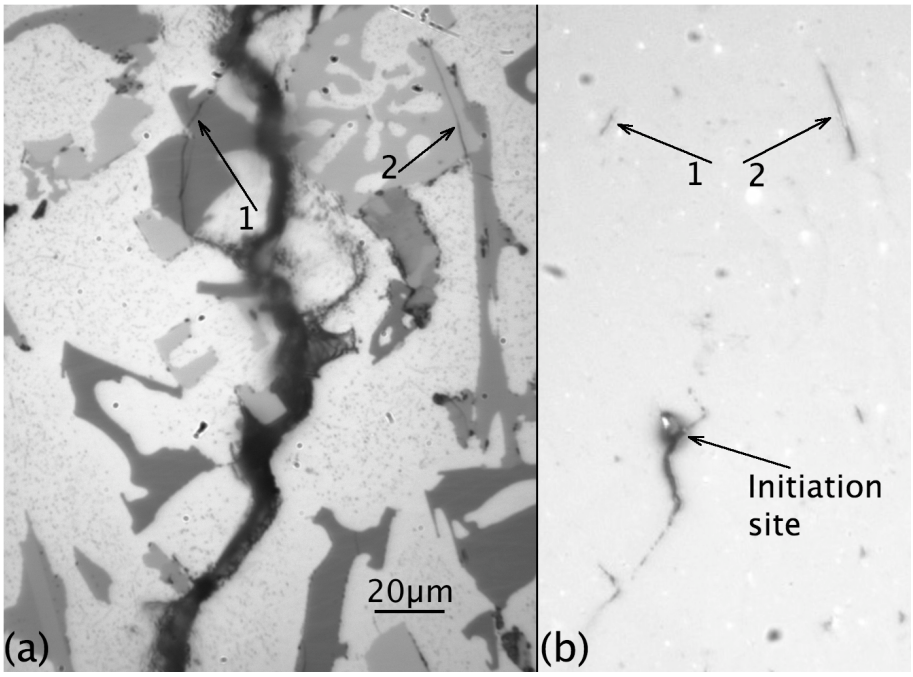

Figure 5-14 Third initiation site in LVD25, (a) is the optical micrograph and (b) is the acetate replica showing initiation.

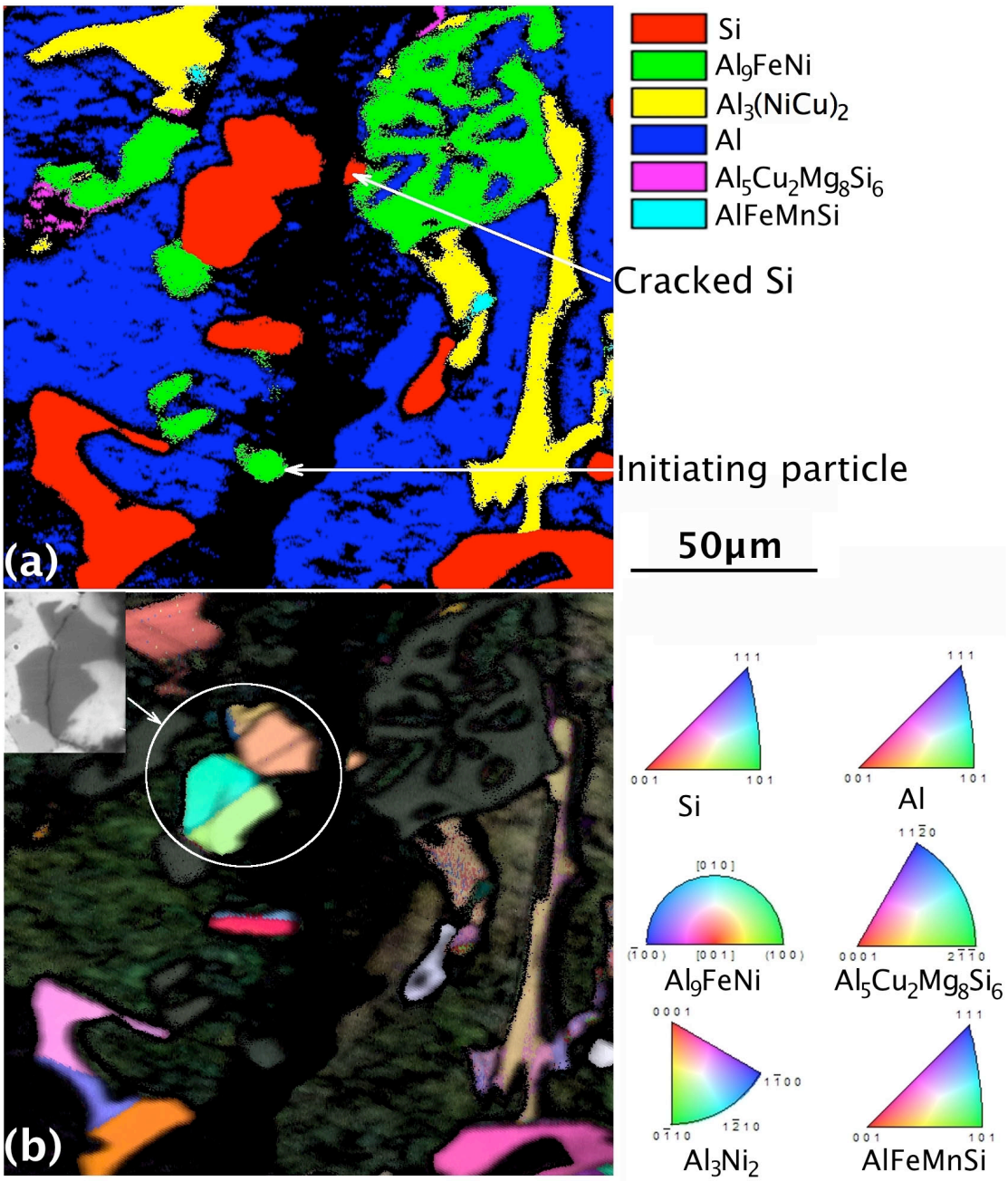

Figure 5-15 (a) phase map and (b) inverse pole figure for the third initiation site in LVD25 (Figure 5-14).

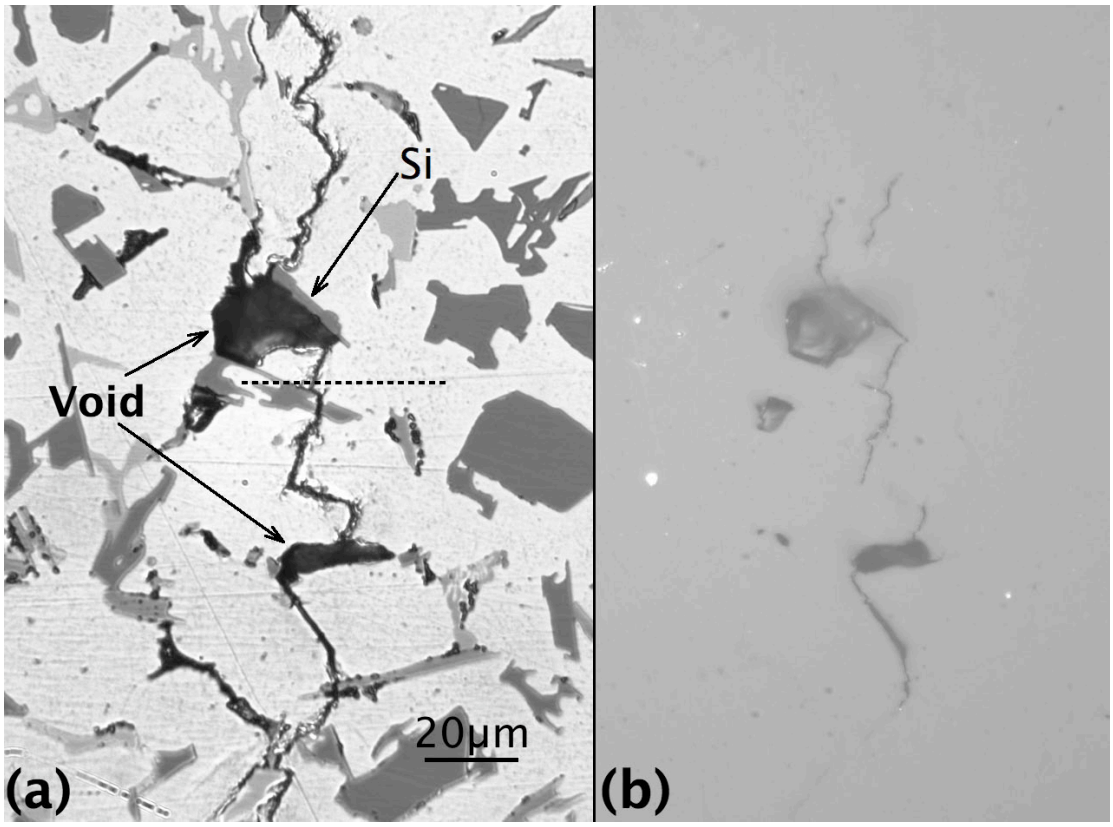

Figure 5-16 Fourth initiation site in LVD25, (a) is the optical micrograph and (b) is the acetate replica showing initiation.

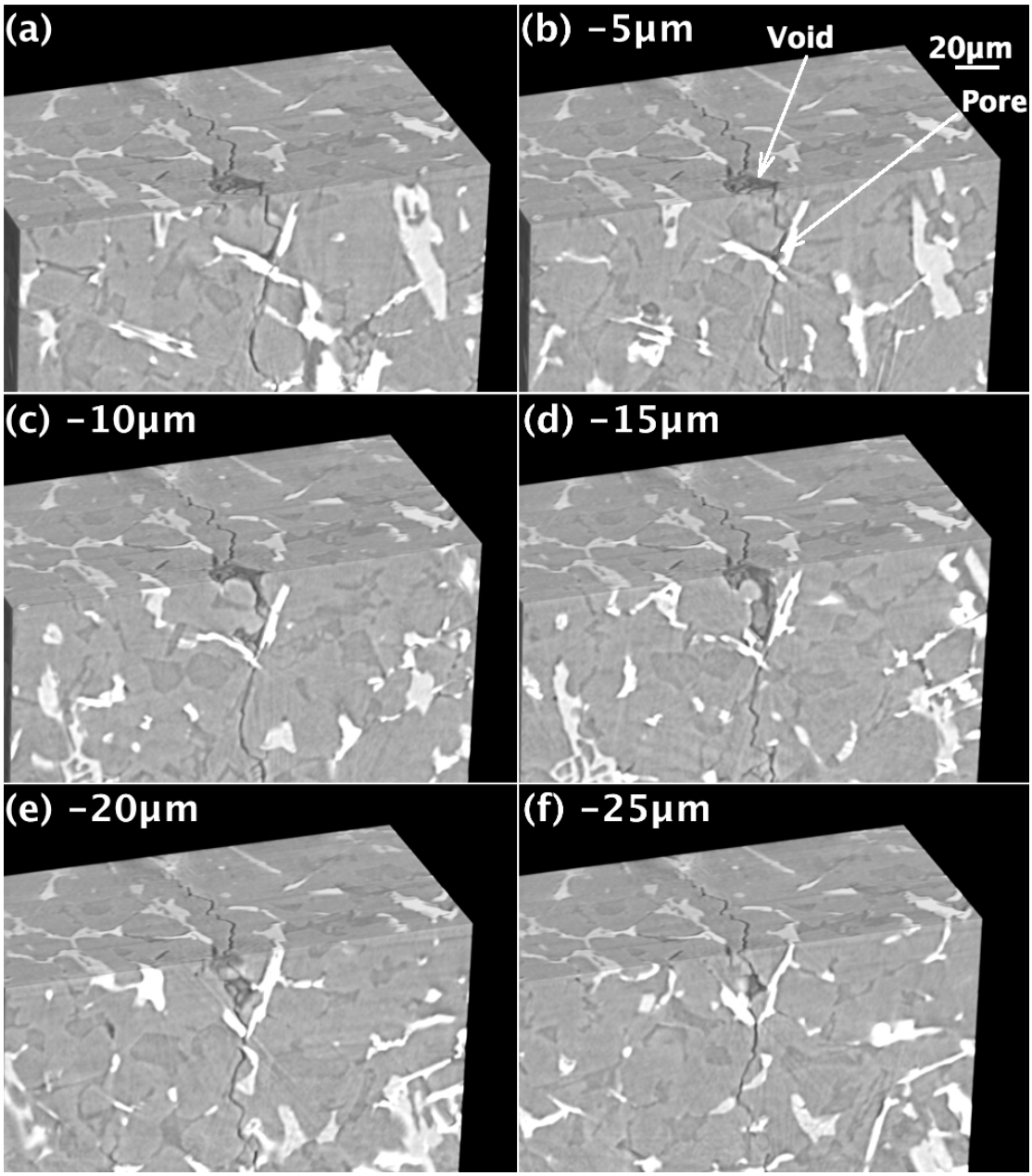

Figure 5-17 X-ray CT images for the fourth initiation site in LVD25, (a) to (f) are taken at 5 µm intervals through the initiation site.

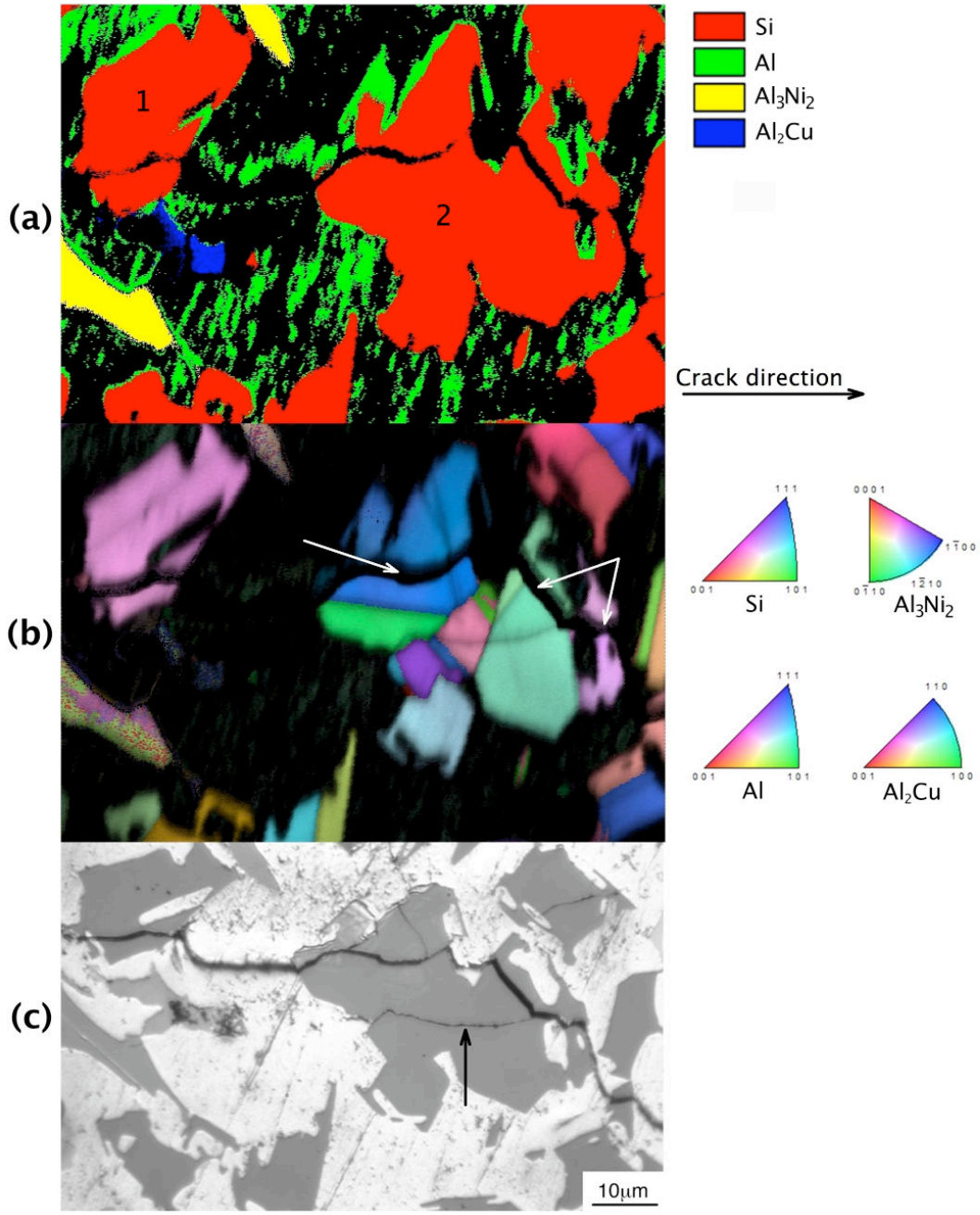

Figure 5-18 Large Si particle cluster in LVD25, (a) is the phase map, (b) the inverse pole figure and (c) the optical micrograph.

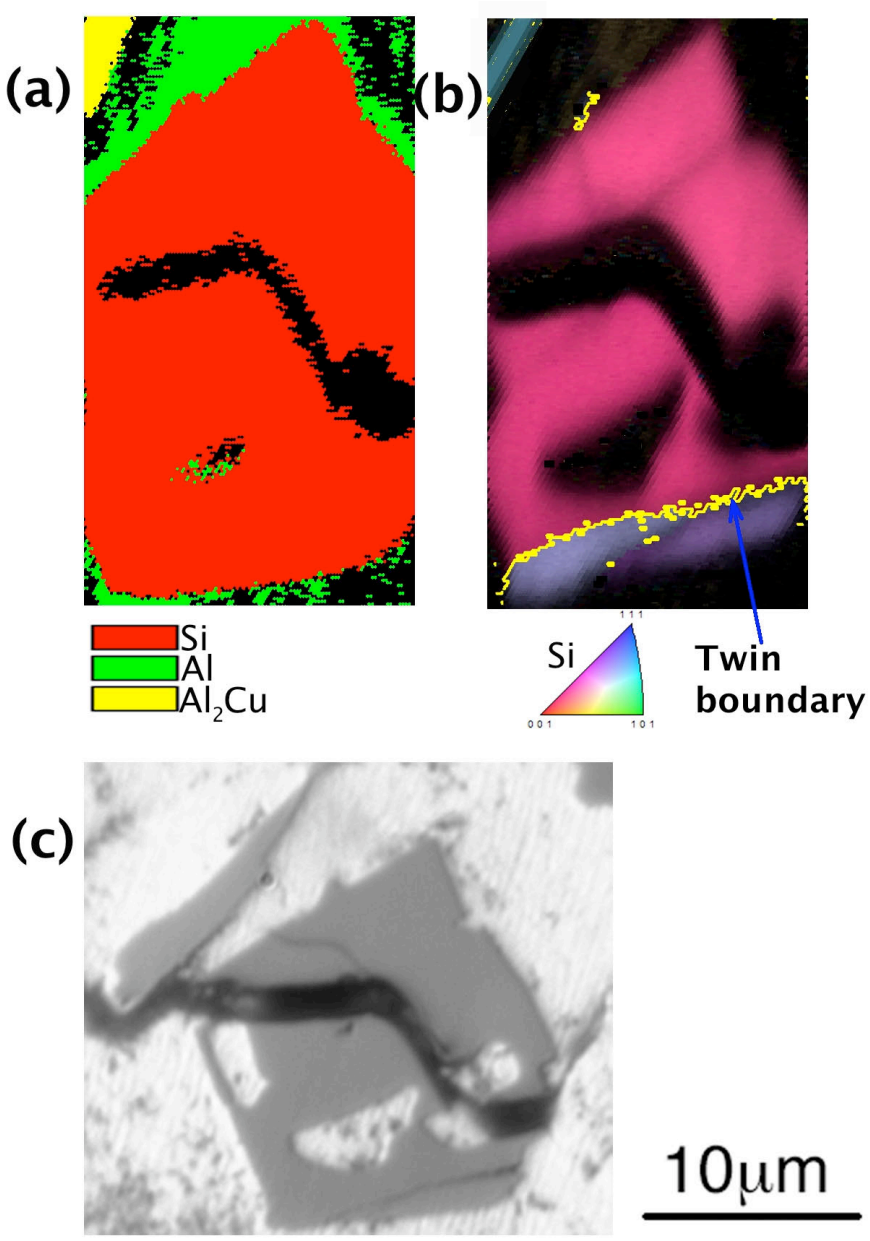

Figure 5-19 Small Si particle in LVD25, (a) is the phase map, (b) the inverse pole figure and (c) the optical micrograph.

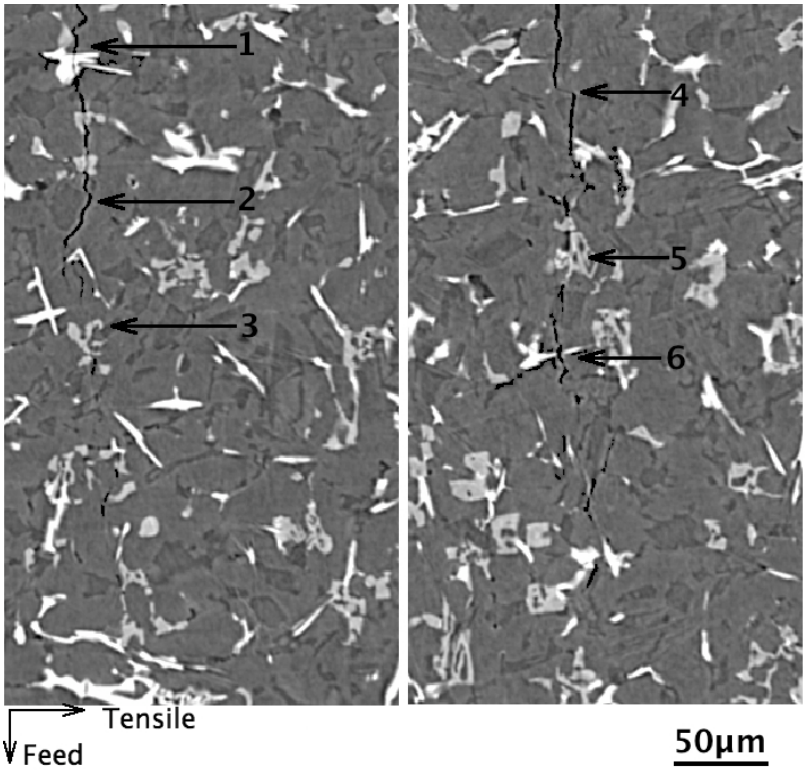

Figure 5-20 X-ray CT sections through the crack tip region, regions 1 to 6 are discussed in the relevant text.

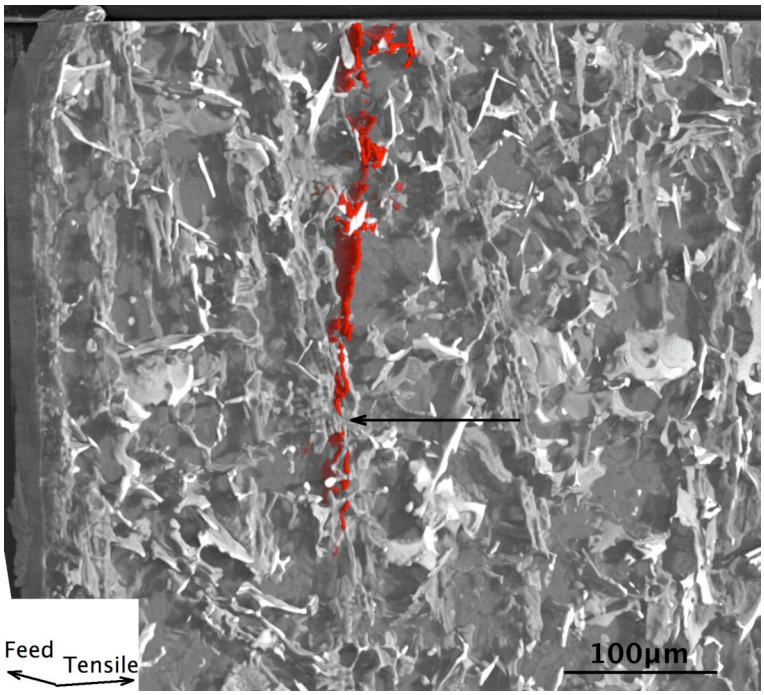

Figure 5-21 3-D image showing the interaction between the fatigue crack and the secondary phase microstructure in LVD25.

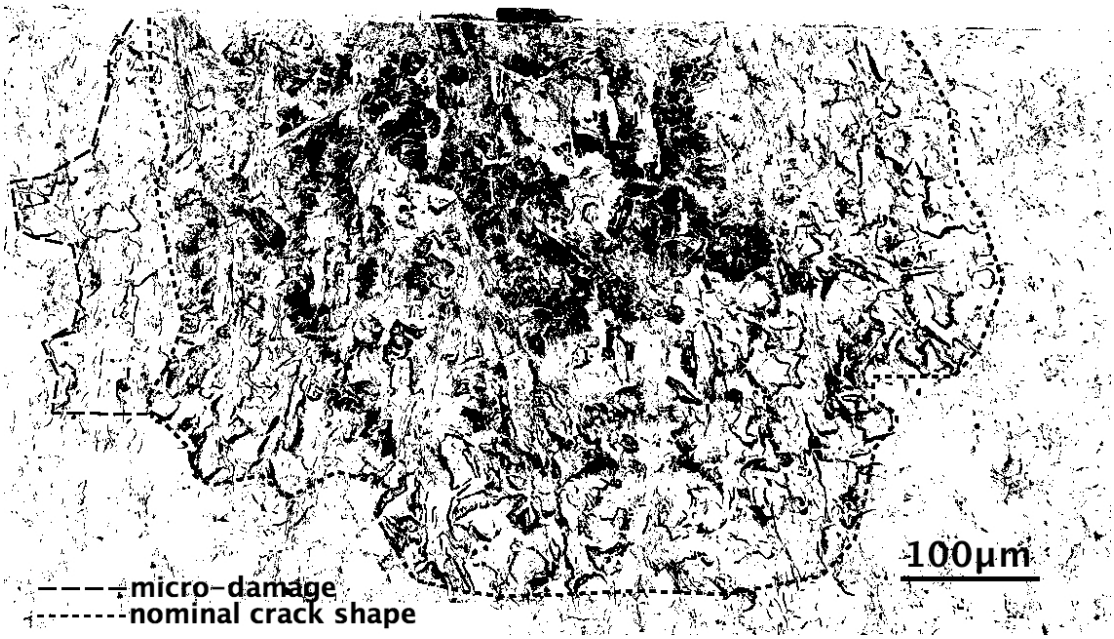

Figure 5-22 2-D projection of the LVD25 crack analysed using X-ray CT.

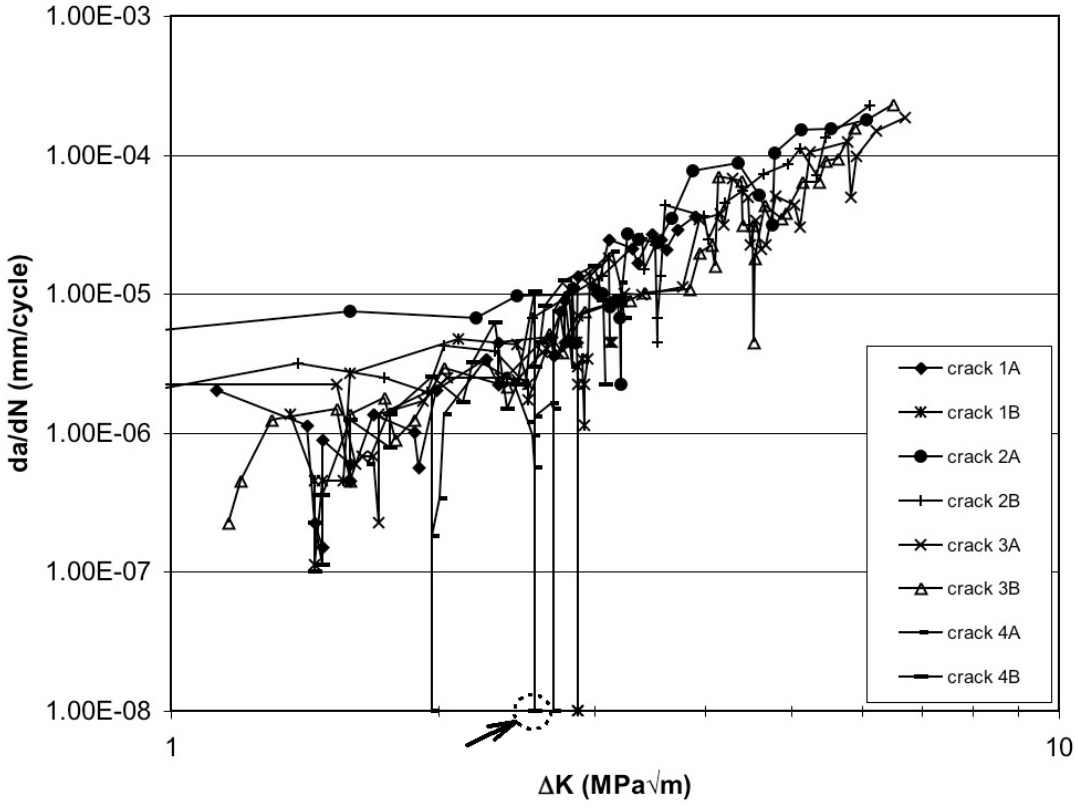

Figure 5-23 Short fatigue crack growth data for LVD25.

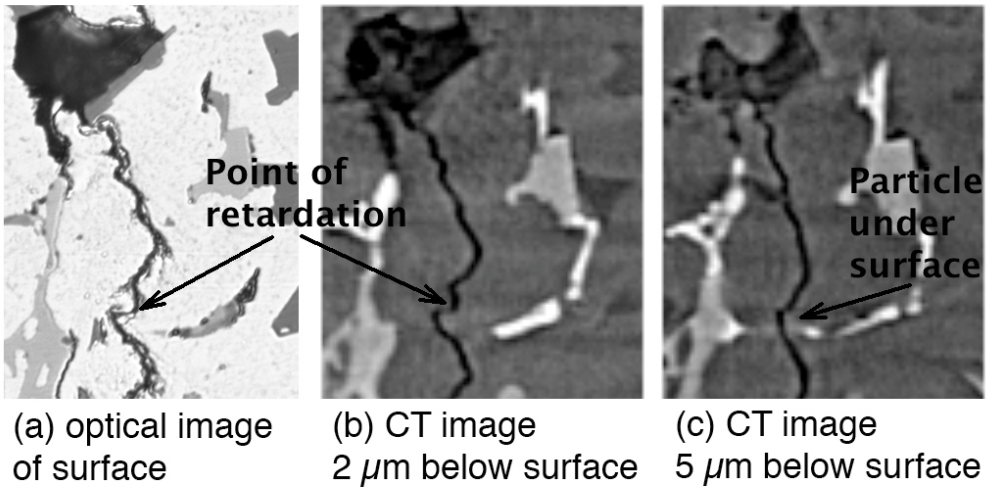

Figure 5-24 (a) optical micrograph of the point of crack arrest in LVD25 and the corresponding X-ray CT image (b) 2 µm and (c) 5 µm below the surface.

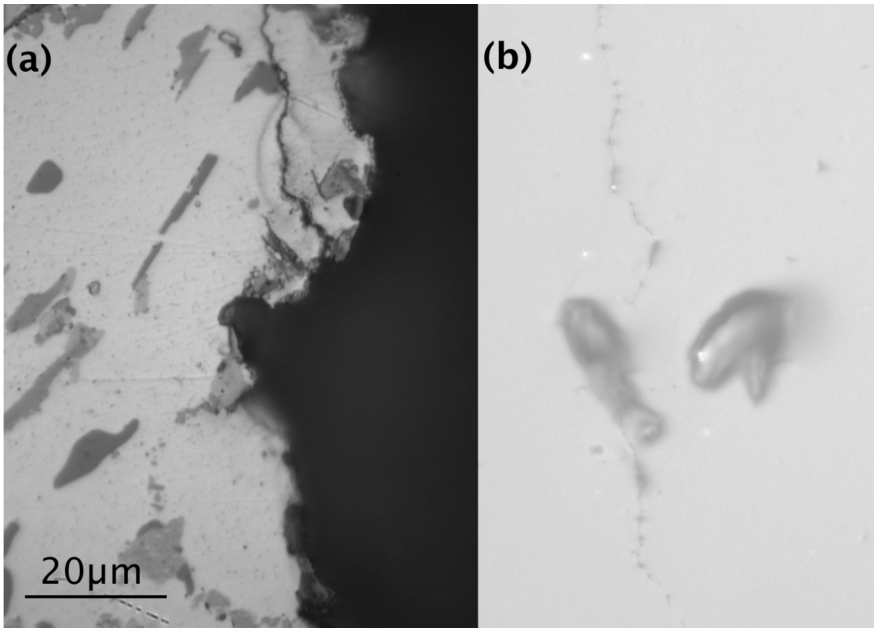

Figure 5-25 First initiation site in LVD26 unmod, (a) is the optical micrograph and (b) is the acetate replica showing initiation.

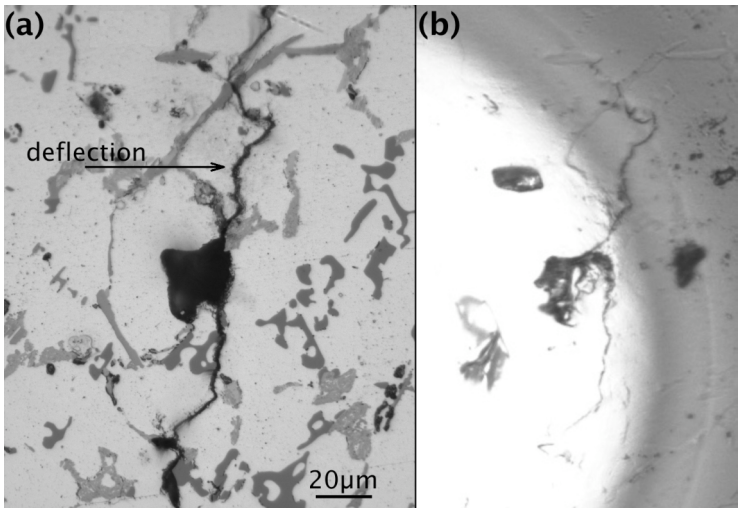

Figure 5-26 Second initiation site in LVD26 unmod, (a) is the optical micrograph and (b) is the acetate replica showing initiation.

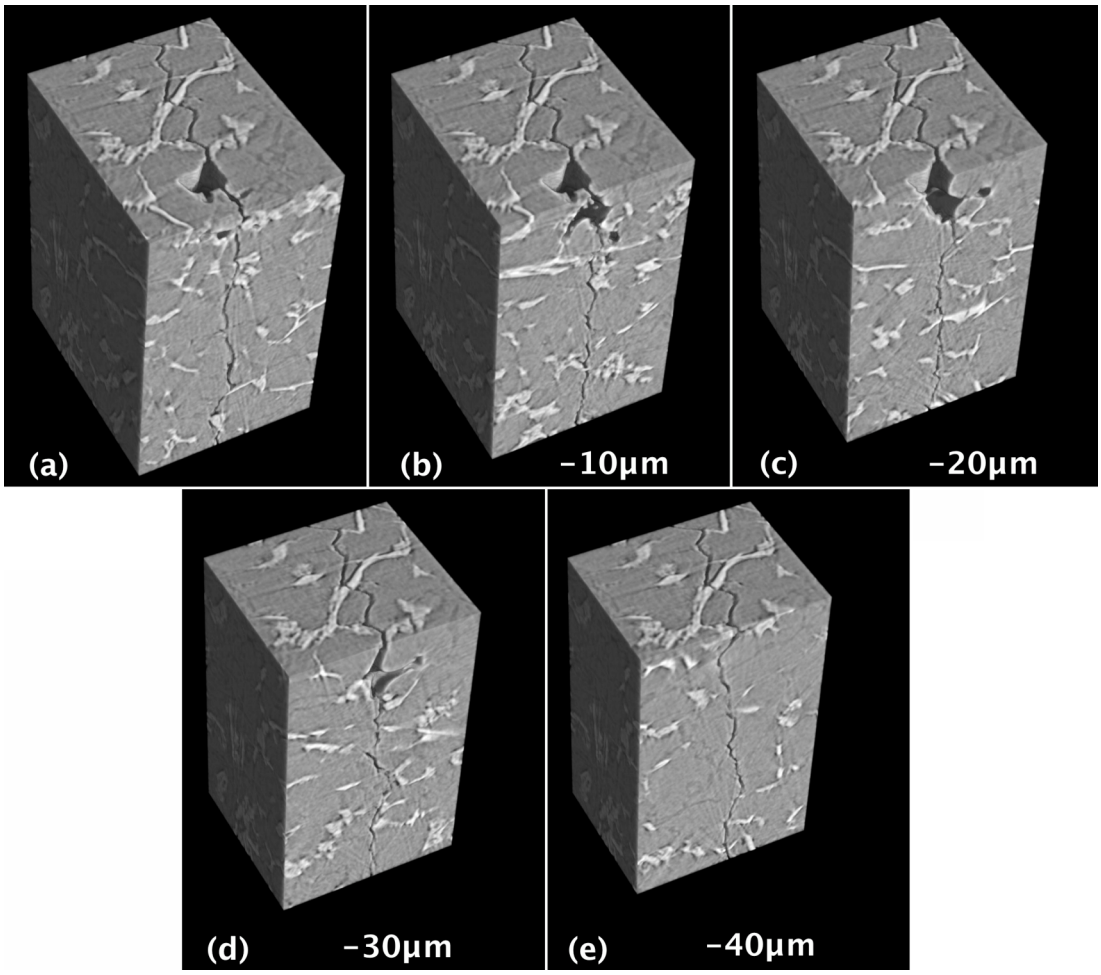

Figure 5-27 X-ray CT images for the second initiation site in LVD26 unmod, (a) to (e) are at 10 μm intervals through the initiation site.

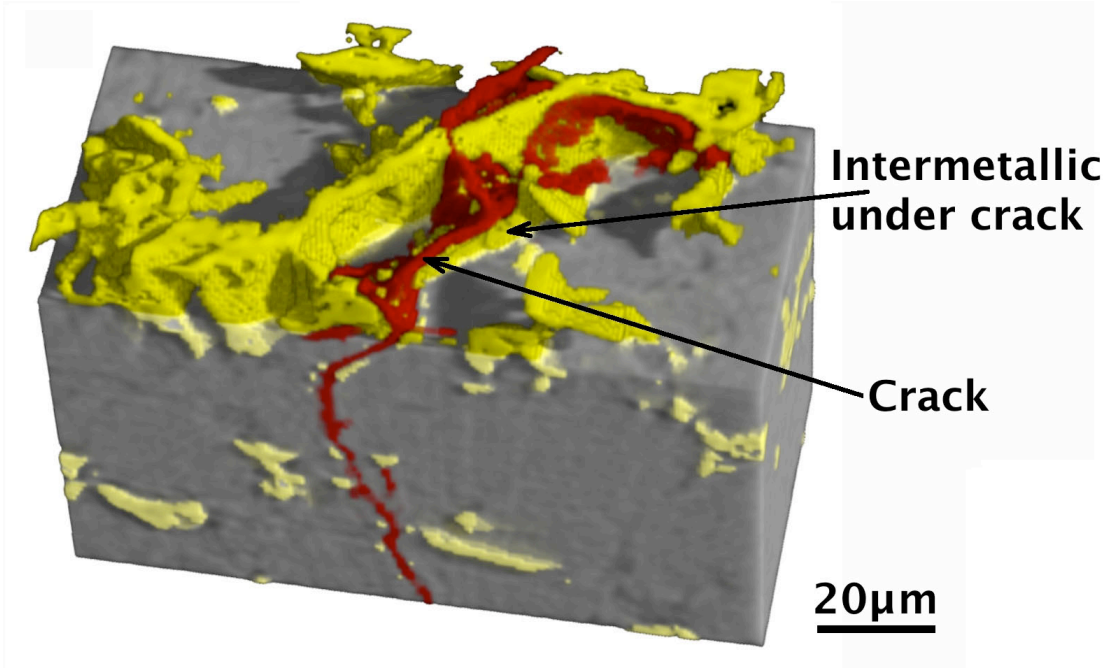

Figure 5-28 X-ray CT image of a deflected crack in LVD26 unmod.

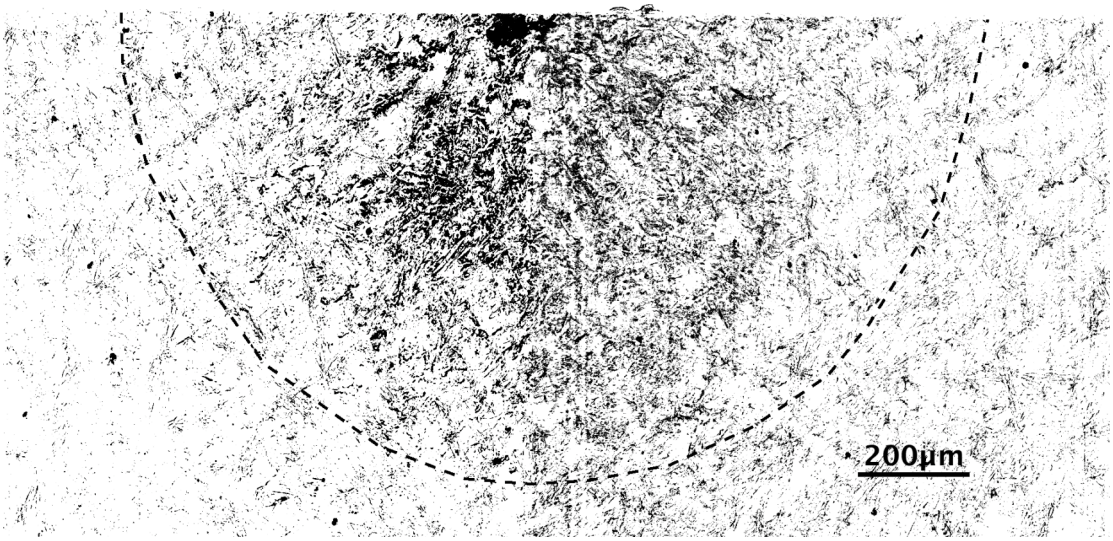

Figure 5-29 2-D projection of the LVD26 unmod crack analysed using X-ray CT.

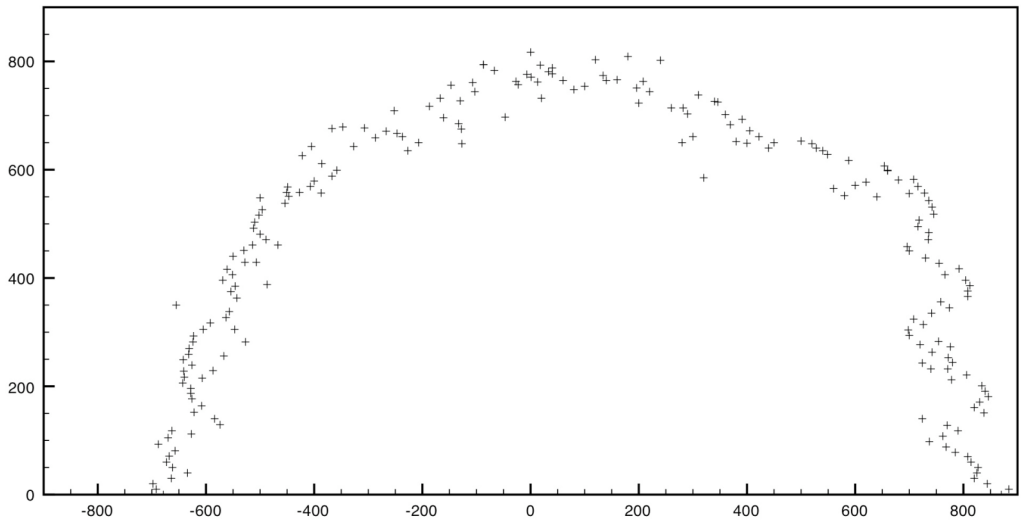

Figure 5-30 Crack tip position from CT slices in LVD26 unmod.

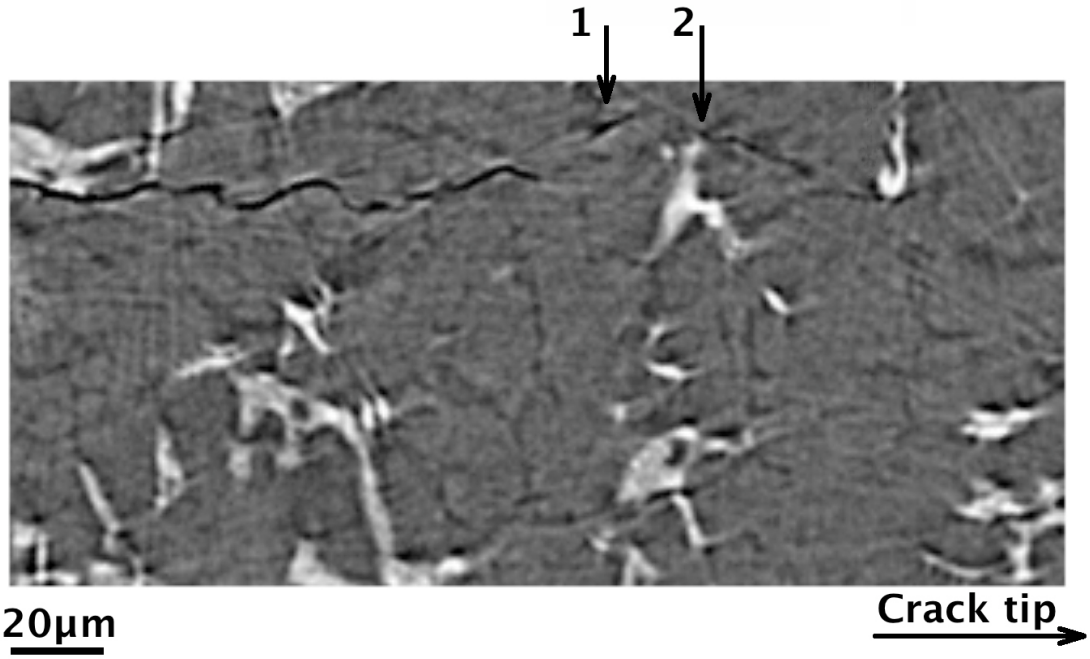

Figure 5-31 X-ray CT 2-D section of the crack tip in LVD26 unmod, positions 1 and 2 are damage ahead of the crack tip and are described in the accompanying text.

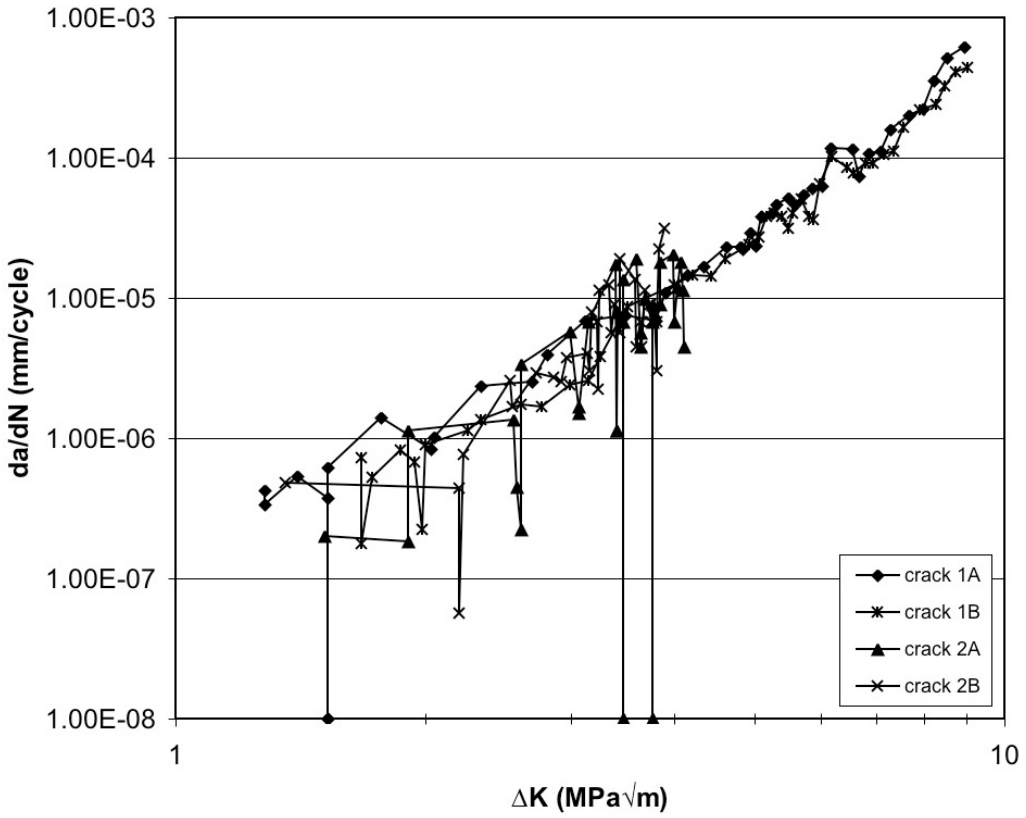

Figure 5-32 Fatigue crack growth data for LVD26 unmod

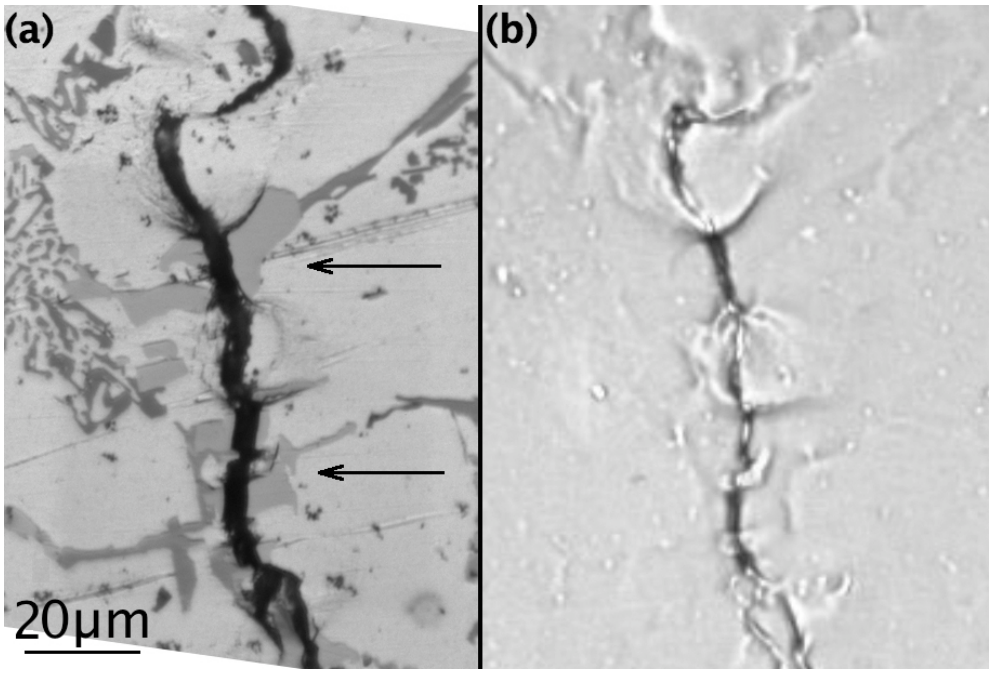

Figure 5-33 First initiation site in LVD26 mod, (a) is the optical micrograph and (b) is the acetate replica showing initiation.

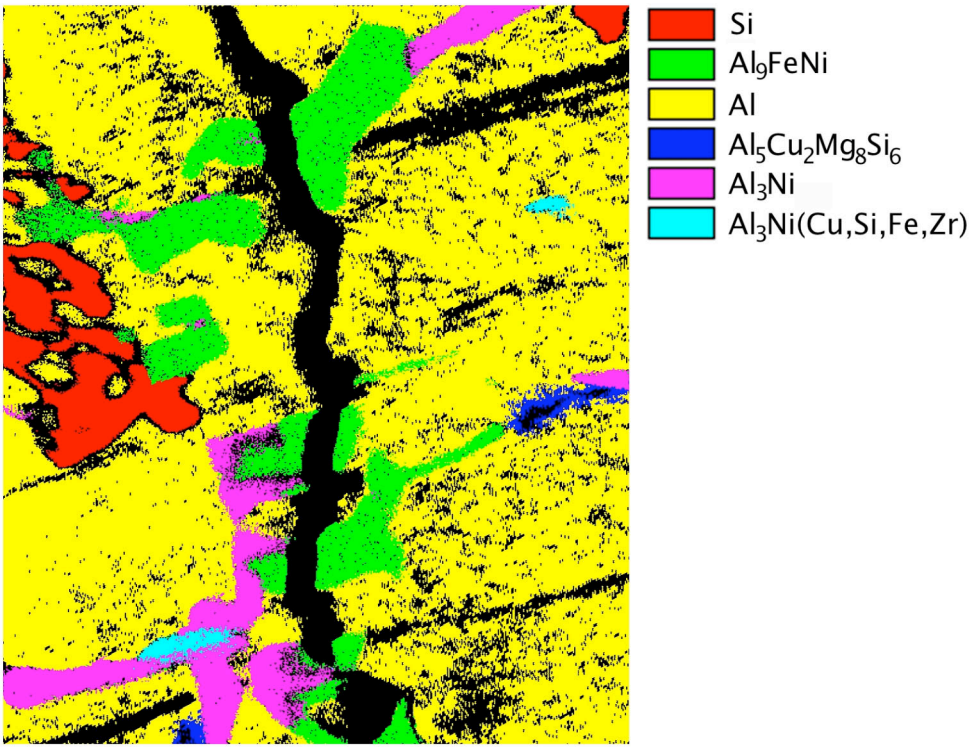

Figure 5-34 Phase map of first initiation site in LVD26 mod.

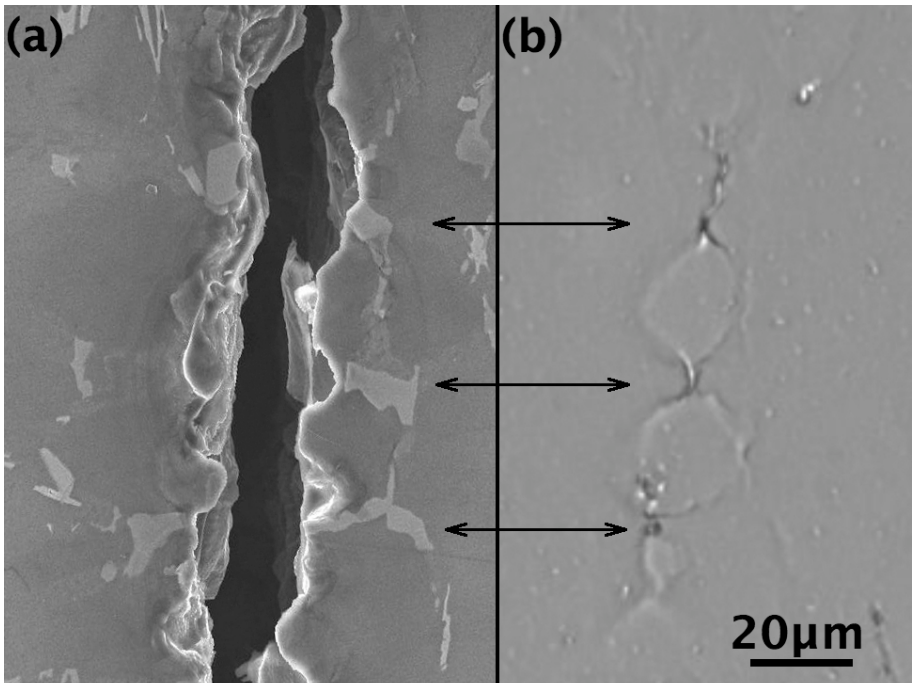

Figure 5-35 Second initiation site in LVD26 mod, (a) is the SEM micrograph and (b) is the acetate replica showing initiation.

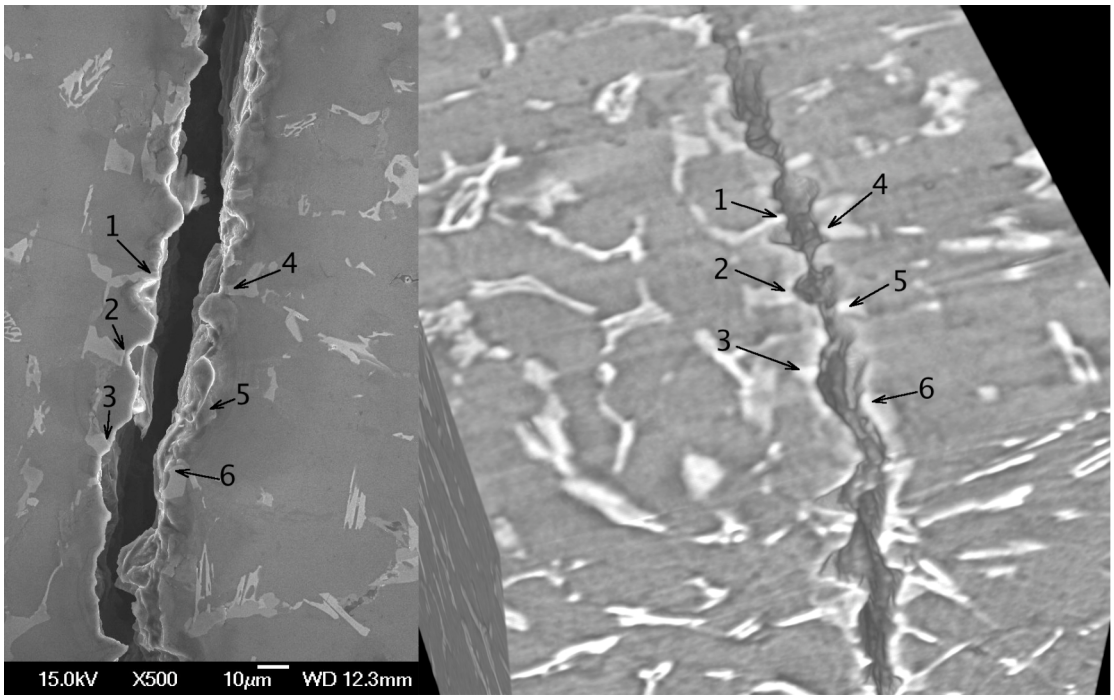

Figure 5-36 (a) SEM image and (b) X-ray CT image of the second initiation site in LVD26 mod, positions 1 to 6 identify the particles which caused initiation in the case.

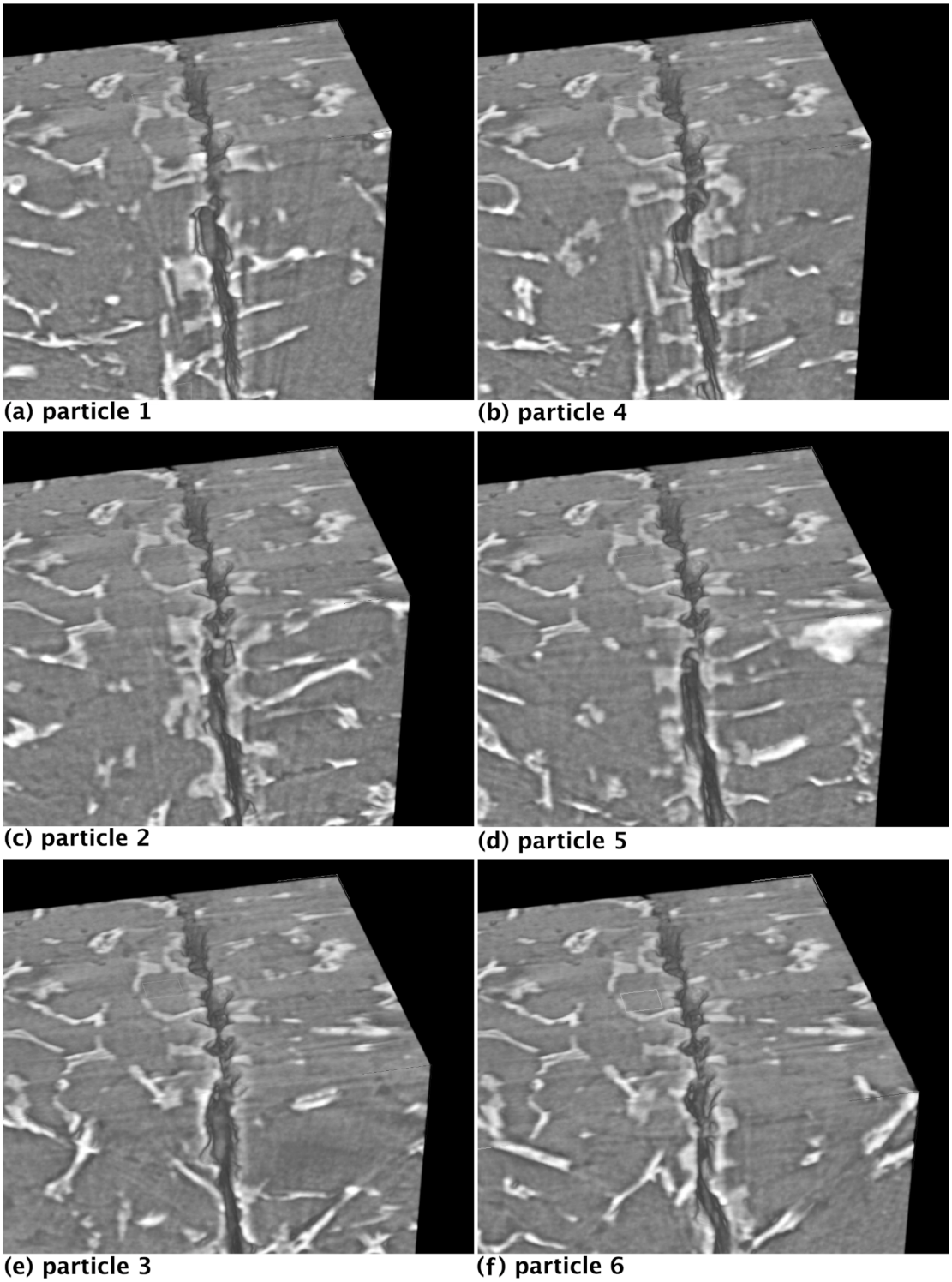

Figure 5-37 X-ray CT images of region under initiating particles in second initiation site, they relate to the numbered particles in Figure 5-36.

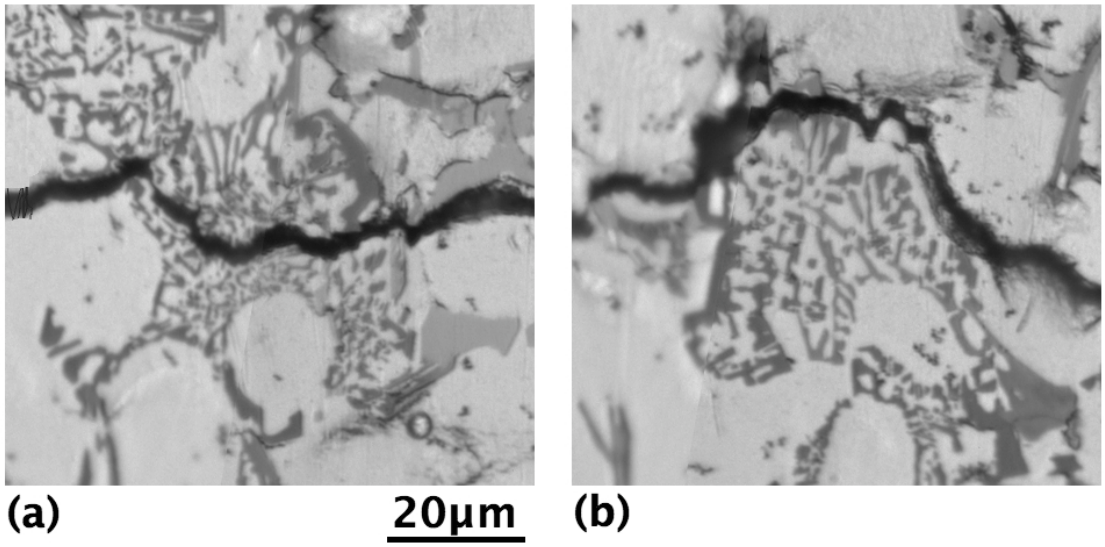

Figure 5-38 Crack interaction with Si particle clusters in LVD26 mod, (a) shows the crack propagating through a Si cluster and (b) around a Si cluster.

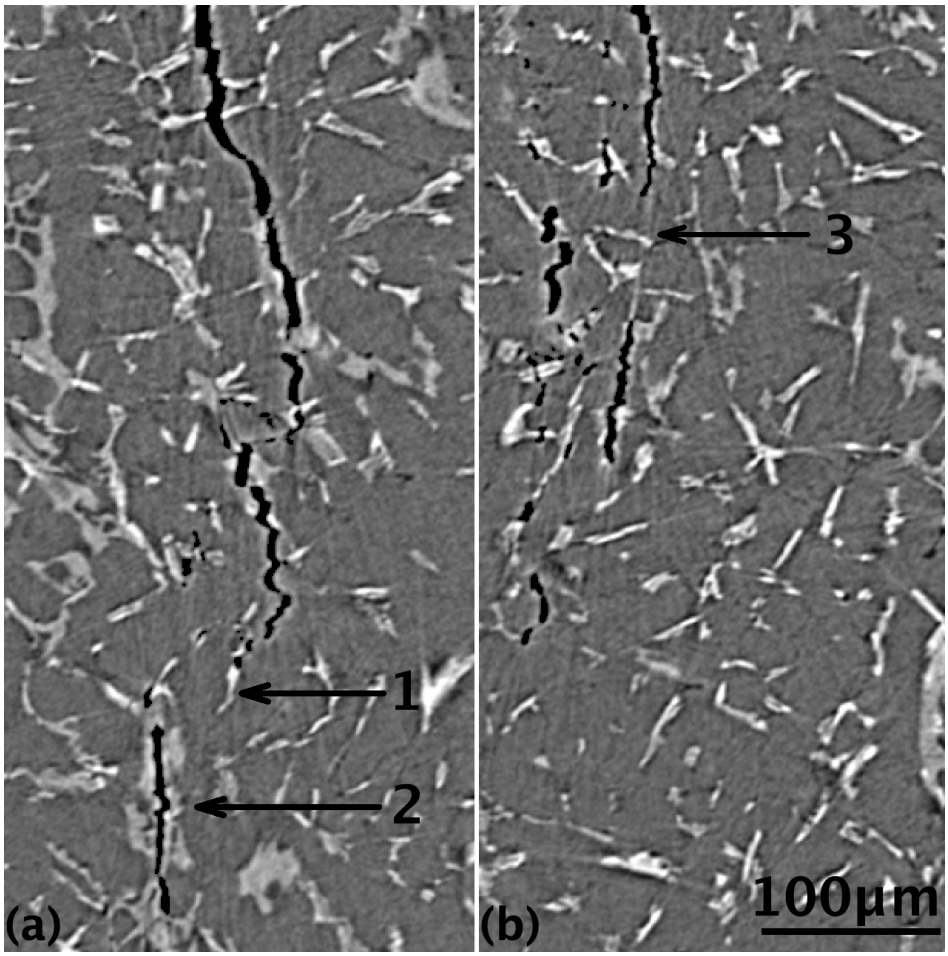

Figure 5-39 (a) and (b) are X-ray CT sections of the crack tip in LVD26 mod.

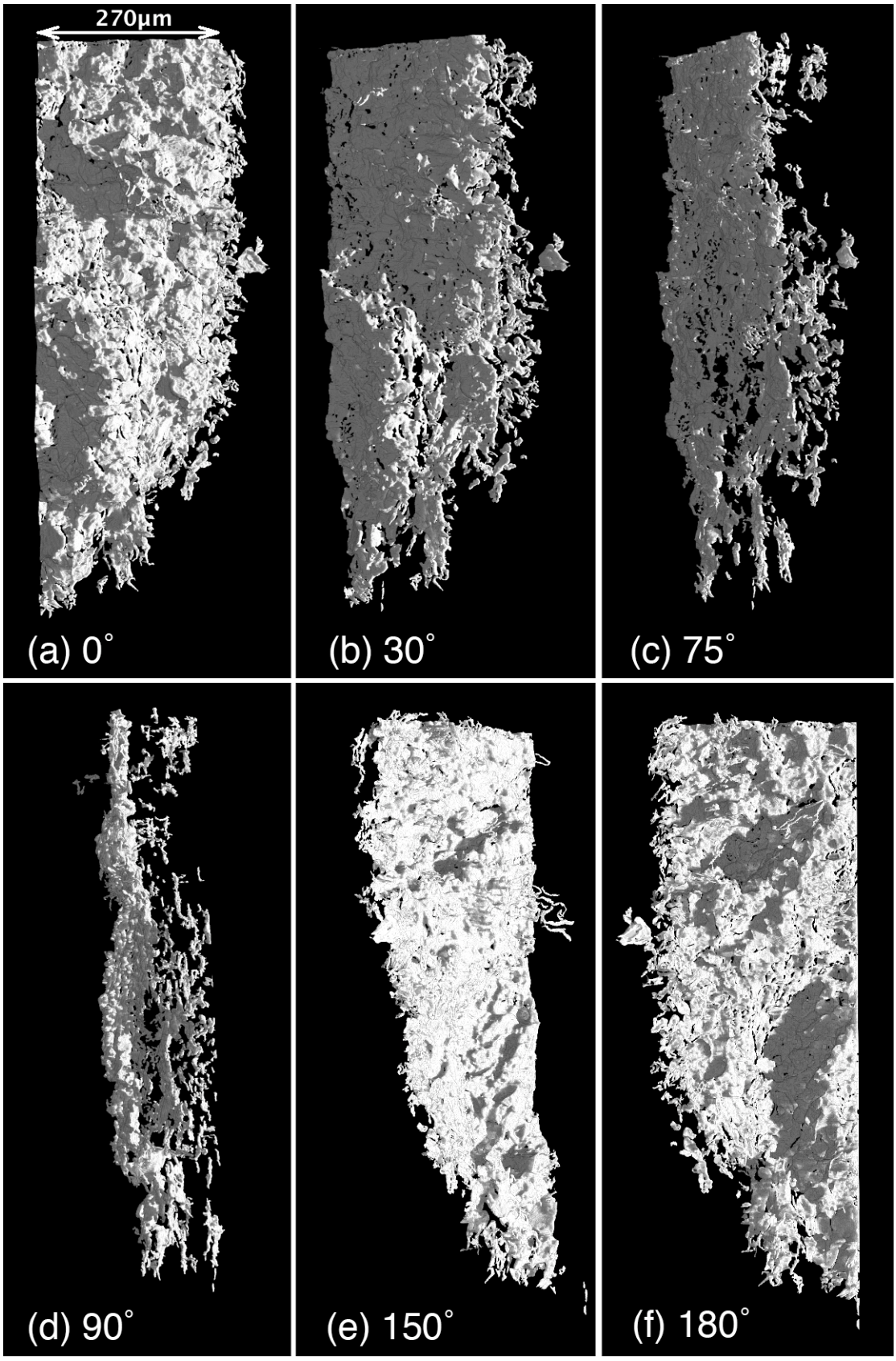

Figure 5-40 X-ray CT image of a crack tip region in LVD26 mod at different angles.

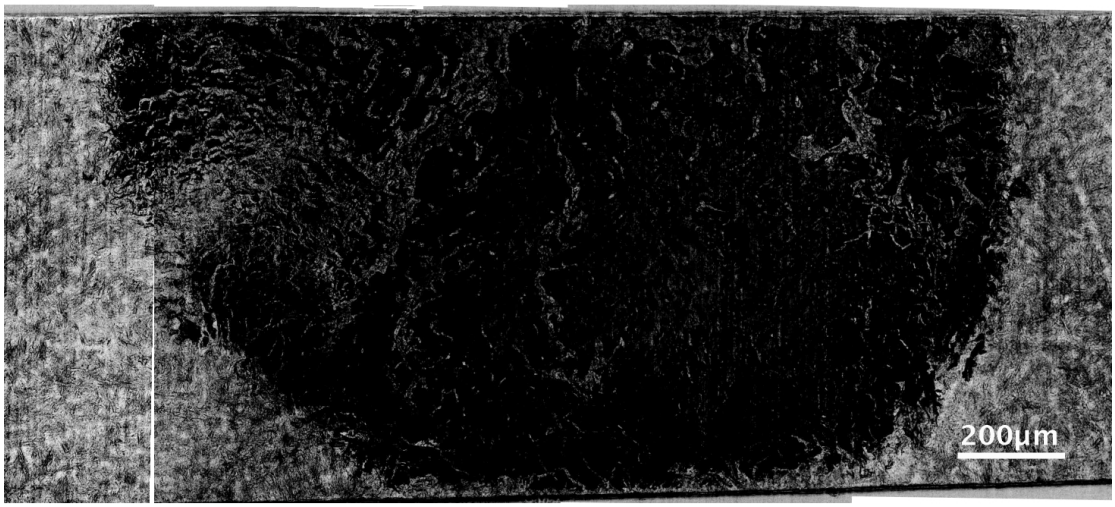

Figure 5-41 2-D projection of the LVD26 mod crack analysed using X-ray CT.

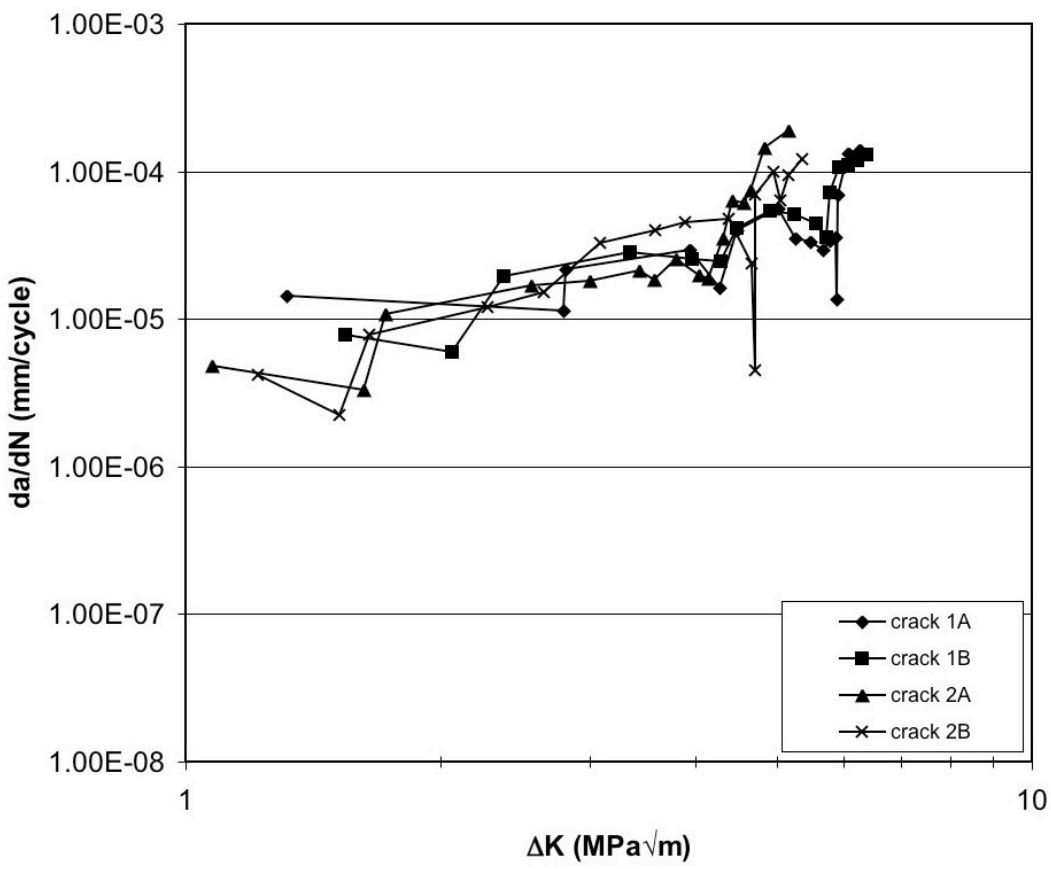

Figure 5-42 Fatigue crack growth data for LVD26 unmod.

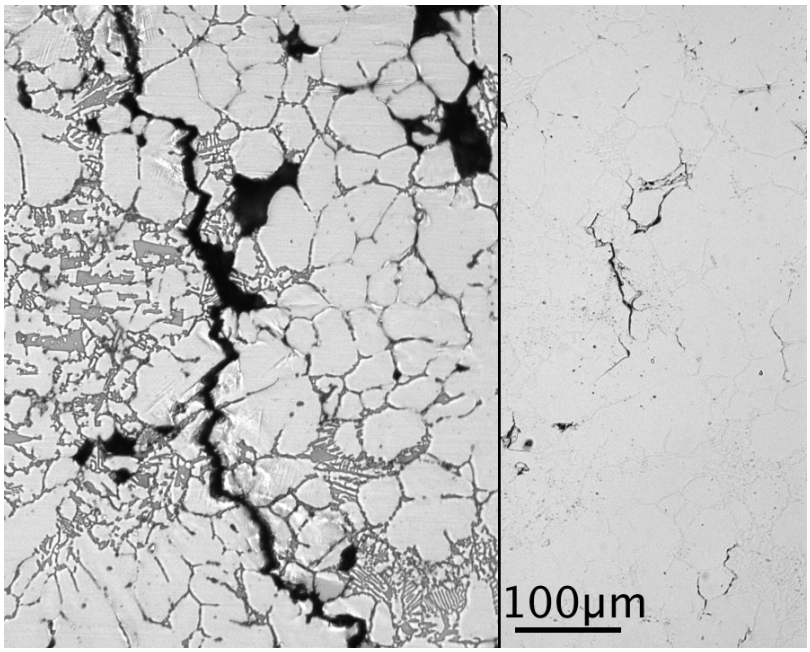

Figure 5-43 First initiation site in LVD27, (a) is the optical micrograph and (b) is the acetate replica showing initiation.

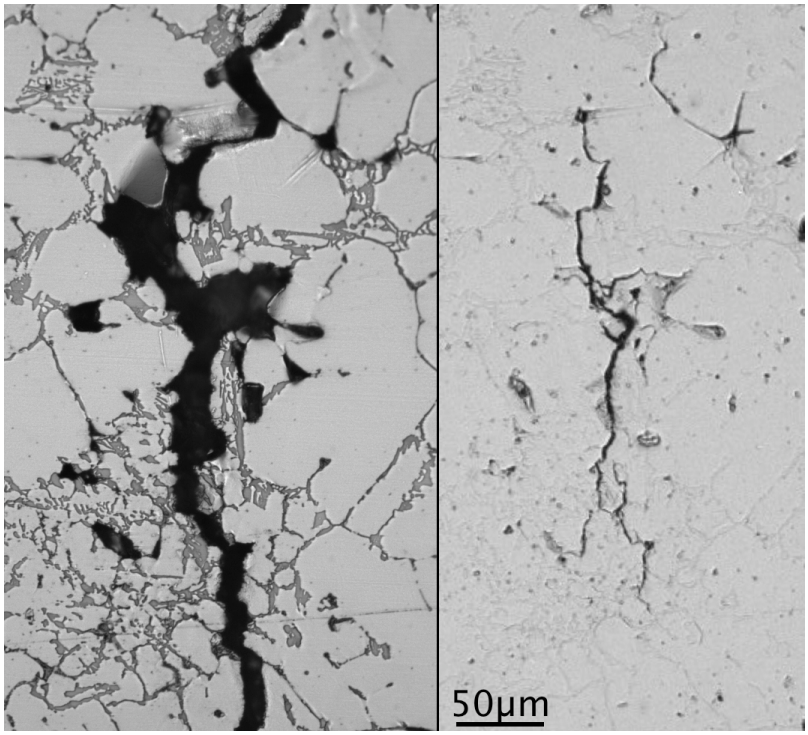

Figure 5-44 Second initiation site in LVD27, (a) is the optical micrograph and (b) is the acetate replica showing initiation.

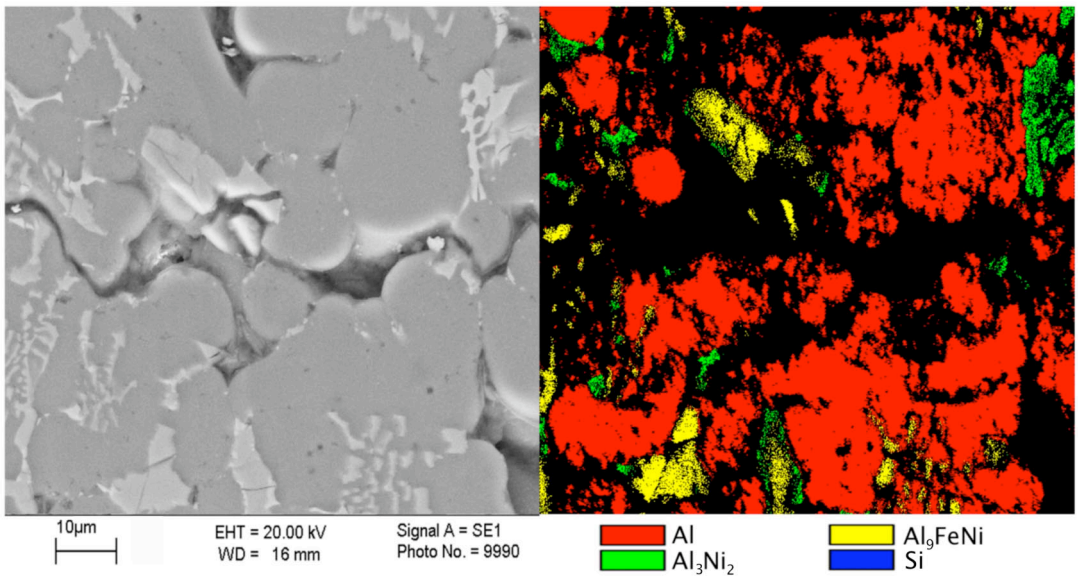

Figure 5-45 Third initiation site in LVD27, (a) is an SEM image and (b) is a phase map.

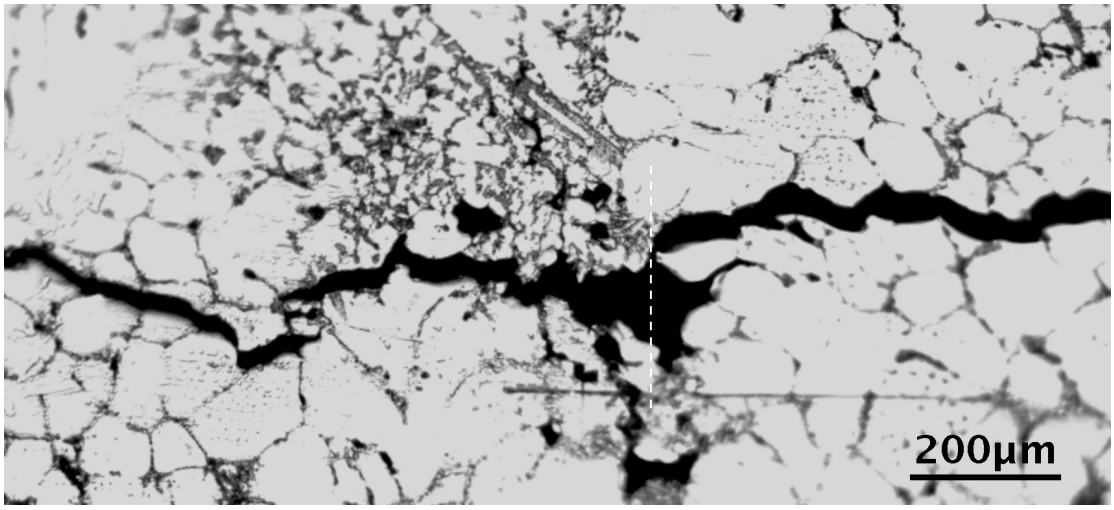

Figure 5-46 Fourth initiation site in LVD27. The white line represents the position of the 'virtual section' in Figure 5-47.

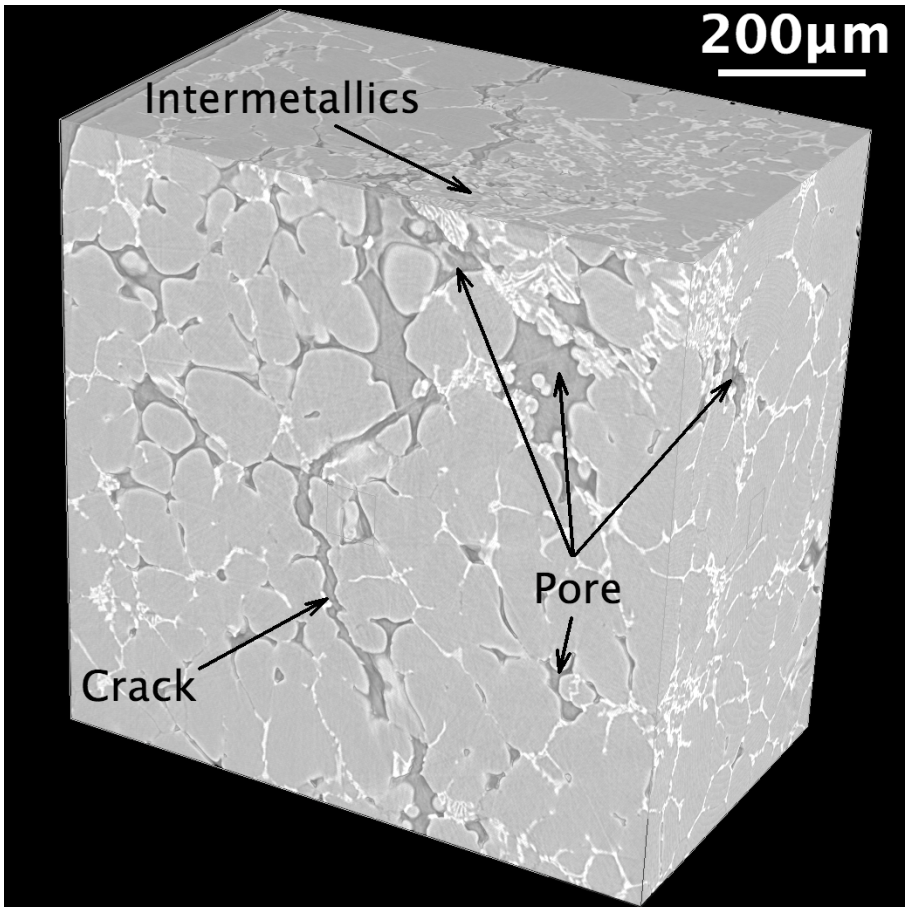

Figure 5-47 X-ray CT section of fourth initiation site in LVD27.

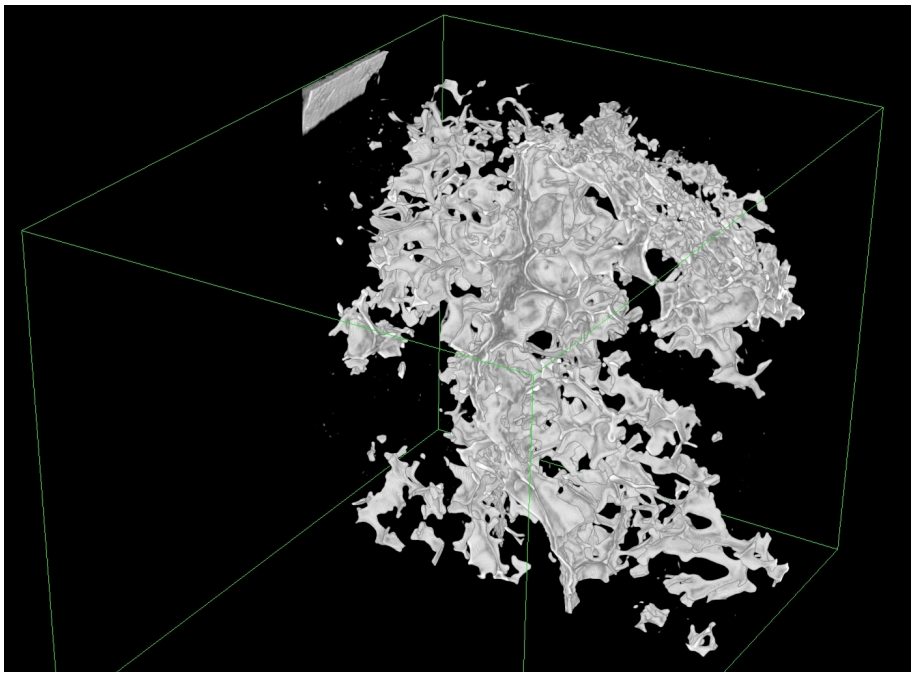

Figure 5-48 Porosity and crack under the fourth initiation site in LVD27.

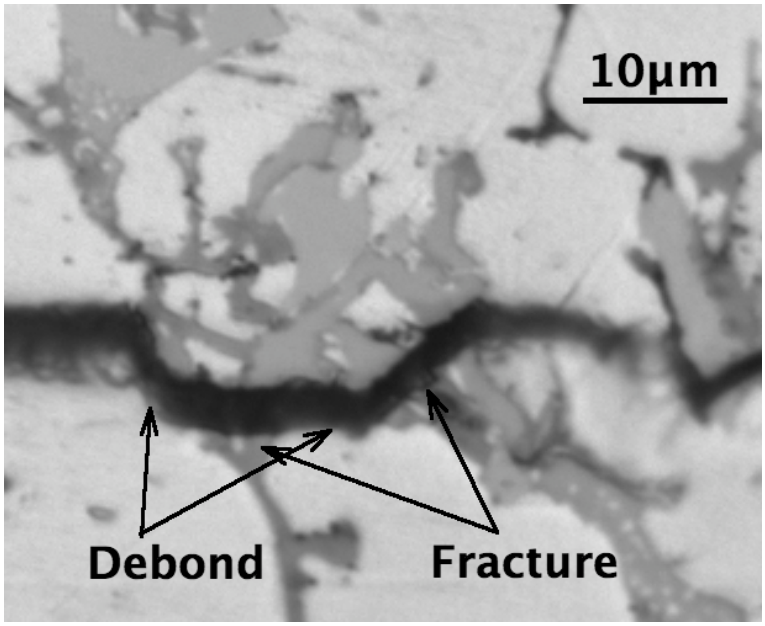

Figure 5-49 Fractured and debonded particle in LVD27.

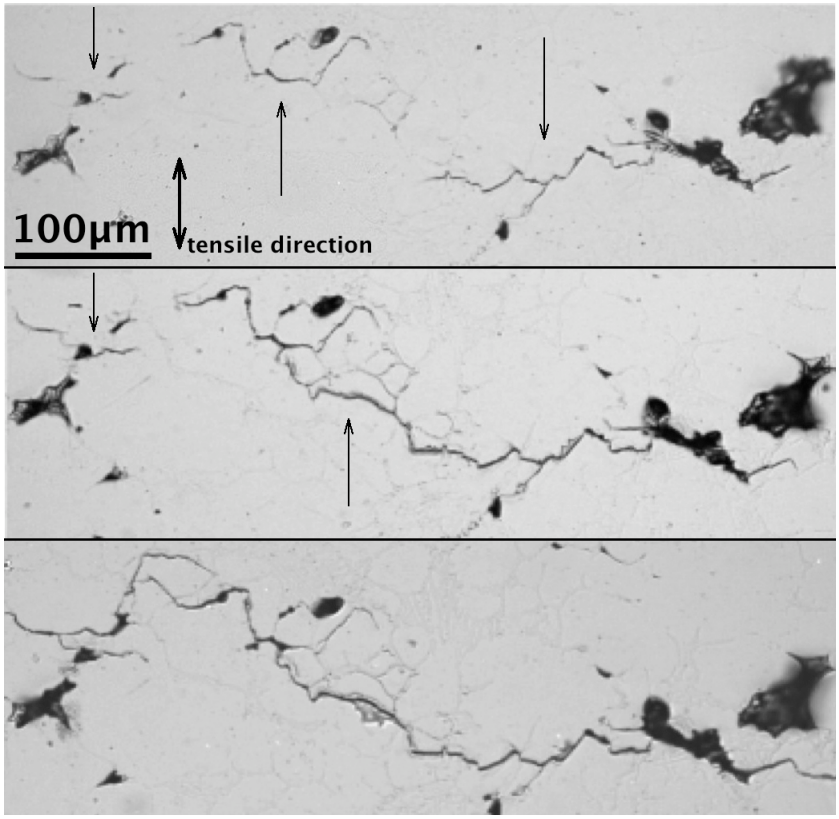

Figure 5-50 Coalescence of cracks in LVD27 (a) 27,000 cycles, (b) 31,000 cycles and (c) 51,000 cycles.

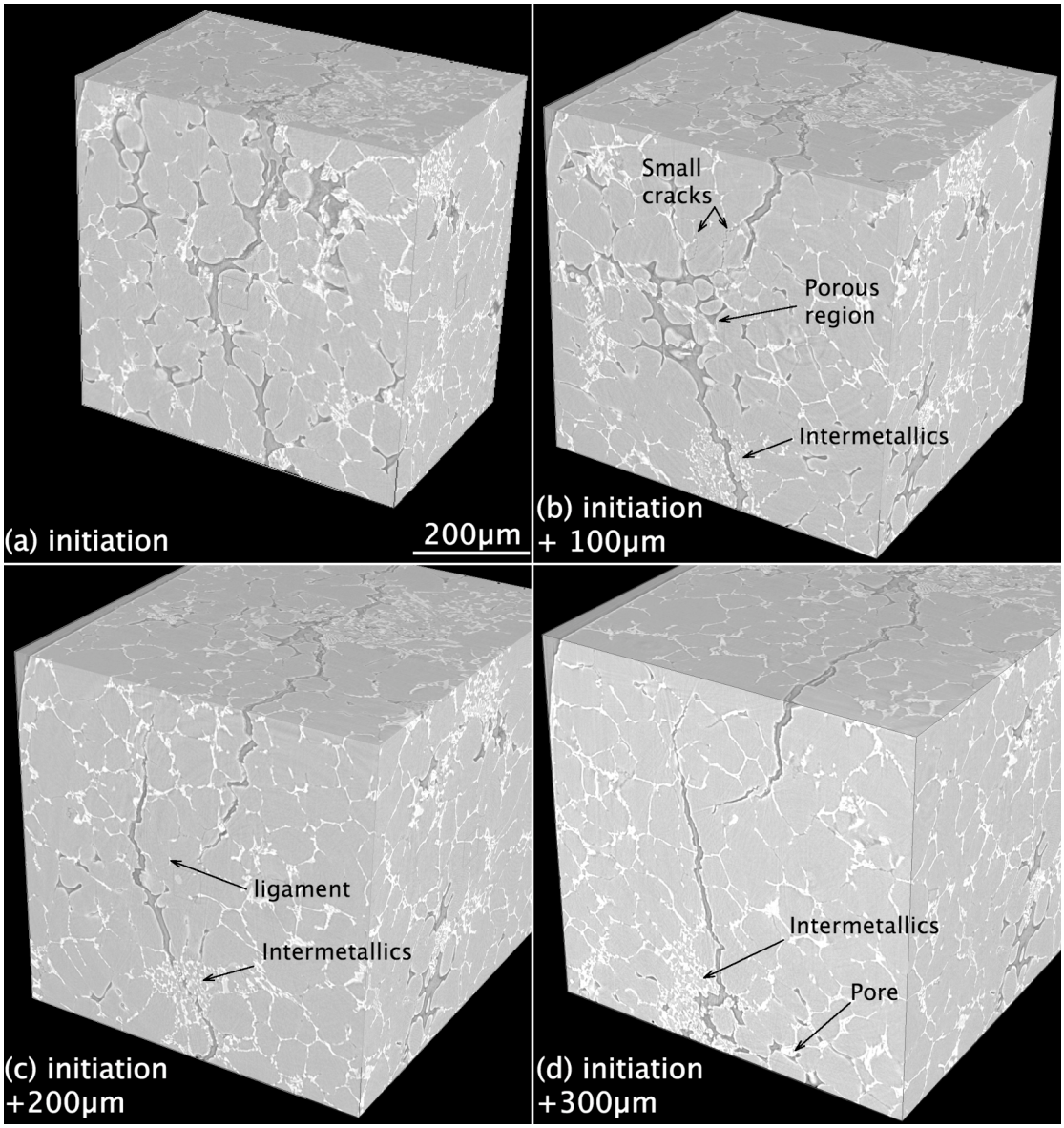

Figure 5-51 X-ray CT sections at different positions along the crack in LVD27, (a) is a section at the initiation site and (b) to (c) are at 100 µm intervals from the section in (a).

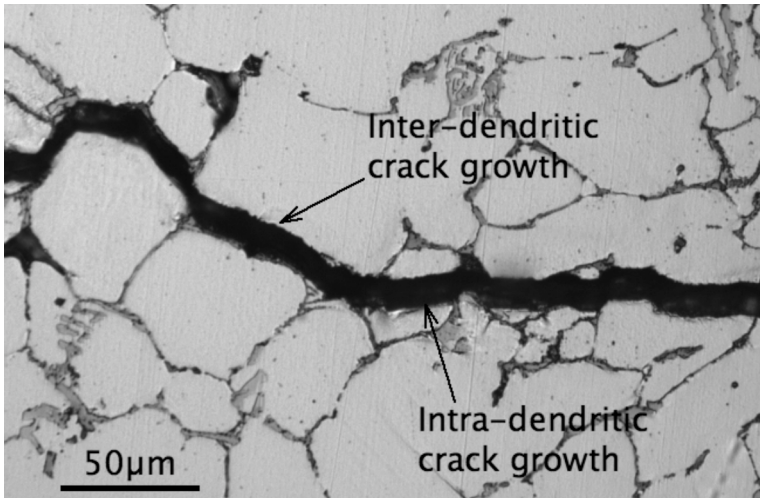

Figure 5-52 Inter and intra-dendritic crack growth in LVD27.

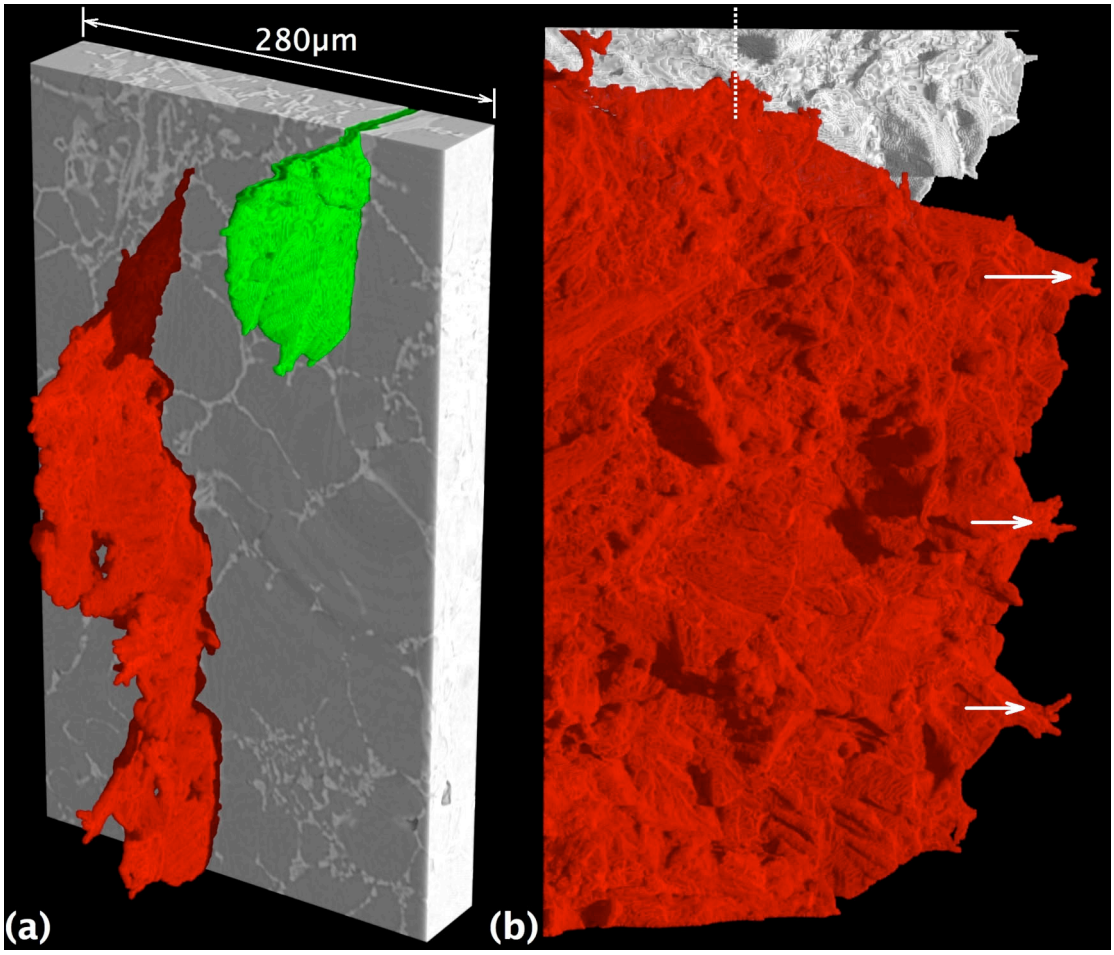

Figure 5-53 X-ray CT images of the first crack tip region in LVD27, (a) the bifurcated cracks are in red and green, (b) is a view parallel to the plane of the crack, the cracks are red and silver in this image.

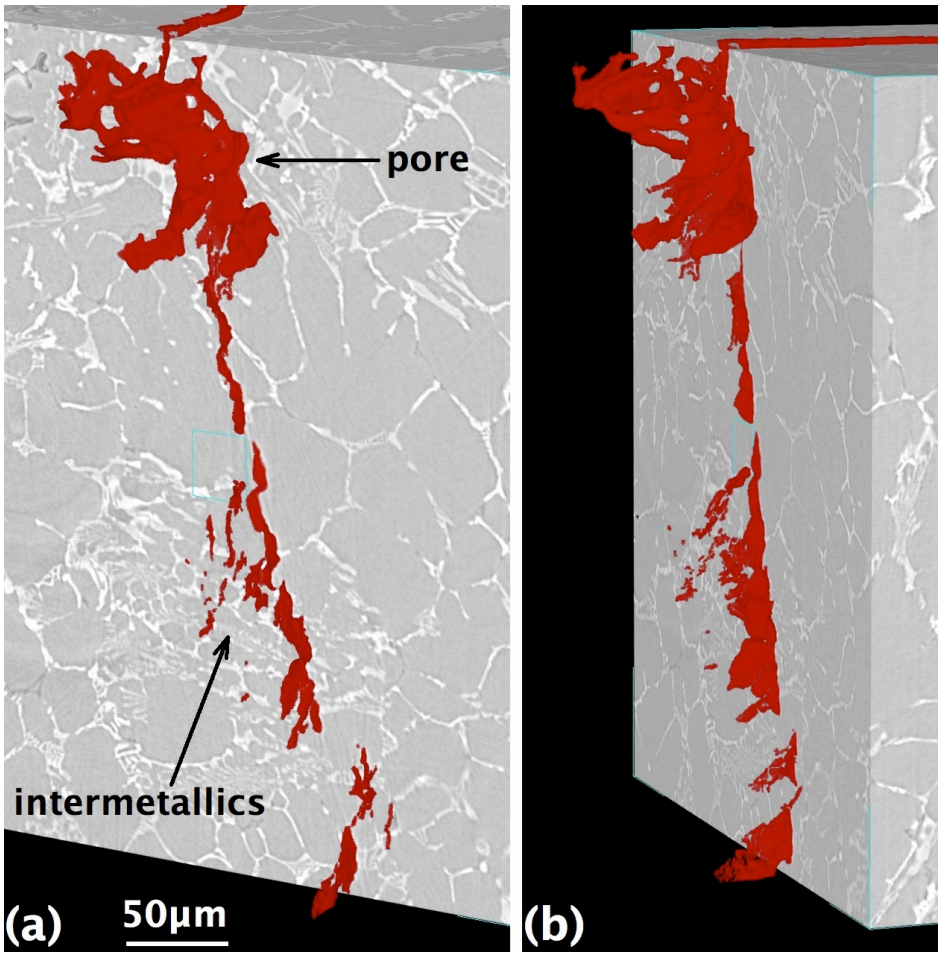

Figure 5-54 X-ray CT images of the second crack tip region in LVD27 (a) and (b) are at different angles.

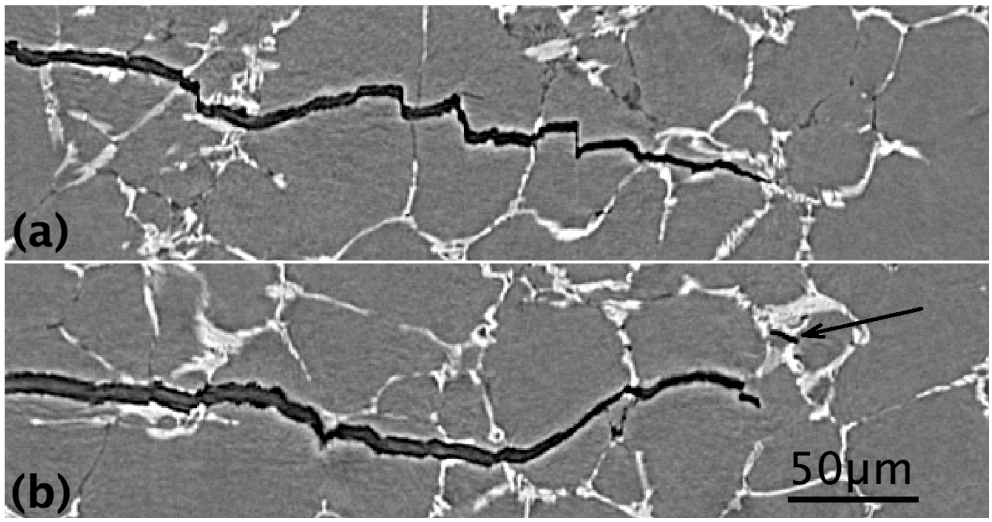

Figure 5-55 X-ray CT sections of the fatigue crack in LVD27 (a) shows a contiguous crack and (b) shows damage ahead of the crack.

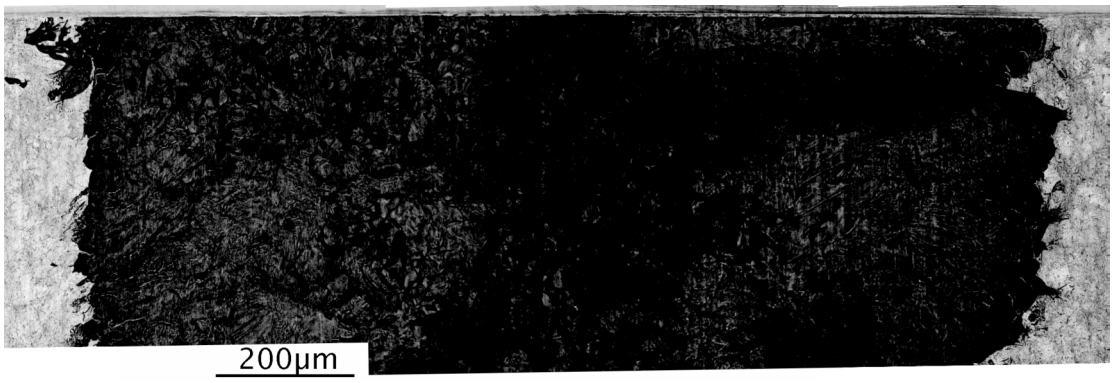

Figure 5-56 2-D projection of the crack in LVD27 from X-ray CT data.

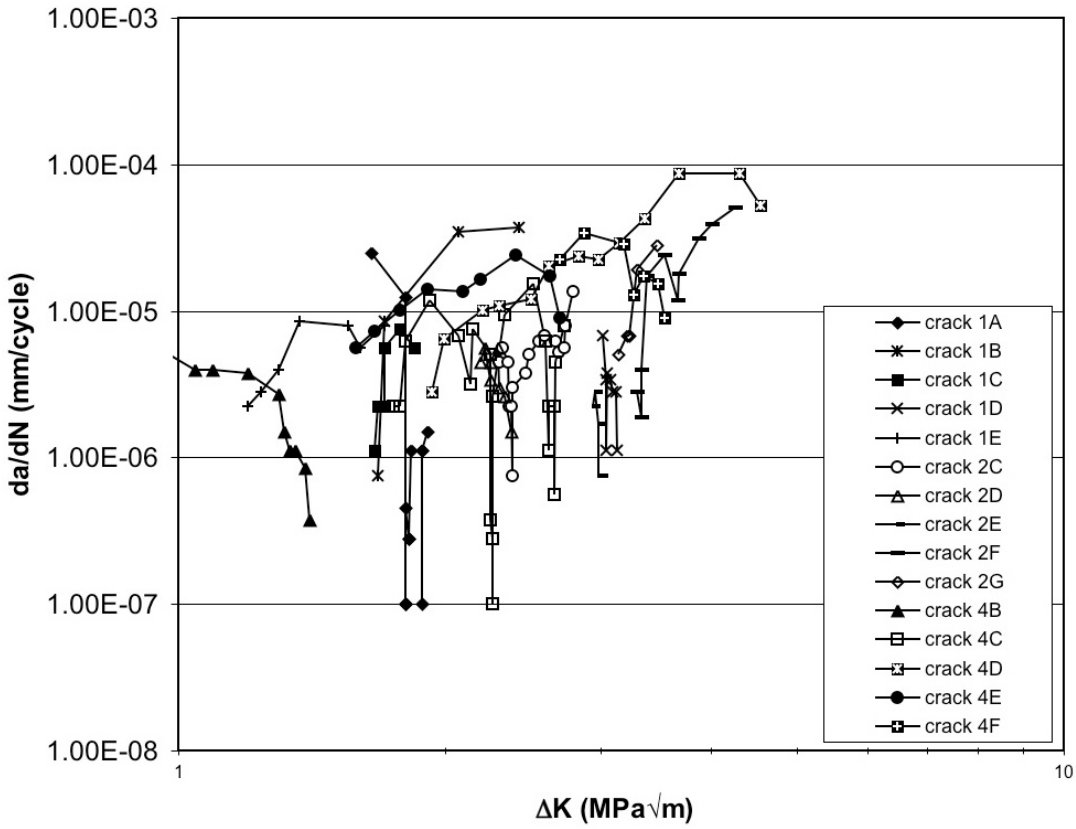

Figure 5-57 Fatigue crack growth data for LVD27.

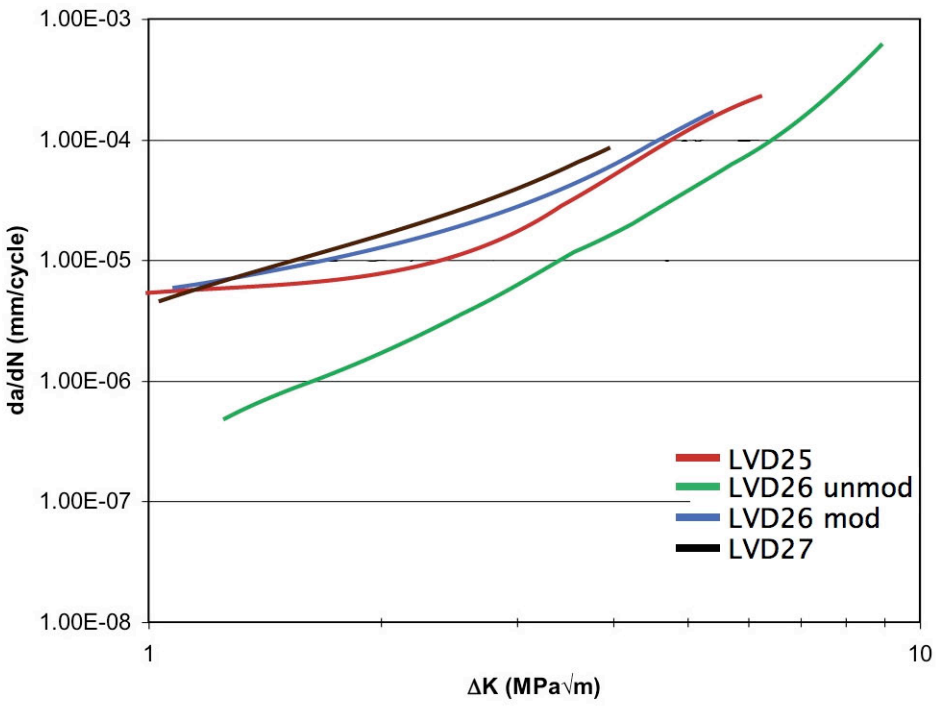

Figure 5-58 The upper bounds of *da/dN* for each alloy plotted as a function of ΔK.

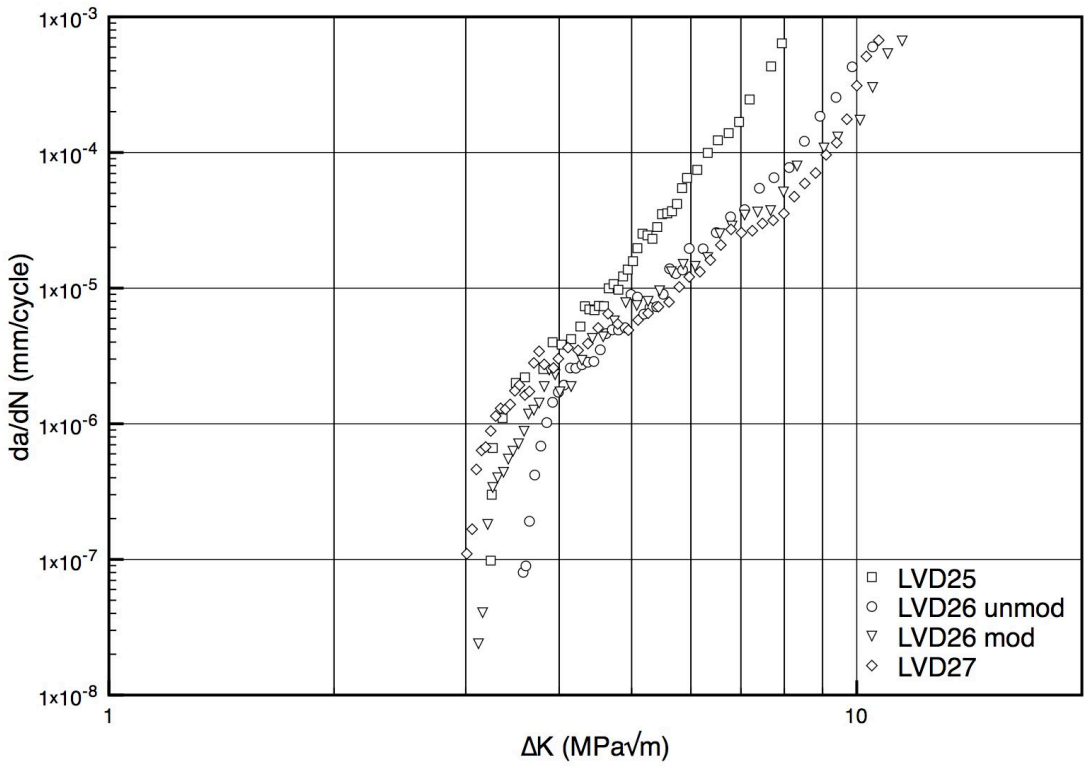

Figure 5-59 Room temperature long fatigue crack growth curves.

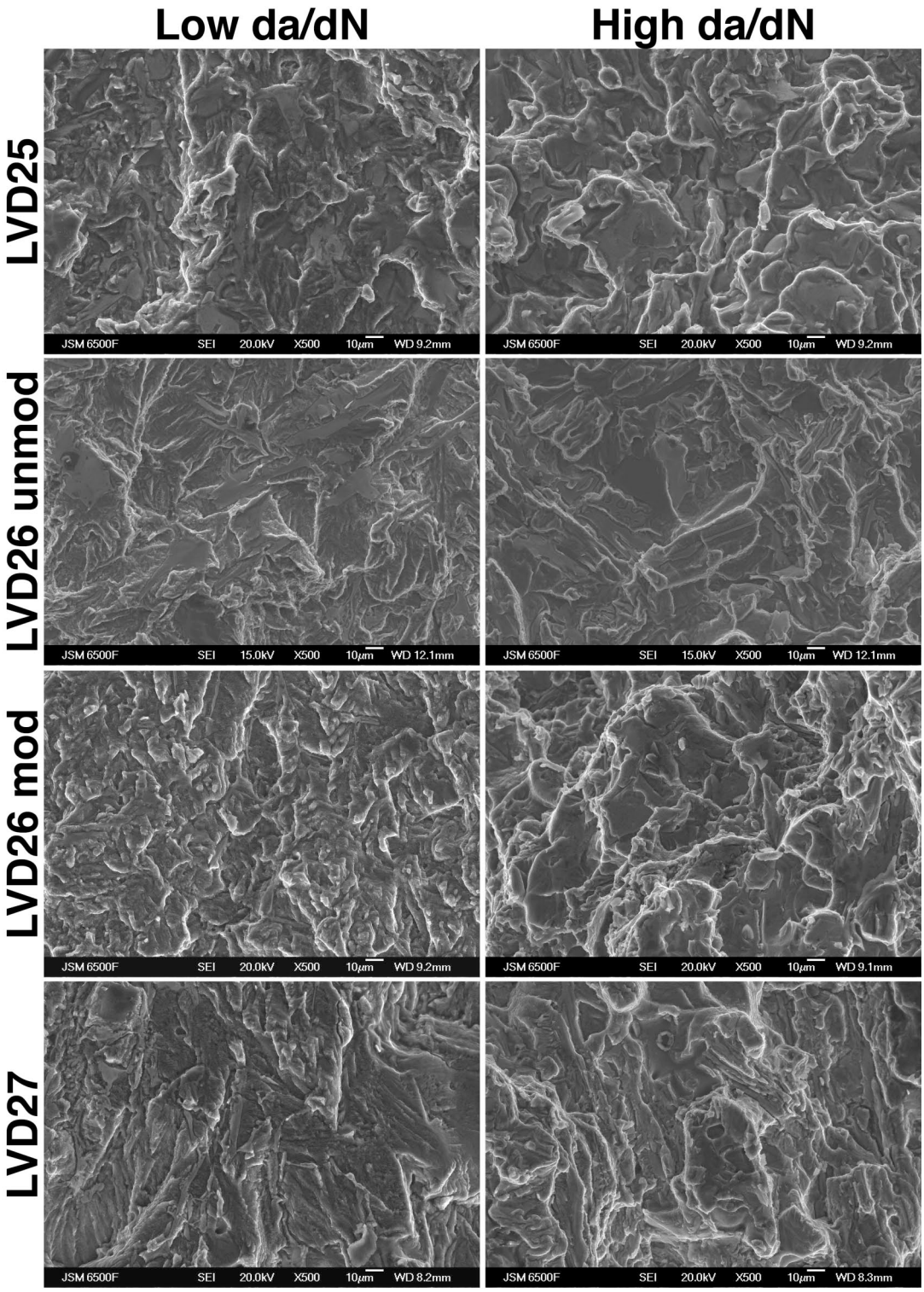

Figure 5-60 SEM fractographs of long fatigue crack growth tests performed at RT, the low *da/dN* is $3x10^{-7}$ mm/cycle and the high *da/dN* is $5x10^{-4}$ mm/cycle.

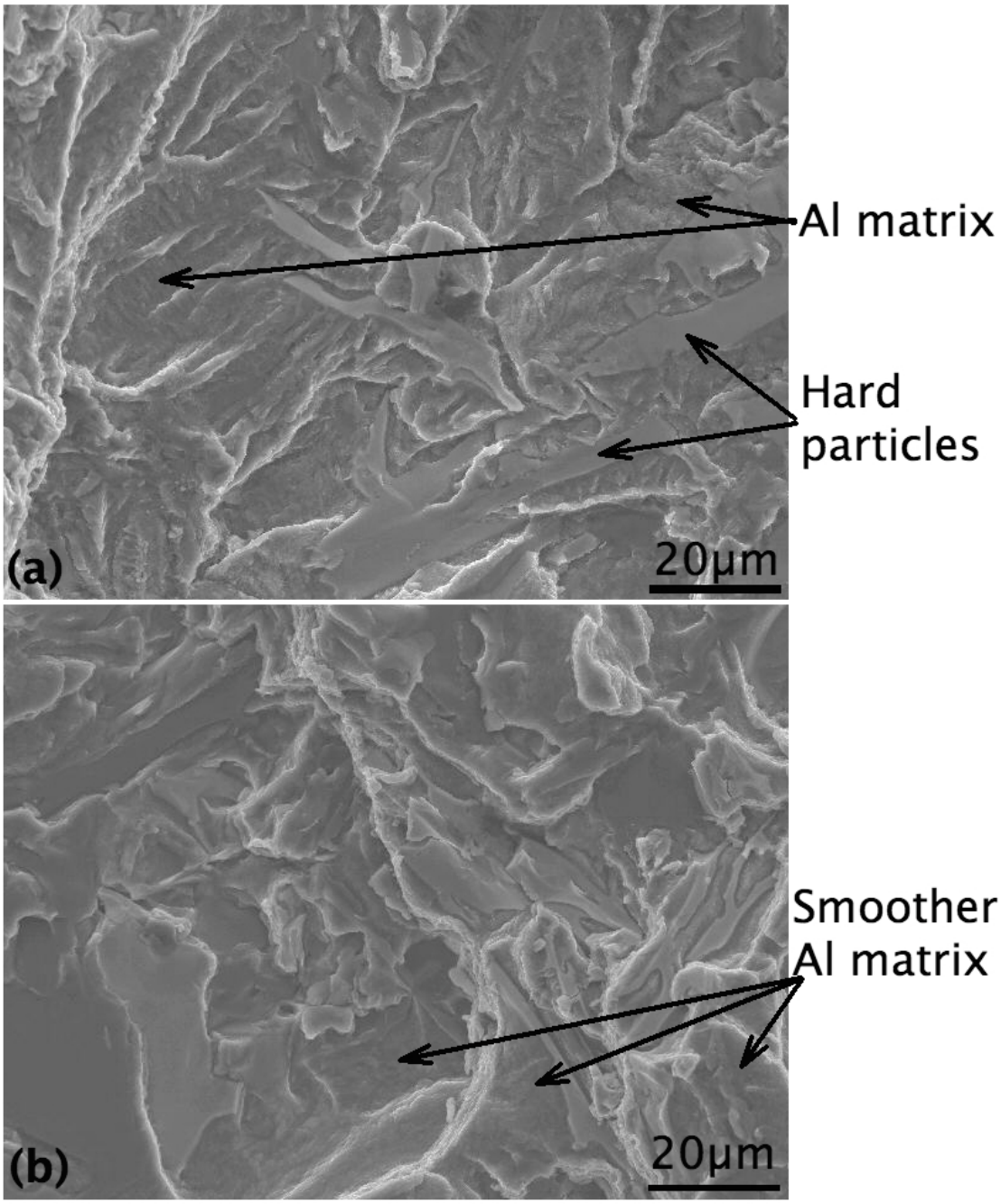

Figure 5-61 SEM fractographs of LVD26 unmod at RT (a) is at low *da/dN* and (b) is at high *da/dN*.

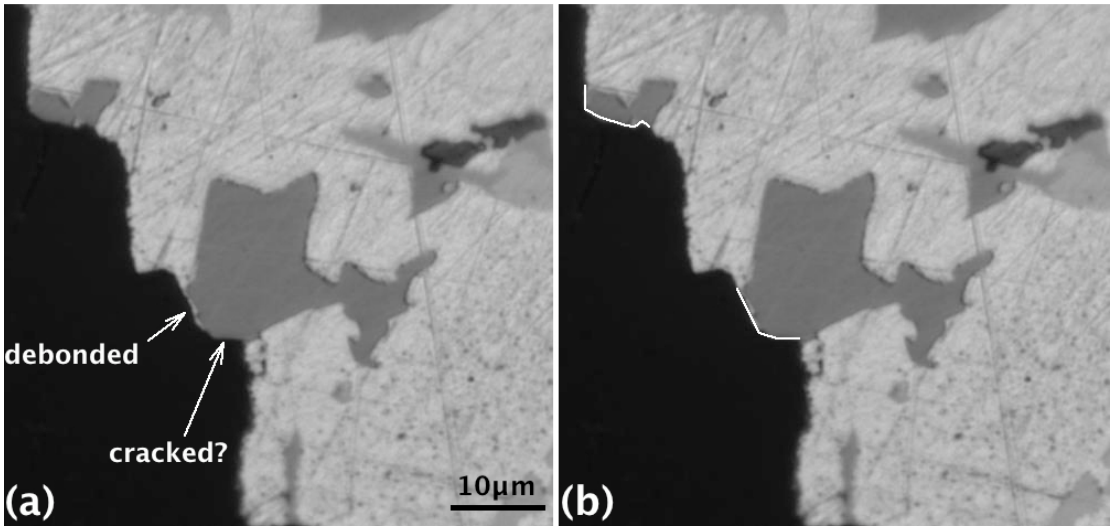

Figure 5-62 (a) Cracked and debonded particles in LVD25, (b) shows where a particle counts as being on the crack profile.

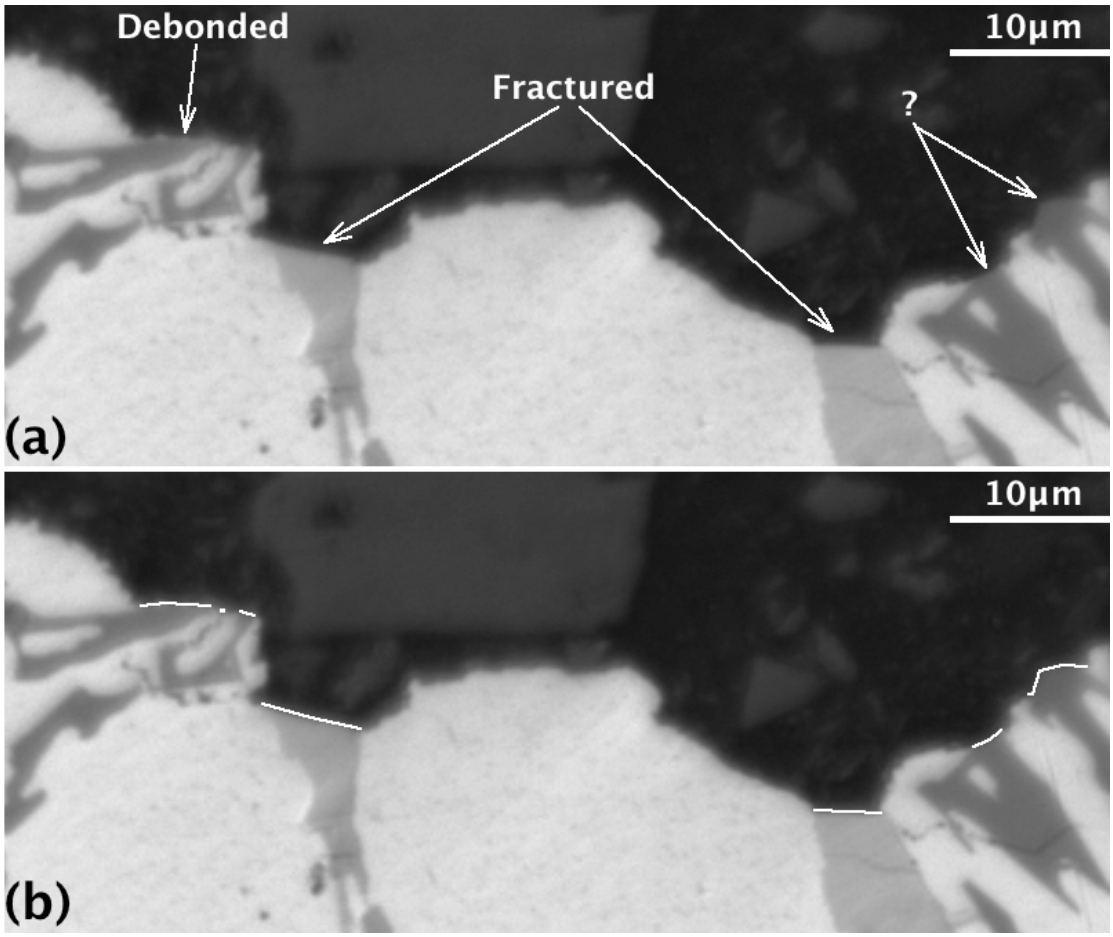

Figure 5-63 (a) Cracked and debonded particles in LVD26 unmod (b) shows where the particles counts as being on the crack profile.

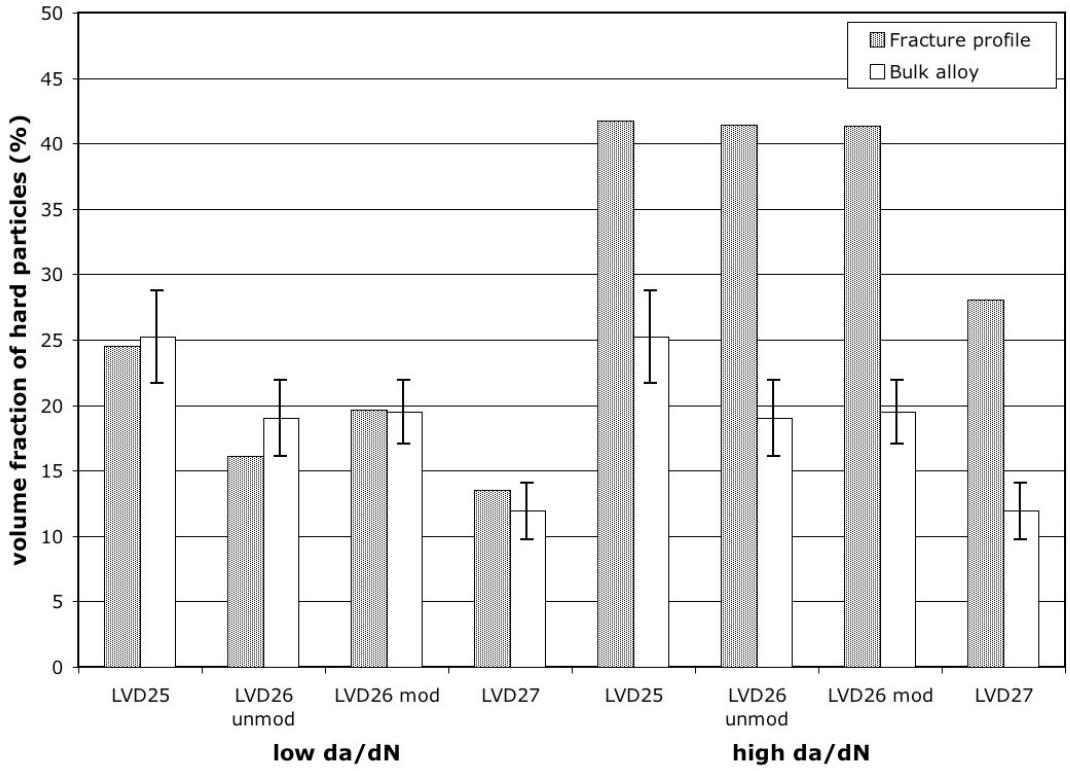

Figure 5-64 L_L of hard particles on the fracture profile at room temperature and the V_f of hard particles in the respective alloys.

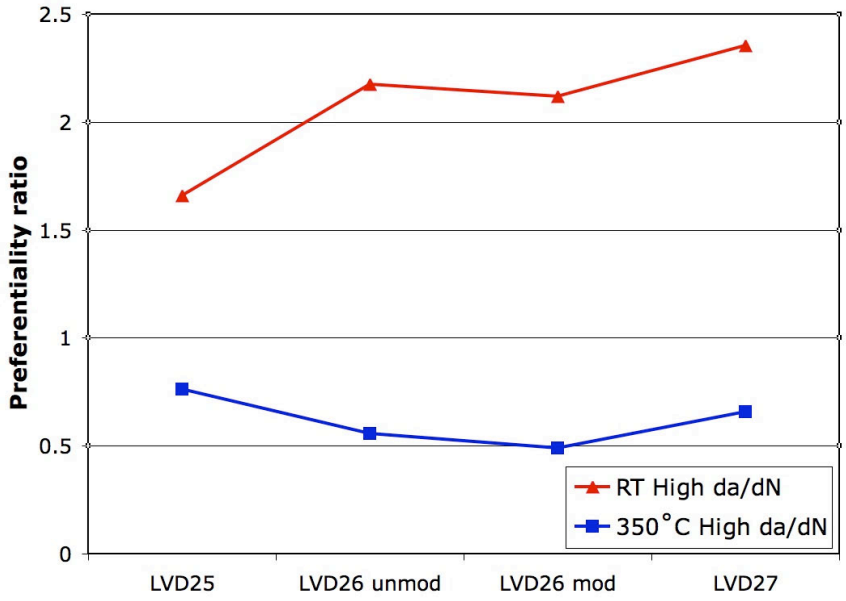

Figure 5-65 Preferentiality ratio at high *da/dN* at RT and 350˚C.

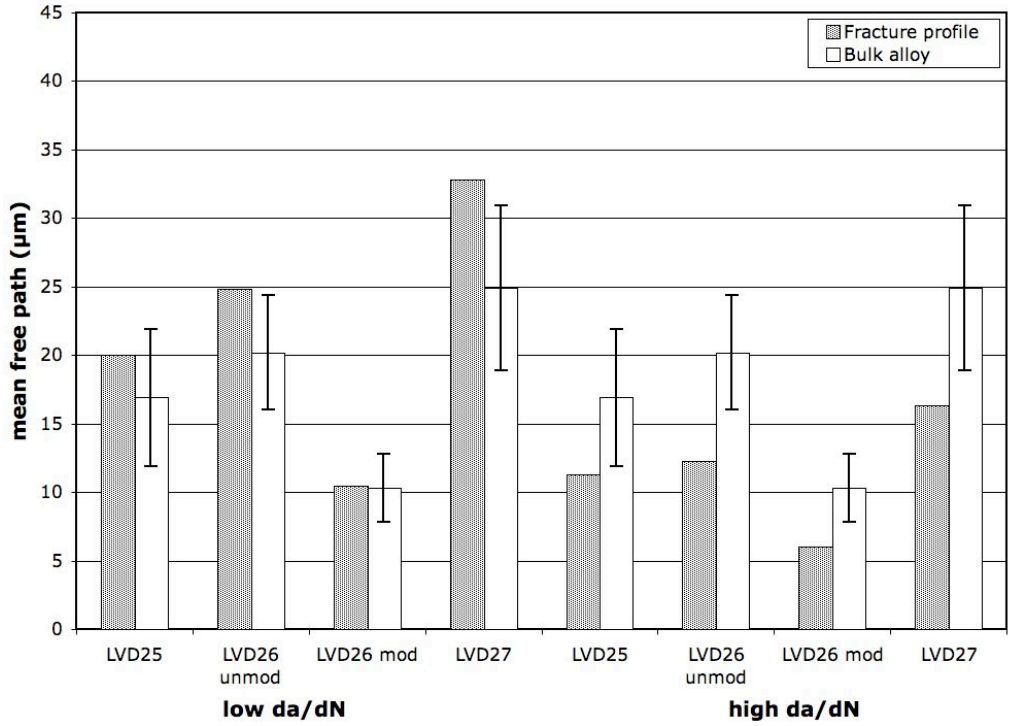

Figure 5-66 Mean free distance (λ) between hard particles on the fracture profile at RT.

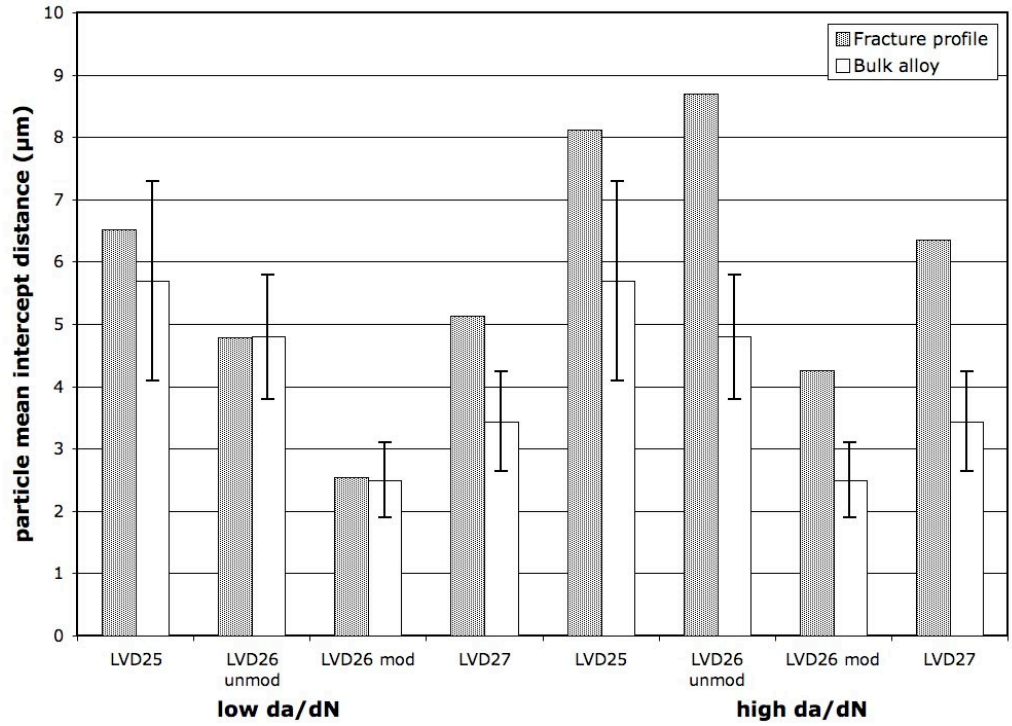

Figure 5-67 Mean particle intercept distance (L_3) on the fracture profiles at RT.

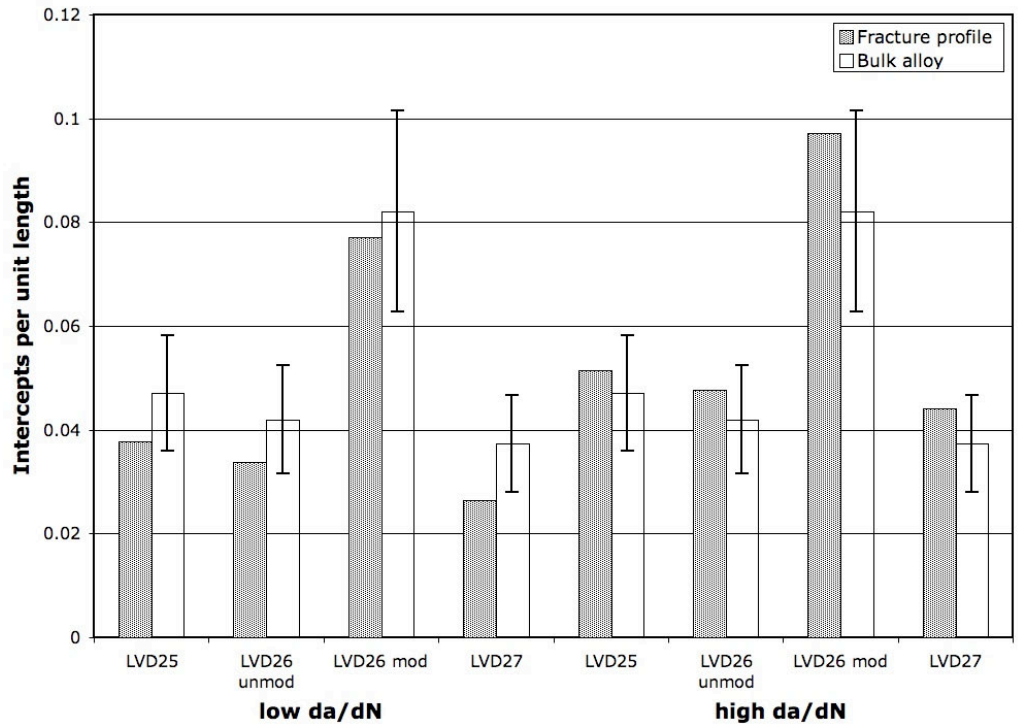

Figure 5-68 Intercepts per unit length (N_L) on the fracture profile at RT.

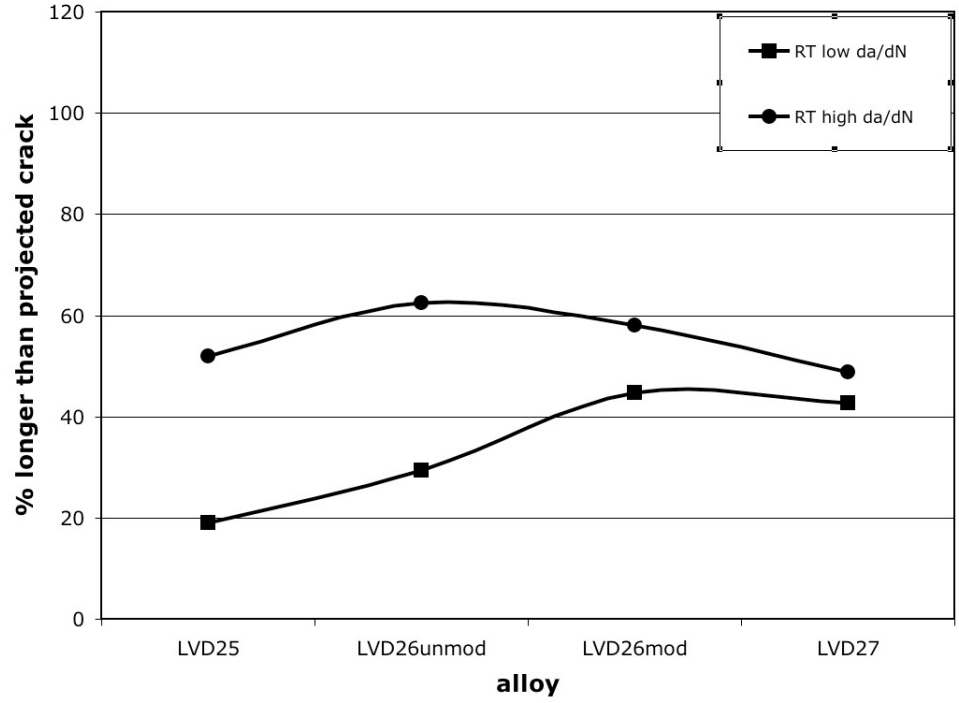

Figure 5-69 Roughness data for the samples test at RT.

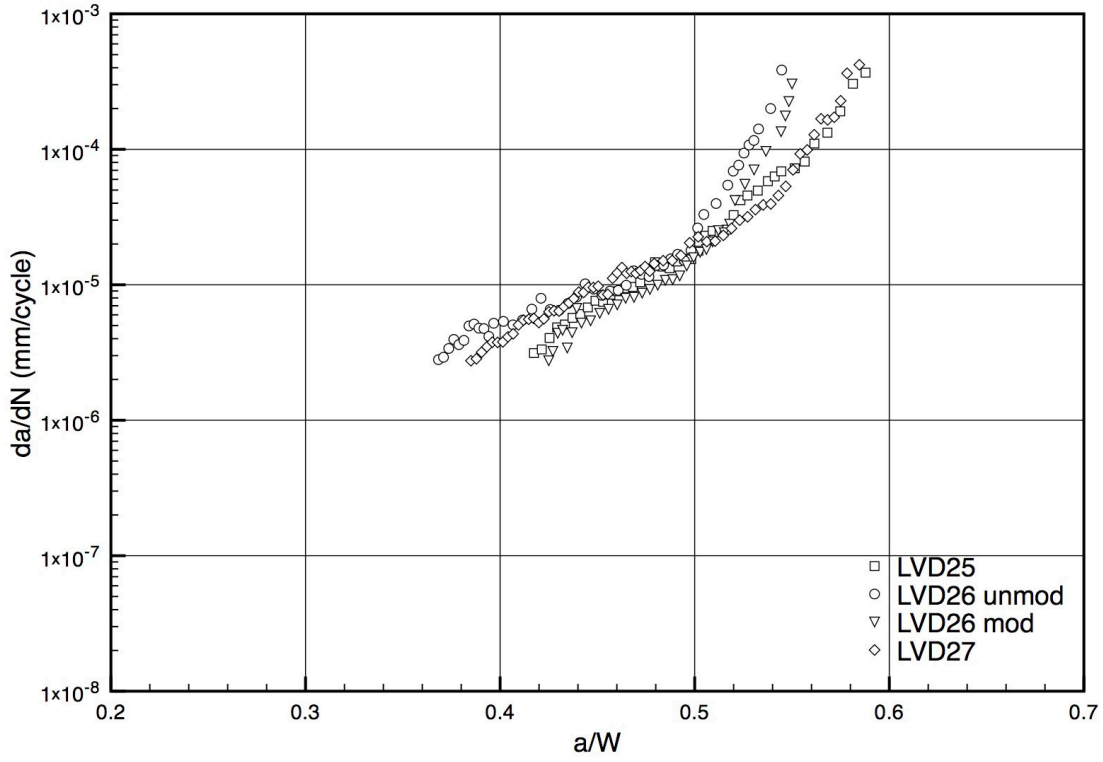

Figure 5-70 350˚C long fatigue crack growth curves.

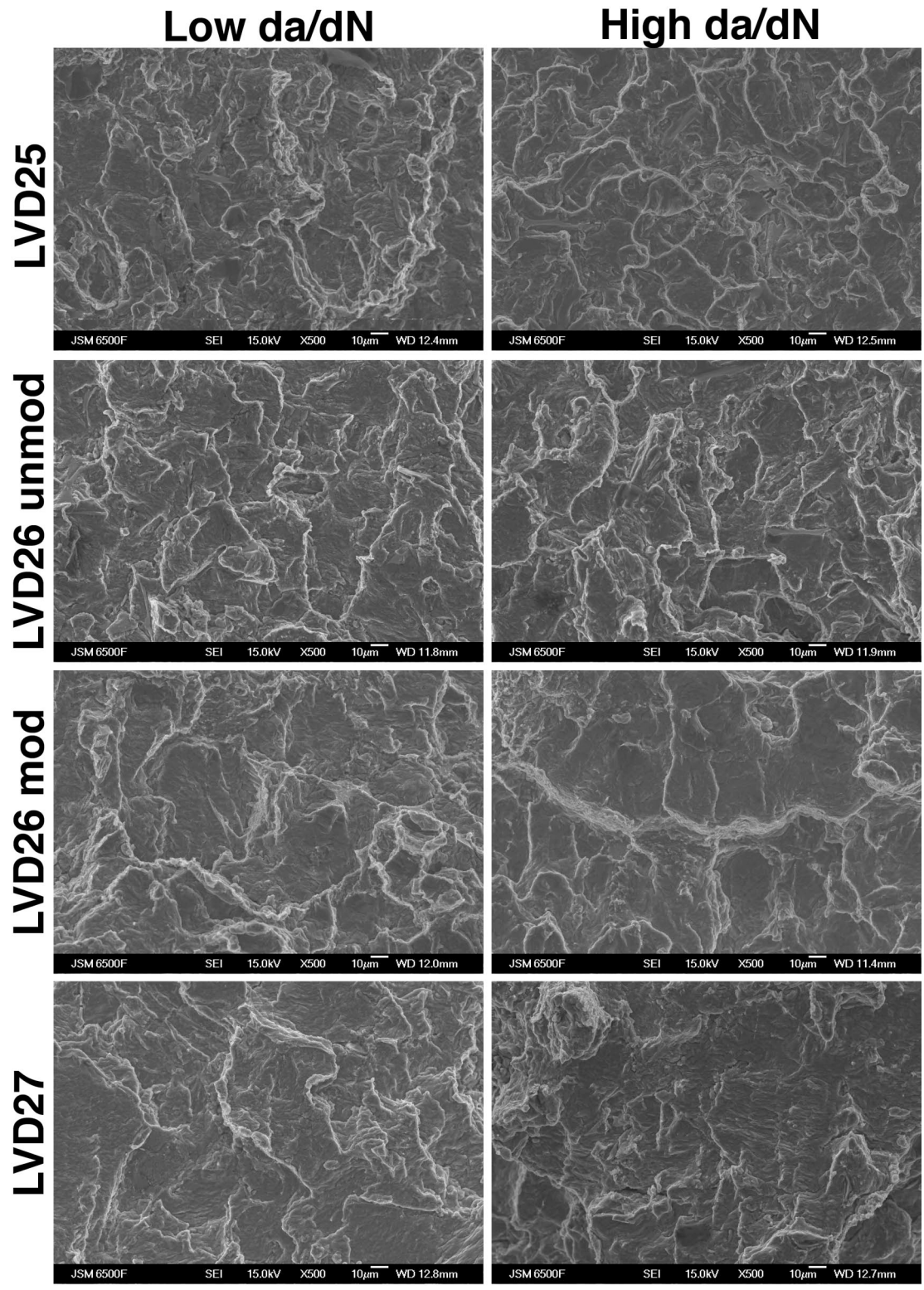

Figure 5-71 SEM fractographs from the 350˚C samples, the low *da/dN* is $3x10^{-6}$ mm/cycle and the high *da/dN* is $3x10^{-4}$ mm/cycle.

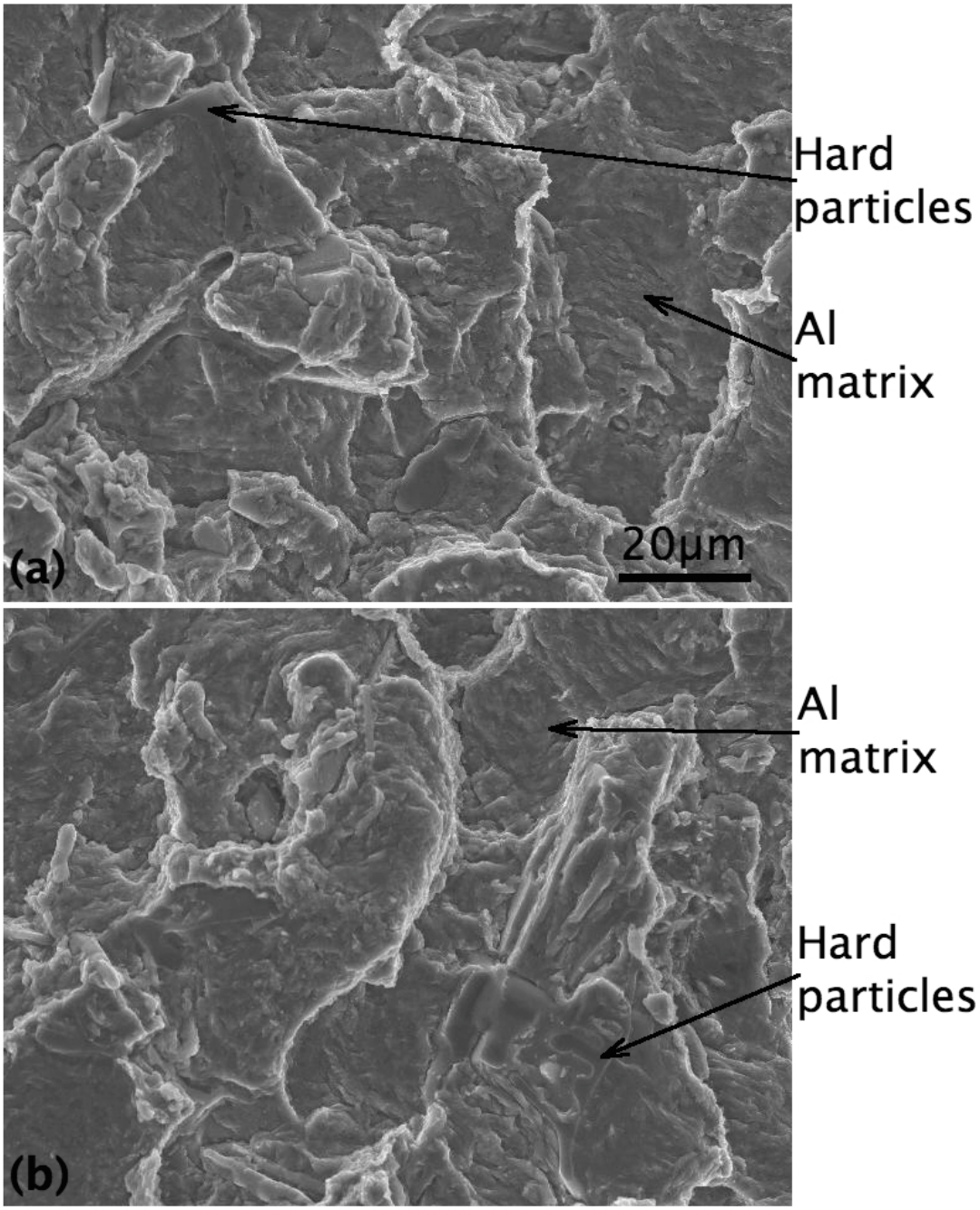

Figure 5-72 SEM fractographs of LVD26 unmod at 350°C (a) is at low *da/dN* and (b) is at high *da/dN*.

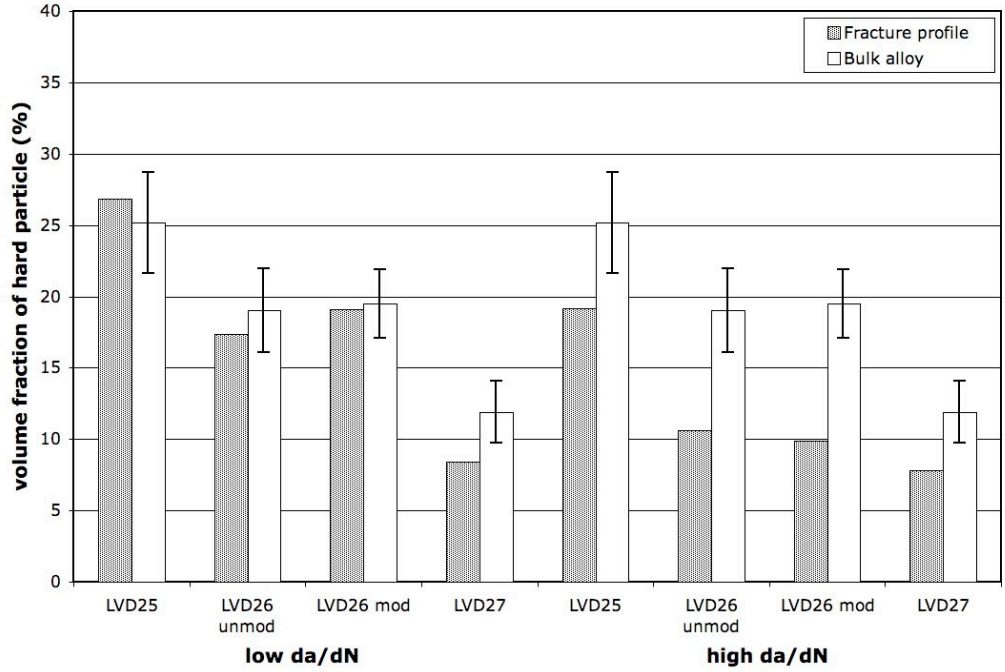

Figure 5-73 L_L of hard particles on the fracture profile at 350˚C and the V_f of hard particles in the respective alloys.

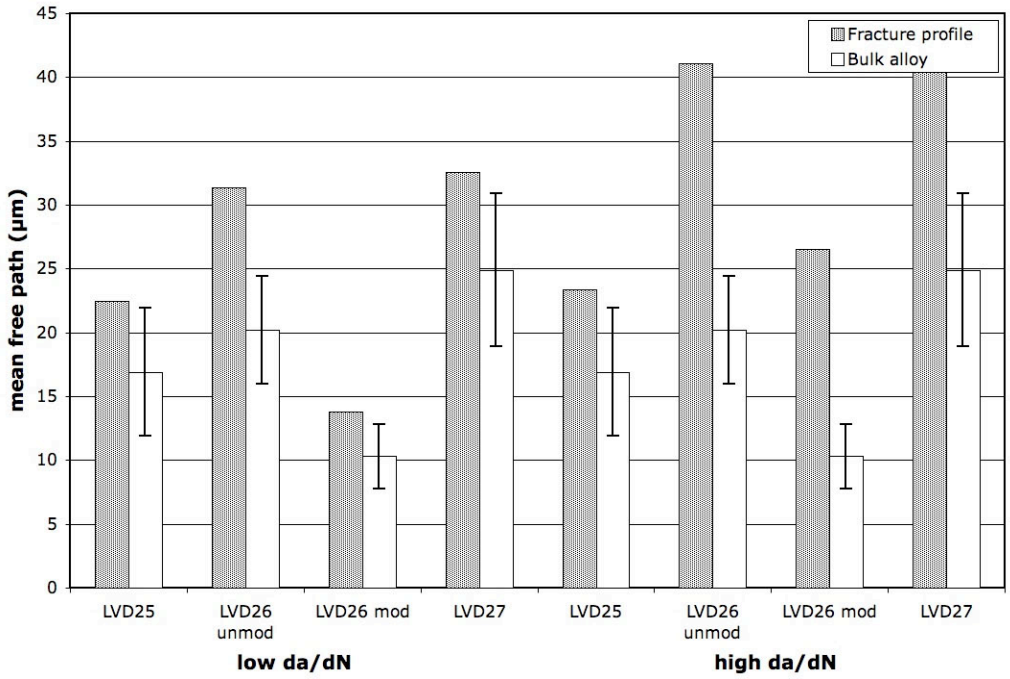

Figure 5-74 Mean free distance (λ) between hard particles on the fracture profile at 350˚C.

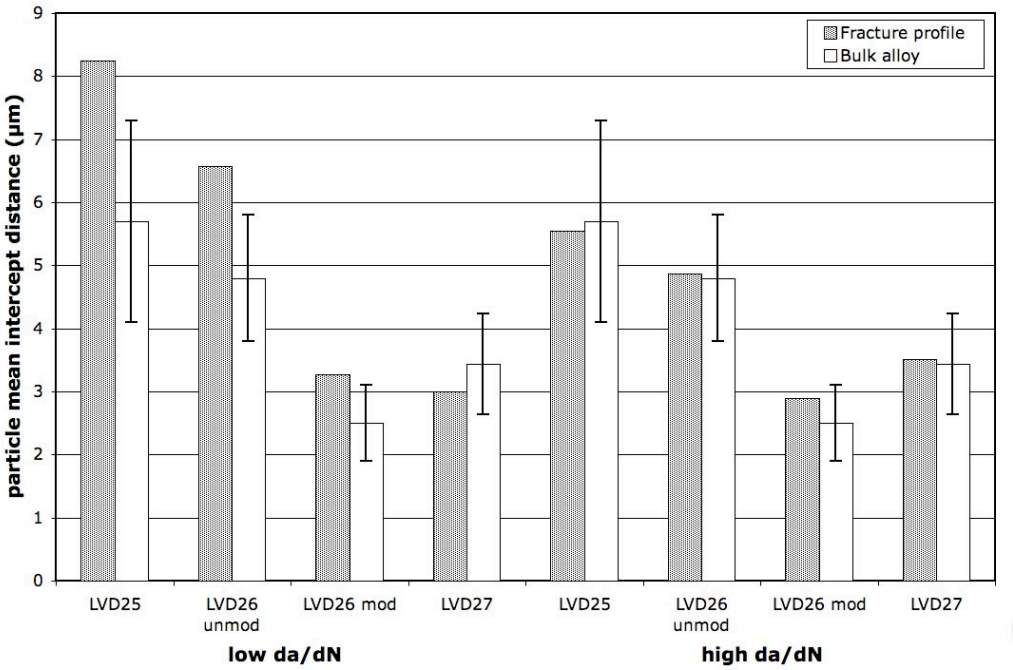

Figure 5-75 Mean particle intercept distance (L_3) on the fracture profiles at 350˚C.

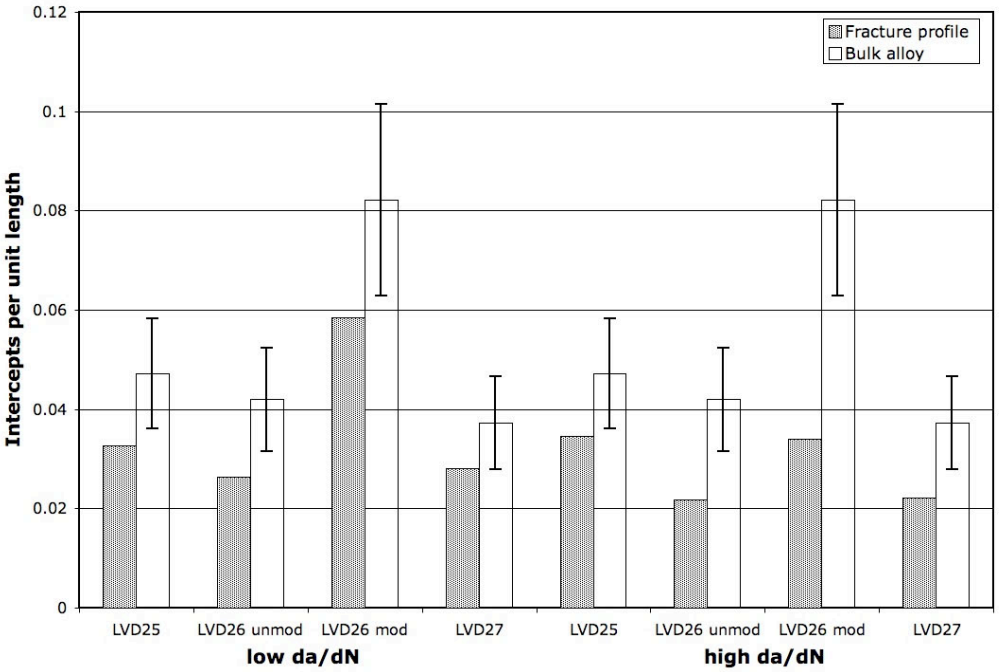

Figure 5-76 Intercepts per unit length (N_L) on the fracture profile at 350˚C.

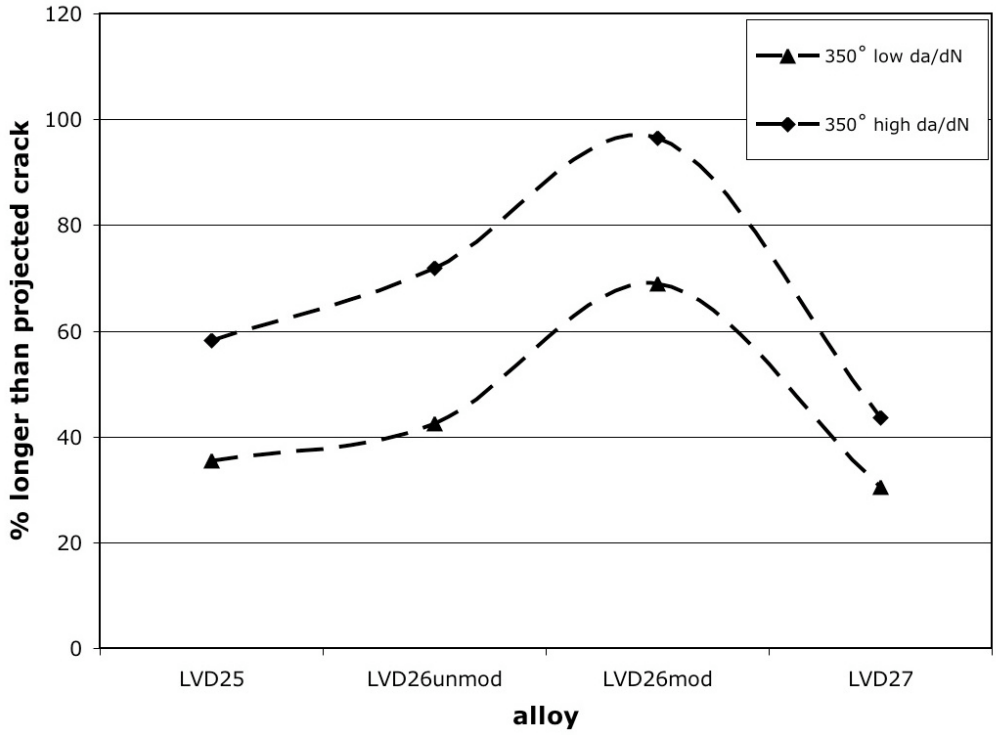

Figure 5-77 Roughness data for the samples test at 350°C.

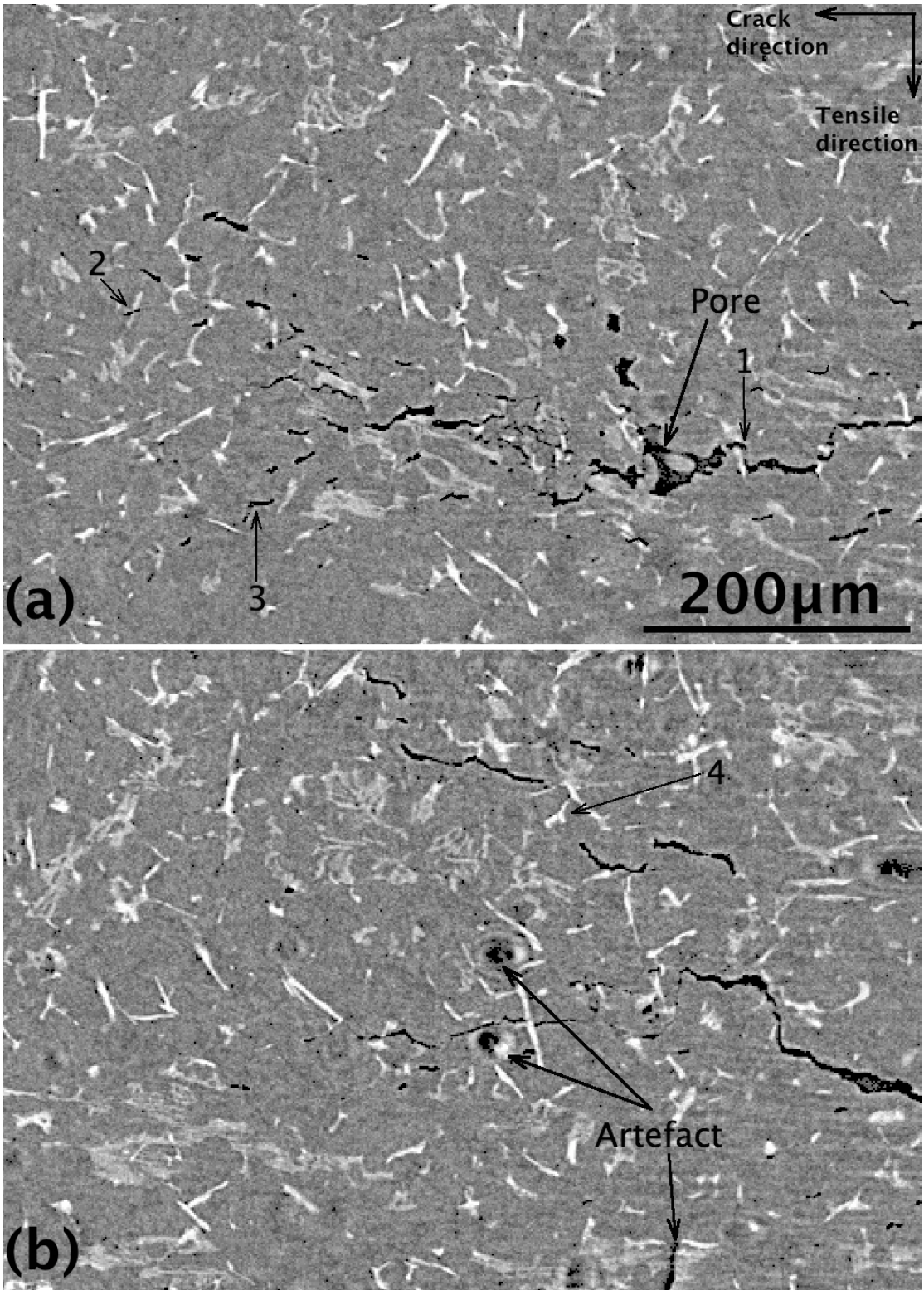

Figure 5-78 X-ray CT image of the crack at low *da/dN* in LVD25 from a side view (a) and (b) are at different positions along the crack

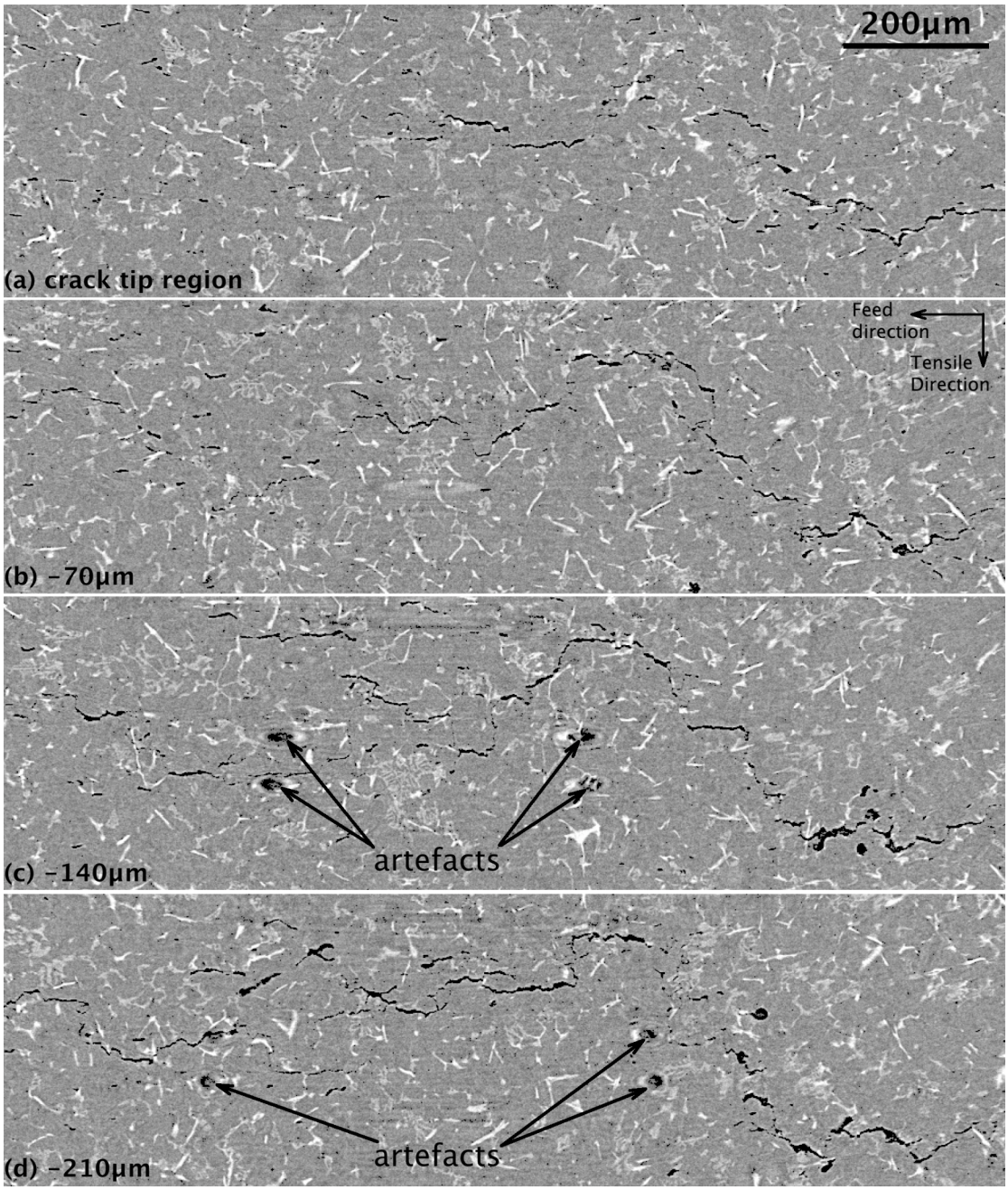

Figure 5-79 X-ray CT image of the crack at low *da/dN* in LVD25 from a front view, (a) is at position in the crack tip region, and (b) to (d) are at 70 µm intervals behind (a).

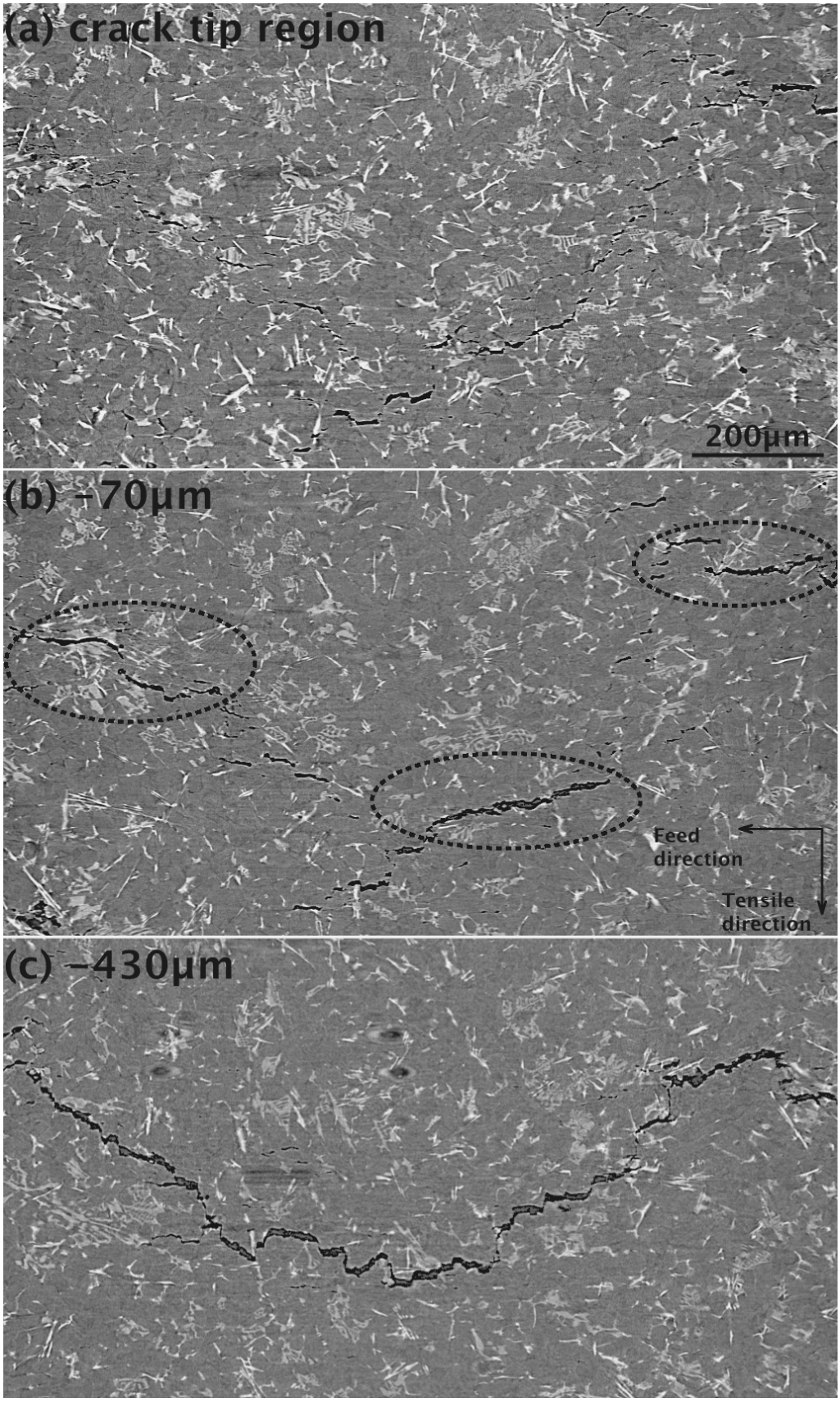

Figure 5-80 X-ray CT image of the crack at high *da/dN* in LVD25 from a front view, (a) is at position in the crack tip region, and (b) and (c) are at intervals behind (a).

Chapter 6

Discussion

6.1 Introduction

All stages of fatigue life have been investigated in this study. The microstructures were thoroughly characterised in order to link the micromechanisms of fatigue to the different microstructural features. Pores, Si particles and intermetallic particles were all shown to cause fatigue crack initiation and play an important role in the subsequent propagation behaviour. This chapter naturally divides into two sections: one on fatigue crack initiation and the other on fatigue crack propagation.

6.2 Fatigue crack initiation

Fatigue crack initiation was observed to occur at:

1) failed (debonded and fractured) particles,

2) pores, and

3) stress concentrations at the sample edge.

In this project the first two causes of initiation are of particular interest; the third cause, failure from sample corners, is of importance to design engineers but their propensity to cause fatigue crack initiation can be mitigated by careful design and manufacture and is not an inherent property of the materials. In all alloys, except LVD27, the three causes of fatigue crack initiation were observed. However, in LVD27 porosity was the principal cause of initiation in all cases.

6.2.1 Effect of porosity

The X-ray CT data showed that LVD27 contained the highest V_f of pores and contained the largest pore (in terms of the maximum pore dimension). X-ray CT analysis of an initiation site in LVD27 showed that a large pore (>300 μm) was at the initiation site and was the cause of fatigue crack initiation; the pore exhibited a highly complex shape and was likely to have formed as a result of shrinkage during the casting process. Large shrinkage pores (>100 μm) were also observed in all the other alloys, and in both the LVD26 alloys were seen to cause fatigue crack initiation. This is consistent with the work of Zhang *et al.* (1999) who demonstrated that when SDAS was between 25-28 μm large pores (>100 μm) were likely to be present and be the cause of fatigue crack initiation. In LVD25, initiation was observed at pores and in one of the S-N samples was the root cause of failure. In the LVD25 short fatigue crack growth test, failure was caused by initiation at an Al_9FeNi particle but initiation was also observed to occur at pores, and sizeable cracks (where $2a > 500$ μm) propagated from these regions. X-ray CT data showed that one of these pores was <100 μm.

It is well established that Si affects the castability of these alloys (Elliot, 1983; Polmear, 1989). In binary Al-Si alloys (under equilibrium conditions) the eutectic Si level is optimum in terms of castability because the change from liquid to solid occurs at a single solidification temperature. As the Si level decreases from the eutectic Si level, the temperature range of the 'mushy zone', where the α-phase and liquid co-exist, increases. Solid α-phase forms in the melt, and as the solid phase cools it shrinks and if liquid cannot be fed into this region a pore forms.

The materials studied in this project are not binary alloys and so the conventional Al-Si phase diagram is not strictly applicable. However, thermodynamic modelling (Chen, 2006) (confirmed by DSC) shows that as the Si level decreases (or increases) from the near eutectic level (in LVD25), the temperature range over which solidification occurs increases and so an increase in porosity may be expected. This cannot be confirmed by the study of porosity using X-ray CT in this work, but the results of the S-N tests show that occurrence of fatigue initiation from porosity is inversely proportional to the Si content and so such a trend seems likely.

Several porous regions were observed using X-ray CT and in all cases the pores had a complex shape (Figures 4-26 and 4-27). Fan and Hao (2004) note "a pore itself is not a crack but a notch with a stress concentration at the blunted tip". Work by Yi *et al.* (2003) shows that the stress concentration is highest around the concave tips of a pore, and Buffière *et al.* (2001) report that fatigue crack initiation often occurs at such concave tips. It is therefore not surprising that such large and complex pores are potent fatigue crack initiators. The pores contained many concave tips, and so many regions of high stress are likely to form around the pores and provide many potential fatigue crack initiation sites.

X-ray CT is an excellent tool for characterising porosity and recently several researchers have used the technique for this purpose (Ferrié *et al.,* 2005; Li *et al.,* 2006). In this study X-ray CT has been used to reveal the true, complex shape of shrinkage pores. Two-dimensional image analysis was considered as a way of characterising the pores in this project, but was discounted for two reasons: 1) because of the low porosity levels and the multiphase microstructures of these alloys (some phases look similar to interdendritic pores) pores are actually difficult to identify on polished surfaces, 2) X-ray CT data showed that pores were generally part of a larger porous network and so 2-D measurements would underestimate pore size. An example to illustrate this point is presented in Figure 6-1, the image is an X-ray CT section similar to that which would be obtained from conventional 2-D sectioning and polishing.

In Figure 6-1 four pores have been identified; the maximum pore dimension is a=28 μm, b=72 μm, c=15 μm and d=18 μm. The 2-D analysis does not reveal that these pores are all connected via a larger porous network and the maximum dimension of the porous region is in the order of 300 μm. In work by Li *et al.* (2006) the difference between the maximum pore dimension measured in 2-D, by conventional sectioning and polishing, and in 3-D, by use of X-ray CT, was shown to be significant. The average pore size was 50% larger when measured in 3-D. This difference may be of particular importance when using porosity measurements as the initial defect size in lifing models (Shiozawa *et al.,* 1997; Wang *et al.,* 2001; Yi *et al.,* 2003), as these models tend to be sensitive to this parameter (Suresh, 1998).

6.2.2 Effect of hard particles

In the absence of porosity, other microstructural features have been shown to be detrimental to fatigue life (Wang *et al.,* 2001) causing fatigue crack initiation; these include: oxides (Zhang *et al.,* 1999), Si particles (Gall *et al.,* 1999) and intermetallic particles (Joyce *et al.,* 2003). In this work oxides were not observed; the piston manufacturer (Federal Mogul) uses a complex proprietary casting process, which aims to reduce oxide levels (Barnes, 2005), and appears to have been successful. The exact details of the casting process are not fully known by the author but the pistons were cast on their side and carefully designed ingates were used to reduce turbulence in the cast. Initiation events were observed at both Si particles and intermetallic particles.

Initiation at Si particles via particle fracture or debonding of the particle/matrix interface has been reported by many researchers (Buffière *et al.,* 2001; Gall *et al.,* 1999; Han *et al.,* 2002; Joyce *et al.,* 2003; Kobayashi, 2002,; Shiozawa *et al.,* 1997; Stolarz *et al.,* 2001; Zhang *et al.,* 1999). However, initiation at intermetallic particles is less common and has been reported in fewer studies (Joyce *et al.,* 2003; Stolarz *et al.,* 2001). Stolarz *et al.* report that initiation occurred at the iron containing β(Al_5FeSi) phase (as well as at Si particles), but this phase does not occur in the alloys considered in this study because the addition of Cu Mn and Ni promoted the growth of other Fe containing phases. Joyce *et al.* (2003) researched near eutectic AlSi alloys, the compositions of which are given in Table 6-1. In AE413 (the low Cu and Ni containing alloy) initiation was observed to occur exclusively at Si particles. In AE160 (the high Cu and Ni containing alloy) initiation was also observed at Si particles. However, two of the twelve cracks were initiated at intermetallic clusters. Joyce *et al.*'s (2003) work indicates that with an increase in Cu and Ni content, and therefore an increase in the volume fraction of intermetallic phases, there is a greater likelihood of intermetallic particles causing an initiation event.

In this study the Al_9FeNi phase appears to be particularly detrimental, causing initiation for both the fatigue cracks not associated with porosity in the LVD25 short fatigue crack sample, and both the fatigue cracks studied in the LVD26 mod short fatigue crack sample. Initiation at Si particles was observed but only in the S-N

samples. In this study the alloys contained higher Cu and Ni content (~3.9 wt% and ~3 wt% respectively) than those studied by Joyce *et al.* (2003). This study confirms the trend in the work of Joyce *et al.* that with an increase in the Cu and Ni content there is a greater likelihood of fatigue initiation occurring at intermetallic particles.

To consider why particles fail it is necessary to consider the mechanism of load transfer. The materials studied in this project comprise a soft, low *E* matrix and harder, high *E* intermetallic and Si phases. When an external load is applied to these alloys an inhomogeneity in the stress distribution will arise because of the mismatch in the elastic properties (*E*) of the different phases (Eshelby, 1957). The stiffer particles reinforce the matrix phase with a greater proportion of the applied load being borne by the stiffer phases (Sinclair and Gregson, 1997). The load is transferred from the matrix to the stiffer particles, the concept of load transfer is therefore important as the mechanism has a large influence on the overall properties of the material (Withers *et al.,* 1989).

It is also the mechanism of load transfer that causes fatigue crack initiation at hard particles in the alloys studied in this project. Load transfer can be used to explain both particle fracture and interfacial decohesion. If the stress induced in the reinforcing particles by load transfer exceeds a critical value (the fracture stress) then failure of the particles will occur (Lee and Mear, 1999). Whilst load transfer reduces the mean matrix stress (Withers *et al.,* 1989), the stress in the matrix around the particle will be locally high, if it exceeds a critical level (related to the interfacial energy between the particle and the matrix) (Huang and Li, 2006) then decohesion will occur. Particle failure may not necessarily occur on the first fatigue cycle. As the material is fatigued the dislocations pile up around the reinforcing particles (Fan and Hao 2004), which has a two-fold effect: firstly the stress in the particles will increase and secondly the local stress in the matrix around the particles also increases. Whilst initially (on the first cycle) the stress distribution may be such that particle failure does not occur, the build up of dislocations by cyclic loading may induce the stress required for failure.

Several factors affect the load transferred from the matrix to the reinforcing particles: the relative mechanical properties of the materials, the morphology of the reinforcing particles, the applied load, the matrix properties and the volume fraction of the reinforcing phase (Clyne and Withers, 1993). To determine why the Al_9FeNi is the

most detrimental phase it is necessary to consider the inherent mechanical properties of all the 'hard particles' in these alloys and their morphology.

Mechanical properties

The nanoindentation results of Chen (2006) in Table 4-4 provide values for the E and the hardness (H) of many of the phases of interest. Hardness is not a direct measure of strength but there are empirical relationships between hardness and the ultimate tensile strength (σ_{UTS}) (Tabor, 1951) and therefore hardness can be defined as a function of σ_{UTS}:

$$H = f\left(\sigma_{UTS}\right) \tag{6-1}$$

The stress-strain curves of the individual hard particles are unknown but from fracture observations, in chapter 5, their failure mode is brittle and so it can be assumed that the intermetallic and Si particles behave in a linear elastic manner and exhibit no (or little) plastic deformation. With knowledge of the modulus of each phase (E_r) it is possible to estimate the strain required for failure, ε_{fr}:

$$\varepsilon_{fr} = \frac{f\left(\sigma_{UTS}\right)}{E_r} \tag{6-2}$$

Since it is the relative differences in ε_{fr} that is of interest an absolute relationship is not required and so equation (6-1) and (6-2) can be combined to give:

$$f\left(\varepsilon_{fr}\right) = \frac{H}{E_r} \tag{6-3}$$

Assuming that the strain distribution in each phase is homogeneous, the values of H and E_r (from table 4-4) have been used in equation (6-3) to calculate a value of the $f(\varepsilon_{fr})$ for each phase and determine which phase is likely to fail preferentially; the results are plotted in Figure 6-2. It can be seen that Si has the largest $f(\varepsilon_{fr})$ and that all the intermetallic phases can be expected to fracture at a lower strain than Si. Specifically the Al_9FeNi phase has the lowest $f(\varepsilon_{fr})$ and so this result is consistent with the Al_9FeNi phase preferentially causing fatigue crack initiation.

Morphology

In investigations of simpler binary or ternary (AlSi or AlSiMg) alloys, particle size and morphology are thought to be influential factors in fatigue crack initiation. For example, Kobayashi (2002) determined that small, refined eutectic Si particles required a higher stress to fracture than larger, primary Si particles and Verdu *et al.* (1996) showed a dependence on particle aspect ratio, and reported that longer particles tend to crack more easily.

It is difficult to define a typical size or morphology for any of the phases in the alloys investigated in this study. Primary Si particles (using 2-D micrographs) appear to have a cuboid structure with a diameter of approximately 25 μm. However, in many of the micrographs presented in chapters 4 and 5, primary Si is often connected to intermetallic particles. Similarly, the coarser eutectic Si found in LVD25 and LVD26 unmod is often connected to intermetallics. In 2-D sections the eutectic Si in LVD26 mod appears to be finer than the eutectic Si in LVD26 unmod. But recent work by Lasagni *et al.* (2006), using a FIB-SEM to produce 3-D images of a Sr-refined eutectic Si region, has shown that these particles can actually form part of a complex 3-D, fibrous network and are not individual particles. The different Si branches form at right angles to each other and so each refined eutectic Si cluster contains many re-entrant angles. It seems probable that all forms of Si in these alloys form part of the larger, interconnected hard particle network.

The X-ray CT data presented in chapter 4.3 show that the intermetallics form an interconnected network throughout the alloys and individual phases rarely exist. Mg_2Si and Al_2Cu phases exhibit a 'chinese script' morphology as reported by Daykin (1998) and Edwards (2002) but are only present in low volume fractions (Chen 2006); these phases are also predominantly attached to larger intermetallics. The intermetallic phases which are present at the highest V_fs (AlNiCu phases and Al_9FeNi) have no such characteristic shape. The X-ray CT data shows that the intermetallic phases contain many acute re-entrant angles and 2-D micrographs show the same for Si particles. Re-entrant sharp angles are an important microstructural feature because they are known to increase stresses in the particles (Qin *et al.,* 1999) and such flaws can affect the fracture strength of particles. It is not possible to determine which phase exhibits the most unfavourable morphology in terms of increasing local stresses in

both it, and the connected phases. In order to further assess the affect of the important microstructural features (phase morphology, distribution and mechanical properties), micromechanical models could be used. In a review of the literature, many models, both analytical and numerical are available. However, none truly reflect the multiphase, interconnected microstructures of the alloys in the study. A brief overview of some interesting approaches and possible routes for advance will be given in the remainder of this section, although specification of a detailed model is beyond the scope of this study.

Analytical models

The Eshelby inclusion method (Eshelby, 1957) provides the mathematical framework for predicting the residual stresses in two-phase materials. This work has been expanded on by many, including Mori and Tanaka (1973) and Withers *et al.* (1989) and the method has proved a useful tool for determining the mechanical properties of metal matrix composite (MMC) materials. MMCs generally comprise a matrix and a single reinforcement phase, which can usually be approximated to an ellipsoid. Using the Eshelby inclusion method it is possible to calculate the average particle and matrix stresses and other properties of the composite (Clyne and Withers, 1993). However, there are several features of the Eshelby inclusion model that preclude its use for the alloys studied in this project:

1) Only one reinforcement phase is considered - these alloys contain several reinforcement phases which each have different mechanical properties, there will also be an elastic and thermal mismatch between the different phases.

2) Individual reinforcing particles are homogeneously distributed - in these alloys the particles are interconnected and have a locally heterogeneous distribution e.g. clustering occurs (Figure 4-16).

3) Stress in the particles is assumed to be isotropic – because of the complex shape of the particles and the many re-entrant angles they contain this is not the case (Qin *et al.* 1999).

Finite element models

With finite element analysis (FEA) methods it is possible to model more realistic microstructures. For example Fan *et al.* (2003) used a 2-D micrograph of an A356 alloy to position the Si particles in the matrix such that they had a 'realistic' distribution. The Si particles could be approximated as ellipsoids so, as in the Eshelby inclusion method, the stress in the particles was assumed to be isotropic. Fan *et al.* (2003) were able to demonstrate how the effective plastic strains may be distributed in realistic microstructures. Shen and Lissenden (2002) performed a 2-D and 3-D FEA of a particle reinforced aluminium alloy. In their analysis the particles had an idealised shape; particles were assumed to remain intact and connected to the matrix and standard properties were given to the matrix. Shen and Lissenden (2002) demonstrated that the equivalent plastic strain distributions in the matrix predicted by 2-D models were significantly different from those for the same plane in a 3-D model. In addition the 2-D models underestimated the maximum principal stress distribution in the particles compared with the 3-D case. Since the maximum principal stress could be used, for example, as a failure criterion for particle fracture, 2-D and 3-D models would be likely to predict initiation at different locations.

Because of recent advances in 3-D imaging techniques it is now possible, using commercially available software such as Amira (Mercury Computer Systems GmbH) and ScanFE (Simpleware Ltd), to convert 3-D X-ray CT image data into a mesh that can be used with commercial FE packages. For example Geandier *et al.* (2005) investigated an Al_2O_3-Cr composite to ascertain the residual thermal stresses after cooling the material from a typical processing temperature (1450˚C) to RT. Using Matsim software Heggli *et al.* (2005) were able to convert X-ray CT data of an Al-C (graphite) interpenetrating composite into an FE mesh that could be used to assess the electrical conductivity of the material. Watson *et al.* (2006) used microfocus X-ray CT to obtain the microstructure of an Al alloy reinforced with Ni. Using ScanFE software Watson *et al.* (2006) converted the data into a tetrahedral and hexahedral mesh, which could be used in Abaqus (Dassault Systèmes). Using this data it was possible to model the elastic-plastic behaviour of the alloy successfully.

The materials investigated in this study have been shown to be complex, multiphase materials. However, as a reasonable first order approximation, four main constituents can be identified:

1) Al-matrix,

2) Si particles (except in LVD27),

3) interconnected intermetallic network and

4) pores.

Using conventional X-ray CT data it is possible to segment the intermetallic phases and the pores from the Al and Si phases, thought it is unfortunately not possible to differentiate between the individual intermetallics. It is also not possible to separate the Al and the Si phases as they have similar X-ray attenuation coefficients. However, the highly coherent X-ray beam in synchrotron tomography allows for phase contrast imaging (Cloetens *et al.,* 2001). At interfaces (phase-phase or phase-air) there is a sharp difference in the phase retardation. Phase contrast forms when these neighbouring sections of the beam interfere as they propagate away from the sample. Phase contrast manifests itself in images as fringes around the interfaces; the fringes observed vary with the sample to detector distance. If images are taken at 2 to 4 different detector positions it is possible to produce a phase map (Cloetens *et al.,* 1999) where the greyscale value is a function of the refractive index and so phases with similar X-ray attenuation coefficients (but different refractive indexes) can be identified. This procedure can be used with the conventional X-ray CT imaging method so that a phase map is produced for each angle; this procedure is called holotomography. The phase maps can be reconstructed using the conventional filtered back projection method to produce an X-ray CT volume, where phases with similar X-ray attenuation coefficients can be sufficiently differentiated (Borbély *et al.,* 2004).

Holotomography has been demonstrated to be a useful tool for differentiating Al and Si phases (Baruchel *et al.,* 2006; Yamamoto *et al.,* 2006). Using holotomography it would be possible to produce volume data in which the four principal components of the alloys could be differentiated by their greyscale level. This segmentation could be performed in ScanFE or Amira software so that the alloy constituents could be

converted into a representative 3-D FE mesh. By combining the volume data obtained from holotomography with the mechanical properties data from nanoindentation it would be possible to produce a good representation of the alloys investigated in this study, which could be interrogated using FEA methods to determine, amongst other things, stress distribution in the alloys so as to identify detrimental microstructural features. For example: does the coarser intermetallic network in LVD25 produce locally higher stresses than the finer intermetallic networks observed in the LVD26 alloys? Similarly are the finer Si clusters in LVD26mod more or less detrimental than the eutectic Si in LVD26 unmod and LVD25, and the primary Si in LVD25? Using the coefficients of thermal expansion for each phase, determined by Chen (2006), it would also be possible to estimate the residual stress distribution due to thermal cycling, which is also an important factor in the design and improvement of engine alloys (Fischersworring-bunk *et al.*, 2006).

6.3 Fatigue crack propagation

6.3.1 Micromechanisms of fatigue crack propagation

From X-ray CT observations it can be seen that these alloys contain a complex 3-D microstructure, therefore the mechanisms of fatigue propagation may be somewhat different from those generally reported in the literature for simpler Al-Si systems (such as Gall *et al.,* 1999; Joyce *et al.,* 2002). However, the materials studied in this work, and in particular their 3-D intermetallic sub-structures, are more representative of complex Al-Si alloys currently used in car engines and so an understanding of their fatigue mechanisms is important.

6.3.1.1 Discrete particulate systems

It is worth considering fatigue propagation mechanisms in simpler Al-Si systems. These systems comprise discrete Si and secondary phase particles dispersed in an Al-matrix, in addition pores may also be present. Crack propagation through the Al-matrix is generally via fatigue failure and is dependent on the properties of the matrix and the stress distribution ahead of the crack tip. As discussed in chapter 6.2 the mismatch between the elastic properties of the alloy constituents results in a heterogeneous distribution of stresses throughout the alloy. A fatigue crack will

propagate through the matrix, avoiding stiff (high *E*) particles and will be attracted to low *E* regions (e.g. pores or failed/debonded particles) (Boselli *et al.,* 2001; Padkin *et al.,* 1987).

As a fatigue crack propagates through the Al-matrix, four interactions are possible; these are shown schematically in Figure 6-3. The crack may interact with a pore, an intact particle, a fractured particle and a debonded particle and each of these interactions can be further divided into a series of possible mechanisms.

Pores

Pores provide a weak path by which a fatigue crack may propagate, when a fatigue crack approaches a pore (Figure 6-5a) it is likely to be attracted towards it, so long as it is beneficial in terms of the crack driving force (Figure 6-5b). Prior to the coalescence of the crack and pore an increase in *da/dN* may be observed (Janssen *et al.,* 2005). When a crack connects with a pore the crack immediately grows (locally) by the length of the pore and this can be described as a static failure mode. Tips of pores are usually blunter than a crack tip (Fan and Hao, 2004b) and so although the crack is longer, the stress intensity at the crack tip is reduced and retardation can occur (Figure 6-5c). However, the crack may reinitiate allowing the continuation of crack propagation (Figure 6-5d). Fatigue cracks can initiate at pores (chapter 6.2.1) and so if several cracks form in close proximity to the same plane this may result in crack coalescence (Lee *et al.*, 1995) (Figure 6-5e), prior to crack coalescence an increase in *da/dN* is expected. In the final scenario (Figure 6-5f) the crack is deflected away, or avoids, the pore. Such an occurrence is unlikely (but included here for completeness) and is only expected to occur if the crack grows under the influence of other, more dominant, microstructural features.

Intact particle

Assuming there are no external influences, fatigue cracks are deflected away from intact stiff particles (Padkin *et al.,* 1987) this is schematically illustrated in Figure 6-6b. Crack deflection by particles has been shown to have a complex effect on the local crack tip *K* (Boselli *et al.,* 2001). The initial deflection causes a reduction in the

local *K* (shielding effect) but as the crack propagates past the particle there is a transient increase in the local *K* (anti-shielding effect).

As illustrated in Figure 6-6c a fatigue crack may directly propagate into a particle, this can happen for two reasons: 1) fatigue cracks are attracted towards low *E* particles (Padkin *et al.,* 1987; Stokes *et al.,* 2007), they locally increase the *K* at the crack tip and so the crack may be expected to accelerate towards low *E* particles, 2) the crack can be 'trapped' by a high *E* particle so that deflection is unfavourable in terms of the crack driving force. This mechanism is unlikely to occur in systems with spherical particles (as in Figure 6-6c) but is possible if the particles exhibit a complex shape (Figure 6-4a). In addition the crack may be 'channelled' by other particles, this is illustrated in Figure 6-4b, in this example the crack has followed the path of least resistance: avoiding the stiff spherical particles until it is trapped by the irregular shaped particle.

If a crack does propagate into the particle as in Figure 6-6c four mechanisms may occur. Firstly the crack may remain trapped and so crack propagation will be halted. The crack may propagate through the particle (Figure 6-6d), the failure mode will be dependent on the properties of the particle. Brittle phases (such as those in Al-Si alloys) are likely to fracture, although fatigue may occur in other, more ductile phases. If the particles exhibit high fracture strength then debonding of the particle/matrix interface may occur (Figure 6-6e) and can be as a result of fatigue or static failure modes. Finally the crack may form on the opposite side of the particle leaving the intact particle in the wake of the crack, forming a ligament.

Fractured particle

A fractured particle has a similar effect on fatigue crack propagation as a pore, it acts as a low stress region and so forms a weak path by which a crack may propagate (Gall *et al.,* 1999) (Figure 6-7b). Particle fracture is often associated with static failure modes ahead of the crack tip, particularly at high values of ΔK where propagation via fractured particles is observed to cause an acceleration in *da/dN* (Lados *et al.,* 2006). As shown in the diagram in Figure 6-7b the crack can be attracted towards the fractured particle, under the correct conditions.

Depending on the distribution of stresses in the material around the particle, the position of the fracture in the particle and the relative location of the crack and the particle, it is possible the crack could propagate into an intact region of the particle, and via debonding of the particle/matrix interface connect with the fractured region (Figure 6-7c). Microcracks can initiate at fractured particles (Figure 6-7d) and so crack coalescence (Stolarz *et al.,* 2001) can occur. Microcracks provide a low stress path and so deviations in the crack path and an increase in *da/dN* may be expected prior to linkage. The final mechanism (Figure 6-7e) is crack avoidance of the fractured particle; this mechanism seems unlikely to occur (as in the case of the pore in Figure 6-5f) but is possible if other microstructural features exert a greater influence on the crack, for example a pore or a larger fractured particle.

Debonded particle

The interface between a particle and the matrix can debond in the high stress region ahead of the crack tip forming a void(s) around the particle (Needleman, 1987) as illustrated in Figure 6-8a. The location at which a void forms is dependent on the local stress distribution (Keer *et al.,* 1973), which in turn is influenced by the particle properties and applied load. A debonded particle has a similar effect on fatigue crack propagation as a pore or a fractured particle. The crack may be attracted to the debonded regions (Figure 6-8b) as it forms a weak path by which the crack may propagate (Lee *et al.,* 1995). Debonding can cause crack blunting and so reduces the driving force of a crack, this mechanism is often utilised to improve the fatigue properties of composite materials where the interface between the reinforcing phase and the matrix is deliberately designed to be weak so that debonding occurs thereby inhibiting crack growth.

A crack can propagate into an intact region of a partially debonded particle and linkage of the crack and the void can occur by further debonding of the interface (Figure 6-8c), this can be via static or fatigue failure modes. Cracks can initiate and propagate away from the debonded region (Lee *et al.,* 1995a) and so crack coalescence (Figure 6-8d) may also occur. The final mechanism is avoidance of the debonded particle by the crack. As with the fractured particle this mechanism is unlikely to occur unless other external influences affect the stress distribution around the crack tip.

In summary, in particulate systems fatigue crack propagation is affected by a series of possible interactions. The path along which a crack chooses to propagate is controlled by the stress distribution ahead of the crack tip and the crack is likely to 'choose' the option, which is preferential in terms of maximising the crack driving force. The concept of load transfer is important in crack propagation, as it is the distribution of stresses that it creates in and around particles and pores that can cause the fatigue crack to be attracted or deflected away from them. In addition it is load transfer that can cause stresses in the particles and the matrix to reach a level where particle fracture or debonding of the particle/matrix interface occurs providing a weak path for the crack to follow. The micromechanisms of fatigue crack propagation will therefore be dependent on the volume fraction of hard particles, their morphology, size and mechanical properties and the applied stress. If a sufficient volume of pores are present, they too will have an influence on fatigue propagation and the important characteristics will be their morphology, size and position relative to the crack.

6.3.1.2 Interconnected particulate systems

In an interconnected particulate system the same three particle interactions (Figure 6-3b to d) may be expected to occur, these are illustrated in Figure 6-9a; the viewer is placed at the crack tip. A section of the particle is fractured, another region is debonded and several sections of the particle remain intact. The principal difference between a discrete and an interconnected particulate system is that crack deflection by the particle network cannot occur indefinitely. At some point, to ensure a level of crack continuity, the crack must propagate either through particles (via fatigue or fracture) or leave them intact in the crack wake.

The propagation mechanisms, of the three particle interactions, are similar to the ones discussed in the previous section. An intact section will block the crack, propagation will continue when the particle fractures or debonds. In addition the particle can remain in the crack wake forming a ligament as the crack grows around either side of the intact particle eventually engulfing it; this is shown schematically in Figure 6-10. The lines A to F represent possible crack front positions as the crack engulfs the particle (this is just one of the possible ways an intact particle can be left in the crack wake). The crack may be attracted towards the debonded or fractured section of the particle network ahead of the crack tip (as in Figure 6-7b and Figure 6-8b), this can

induce further debonding of the particle/matrix interface (Figure 6-7c and Figure 6-8c). In addition microcracks may initiate at the voids caused by fracture and debonding, which can coalesce with other cracks (Figure 6-7d and Figure 6-8d).

Considering the example in Figure 6-9b, a complex distribution of stresses will occur ahead of the crack tip. The crack may be attracted towards the debonded and/or fractured sections, both of these sections will allow local crack advance and may be expected to increase the local driving force. But, the intact region cannot be avoided and there will be an opposing effect that is likely to reduce the local driving force. In addition the fractured and debonded regions are on different planes, if the crack propagates via both of these regions the crack shape will become 'rough'. Such deflections will inhibit the crack from growing in the favoured mode I direction, and may cause roughness induced crack closure (Suresh and Ritchie, 1984; Parry *et al.,* 2000), both mechanisms affect fatigue crack propagation by reducing the effective driving force at the crack tip.

6.3.2 Short fatigue crack propagation observations

In the previous section the possible mechanisms of fatigue crack propagation in particulate reinforced systems were discussed. Many of the mechanisms have been observed to occur in the alloys studied in this project through a combination of *in-situ* and post failure analysis. In this section the direct evidence of these mechanisms will be highlighted and their consequence on short fatigue crack propagation will be explored. It should be noted that the calculated ΔK values of the cracks analysed in this section were approximately 5 MPa√m or less and the crack growth rates observed were between $1x10^{-7}$ mm/cycle (crack arrest) and $1x10^{-4}$ mm/cycle. Therefore, the mechanisms described in this section may not be representative of those near final failure. Crack growth near failure will be assessed using the long fatigue crack samples.

Deflection of the fatigue crack around intact particles was observed; an example of the crack deflecting around a primary Si particle in LVD25 was presented in Figure 5-20 (position 2). However, this mechanism was not common and this is most likely a reflection of the complex microstructures of these alloys. The alloys contain an interconnected hard particle network, which is irregular in terms of both the

morphology and inherent mechanical properties; therefore the distribution of stresses in these alloys is complex. As a fatigue crack propagates through the alloy the complex stress distribution results in a rough fatigue crack with an irregular crack front. The irregular stress distribution and crack front contribute to a complex distribution of the driving force along the crack so that deflection away from a particle may not be most advantageous in terms of maximising the driving force. The channelling mechanism in Figure 6-4 is a reasonable representation of a situation that may occur in a dendrite and illustrates how crack deflection may not be possible.

It was more usual for the crack to propagate via failed particles or to grow into intact particles. Intact particles blocked fatigue cracks and were the cause of several of the retardations observed in *da/dN* in LVD25 and both LVD26 alloys. An example was presented for the LVD25 alloy in Figure 5-24, which showed that a sub-surface particle retarded crack growth not just at the particle but adjacent to it, at the sample surface. In this example it was shown that the particle eventually fractured allowing the continuation of fatigue crack propagation. The sequence of events that caused the fracture of the particle below the surface is unknown (since only the surface was observed *in-situ*) but a probable sequence is presented in Figure 6-11. In Figure 6-11a, the crack tip and the particle are in contact, this locally stops fatigue crack growth. The remainder of the crack below the particle is not blocked and so is able to propagate forward (Figure 6-11b). By doing so it raises the local crack tip driving force of the blocked section of the crack (Fares, 1989) and therefore increases the stress within the particle. As the unblocked crack continues to advance the particle may be partially engulfed by the crack (Figure 6-11c). Eventually the stress in the particle reaches a critical level and it fractures allowing propagation to continue (Figure 6-11d). Similarly an increase in the stress intensity at the crack tip because of crack advance to the side of the particle (Figure 6-11b) could cause debonding to occur. However, if the particle is interconnected it will still need to fracture for propagation to completely resume.

Particles failed ahead of the crack tip in all the alloys studied in this project. In chapter 6.2.2 it was noted that particle failure was dependent on the shape, size, distribution and mechanical properties of the particles and the applied stress. As a result, the number of particles that fail in the plastic zone ahead of the crack tip will

have a statistical distribution dependent on these variables and so may differ between the alloys. 3-D post failure analysis using X-ray CT showed that in LVD25 and both LVD26 alloys micro-damage, from particle failure, formed ahead of the contiguous crack and at all positions along it. However, in LVD27 micro-damage only occurred in localised regions in front of the crack at dense regions of secondary phase particles (Figures 5-53 and 5-54), and so the level of micro-damage was much lower in LVD27. The crack tip of LVD25 and both LVD26 alloys is more accurately described as a region comprised of micro-damage and intact ligaments. Damage in this region formed as a result of both particle fracture (for example: position 2 in Figure 5-39) and debonding of the particle/matrix interface (for example: below position 6 in Figure 5-20) and both mechanisms were observed to occur at Si and intermetallic particles.

An example of a crack making a large deflection to propagate through a fractured Si particle was given in Figure 5-20 (position 4) and crack deflection was observed on the polished surfaces during the short fatigue tests of all the alloys. Micro-damage ahead of the crack tip was not always confined to fractured or debonded particles. X-ray CT data showed that small cracks emanated from either side of failed particles into the matrix (position 6 in Figure 5-20). It seems likely that fatigue cracks initiated at failed particles ahead of the 'crack tip', which propagated through the Al-matrix eventually coalescing with other cracks (similar to that shown in Figure 6-7d).

It is difficult to define the crack tip in LVD25 and both LVD26 alloys. The 2-D projections obtained from the X-ray CT data (for example: Figure 5-41) provide a reasonable approximation of the crack front (Ferrie *et al.,* 2005). The crack has a 'regular' shape and micro-damage can be seen to form ahead of the crack tip. However, the 3-D images (Figure 5-40) show that there are intact ligaments behind what would be defined as the 2-D projected crack front. The situation is shown schematically in Figure 6-12, (a) to (c) show the same situation from different angles. The green crack identified in Figure 6-12 is the 2-D projected crack shape, failed particles are in front of the crack tip and intact ligaments are left in the wake behind the crack tip. The intact sections between the regions of micro-damage (ahead of the 2-D projected crack tip) can also be described as ligaments and are comprised of the Al-matrix and hard particles (positions 1 and 3 in Figure 5-39). These ligaments are

subject to fatigue and static failure modes and their lifetime will depend upon their composition. Some of the ligaments do not fail ahead of the 2-D projected crack tip and they form the intact ligaments in the crack wake. As the fatigue crack propagates the stress in the ligaments increases until they eventually fail. Before they fail, however, they act as a traction on crack opening (Gerberich and Moody, 1979) and so limit the CTOD and shield the crack tip (Shang and Ritchie, 1989).

The driving force and so crack growth rate of cracks in LVD25 and both LVD26 alloys will therefore be influenced by a series of competing mechanisms, which are all linked to the microstructure. The micro-damage that forms ahead of the crack tip (zone 2) acts as an anti-shielding mechanism (Blanchette *et al.* 1989) and provides a weak path along which the crack may propagate (Gall *et al.*, 1999; Lados and Apelian, 2004). However, the intact ligaments in the crack wake (zone 1) (Gerberich and Moody, 1979), and the deflections from the mode 1 direction will shield the crack tip and reduce the driving force. In addition RICC (Suresh, 1998) may also cause shielding of the crack tip although this mechanism is not exclusively associated with the crack tip region.

Micro-damage did form ahead of the crack tip in LVD27 but to a much lesser extent than in the other alloys studied. The damage formed in localised regions and was associated with clusters of intermetallic phases. Particle failure ahead of the crack tip caused local crack advance (arrows in Figure 5-53) suggesting that particles do provide a weak path for fatigue propagation, locally increasing the crack growth rate (i.e. particle failure ahead of the crack tip is an anti-shielding mechanism). The materials do, however, have an interconnected, hard particle network that the fatigue crack must propagate through and so intact particles may act as a barrier and retard fatigue crack growth. Corresponding with the lower level of particle fracture ahead of the crack tip there are fewer ligaments in the crack wake and so less shielding may be expected from such a mechanism.

In LVD27 pores played a more dominant role in short fatigue crack propagation than in the other alloys. X-ray CT showed that large pores were linked by the crack. Crack coalescence in LVD27 was observed to be an important fatigue crack propagation mechanism (Figure 5-50) and this is consistent with cracks forming at several pores and coalescing to produce a larger crack. In addition, in Figure 5-54 a pore was

observed on the crack front and the crack was locally advanced in this region. This confirms that pores provide a weak path that cracks are attracted towards.

An interesting feature was observed in the LVD27 crack analysed using X-ray CT, one side of the crack was ligamented or bifurcated (Figure 5-53b). Bifurcated or ligamented cracks have been observed and reported before, for example in a 2024 Al alloy, by Toda *et al.* (2004). They reported that crack growth occurred along different planes and that the cracks overlapped by approximately 80 μm. They demonstrated that where the cracks overlapped, both sections of the crack were retarded in this region so that when looking at a 2-D projection of the crack it appeared to be pinned at the point of overlap, this was similarly observed in LVD27 (Figure 5-53). Toda *et al.* (2004) noted that the planes converged approximately 280 μm behind the crack tip and the bifurcation was likely to have occurred because of the twist and tilt in the crack direction as the crack entered different grains.

In the LVD27 alloy the bifurcation occurred at a porous region near the initiation site. Cracks are known to initiate at the tips of pores (Buffière *et al.,* 2001) and the small cracks emanating from the porous region in Figure 5-52b, suggest that multiple initiation events did occur at this pore. The X-ray CT data indicates that the two sections of the bifurcated crack initiated at different positions in the pore and so caused the bifurcation. In the LVD25 long fatigue crack samples assessed using X-ray CT, cracks were also observed to grow along different planes. The large deflections observed on the fracture profiles of both LVD26 alloys suggest that cracks also grew along different planes in these alloys. In the LVD25 sample, the X-ray CT data indicates that the crack growth along planes was associated with the coalescence of micro-damage ahead of the crack tip. The formation of a ligamented or bifurcated crack can therefore be attributed to a series of microstructural features: twists at grain boundaries (Toda *et al.*, 2004), multiple initiations at pores (LVD27 and coalescence of micro-damage at hard particles (LVD25).

The bifurcation in LVD27 was not observed from in-situ analysis of the polished surface because only one of the ligaments breached the surface. Both sections of the crack grew to approximately the same length, suggesting that they grew in a complementary manner. The bifurcated side of the crack (Figure 5-53) also grew to a similar length as the non-bifurcated single crack on the opposite side (Figure 5-54).

Whilst a bifurcated and non-bifurcated crack may have different shielding mechanisms these results suggests that the bifurcation did not have an overall, significant impact on the crack growth rate in this case.

6.3.3 Comparison of short fatigue crack behaviour

The short fatigue crack growth rate is only measured on the surface sample and is not an average measurement of crack growth such as that obtained from p.d. measurements in the long fatigue crack samples. Because of this, the crack growth data are spread over a range of *da/dN* values, which reflect the retardations and accelerations in growth due to local microstructural features. In Figure 5-58 the upper bound of the crack growth curves for each alloy were compared. The upper bound represents the fastest growth rates observed in each alloy and is therefore an important measure of the alloy performance. LVD27 exhibited the highest *da/dN* for a nominal value of ΔK, followed by LVD26 mod and LVD25, with the performance of LVD26 unmod being significantly better than the other alloys. The performance of LVD25 and LVD26 mod was similar, particularly at the higher ΔK values. In the S-N tests LVD26 unmod had a significantly better performance than the other alloys, LVD25 exhibited a similar performance to LVD26 mod and LVD27 had the worst performance. The results of the short fatigue crack experiments are therefore consistent with the S-N test results.

Comparison of both LVD26 alloys shows that they contain the same V_f of hard particles and exhibit a similar SDAS. Qualitatively the X-ray CT data shows that the intermetallic network is similar in both alloys. The principal difference between the alloys is the morphology of the Si particles. The 2-D image analysis showed that the Si particles are larger in the LVD26 unmod alloy, but they do not appear to have many re-entrant angles or sharp corners (Figure 4-4). The 2-D image analysis data suggests that the Si particles are much finer in LVD26 mod. However, recent work by Lasagni *et al.* (2006) has shown that Sr-modified Si particles actually form a fibrous network with many 90˚ angles between branches of the network. It might therefore be expected that the Sr-modified Si is the more detrimental Si morphology because of the acute angles between branches. For example, this could allow higher stresses to develop in the particle, particularly at the junction of the branches, and so fracture

more easily and act as a weaker barrier to fatigue crack propagation. This may account for the worse performance of LVD26 mod compared with LVD26 unmod.

The upper bound of *da/dN* in LVD27 was the highest of all the alloys studied. This may be a reflection of several factors. LVD27 contains the lowest V_f of hard particles, the smallest particles (L_3 from Table 4.1) and the largest distance between particles (λ and SDAS from Table 4.1). As a result, less micro-damage occurs ahead of the crack tip (lower anti-shielding) but also the crack impinges on fewer particles and there are fewer intact ligaments in the crack wake (lower shielding). In addition, because of the low Si content in LVD27, there is an increased level of porosity compared with the other alloys and the naturally occurring cracks initiate at pores. Propagation of fatigue cracks in LVD27 is partially via the coalescence of these smaller cracks and such coalescence has been observed to increase *da/dN* (Janssen *et al.,* 2005). The competing propagation mechanisms determine the crack driving force and the balance of these mechanisms results in the fastest fatigue crack growth rates of LVD27.

The LVD25 alloy contains a higher V_f of hard particles (because of the greater Si content) than the LVD26 alloys. The particles in the LVD25 alloy are larger than in the LVD26 alloys (L_3 in Table 4.1). Larger particles are thought to fracture at a lower stress (Kobayashi, 2002) since they are likely to contain more flaws (Joyce *et al.*, 2003). Primary Si particles do form large complex shapes and have been shown to fracture in a multifaceted manner (Figure 5-18). Qualitatively, the X-ray CT results show that LVD25 has a coarser intermetallic microstructure than the LVD26 alloys and large sheets of intermetallic phases make up part of the hard particle network (Figure 4-19). Because of their larger size, the particles in LVD25 may be expected to fracture more readily and so produce more micro-damage ahead of the crack tip causing an increase in *da/dN*. Conversely, because of the greater V_f of particles in LVD25, the fatigue crack may be expected to impinge on more particles and this would reduce *da/dN*.

It is the stress distribution around the crack tip that controls the driving force and therefore crack growth rate in these alloys. The stress distribution (as previously discussed in section 6.2.2) is controlled by a number of factors (particle size, morphology, distribution and mechanical properties in addition to the applied load). For example the competing microstructural factors that affect the *da/dN* in LVD25

and LVD26 mod appear to cancel one another so that they exhibit similar short crack growth behaviour and S-N test performance. To fully understand the complex micromechanisms in these alloys the micromechanical load transfer model, discussed in section 6.2.2, may be a useful tool. Such a model could provide important information about the distribution of stresses ahead of the crack tip in these alloys so that the competing microstructural effects may be better understood.

6.3.4 Room temperature long fatigue crack propagation

6.3.4.1 Room temperature threshold behaviour

Only a small number of long fatigue crack propagation studies have been performed on Al-Si casting alloys but closure has been shown to occur in the near-threshold regime by both Lee *et al.* (1995a) and Lados *et al.* (2006). Maximum crack closure levels (K_{cl}) of 0.66 K_{max} were observed by Lee *et al.* (1995a). Lados *et al.* (2006) reported that roughness induced crack closure (RICC) was observed in a series of AlSiMg casting alloys with similar Si and Mg content to those investigated in this study (although without the other alloying elements). Lados *et al.* (2006) noted that the threshold ΔK value was inversely proportional to the Si content and this was primarily because of the resultant microstructural features in the alloys and the way in which they affected near threshold crack growth. In a low Si (1 wt%) alloy the dendrites were large, causing large deflections, hence a rougher crack than in a mid Si (7 wt%) alloy where the dendrites were smaller. In the eutectic alloy the important microstructural feature was the Si particle size, which was smaller than the dendrite size in the mid Si alloy and so the crack in the eutectic alloy was the least rough. The long fatigue crack growth curves from Lados *et al.* (2006) are shown in Figure 6-13 (along with those of Joyce *et al.* (2002) and the RT curves previously presented in Figure 5-59).

The trend identified by Lados *et al.* (2006) in simpler AlSiMg alloys does not hold true for the alloys investigated in this study. The lowest Si alloy (LVD27) contained the largest dendrites and mean free distance between particles (λ) and exhibited a rougher crack profile than LVD25 and LVD26 unmod (as would be expected from the work of Lados *et al.* (2006)). However, LVD27 had the lowest threshold ΔK value (~3 MPa√m, see Figure 5-69). A rougher crack did not result in a higher ΔK threshold

value for the LVD27 alloy. In addition LVD26 mod exhibited higher roughness than LVD27, it is therefore not possible to attribute the level of roughness to the dendrite size.

LVD26 unmod exhibited a higher threshold ΔK (ΔK_{th}) value than LVD26 mod. A similar trend was observed by Lados *et al.* (2006) and was attributed to the larger Si particles in the unmodified alloy causing larger deflections and therefore greater RICC. The roughness results in Figure 5-69 show that LVD26 mod was actually rougher than LVD26 unmod and so it is again not possible to attribute higher roughness to a higher ΔK_{th} value. The eutectic Si alloy (LVD25) had an intermediate ΔK_{th} value between that of LVD27 and LVD26 unmod but was the least rough crack. These results suggest that roughness is not related to dendrite size (for example LVD26 mod is rougher than LVD27), and that roughness does not account for the different ΔK_{th} values observed in these alloys. Whilst RICC may be expected in these alloys, other crack shielding/anti-shielding mechanisms (which are dependent on the interconnected microstructure, for example static failure ahead of the crack or intact ligaments in the crack wake) occur which affect *da/dN* as previously discussed for short crack propagation in chapter 6.3.3.

The long fatigue crack growth curves of Lados *et al.* (2006) and Joyce *et al.* (2002) are compared with the curves from this study in Figure 6-13. The set of alloys tested by Lados *et al.* (2006) had the lowest quantity of alloying elements and the highest ΔK_{th} values. Conversely the set of alloys investigated in this study had the highest quantity of alloying elements and the lowest ΔK_{th} values. The set of alloys studied by Joyce *et al.* (2002) had intermediate quantities of alloying elements and intermediate ΔK_{th} values. This result suggests the trend that with an increase in the quantity of alloying additions, such as Cu and Ni, there is a decrease in the range of ΔK_{th} values. The shielding/anti-shielding mechanisms may be different between the sets of alloys in each study and this could account for the differences between the ΔK_{th} ranges. These mechanisms may be influenced to the quantity of alloying elements and the associated microstructural features that form as a result (for example the interconnected network in this study).

There are differences in the casting and aging conditions of the alloys tested by Lados *et al.* (2006) compared to those tested in this study and the work of Joyce *et al.*

(2002). The alloys in the work of Lados *et al.* were solution treated and not aged for 100 hours at 260˚C, as a result the morphology of the Si is different. In addition the distribution, size and composition of precipitates in the Al-matrix will also be different and so the properties of the matrix may also differ. This may account for the difference in the range of ΔK_{th} values observed between the work of Lados *et al.* and this study. But the alloys investigated in this study and by Joyce *et al.* (2002) underwent the same aging treatment and therefore the aging conditions cannot be used to account for differences between these studies.

In general the distribution of particles along the fracture profiles in LVD25 and both LVD26 alloys, at low *da/dN* (near threshold), were close to the average distribution of particles that were observed along a line in the bulk of the alloys (Figures 5-64, and Figures 5-66 to 5-68). Whilst the L_L was within one standard deviation of the V_f in the LVD27 alloy, the number of particles intercepted was lower, and the distance between them and their size on the fracture profile was larger than the average for the bulk alloy. Whilst in a discrete particulate system it would be expected that the crack would avoid hard particles at low crack tip stresses (Gall *et al.,* 1999) there is a requirement for crack continuity through the 3-D interconnected network and so particle cracking must occur so that the crack may propagate (as discussed in chapter 6.3.1.2). Cracks in LVD25 and the LVD26 alloys appear to show no preferentiality for the particles via which they propagate. In LVD27, however, the crack preferentiality avoided the hard particle network. The larger particle size on the fracture profile in LVD27 indicates that either the crack propagated via larger than average sections of the hard particle network or that the particle network failed such that a larger cross-section was left on the crack surface.

The relative performance of the alloys in the short crack propagation tests and the S-N tests was also reflected in the ΔK_{th} values of the long fatigue crack growth tests. In all three experiments LVD26 unmod had the best performance, with the longest lifetimes in the S-N tests, the lowest *da/dN* upper bound in the short fatigue crack growth tests and the highest ΔK_{th} value in the long fatigue crack growth tests. In all these experiments LVD27 was observed to give the worst performance with LVD25 and LVD26 mod giving similar performances, both of which were better than LVD27. The short fatigue crack growth test results indicated that the balance of the competing

micromechanisms of fatigue crack growth in the LVD26 unmod alloy were such that this alloy had the lowest *da/dN* for a nominal ΔK value and so exhibited the best fatigue crack growth resistance. The *da/dN* was thought to be reliant on the distribution of stresses ahead of the crack tip and so was dependent on features such as the size, distribution, morphology and the mechanical properties of the particles in the alloys. The correlation in the short crack results and the ΔK_{th} values suggests that the microstructural features that control short fatigue crack growth may also control the ΔK_{th} value in the long fatigue crack growth tests. The load transfer model proposed in chapter 6.2.2 may therefore also be used to help understand the threshold behaviour in these alloys.

6.3.4.2 Room temperature, high *da/dN* behaviour

At high crack growth rates, fatigue crack propagation is thought to be primarily controlled by the static failure modes that occur ahead of the crack tip (Gall *et al.*, 1999). Particle failure, for example debonding of the particle/matrix interface and particle fracture, provides a weak path via which a fatigue crack may propagate (Lee *et al.*, 1995). Lados (2004) demonstrated that in eutectic and hypoeutectic AlSiMg alloys, toughness (K_Q) was inversely proportional to the Si content. At high *da/dN*, when particle fracture is more likely (Gall *et al.*, 1999), the number of particles that failed ahead of the crack tip in each alloy was related to the V_f of particles in the alloy. The eutectic alloy, which contained the highest quantity of Si, exhibited the most particle failure providing a relatively weak path for propagation and therefore the lowest K_Q (Lados *et al.* 2006).

Joyce *et al.* (2002) demonstrated that increasing the quantity of alloying additions caused a corresponding decrease in the toughness (K_Q), this was again attributed to an increase in the amount of particle failure and the relatively weak path this provides. In Figure 6-14 the LVD25 alloy and those of Joyce *et al.* (2002) are compared; LVD25 contains the highest quantity of alloying additions and the lowest K_Q value, and so is consistent with the trend observed by Joyce *et al.* (2002).

The fatigue crack propagation curves of LVD26 unmod and LVD26 mod above a *da/dN* of 1×10^{-5} mm/cycle were similar. Sr modification and the effect this had on the morphology of the Si particles did not appear to affect fatigue crack propagation. This

is consistent with the work of Lados (2004) who showed that in mid Si alloys fatigue crack propagation was independent of the Si morphology in the *da/dN* range from $1x10^{-5}$ mm/cycle to $1x10^{-3}$ mm/cycle, as can be seen in Figure 6-13. However, contrary to the findings of Lados (2004) the lowest Si alloy (LVD27) did not have the highest K_Q value and exhibited similar fatigue propagation rates to the LVD26 alloys. This indicates that there is either one microstructural feature which is common to the LVD26 and LVD27 alloys which controls fatigue crack propagation at high *da/dN* or that several competing mechanisms occur, which compensate for each other so that fatigue propagation rates are ultimately similar. It is therefore worth considering the micromechanisms of fatigue propagation that occur in these alloys in more detail.

As a fatigue crack propagates under constant load amplitude conditions, ΔK increases. Therefore the size of the corresponding plastic zone ahead of the crack tip also increases and a greater quantity of hard particles will be sampled. The number of static failure events at hard particles ahead of the crack tip is a function of both the number of particles sampled and the probability of the particles failing. This probability is linked to the distribution of stresses in the plastic zone, which are determined by the size, shape, morphology and mechanical properties of the particles in the plastic zone.

For a given microstructure, the level of particle fracture will only be related to the size of the plastic zone and so with an increase in ΔK more particles would be expected to fail ahead of the crack tip. Increased roughness (larger deflections) is possible as the crack will be attracted towards the failed particles in the larger crack tip process zone; this was observed (Figure 5-69). Whilst the number of static failure events ahead of the crack tip may be high near final failure, the quantitative analysis performed on the fracture profiles indicates that the number of particles sampled by the crack is the same that a straight line would sample in the bulk alloy (see Figure 5-68). This is contrary to the work of Joyce (2002b) who used a line-counting approach to show that the number of particles on the crack path was greater than average. However, in this study the particles on the fracture profile are fractured in such a way that their line fraction (and therefore area on the fracture surface) is larger than average (Figure 5-67). In addition there is less distance between the particles (Figure 5-66).

In a discrete particulate system the larger than average $L_{3(FP)}$ would provide two possibilities 1) the crack propagated via larger particles or 2) the distribution of failed particle sizes followed that of the average distribution but they failed at wider sections. But in an interconnected particulate system, like those investigated in this study, it is difficult to define characteristic particle sizes. L_3 is a useful measurement that can be obtained from 2-D data and is representative of a statistical average particle intercept distance, but it does not reflect the 3-D nature of the hard particle network. X-ray CT data showed that at low *da/dN* (in short cracks) damage occurred ahead of the crack tip and the level of damage scaled with ΔK. The hard particle network failed in many places ahead of the crack tip and the average $L_{3(FP)}$ at low *da/dN*s indicates that the size of the failed sections follows a normal distribution. At high *da/dN*s the larger plastic zone means that the crack can meander further (than at low *da/dN*) to seek out the lowest stress path. Larger failed sections shield a greater proportion of the material either side of them and so provide a preferable path for fatigue crack propagation. Propagation via these larger failed sections of the hard particle network is consistent with the larger than average $L_{3(FP)}$. The roughness results (Figure 5-69) indicate that deflections were larger in each alloy at high *da/dN* (compared with low *da/dN*) suggesting that the crack was more mobile in searching out a preferable route.

Each alloy contained different microstructural features, for example LVD25 contained a coarser intermetallic network than the other alloys, Si particles in LVD26 exhibited a different Si morphology to LVD25 and LVD26 unmod and LVD27 contained no Si particles. As previously discussed in chapter 6.3.1 the different features are likely to have a significant effect on the micromechanisms of fatigue propagation in these alloys. For example the X-ray CT data of the LVD27 short crack showed that less particle fracture was observed ahead of the crack, which may be advantageous because the anti-shielding effect caused by static failure events will be lower, but also the crack impinges on fewer particles which may enable faster crack growth. At high *da/dN*s the different mechanisms controlling fatigue crack growth appear to be mutually compensatory in LVD27 and the LVD26 alloys. Relating high *da/dN* behaviour and K_Q to the Si level is an oversimplification in these alloy systems because of the complex nature of the microstructure and therefore the different fatigue crack propagation mechanisms that occur.

The worse performance of LVD25 cannot be attributed to a greater number of particles or a greater line fraction of particles along the crack. It may also not be attributed to the size of the particle intercept distance, as this was larger in LVD26 unmod. It therefore seems likely that a different balance of shielding/anti-shielding mechanisms account for the performance of LVD25. For example, the LVD25 crack was less rough than that of the LVD26 alloys at high *da/dN* and therefore experienced less shielding from deflections and RICC. In addition other shielding mechanisms such as crack bridging by intact particles may be less prevalent in LVD25. To confirm these mechanisms further investigation would be required which due to resource (time) constraints has not been possible in this study. It seems clear, however, that the trend in crack growth rate is related to a greater number of factors than simply the respective Si content of these alloys.

6.3.5 350˚C long fatigue crack propagation

Long fatigue crack propagation tests were performed at 350˚C. This higher test temperature is representative of the upper temperature limit that automotive diesel engine pistons experience in-service. At this temperature the 0.2% proof strength is approximately 50% lower than at RT, consequently at 350˚C the plastic zone size is larger. Use of *K* at 350˚C is questionable because LEFM conditions are not likely to be valid at any point during propagation in these materials due to a lack of elastic constraint. Using the Irwin (1957) method, the plane stress plastic zone size at the start of the growth out phase in LVD25 was ~ 1.6 mm. Considering that the sample size was 12 mm, it can be seen why a lack of elastic constraint was expected. (n.b. The Irwin (1957) method of calculating plastic zone size assumes small-scale yielding conditions apply and so uses K_{max}. However, since it is believed that small scale yielding does not apply it is also likely that this value of plastic zone size is inaccurate.) Assessment using *J* was not possible because of the necessary experimental equipment (high temperature clip guage) was not available. Because of the uncertainty over LEFM conditions the samples were pre-cracked to the same length (estimated from p.d. readings) and grown out to failure under the same constant load amplitude conditions, this enabled a comparison of propagation behaviour.

6.3.5.1 350˚C low *da/dN* behaviour

Threshold *da/dN* was not obtained in these alloys, therefore the samples were sectioned at the lowest *da/dN* possible, which was approximately $3x10^{-6}$ mm/cycle. Different micromechanisms of fatigue may be expected to occur at 350˚C compared with that at RT. As previously mentioned these alloys contained a larger plastic zone *c.f.* that at RT and so a larger volume of hard particles may be sampled in the plastic zone. However, at 350˚C load transfer from the Al-matrix to the hard particles was expected to be lower because of the considerably reduced flow stress of the Al-matrix at 350˚C (inferred from the nanoindentation results of Chen (2006) in Table 4.4). As a result, whilst more particles are sampled there is likely to be a lower probability that a particle will fracture. Previous research (Joyce *et al.,* 2002b) suggests that at high temperature, debonding is the primary mechanism of fatigue propagation at low *da/dN* and that the crack is expected to avoid hard particles. In addition damage due to time dependent processes may be expected at these temperatures (Myers and Hurd, 1990), this can take the form of voids formed due to Si or intermetallic particle fracture or decohesion. It has not been possible to separate the contributions of fatigue and creep in these experiments but Joyce *et al.* (2002) showed that another high Cu and Ni containing alloy (AE160, Table 6-1) did not exhibit a time dependence effect on fatigue crack propagation and so fatigue was expected to be the dominant cyclic failure process in the alloys investigated in this study.

X-ray CT data (Figures 5-78 and 5-79) showed that damage occurred ahead of the crack tip in LVD25 at low *da/dN*. Both particle fracture and debonding of the particle/matrix interface were observed. It was not possible to ascertain which was the principal failure mechanism but it was clear that a sufficient level of stress could develop in the hard particles to cause fracture. Cracks appeared to propagate via the linkage of the micro-damage and, as in the room temperature tests, the crack tip may be described as a region of micro-damage connected by intact ligaments. The ligaments were comprised of both the Al-matrix and sections of the hard particle network.

In all the alloys the crack preferentially avoided the hard particle network (Figure 5-76). However, in LVD25 and both LVD26 alloys the crack propagated via larger than average, failed sections of the hard particle network so that the line fraction of hard

particles on the fracture profiles was within one standard deviation of the average value (Figure 5-73). The X-ray CT data showed that the LVD25 crack had a rough appearance and the quantitative analysis of the fracture profiles confirmed that all three alloys exhibited a rougher crack at 350˚C than at RT (compare Figure 5-69 and Figure 5-77). The higher roughness indicates that at 350˚C the cracks were able to make large deflections, because of the larger plastic zone, in order to propagate via the route of least resistance. This route appears to be via statistically larger sections of micro-damage (because they provide the lowest stress path shielding more material around them) and propagation through the matrix avoiding hard (and high *E*) particles when possible (Padkin *et al.,* 1987 and Figure 6-6b). It is likely that all three particle interactions (Figure 6-3 b, c and d) occur but avoidance of hard particles is more prevalent at 350˚C than at RT.

The LVD27 alloy differs from the others in that whilst it preferentially avoided hard particles, the ones via which it did propagate were of approximately the same size as the average particle size ($L_{3(B)}$) in the alloy (Figure 5-75). This indicates that the fatigue cracks in LVD27 (at low *da/dN* and 350˚C) propagate in a different manner to those in the other alloys studied. In the LVD27 short crack sample, it was shown that a low level micro-damage occurred ahead of the crack tip (Figure 5-53), and this was primarily associated with failure at clusters of intermetallic phases. A similar low level of micro-damage may be expected at 350˚C. Therefore the crack is likely to make fewer large deflections since there is less micro-damage to coalesce with. This is reflected in the roughness value of the crack at low *da/dN* (Figure 5-77), which is low compared to the other alloys at 350˚C and compared to LVD27 at RT. Whilst the crack may avoid hard (high *E*) particles, the 3D interconnected intermetallic network in this alloy means that at all operating temperatures particle fracture is still necessary to ensure a level of crack continuity and so the crack/particle interactions described in 6.3.1 still occur.

It is difficult to assess the relative performance of the alloys for two reason: 1) the behaviour of the alloys between the threshold and the minimum *da/dN* obtained in these experiments is unknown and 2) because the samples were grown to different crack lengths they experienced different loading histories with quicker turn downs in LVD26 unmod and LVD27 compared with the other two alloys. It is not clear from

these results if this has an effect on the low *da/dN* behaviour. The alloy, which exhibited the best performance at RT and low *da/dN* was LVD26 unmod but at 350˚C this alloy exhibited the worst low *da/dN* behaviour. The quantitative analysis provides no clear explanation for the poor performance of LVD26 unmod. Further investigation is clearly required to ascertain if there is a true difference in the performance of the alloys at low *da/dN* or if the results simply reflect a transient due to the loading history.

6.3.5.2 350˚C high *da/dN* behaviour

At high *da/dN*, micro-damage formed ahead of the crack tip in the LVD25 sample (Figure 5-80). However, whilst the crack was rough the damage was locally confined to a narrow band (approximately ± 75 μm in the tensile direction) in front of the crack. The crack appeared to form along three dominant planes. It was not possible to associate this with any particular microstructural feature but this type of crack growth is reminiscent of that observed in the LVD27 short crack sample (Figure 5-53b), i.e. a low level of micro-damage close to the contiguous crack tip with local crack advance at the micro-damage. In-between the dominant planes the contiguous crack 'lagged' behind and so these regions were comprised of micro-damage, which formed perpendicular to the tensile direction with intact ligaments in-between. The intact ligaments eventually failed forming sections of the crack that were parallel to the tensile direction.

Quantitative analysis showed that the crack preferentially avoided hard (high *E*) particles, but in all the alloys the particles it encountered were within one standard deviation of average particle size in the respective alloys. This represents a change in the method of crack propagation from that observed at low *da/dN* in LVD25 and both LVD26 alloys, but not in LVD27. The observations of fatigue crack growth (from the X-ray CT data) for LVD25 at high *da/dN* are consistent with the proposed method of crack growth in LVD27 at low *da/dN*, i.e. low level of micro-damage and avoidance of hard particles, although larger deflections were observed due the larger plastic zone.

The lower level of particle failure at high *da/dN* (*c.f.* low *da/dN*) is counter-intuitive. The larger plastic zone samples a greater number of particles and so more particles

may be expected to fail. For particle failure to occur the stress either in the particle or at the particle/matrix interface must reach a critical value. This may occur on the first loading cycle or it can be as a result of an accumulation of dislocations around the particles because of multiple cycles (Fan and Hao, 2004b), which gradually increase the local stresses at and around the particles. At high temperature dislocations are more mobile (Dieter, 1988), this can limit the dislocation density around the particles thereby causing a lower level load transfer compared with that at lower temperatures. If the critical stress for particle failure is dependent on an accumulation of dislocations as a result of fatigue loading, then at higher temperatures the increase in dislocation mobility implies that dislocation pile-up will be slower and require a greater number of cycles. Considering a section of the material in the plastic zone 100 μm ahead of the crack tip: at the low *da/dN* investigated ($3x10^{-6}$ mm/cycle) this region will undergo approximately 33000 cycles before it is engulfed by the crack. However, at a high *da/dN* (for example at $1x10^{-4}$ mm/cycle) the region will only undergo approximately 1000 cycles before being engulfed by the crack. Therefore at high *da/dN* the dislocations required to produce the critical stress for particle failure may not have time to accumulate before the section of material is engulf by the crack. This may account for the lower level of particle failure observed at high *da/dN* compared with low *da/dN*.

As discussed in previous sections there are several possible particle interactions that may occur in these alloys. Fractured and debonded particles were found ahead of the crack tip and there are also intact sections, which are likely to block or deflect the crack. Since there is no single mechanism of fatigue crack propagation in these alloys, there are no clear trends between the crack propagation behaviour (Figure 5-70). For example at final failure the performances of LVD25 and LVD27 are similar even though the alloys contain very different microstructures. The different micromechanisms of fatigue that occur in each alloy have different effects on fatigue crack propagation. As previously discussed some of these mechanisms shield the crack tip and other mechanisms cause anti-shielding and in these alloys are mutually compensatory.

Whilst the LVD25 and LVD26 unmod cracks exhibited similar levels of roughness (and so similar levels of shielding from deflections and RICC) the LVD25 alloy

exhibited better performance (failing with a smaller uncracked ligament). Whilst more particles may be expected to fail ahead of the crack tip in LVD25, because of the higher V_f of particles in the alloy, more particles also impinge on the fatigue crack. Since a lower level of particle fracture is expected at high temperature and *da/dN* the shielding caused by particles impinging on the crack may be the more dominant mechanism and so the lower volume of hard particles in LVD26 may account for its worst performance. From these results it has not been possible to separate the mechanisms of crack propagation that occur, but it has provided a greater understanding of the expected mechanisms in what are microstructurally complex alloys.

6.3.6 Comparison of long and short crack propagation at RT

Long and short fatigue crack propagation curves are compared in Figure 6-15. Short crack growth occurred at *da/dN*s higher than that of the long crack data and therefore at ΔK values below the (long crack) ΔK_{th}. In LVD25 the short and long crack propagation curves converged just before final failure. However, the LVD26 unmod curves did not converge and although the final stages of crack propagation were not captured for LVD26 mod and LVD27, the trend of their curves suggests that they would not converge with the long crack data either. This is not consistent with the classical short crack behaviour as described by Suresh (1998) where convergence between long and short crack data are expected in the lower part of the 'Paris' region.

The difference between the long and short crack fatigue propagation curves is often attributed to the non-validity of LEFM conditions (Suresh, 1998), and therefore ΔK, due to a lack of elastic constraint around the crack (i.e. a, B and $W\text{-}a < 2.5(K_{max}/\sigma_y)^2$ from BS 7448-1:1991). Because of the low 0.2% proof strengths of these alloys the British Standard condition is not met for a large proportion of fatigue crack propagation in either the short or long crack samples. For example, in the long fatigue crack propagation tests, $W\text{-}a < 2.5(K_{max}/\sigma_y)^2$ at ΔK values greater than 5 MPa$\sqrt{m}$. And in the short crack propagation tests $a < 2.5(K_{max}/\sigma_y)^2$ at all times. Because ΔK is equally invalid for all the alloys in the long fatigue crack propagation tests it is possible to compare between the alloys, and likewise in the short crack tests. But

similitude cannot be expected between the short and long crack propagation tests and this is likely to account for the lack of convergence between the data in Figure 6-15.

Anomalies between the short and long crack data have also been attributed to differences in the RICC mechanism (Suresh, 1998). For RICC to occur the crack must propagate a certain distance to allow the necessary roughness to develop (Singh, 2005). Therefore RICC may be expected to be initially lower in short cracks. However, in the short crack tests performed in this study the cracks were microstructurally large for the majority of crack growth and deflections were observed soon after initiation. The roughness of the first 400 μm of a small crack in each alloy was measured (the ratio of the crack length to the projected crack length) and the results are presented in Figure 6-16. It can be seen that the low *da/dN* roughness values from the long fatigue crack test and the short fatigue crack tests are similar indicating comparable levels of roughness and therefore RICC. It is therefore unlikely that RICC accounts for the anomaly in the short and long fatigue crack propagation curves.

6.3.7 Propagation lifing of AlSi casting alloys

The concept of similitude in fracture mechanics implies that there is an intrinsic value of ΔK_{th} for each material regardless of the geometry of the sample or crack. However, as shown in this work, short fatigue crack growth occurs at values of ΔK below ΔK_{th}. Therefore, using long crack data to provide lifetimes for the propagation of small cracks would lead to an overestimation in life. Kitagawa and Takahashi (1976) demonstrated that there is a critical crack length (a_0) below which ΔK_{th} decreases proportionally with a. It was also shown that for a range of engineering materials the threshold condition could be characterised by a critical stress ($\Delta\sigma_{th}$), which when $a<a_0$ was constant and equal to the fatigue limit (σ_e see Table 5.1). It is therefore possible to calculate a_0 from experimental data:

$$a_0 = \frac{1}{\pi}\left(\frac{\Delta K_{th}}{\sigma_e}\right)^2 \tag{6-4}$$

Equation (6-4) may be used as an indicator to determine if a crack is ‘small’; if the measured a is less than a_0 then it may be classified as small. Using the experimental

values from chapter 5, a_0 can be calculated as approximately 200-300 μm. El Haddad *et al.* (1979) suggested that a_0 could be added to the measured a, as an empirical parameter, to provide a method of calculating ΔK which is independent of crack size:

$$\Delta K_{\mathrm{mod}} = Q\Delta\sigma\sqrt{\pi\left(a + a_0\right)} \tag{6-5}$$

where Q is a geometry correction factor. Equation (6-5) was used to calculate ΔK_{mod} for the short crack data and the results are plotted, along with the long crack propagation curves, in Figure 6-17. The curves collapse so that the short crack data have a similar trend to the long crack data. Between da/dN=1x10^{-7} to 1x10^{-5} mm/cycle the LVD26 unmod curves are similar. However, above da/dN=1x10^{-5} mm/cycle the LVD26 unmod curves diverge. Fatigue crack propagation in the other three alloys occurs at higher da/dNs than in the long crack case for all values of ΔK.

The method of El Haddad *et al.* (1979) provides an approach for using long fatigue crack propagation data and S-N data (which are easier to obtain than short crack propagation data) to estimate the lifetime for a short crack to propagate from an initiation event to final failure. For example by using ΔK_{mod} in the Paris law:

$$\frac{da}{dN} = C\Delta K_{\mathrm{mod}}{}^{m} \tag{6-6}$$

where C and m are taken from the long crack propagation curves (Table 5.3), and combining equations (6-5) and (6-6) it is possible to integrate between the bounds a_i+a_0 and a_f (a_i is the size of the crack when first detected and a_f is the size of the crack when the sample failed). Whilst Q is dependent on a it was reasonably constant over the lifetime of the crack at 0.70±0.1, by treating this as a constant the integration is easier and the propagation lifetime (N_p) can be calculated using:

$$N_p = \frac{2}{(m-2)CQ^m\Delta\sigma\pi^{\frac{m}{2}}}\left[\frac{1}{(a_i + a_0)^{\frac{m-2}{2}}} - \frac{1}{a_f{}^{\frac{m-2}{2}}}\right] \tag{6-7}$$

Lifetime predictions were made for two cracks from each short crack sample; the results are presented in Table 6-2. Initiation was not considered in these predictions since and the a_i, and measured N_p values were taken from when the crack was first

observed on the acetate replicas ($N_p=N_f-N_i$). For a total life prediction, particularly in the high cycle regime, prediction of the initiation life is clearly important but is unfortunately not within the scope of this study, as this would require a statistical study for example the monte carlo approach used by Yi *et al.* (2003; 2006). The errors in the lifetime predictions, because of the assumption that Q is constant, are given in Table 6-2. The predictions are sensitive to both a_i and a_f but these can be measured accurately from the short crack samples.

In all the alloys the lifetime was over predicted. This is not surprising because the lack of similitude meant that after the El Haddad *et al.* (1979) correction, the short fatigue crack *da/dN*s were higher than those of the long fatigue cracks (Figure 6-17). There are also differences in the predicted lifetimes between the two cracks in a single sample for LVD25, LVD26 unmod and LVD27. These differences arise because this lifing method does not account for the non-continuum behaviour of short cracks, e.g. crack accelerations and arrests. Consistent with the closer crack propagation curves in Figure 6-17, the predictions for LVD26 unmod were the most accurate.

These results suggest that in materials with a low 0.2% proof strength, the non-validity of LEFM conditions results in a lack of similitude between the short and long fatigue crack propagation behaviour. Whilst the modification to ΔK suggested by El Haddad *et al.* (1979) collapses the curves somewhat, it is not possible to make accurate predictions using this non-LEFM data. The use of EPFM is a possibility, and was used by Lados (2004) to assess long fatigue crack propagation in Al-Si alloys. However, it is experimentally difficult to measure the displacement of a 'small' crack and this is required to calculate CTOD or J, so the use of EPFM is not straightforward.

The approach taken by Caton *et al.* (2001) and employed by Yi *et al.* (2006) uses short fatigue crack propagation data to predict propagation lifetime. This data is more difficult to obtain than long fatigue crack propagation data but is likely to provide more accurate results when LEFM conditions do not apply. Caton *et al.* (2001) demonstrated that for several A319 Al-alloys, which had undergone different heat treatments, the following relationship could be used to describe crack growth:

$$\frac{da}{dN} = C_1\left[\left(\frac{\varepsilon_{\max}\sigma}{\sigma_y}\right)^n a\right]^s \tag{6-8}$$

where ε_{max} is the maximum strain at the maximum stress (σ) and n is a fitting parameter that is used to collapse the data for different alloys onto a single curve; C_1 and s are the power law exponents of that curve. This is not a universal relationship and requires the parameters C_1, s and n be obtained from experimental data for each alloy.

The short crack propagation data are presented as a function of $[\varepsilon_{max}\sigma/\sigma_y]^n a$ in Figure 6-18. The data have been collapsed into a single band, the different alloys required different n values and these are given in Table 6-3. The C_1 and s values are the extrapolated values for a power law trend line through the band of data in Figure 6-18. Both LVD26 alloys may be represented by the same set of fitting parameters indicating that whilst n is material dependent it is independent, in this case, of the Si morphology. Caton *et al.* (2001) also showed the n value was insensitive to another morphological feature: SDAS. Because of the log-log linear relationship, equation (6-8) may be used to predict the life of short cracks by integrating between a_i and a_f so that:

$$N_p = C^{-1}\left(\frac{\varepsilon_{\max}\sigma}{\sigma_y}\right)^{-ns}\left[a_i^{\,s+1} - a_f^{\,s+1}\right] \tag{6-9}$$

The lifetimes of two cracks for each sample were predicted using equation (6-9); the results are presented in Table 6-3. Using the Caton *et al.* (2001) lifing method the results were not consistently underestimated as with the El Haddad *et al*. (1979) method. However, there was a large scatter in the results and so the predictions were no more accurate. This method does also not account for the non-continuum behaviour of short fatigue cracks, which are the likely cause of the scatter. Again, this illustrates the statistical nature of short fatigue crack growth, which is particularly sensitive to microstructural features. The difficulty in lifing using either long or short fatigue crack propagation data highlights that a greater understanding of the micromechanics of fatigue in this class of alloys is of particular importance as this may help inform a more physical based model and so improve lifing methodologies.

Alloy	Si (wt.%)	Cu (wt.%)	Ni (wt.%)	Mg (wt.%)	Fe (wt.%)	Mn (wt.%)	Ti (wt.%)	Zr (wt.%)	V (wt.%)	P (ppm)
AE160	11.22	3.1	2.27	1.05	0.3	0.08	0.17	0.15	0.06	53
AE413	11.15	0.94	0.96	0.88	0.49		0.07	-	-	35

Table 6-1 Compositions of the alloys studied by Joyce *et al.* (2003).

$\Delta\sigma$ (MPa)	153		144		153		119	
Q	0.7		0.7		0.7		0.7	
a_0 (m)	2.3E-04		2.3E-04		2.0E-04		3.0E-04	
m	7.2		4.9		4.7		4.8	
C (m/cycle)	1.5E-13		2.7E-12		4.0E-12		3.4E-12	
measured a_i (m)	27	10	70	65	55	35	200	160
measured a_f (m)	1.2E-03	1.0E-03	2.9E-03	5.2E-04	1.2E-03	7.9E-04	1.3E-03	7.1E-04
measured N_p	137000	97000	268500	138500	40000	40000	66000	66000
Predicted N_p	206222	244481	304832	179848	229517	236416	241105	166635
Error in prediction because of Q assumption	10%	7%	7%	7%	10%	7%	7%	7%
measured N_p / predicted N_p	0.66	0.40	0.88	0.77	0.17	0.17	0.27	0.40

Table 6-2 Lifetime predictions using equation (6-7).

$\Delta\sigma$ (MPa)	170		160		170		132	
ε_{max} (%)	0.71		1.03		1.10		0.55	
n	2		2.3		2.3		1.8	
s	1.82		1.82		1.82		1.82	
C_1 (m/cycle)	$3.6\text{x}10^{-5}$		$3.6\text{x}10^{-5}$		$3.6\text{x}10^{-5}$		$3.6\text{x}10^{-5}$	
measured a_i (m)	27	10	70	65	55	35	200	160
measured a_f (m)	1.2E-03	1.0E-03	2.9E-03	5.2E-04	1.2E-03	7.9E-04	1.3E-03	7.1E-04
measured N_p	137000	97000	268500	138500	40000	40000	66000	66000
Predicted N_p	194780	449545	222474	203025	180385	262629	49717	53673
measured N_p / predicted N_p	0.70	0.22	1.21	0.68	0.22	0.15	1.33	1.23

Table 6-3 Lifetime predictions using equation (6-9).

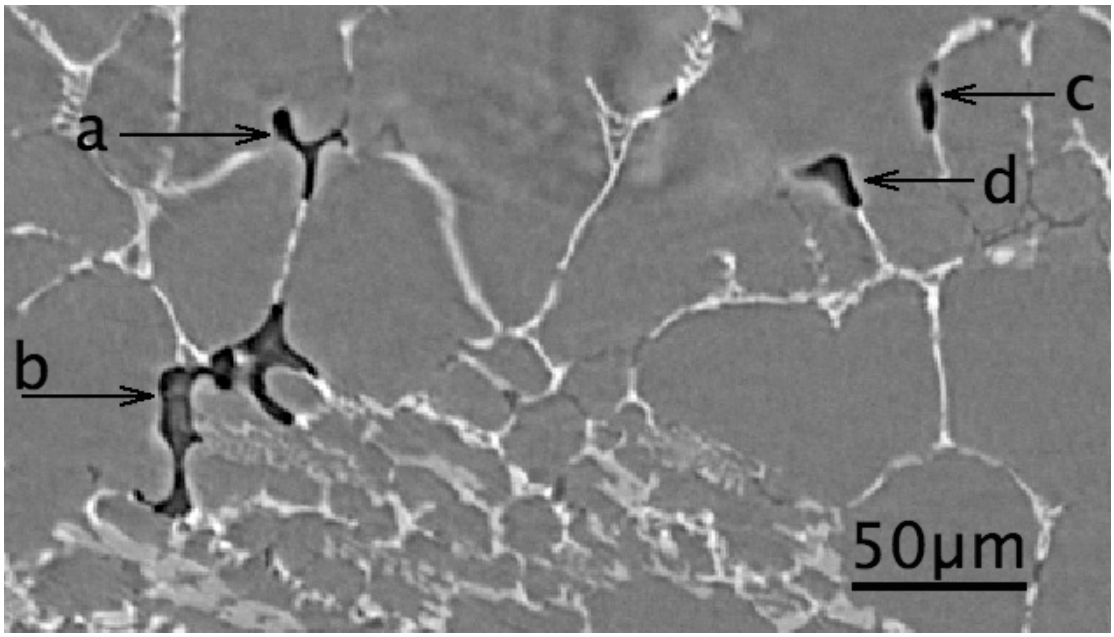

Figure 6-1 X-ray CT image of pores in LVD27, a to d are different pore sections but they are actually interconnected via a larger porous network in the bulk alloy.

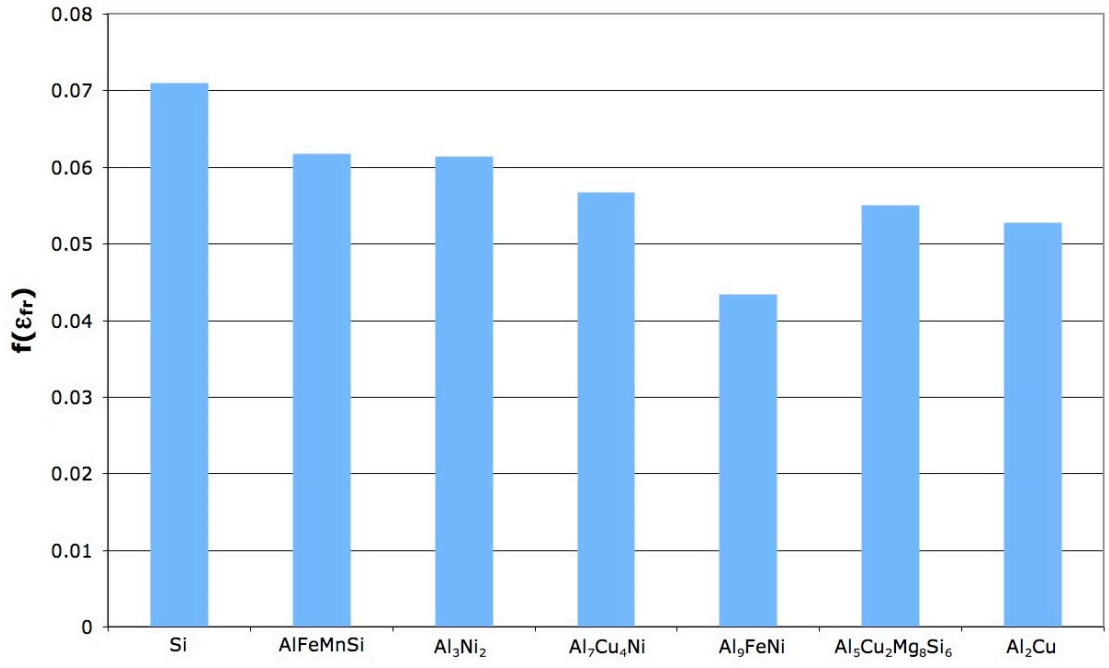

Figure 6-2 The relative fracture strains of the intermetallic and Si particles estimated from Nanoindentation data.

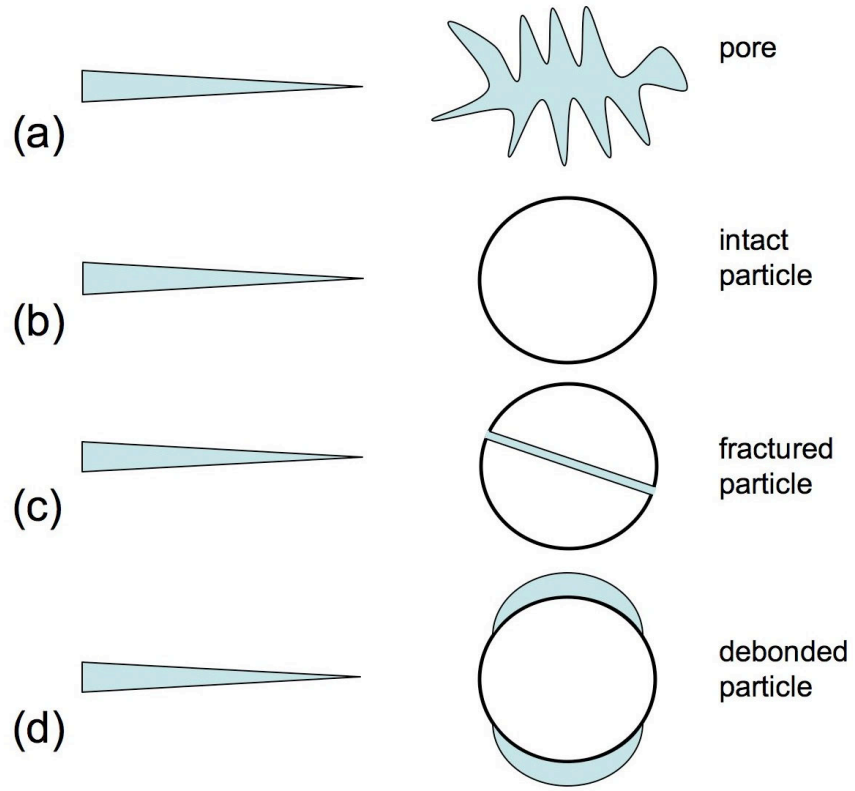

Figure 6-3 Schematic diagram of particle interactions with (a) a pore, (b) an intact particle, (c) a fractured particle and (d) a debonded particle.

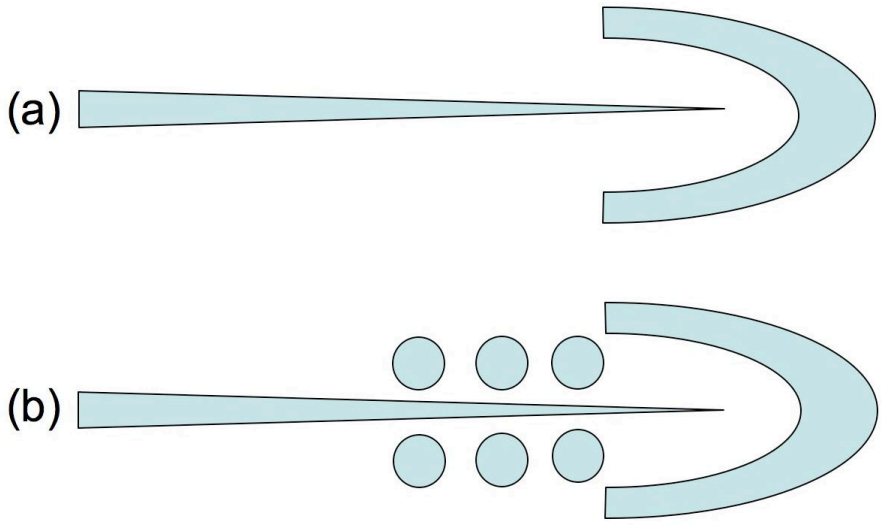

Figure 6-4 Schematic diagram illustrating how a crack may be (a) trapped by a particle of irregular shape and (b) channelled towards an irregular particle where it is trapped.

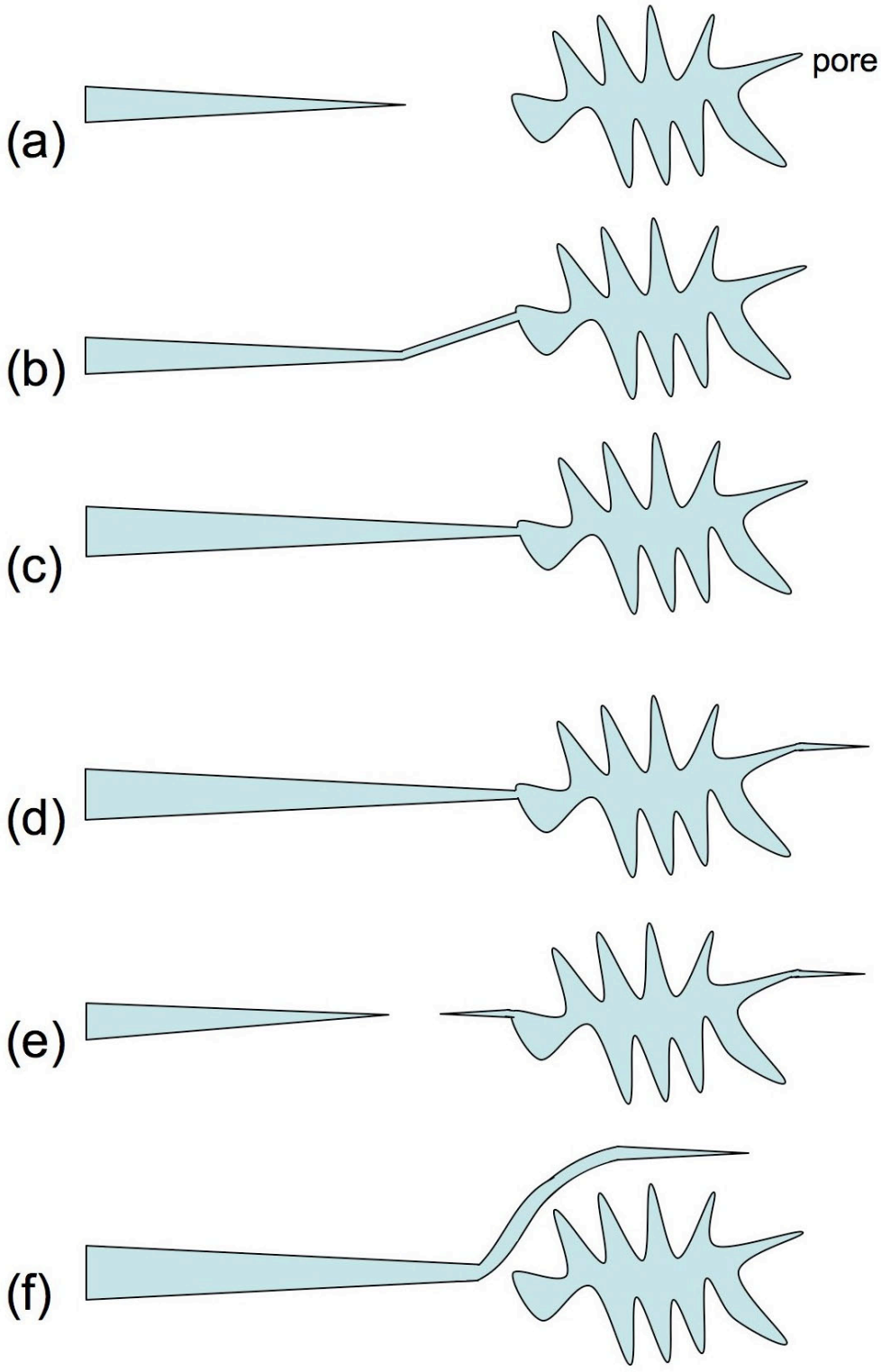

Figure 6-5 Schematic diagram of interactions between a crack and a pore (a) before the interaction, after which (b) the crack is attracted towards the pore, (c) local blunting of the crack tip retards crack propagation, (d) the crack reinitiates after being blunted (e) crack coalescence occurs and (f) the crack is deflected.

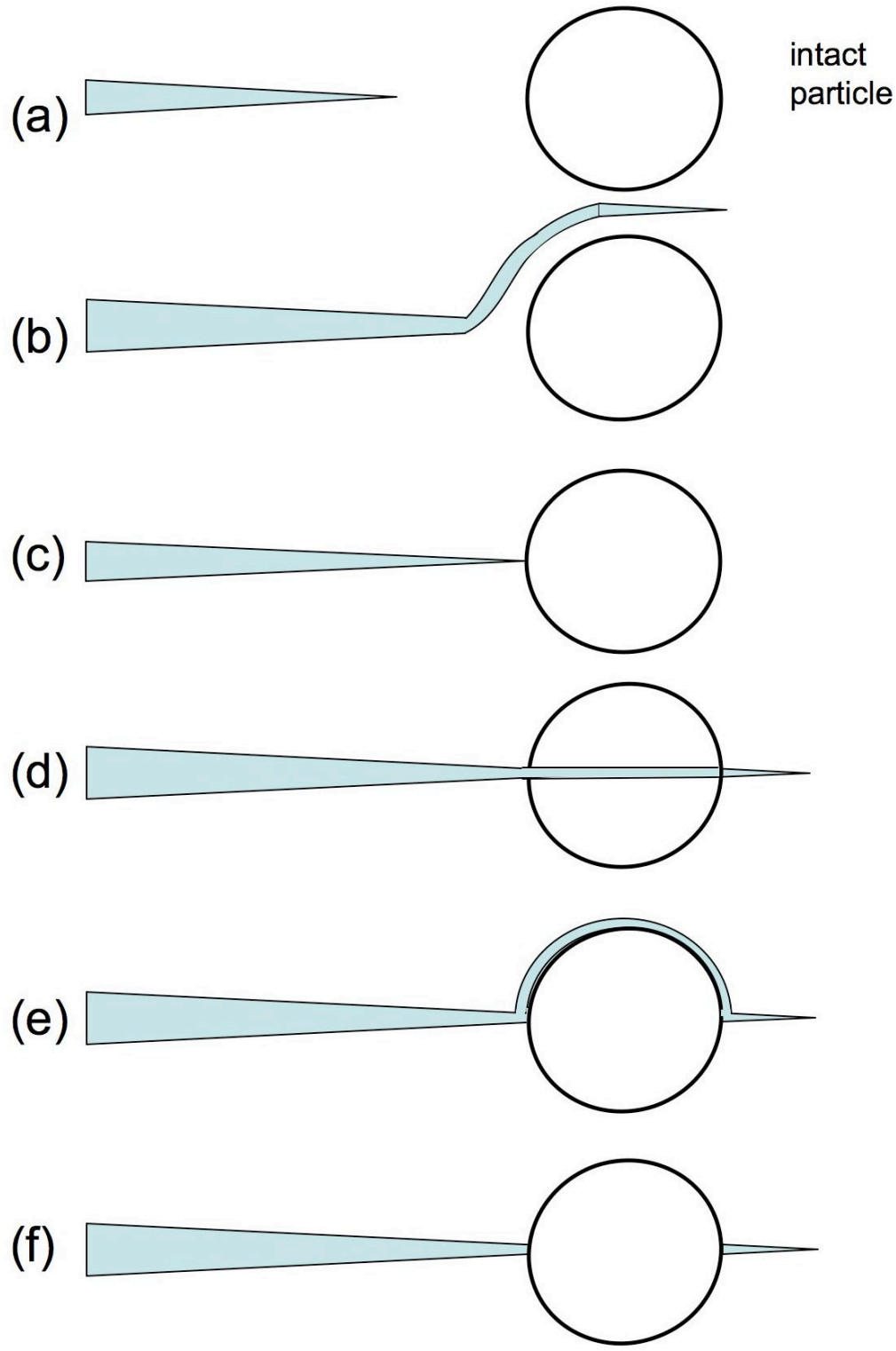

Figure 6-6 Schematic diagram of interactions between a crack and an intact particle (a) before the interaction, after which (b) the crack is deflected away from the particle, (c) the crack is stopped by the particle, (d) the particle fractures allowing propagation (e) debonding of the particle/matrix interface occurs and (f) the crack reinitiates on the opposite side of the particle.

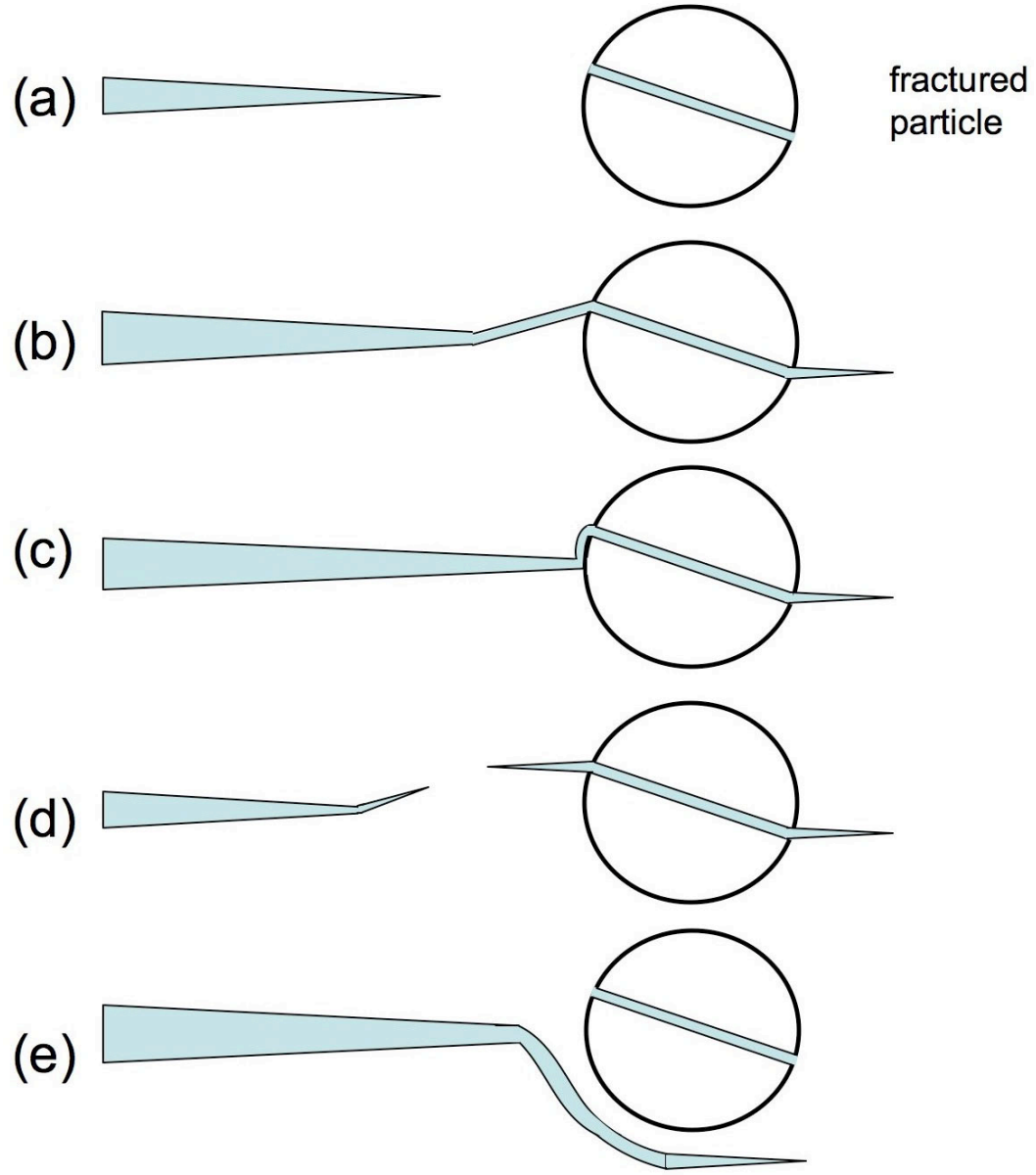

Figure 6-7 Schematic diagram of interactions between a crack and a fractured particle (a) before the interaction, after which (b) the crack is attracted towards the particle, (c) interfacial decohesion occurs before the crack propagates through the particle, (d) a micro-crack initiates at the fractured particle causing crack coalescence (e) the crack is deflected away from the particle.

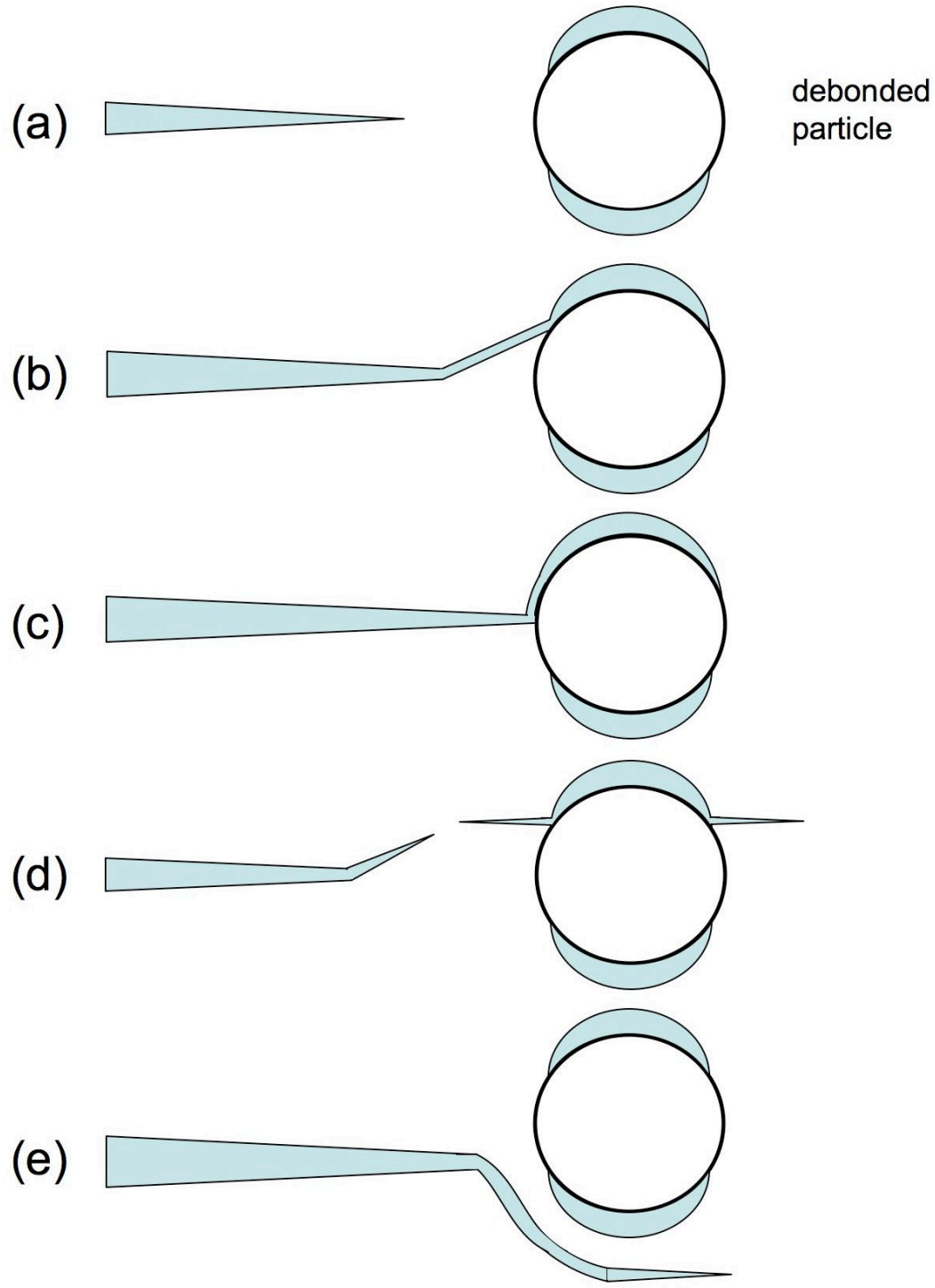

Figure 6-8 Schematic diagram of interactions between a crack and a debonded particle (a) before the interaction, after which (b) the crack is attracted towards the debonded region, (c) linkage of the crack and void by further debonding occurs, (d) a microcrack initiates at the debonded region causing crack coalescence (e) the crack is deflected away from the particle.

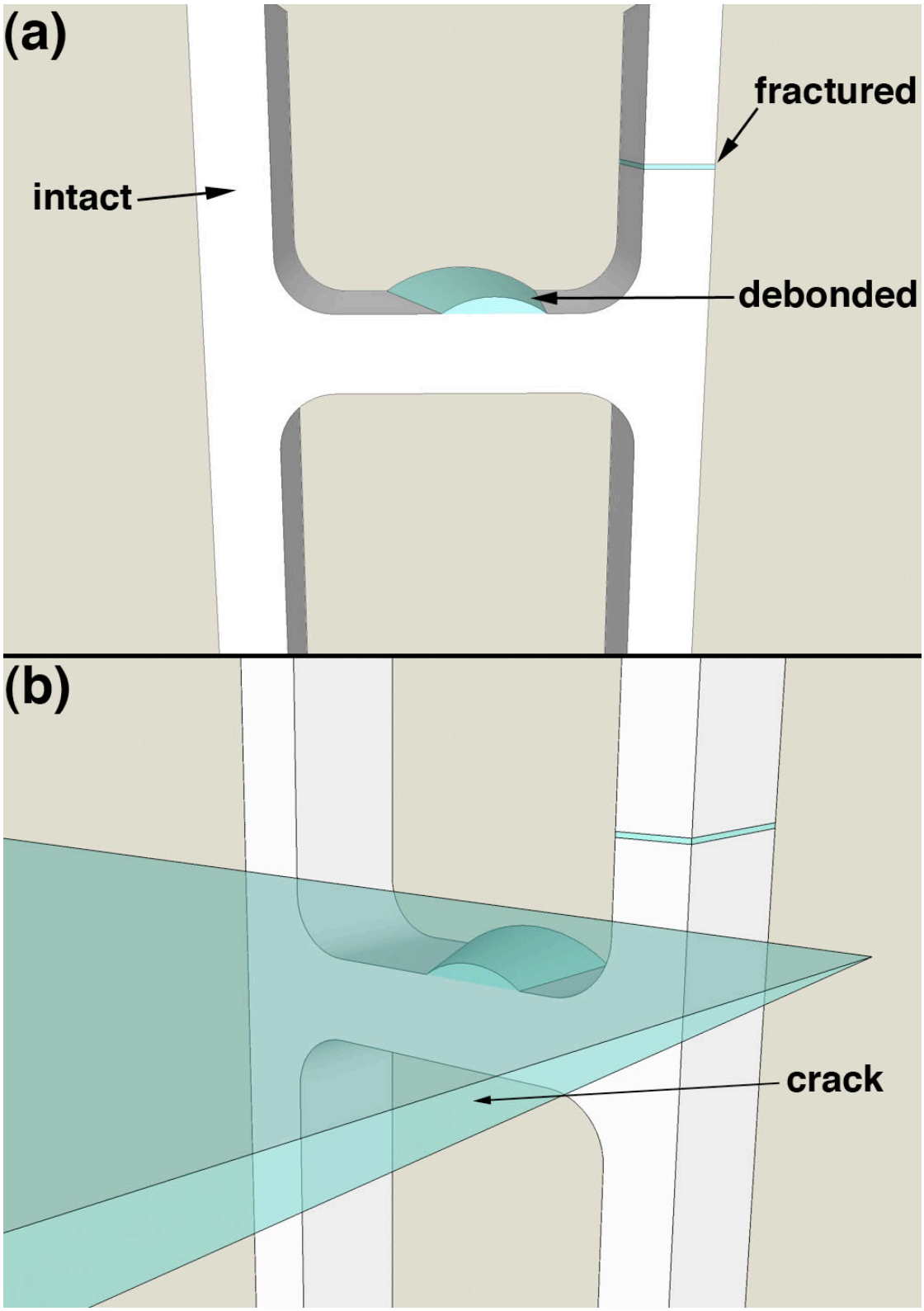

Figure 6-9 Schematic diagram showing the possible interactions between a crack and an interconnected particle (a) is a view of the particle from the crack tip and (b) is a view of the crack and the particle.

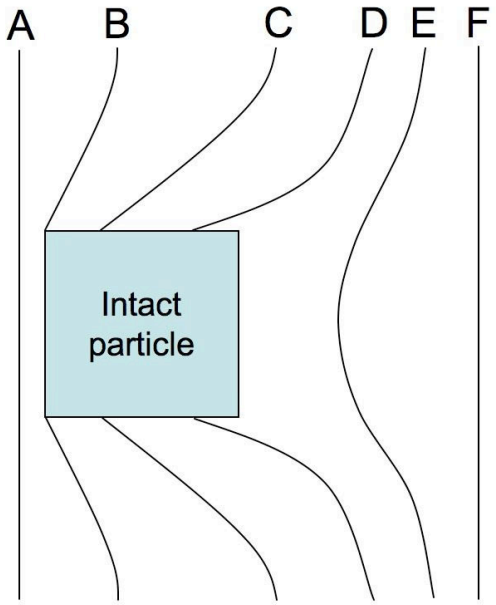

Figure 6-10 Schematic diagram illustrating how a particle may remain in the crack wake forming an intact ligament.

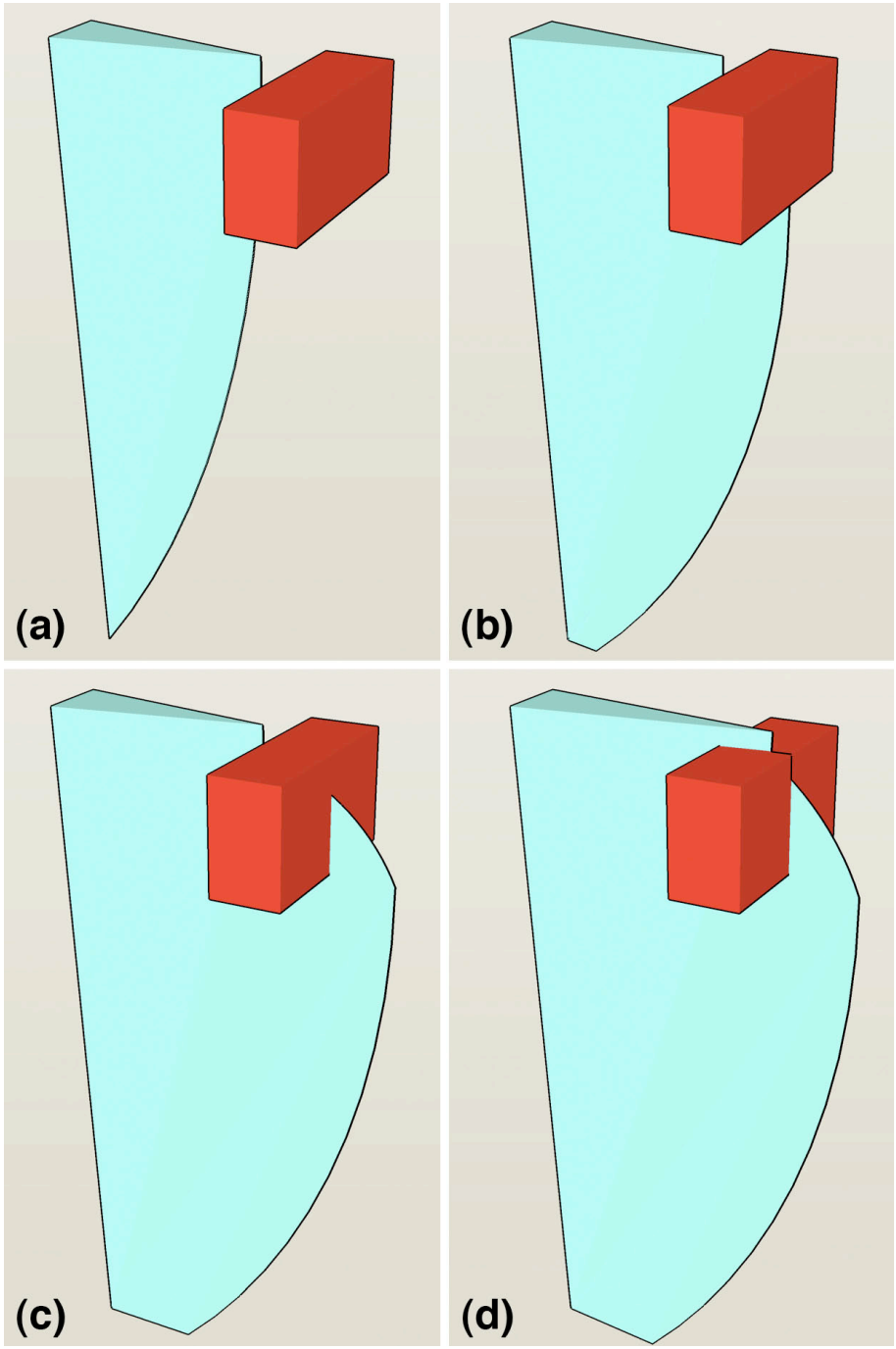

Figure 6-11 Schematic diagram illustrating how a particle may fracture as a crack advances past it (a) is at the point of contact between the crack and the particle, (b) the unblocked section of the crack has advanced so that it (c) engulfs the particles and eventually (d) fractures allowing the continuation of fatigue crack propagation.

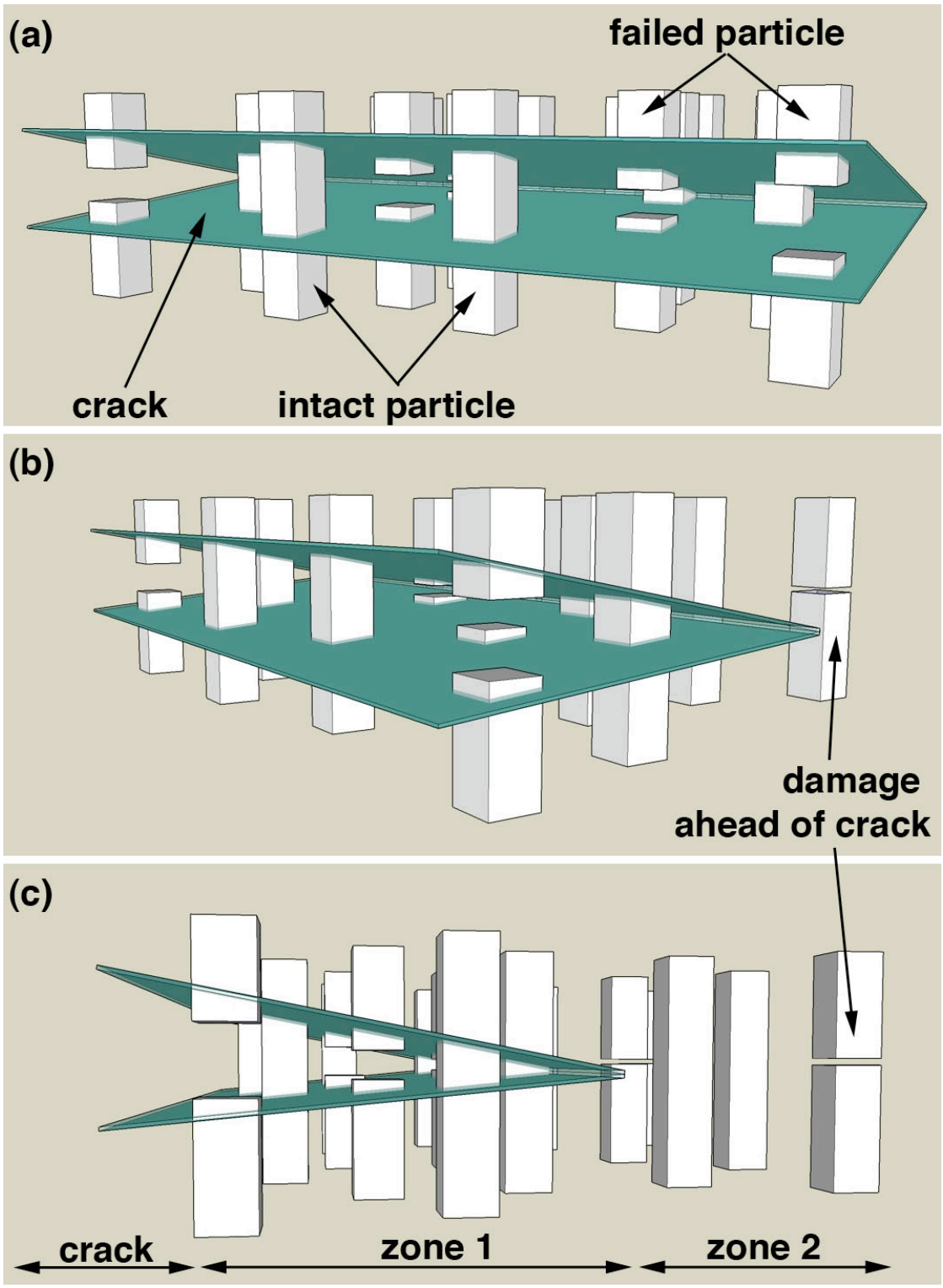

Figure 6-12 Schematic diagram of the situation in the crack tip region with micro-damage ahead of the 2-D projected crack and intact ligaments in its wake, (a) to (c) are the same image from different angles.

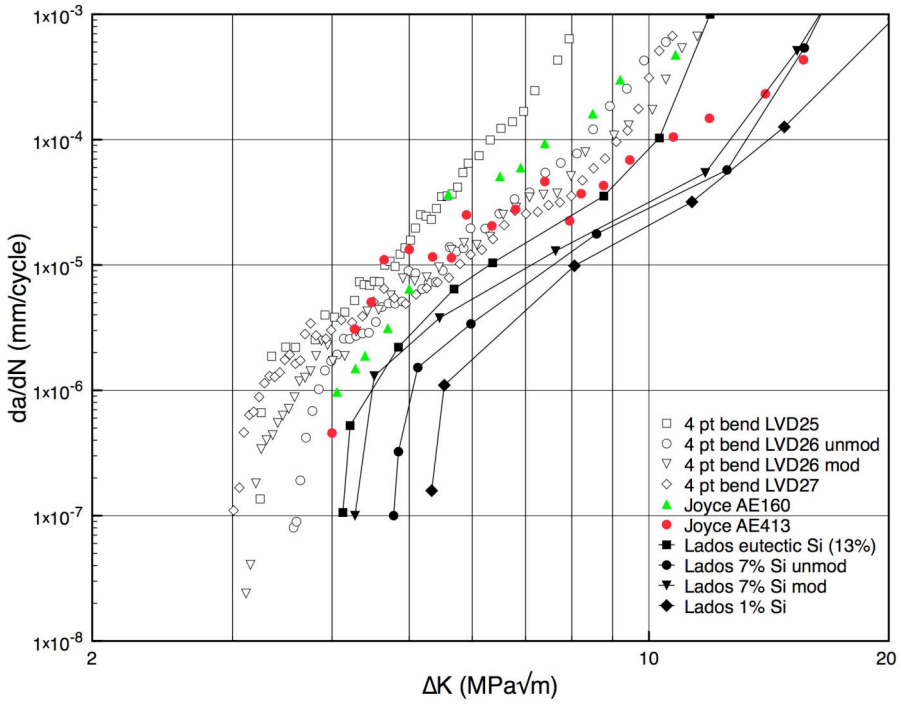

Figure 6-13 Long fatigue crack growth curves from this project, the work of Lados *et al.* (2006) and Joyce *et al.* (2002).

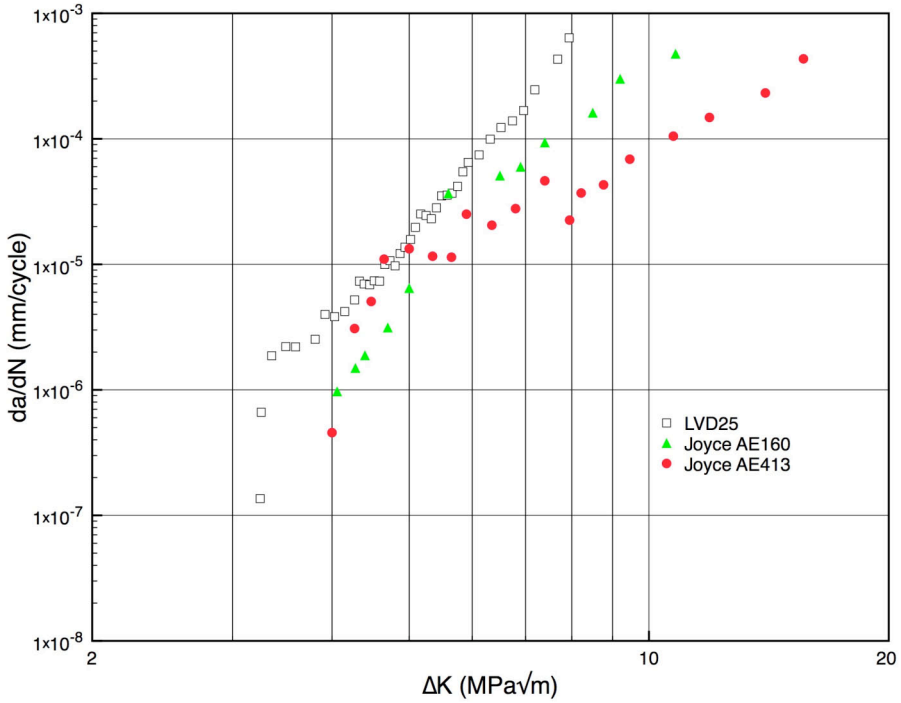

Figure 6-14 Comparison of the fatigue crack propagation curves of Joyce *et al.* (2002) and the eutectic LVD25 investigated in this study.

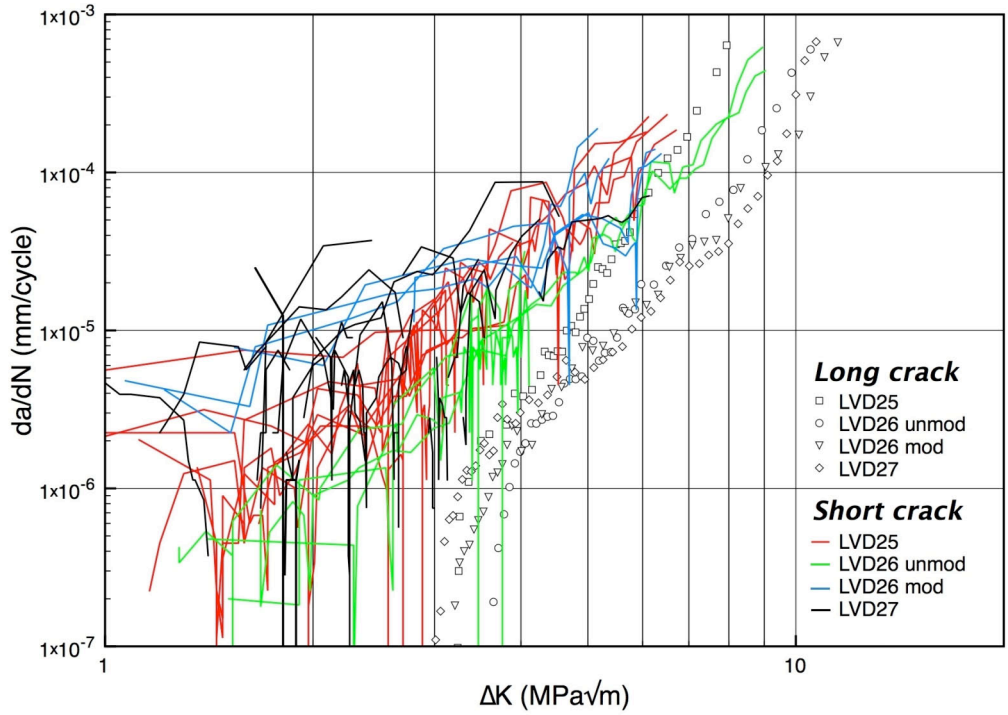

Figure 6-15 Comparison of short and long fatigue crack propagation curves.

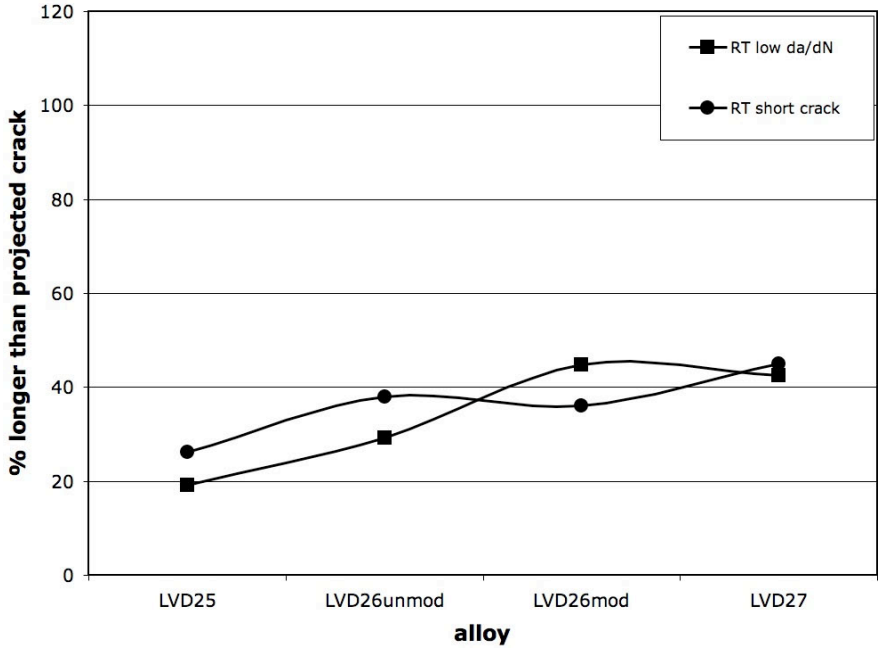

Figure 6-16 Comparison of roughness values for the first 400 µm of crack growth in the short crack samples and at low *da/dN* in the long crack samples at RT.

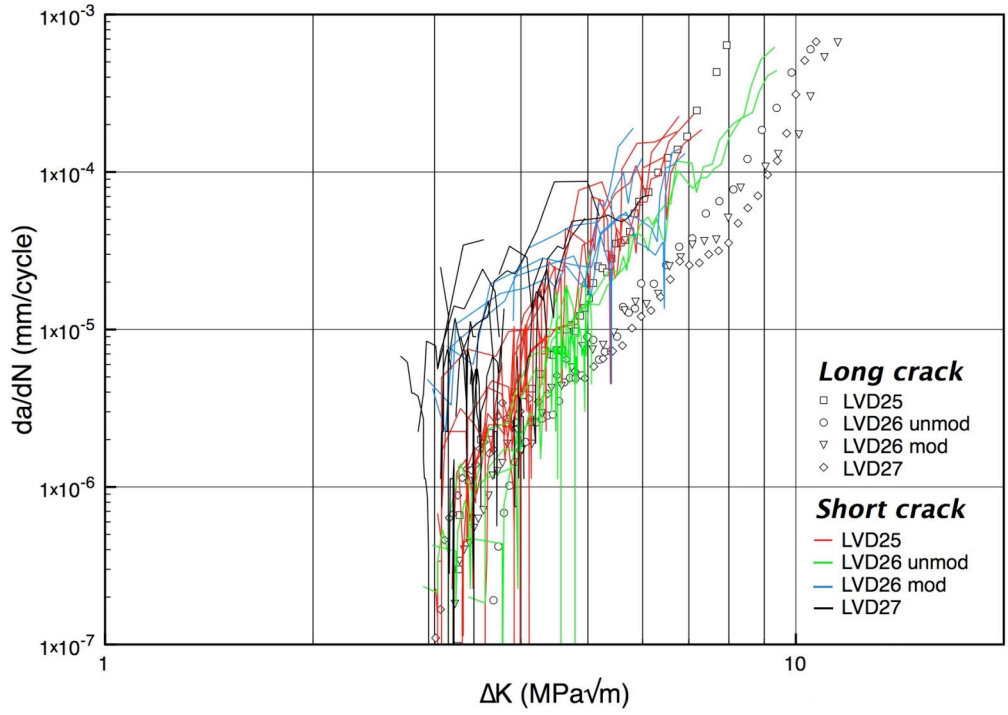

Figure 6-17 Comparison of short and long fatigue crack propagation curves where the short crack data has been modified using the method of El Haddad *et al.* (1979).

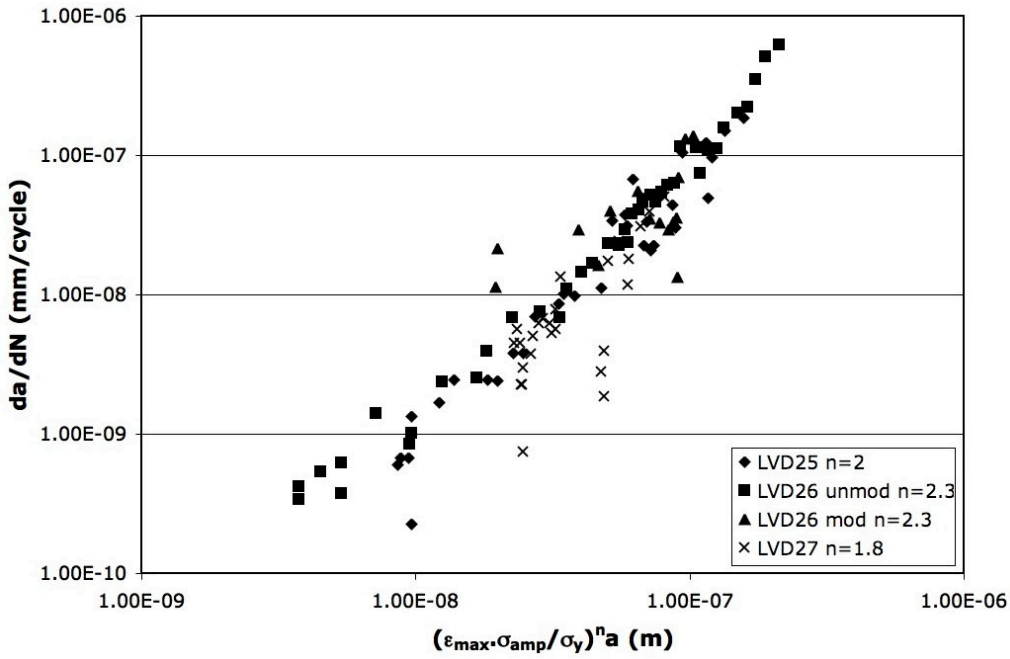

Figure 6-18 Small crack growth data correlated using the relationship $[\varepsilon_{max}\sigma/\sigma_y]^n a$.

Chapter 7

Conclusions

All the alloys investigated in this study exhibited complex, multiphase microstructures. The microstructural features can be grouped into four categories:

- Intermetallic phases,
- Si particles,
- α-Al matrix, and
- Pores.

Microstructural characterisation established that all the alloys investigated contained an interconnected network of hard particles, which formed in the interdendritic regions. The Si content influenced the formation of the dendrite size and morphology as well as the porosity levels in each alloy. This was primarily attributed to the increase in the temperature range of the 'mushy zone', i.e. the freezing range of the alloy, during the casting process as the Si level was reduced from the eutectic level.

Interdendritic pores were observed in all the alloys investigated. X-ray CT analysis revealed the complex 3-D shape of pores. Pores with a maximum dimension of greater than 200 μm were observed in all the alloys and such large pores contain many 'tips' which are associated with high stresses. Therefore, pores acted as potent fatigue crack initiation sites, particularly in LVD27 where porosity levels were highest. However, fatigue cracks were also observed to initiate at Si and intermetallic particles in the other alloys. It is also important to stress that the real sizes of the pores as revealed in 3-D were greater than their apparent size measured from 2-D sections.

The load transferred from the α-Al matrix to the hard particle network controls fatigue crack initiation at hard particles in Al-Si casting alloys. A first order analysis, using the modulus and the hardness (which was used as an estimation of strength)

obtained from nanoindentation, showed that using mechanical properties data alone the Al_9FeNi phase would be expected to fracture at the lowest applied stress. This simplistic analysis correlated well with experimental data; the short crack propagation tests revealed that the Al_9FeNi was the most detrimental phase causing fatigue crack initiation in both LVD25 and LVD26mod. It is acknowledged that the stresses, which develop throughout Al-Si casting alloys during loading are likely to be controlled by the morphology and V_f or hard particles in addition to their mechanical properties.

The mechanisms of fatigue crack propagation in LVD25 and both LVD26 alloys are broadly similar. Most importantly, the crack tip can be better described as a diffuse region of micro-damage and intact ligaments. The damage in this region is formed by the failure of hard particles and several mechanisms were observed:

- Particle fracture,
- Debonding of the particle/matrix interface, and
- Failure at the particle/particle interface.

Fatigue cracks were observed to initiate at micro-damage and these could coalesce with each other or the 'main' fatigue crack. Micro-damage might therefore be expected to accelerate fatigue crack growth and so the formation of micro-damage acts as an anti-shielding mechanism. A particle will fracture or debond when a critical stress is achieved. The development of local stresses during loading is therefore important, as this will govern the likelihood of one particle failing over another. The morphology, distribution and mechanical properties of the particles in addition to the applied load are critical in determining which particles are likely to fail in the crack tip region.

The regions between the micro-damage can be described as intact ligaments. They were comprised of intermetallic and Si particles, in addition to the α-Al matrix (or any combination of these). If the ligaments were not destroyed by the coalescence of micro-damage with the 'main' crack they would impinge on the crack and on occasion be left in the crack wake. The ligaments therefore acted as a traction on crack opening and so shielded the crack tip thereby locally reducing the stress intensity. It is the competition between the different shielding and anti-shielding mechanisms that is likely to be the cause of differences in the fatigue crack

propagation rates. For example, in LVD26 the larger Si particles in the unmodified variant were apparently less detrimental than the refined Si particles in the modified alloy. This microstructural difference resulted in a greater level of crack shielding (or lower anti-shielding) in the unmodified alloy so that LVD26 unmod exhibited superior short fatigue and near threshold crack propagation behaviour.

The short fatigue crack propagation results indicated that the crack grows in a more contiguous manner in LVD27. Micro-damage does form ahead of the crack tip at clusters of intermetallics and intact ligaments were observed in the crack wake, but on a much lower scale. The competing shielding/anti-shielding mechanisms still occur in LVD27 but the balance of the mechanisms resulted in LVD27 exhibiting the worst short fatigue and near threshold crack growth performance.

At RT and low *da/dN* failed particles were observed on the fracture surfaces of all the alloys. However, fatigue cracks in LVD25 and both LVD26 alloys showed no preferentiality for hard particles whilst in LVD27 the crack tended to avoid hard particles. At 350˚C and low *da/dN* crack propagation in LVD27 was similar to that at RT, the crack preferentially avoided hard particles. The fatigue cracks in the other alloys also preferentially avoided hard particles representing a change in their crack propagation mechanism at the higher temperature. However, the particles failed so that a larger section was exposed on the fracture surface and so that the volume fraction of particles on the fracture surface was similar to the volume fraction of hard particles in the bulk.

At RT and high *da/dN*, fatigue cracks in all the alloys investigated were preferentially attracted to hard particles. Significantly the line fraction of particles on the fracture profile was similar for LVD25 and both LVD26 alloys suggesting that it was not simply the increase in the volume fraction of hard particles in LVD25 that accounted for its lower K_Q value. It is therefore likely that the lower K_Q value of LVD25 can be attributed to the balance of several shielding mechanisms resulting in less effective crack shielding.

At high *da/dN* and high temperature, fatigue cracks preferentially avoided hard particles. However, the regions of the particle network they did encounter fractured so that they exposed an average area of the particle on the fracture surface. At 350˚C

dislocations have increased mobility (compared with at RT). For sufficient stress to develop in and around particles a large number of cycles are therefore required to allow dislocations to pile-up. At high *da/dN* the material in the crack tip region experiences fewer loading cycles than at low *da/dN* and therefore particles experience lower stresses at high *da/dN*. Additionally the larger plastic zone size at high *da/dN* allows the fatigue crack to meander greater distances in search of the lowest stress path resulting in fewer particle encounters.

In summary, this study has demonstrated that the new generation of piston alloys, which contain increased levels of alloying additions, exhibit complex, interconnected, multiphase microstructures. The micromechanisms of both fatigue crack initiation and propagation are dependent upon the transfer of load from the matrix to the hard particle network during cyclic loading, and therefore the local distribution of stresses throughout the alloy. During fatigue crack propagation, this results in complex crack formation with several different shielding/anti-shielding mechanisms in operation. The micromechanisms of fatigue crack propagation are different, at the representative in-service temperature studied, to those at room temperature. This highlights the importance of fatigue studies at temperatures that are characteristic of those experienced in service.

Chapter 8

Future Directions

X-ray CT has proven to be a useful tool for assessing both the 3-D nature of Al-Si casting alloy microstructures and the interactions of fatigue cracks with these microstructures. However, conventional X-ray CT does not allow for the separation of the Al and Si phases. It is therefore recommended that holotomography be used as a method to characterise Al-Si casting alloys and so allow the four principal microstructural features (intermetallics, Si particles, α-Al matrix and pores) to be identified. Such information would be particularly valuable is assessing the way in which local stresses develop in such complex microstructures.

It was proposed in the discussion chapter (Chapter 6.2.2) that 3-D imaging software, such as ScanIP (Simpleware Ltd.), could be used to segment the different features (identified using holotomography) and produce representative 3-D microstructural models. Using the nanoindentation and thermal expansion data of Chen (2006) to assign properties to the individual constituents, such a model may be used to further understand a series of interesting problems. Examples of such problems could include: how stresses develop in the microstructures upon loading, whether mechanical properties can be predicted at both room and elevated temperatures, and how internal stresses vary during thermal cycling representative of that experienced in-service.

X-ray CT has been successfully used to perform *in-situ* monitoring of fatigue crack propagation in Al alloys (Ferrié *et al.*, 2006; Moffat *et al.*, 2007). A similar analysis using holotomography could be employed to monitor the various mechanisms of fatigue in Al-Si alloys. Such analysis is likely to reveal the evolution of damage in the crack tip region: the initial formation of micro-damage, coalescence of micro-damage, and final failure of intact ligaments in the crack wake. The identifiable microstructural

features in these alloys may also make them suitable candidates for strain mapping by tracking the relative positions of these features at different loads. For example**,** Toda *et al.* (2004b) used the movement of pores distributed around the crack tip in a 2024-T6 alloy to estimate the COD and therefore the stress intensity along the crack front.

The high temperature properties of Al-Si alloys are of particular importance because the normal operating temperature of these materials is between 200˚C and 440˚C. At these temperatures the mechanisms of fatigue crack propagation have been shown to be different to those at room temperature. High temperature *in-situ* monitoring of fatigue crack propagation using holotomography would be a very interesting experiment to investigate the micromechanisms of fatigue crack propagation in Al-Si casting alloys. At present, facilities are not available at either ESRF or the new Diamond facility in the UK for such high temperature tests. However, high temperature facilities are planned for development at the Joint Engineering, Environment and Processing (JEEP) beamline of the Diamond facility and so this may be a future possibility.

Chapter 9

References

ANDERSON, T. L. (1994) *Fracture mechanics: fundamentals and applications*, CRC Press, New York.

BAMBERY, H. M. (1932) Piston for internal combustion engine and the like, U.S. Patent No. 1852602. USA.

BARNES, S. & BARNES, S. (2002) Manufacturing pistons. WIPO patent number WO/2002/001059.

BARNES, S. (2005) Personal communication.

BARUCHEL, J., BUFFIERE, J.-Y., CLOETENS, P., DI MICHIEL, M., FERRIE, E., LUDWIG, W., MAIRE, E. & SALVO, L. (2006) Advances in synchrotron radiation microtomography. *Scripta Materialia,* 55**,** 41-46.

BEAKE, B., GOODES, S., JONES, S., PARKINSON, R., PICKFORD, N. & SMITH, J. (2003) NanoTest User Manual Version 2.0. Wrexham, Micromaterials Ltd.

BEERE, W. & RUTTER, E. H. (1978) Stresses and Deformation at Grain Boundaries [and Discussion]. *Philosophical Transactions of the Royal Society of London. Series A, Mathematical and Physical Sciences,* 288**,** 177-196.

BENSUSSAN, P. (1990) A critical review of the application of global and local approaches to creep crack initiation and growth. IN BENSUSSAN, P. (Ed.) *Proceedings of the MECAMAT International Seminar on High Temperature Fracture Mechanisms and Mechanics, Oct 13-15 1987.* Dourdan, Fr, MEP, London.

BLANCHETTE, Y., DICKSON, J. I. & BAILON, J. P. (1989) Influence of simultaneously occurring brittle cracking on ductile fatigue crack growth rates. Part I. Modelling of the semi-cohesive zone. *Engineering Fracture Mechanics,* 33**,** 633-642.

BOLSHAKOV, A. & PHARR, G. M. (1998) Influences of pileup on the measurement of mechanical properties by load and depth sensing indentation techniques. *Journal of Materials Research,* 13**,** 1049-1058.

BORBELY, A., CSIKOR, F. F., ZABLER, S., CLOETENS, P. & BIERMANN, H. (2004) Three-dimensional characterization of the microstructure of a metal-matrix composite by holotomography. *Materials Science and Engineering A,* 367**,** 40-50.

BOSELLI, J., PITCHER, P. D., GREGSON, P. J. & SINCLAIR, I. (1998) Quantitative Assessment of Particle Distribution Effects on Short Crack Growth in SiCp Reinforced Al-Alloys. *Scripta Materialia,* 38**,** 839-844.

BOSELLI, J., PITCHER, P. D., GREGSON, P. J. & SINCLAIR, I. (1999) Secondary phase analysis via finite body tessellation. *Journal of Microscopy,* 195**,** 104-112.

BOSELLI, J., PITCHER, P. D., GREGSON, P. J. & SINCLAIR, I. (2001) Numerical modelling of particle distribution effects on fatigue in Al-SiCp composites. *Materials Science and Engineering A,* 300**,** 113-124.

BUCAILLE, J. L., ROSSOLL, A., MOSER, B., STAUSS, S. & MICHLER, J. (2004) Determination of the matrix in situ flow stress of a continuous fibre reinforced metal matrix composite using instrumented indentation. *Materials Science and Engineering A,* 369**,** 82-92.

BUFFIERE, J.-Y., SAVELLI, S., JOUNEAU, P. H., MAIRE, E. & FOUGIERES, R. (2001) Experimental study of porosity and its relation to fatigue mechanisms of model Al-Si7-Mg0.3 cast Al alloys. *Materials Science & Engineering A (Structural Materials: Properties, Microstructure and Processing),* A316**,** 115-26.

CACERES, C. H., DAVIDSON, C. J., GRIFFITHS, J. R. & WANG, Q. G. (1999) The effect of Mg an the microstructure and mechanical behavior of Al-Si-Mg casting alloys. *Metallurgical and Materials Transactions A (Physical Metallurgy and Materials Science),* 30A**,** 2611-18.

CALLISTER, W. D. (2000) *Materials science and engineering : an introduction,* New York, John Wiley & Sons, Inc.

CARLSON, R. L., KARDOMATEAS, G.A. (1996) *An introduction to fatigue in metals and composites,* London, Chapman and Hall.

CATON, M., JONES, J., BOILEAU, J. & ALLISON, J. (1999) The effect of solidification rate on the growth of small fatigue cracks in a cast 319-type aluminum alloy. *Metallurgical and Materials Transactions A,* 30**,** 3055-3068.

CATON, M. J., JONES, J. W. & ALLISON, J. E. (2001) The influence of heat treatment and solidification time on the behavior of small-fatigue-cracks in a cast aluminum alloy. *Materials Science and Engineering A,* 314**,** 81-85.

CHAN, K. S., JONES, P. & WANG, Q. (2003) Fatigue crack growth and fracture paths in sand cast B319 and A356 aluminum alloys. *Materials Science and Engineering A,* 341**,** 18-34.

CHEN, C. (2006) PhD Thesis: Characterisation of Intermetallic phases in multicomponent Al-Si alloys for piston applications. *IPTME.* Loughborough University.

CHEN, C. L., WEST, G. & THOMSON, R. C. (2006) Characterisation of intermetallic phases in multicomponent Al-Si casting alloys for engineering applications. *Materials Science Forum,* 519-521**,** 359-64.

CHEN, Y.-C. & DAEHN, G. (1991) The deformation of an aluminum-silicon eutectic alloy under thermal cycling conditions. *Metallurgical and Materials Transactions A,* 22**,** 1113-1115.

CLOETENS, P., BOLLER, E., LUDWIG, W., BARUCHEL, J. & SCHLENKER, M. (2001) Absorption and phase contrast imaging with synchrotron radiation. *Europhysics News,* 32.

CLOETENS, P., LUDWIG, W., BARUCHEL, J., VAN DYCK, D., VAN LANDUYT, J., GUIGAY, J. P. & SCHLENKER, M. (1999) Holotomography: Quantitative phase tomography with micrometer resolution using hard synchrotron radiation X-rays. *Applied Physics Letters,* 75**,** 2912-2914.

CLYNE, T. W. & WITHERS, P. J. (1993) *An Introduction to metal matrix composites,* Cambridge, U.K., Cambridge University Press.

CONLEY, J. G., HUANG, J., ASADA, J. & AKIBA, K. (2000) Modelling the effects of cooling rate, hydrogen content, grain refiner and modifier on microporosity

formation in Al A356 alloys. *Materials Science and Engineering A,* 285**,** 49-55.

DA C. ANDRADE, E. N. & CHALMERS, B. (1932) The Resistivity of Polycrystalline Wires in Relation to Plastic Deformation, and the Mechanism of Plastic Flow. *Proceedings of the Royal Society of London. Series A, Containing Papers of a Mathematical and Physical Character,* 138**,** 348-374.

DAI, X., YANG, X., CAMPBELL, J. & WOOD, J. (2003) Effects of runner system design on the mechanical strength of Al-7Si-Mg alloy castings. *Materials Science and Engineering A,* 354**,** 315-325.

DAYKIN, C. R. S. (1998) PhD thesis: Microstructural Modelling of Commercial Aluminium - Silicon Alloys for Piston Design. *Department of Materials Science and Metallurgy.* Cambridge, Magdalene College, Cambridge.

DEITER JR., G. E. (1988) *Mechanical Metallurgy SI Metric Edition*, McGraw-Hill Book Company (UK) Ltd.

DODDS, R. H. J., ANDERSON, T. L. & KIRK, M. T. (1991) Framework to correlate a/W ratio effects on elastic-plastic fracture toughness (J_c). *International Journal of Fracture,* 48**,** 1-22.

DVLA (2007) *DVLA annual report and accounts 2006-07*, HMSO, UK.

EDWARDS, W. M. (2002) PhD Thesis: Microstructural and Mechanical Property Modelling for the Processing of Al-Si Alloys. *Institute of Polymer Technology and Materials Engineering.* Loughborough, Loughborough University.

EEA (2007) Report number 1/2007. Transport and the environment: on the way to a new common transport policy. Brussels.

EL HADDAD, M. H., TOPPER, T. H. & SMITH, K. N. (1979) Prediction of non-propagating cracks. *Engineering Fracture Mechanics,* 11**,** 573-584.

ELLIOT, R. (1983) *Eutectic Solidification Processing Crystalline and Glassy Alloys,* London, Butterworths.

ESHELBY, J. D. (1957) The determination of the elastic field of an ellipsoidal inclusion, and related problems. *Proceedings of the Royal Society of London, Series A (Mathematical and Physical Sciences),* 241**,** 376-396.

ESKIN, D. G., MASSARDIER, V. & MERLE, P. (1999) Study of high-temperature precipitation in Al-Mg-Si alloys with an excess of silicon. *Journal of Materials Science,* 34**,** 811-820.

ESRF (2007) Principle of computerized tomography, http://www.esrf.eu/, accessed 04/06/07.

EU (2007) *Memo 07/46 Questions and answer on the EU strategy to reduce CO2 emission from cars,* Brussels.

EVANS, R. W. & WILSHIRE, B. (1993) *Introduction to creep*, Maney Publishing, UK.

FAN, J. & HAO, S. (2004) A design-centered approach in developing Al-Si-based; lightweight alloys with enhanced fatigue life and strength. *Journal of Computer-Aided Materials Design,* 11**,** 139-61.

FAN, J., MCDOWELL, D. L., HORSTEMEYER, M. F. & GALL, K. (2003) Cyclic plasticity at pores and inclusions in cast Al-Si alloys. *Engineering Fracture Mechanics,* 70**,** 1281-1302.

FARES, N. (1989) Crack fronts trapped by arrays of obstacles: numerical solutions based on surface integral representation. *Journal of Applied Mechanics,* 56**,** 837-843.

FEDERAL MOGUL, (2005) Media downloads, http://federal-mogul.com/en/media/download/.

FEDERAL MOGUL, (2007) Pistons, http://www.federal-mogul.com/en/oetecnology/powertrain/pistons/.

FERRIE, E., BUFFIERE, J. Y. & LUDWIG, W. (2005) 3D characterisation of the nucleation of a short fatigue crack at a pore in a cast Al alloy using high resolution synchrotron microtomography. *International Journal of Fatigue,* 27**,** 1215-1220.

FISCHERSWORRING-BUNK, A., THALMAIR, S., EIBL, M. & DIETSCHE, A. (2006) High temperature fatigue and creep - automotive powertrain application perspectives. *High Temperature Fatigue – Influences of Environment and Creep.* London, IOM^3.

FORSYTH, P. J. E. (1962) A two stage process of fatigue crack growth. *Crack Propagation: Proceeding of Cranfield Symposium.* London, HMSO.

GALL, K., YAN, N., HORSTEMEYER, M., MCDOWELL, D. L. & FAN, J. (2000) The influence of modified intermetallics and Si particles on fatigue crack paths in a cast A356 Al alloy. *Fatigue and Fracture of Engineering Materials and Structures,* 23**,** 159-72.

GALL, K., YANG, N., HORSTEMEYER, M., MCDOWELL, D.L. FAN, J. (1999) Debonding and fracture of Si particles during the fatigue of a cast Al-Si alloy. *Metallurgical and Materials Transactions A: Physical Metallurgy and Materials Science,* 30A**,** 3079-3088.

GAO, Y. X., YI, J. Z., LEE, P. D. & LINDLEY, T. C. (2004) The effect of porosity on the fatigue life of cast aluminium-silicon alloys. *Fatigue and Fracture of Engineering Materials and Structures,* 27**,** 559-570.

GEANDIER, G., HAZOTTE, A., DENIS, S., MOCELLIN, A. & MAIRE, E. (2003) Microstructural analysis of alumina chromium composites by X-ray tomography and 3-D finite element simulation of thermal stresses. *Scripta Materialia,* 48**,** 1219-1224.

GERBERICH, W. W. & MOODY, N. R. (1979) Review of fatigue fracture topology effects on threshold and growth mechanisms. *ASTM Special Technical Publication***,** 292-341.

GREER, A. L., COOPER, P. S., MEREDITH, M. W., SCHNEIDER, W., SCHUMACHER, P., SPITTLE, J. A. & TRONCHE, A. (2003) Grain refinement of aluminium alloys by inoculation. *Advanced Engineering Materials,* 5**,** 81-91.

GRIFFITH, A. A. (1921) The phenomenon of rupture and flow in solids. *Philosophical Transactions of the Royal Society, London,* A221**,** 163-197.

GUPTA, M. & LING, S. (1999) Microstructure and mechanical properties of hypo/hyper-eutectic Al-Si alloys synthesized using a near-net shape forming technique. *Journal of Alloys and Compounds,* 287**,** 284-294.

HAMILTON, R. W., SEE, D., BUTLER, S. & LEE, P. D. (2003) Multiscale modelling for the prediction of casting defects in investment cast aluminum alloys. *Materials Science and Engineering A,* 343**,** 290-300.

HAN, S.-W., KUMAI, S. & SATO, A. (2002) Effects of solidification structure on short fatigue crack growth in Al-7%Si-0.4%Mg alloy castings. *Materials Science and Engineering A,* 332**,** 56-63.

HAQUE, M. M. & MALEQUE, M. A. (1998) Effect of process variables on structure and properties of aluminium-silicon piston alloy. *Journal of Materials Processing Technology,* 77**,** 122-128.

HARUN, M., DAUD, A. R. & TALIB, I. A. (1996) Effect of element additions on wear property of eutectic aluminium-silicon alloys. *Wear,* 194**,** 54-59.

HEGGLI, M., ETTER, T., WYSS, P., UGGOWITZER, P. J. & GUSEV, A. A. (2005) Approaching representative volume element size in interpenetrating phase composites. *Advanced Engineering Materials,* 7**,** 225-229.

HORSTEMEYER, M. F., GALL, K., DOLAN, K. W., WATERS, A., HASKINS, J. J., PERKINS, D. E., GOKHALE, A. M. & DIGHE, M. D. (2003) Numerical, experimental, non-destructive, and image analyses of damage progression in cast A356 aluminum notch tensile bars. *Theoretical and Applied Fracture Mechanics,* 39**,** 23-45.

HUANG, M. & LI, Z. (2006) Influences of particle size and interface energy on the stress concentration induced by the oblate spheroidal particle and the void nucleation mechanism. *International Journal of Solids and Structures,* 43**,** 4097-4115.

IRWIN, G. R. (1956) Onset of fast crack propagation in high strength steel and aluminum alloys. *Proceeding of the Second Sagamore Conference.* New York, Syracuse University.

IRWIN, G. R. (1957) Analysis of stresses and strains near the end of a crack traversing a plate. *Journal of Applied Mechanics,* 24**,** 361-364.

IRWIN, G. R. (1961) Plastic zone near a crack and fracture toughness. *Sagamore research conference proceedings.*

JAGLINSKI, T. & LAKES, R. (2004) Creep behavior of Al-Si die-cast alloys. *Transactions of the ASME. Journal of Engineering Materials and Technology,* 126**,** 378-83.

JANSSEN, D., AQUARIUS, R., STOLK, J. & VERDONSCHOT, N. (2005) The contradictory effects of pores on fatigue cracking of bone cement. *Journal of Biomedical Materials Research Part B: Applied Biomaterials,* 74B**,** 747-753.

JOHN, V. (2003) *Introduction to Engineering Materials*, Palgrave Macmillan, Basingstoke.

JOYCE, M. R., STYLES, C. M. & REED, P. A. S. (2002) Elevated temperature fatigue of Al-Si piston alloys. *Aluminium Alloys 2002 Their Physical and Mechanical Properties: Proceedings of the 8th International Conference ICAA8, Jul 2-5.* Cambridge, United Kingdom, Trans Tech Publications Ltd.

JOYCE, M. R., STYLES, C. M. & REED, P. A. S. (2002b) Microstructural and mechanical property modelling for the processing of Al-Si Alloys: Final report on MAPEA EPSRC grant GR/M38667. Southampton, University of Southampton.

JOYCE, M. R., STYLES, C. M. & REED, P. A. S. (2003) Elevated temperature short crack fatigue behaviour in near eutectic Al-Si alloys. *International Journal of Fatigue,* 25**,** 863-869.

KAK, A. & SLANEY, M. (1988) *Principles of computerized tomographic imaging,* New York, USA, IEEE press.

KALKA, M. & ADAMIEC, J. (2006) Complex procedure for the quantitative description of an Al-Si cast alloy microstructure. *Materials Characterization,* 56**,** 373-8.

KEARNEY, A. & ROOY, E. L. (1990) Aluminum foundry products. *ASM handbook 2.* Ohio, USA, ASM.

KEER, L. M., DUNDURS, J. & KIATTIKOMOL, K. (1973) Separation of a smooth circular inclusion from a matrix *International Journal of Engineering Science,* 11**,** 1221-1233.

KHOR, K. H., BUFFIERE, J.-Y., LUDWIG, W., TODA, H., UBHI, H. S., GREGSON, P. J. & SINCLAIR, I. (2004) In situ high resolution synchrotron

x-ray tomography of fatigue crack closure micromechanisms. *Journal of Physics Condensed Matter,* 16**,** 3511-3515.

KIM, H. R., SEO, M. G. & BAE, W. B. (2002) A study of the manufacturing of tie-rod ends with casting/forging process. *Journal of Materials Processing Technology,* 125-126**,** 471-476.

KITAGAWA, H. & TAKAHASHI, S. (1976) Applicability of fracture mechanics to very small cracks or cracks in the early stage. In *Proceedings of Second International Conference on Mechanical Behaviour of Materials.* Boston, MA, ASM.

KLESNIL, M., LUKAS, P. & POLAK, J. (1993) General features of the fatigue process. IN BILY, M. (Ed.) *Cyclic deformation and fatigue of metals.* London, Elsevier.

KOBAYASHI, T. (2002) Effects of damage at eutectic and primary Si particles in cast Al-Si alloys. *Aluminium Alloys 2002 Their Physical and Mechanical Properties: Proceedings of the 8th International Conference ICAA8, Jul 2-5 2002.* Cambridge, United Kingdom, Trans Tech Publications Ltd.

LADOS, D. A. (2004) PhD thesis: Fatigue crack growth mechanisms in Al-Si-Mg alloys. *Materials Science and Engineering.* Worchester Polytechnic Institute.

LADOS, D. A. (2004b) Fatigue crack growth mechanisms in Al-Si-Mg alloys. *Surface Engineering,* 20**,** 416-24.

LADOS, D. A. & APELIAN, D. (2004) Fatigue crack growth characteristics in cast Al-Si-Mg alloys: Part I. Effect of processing conditions and microstructure. *Materials Science and Engineering A,* 385**,** 200-211.

LADOS, D. A., APELIAN, D. & DONALD, J. K. (2006) Fatigue crack growth mechanisms at the microstructure scale in Al-Si-Mg cast alloys: Mechanisms in the near-threshold regime. *Acta Materialia,* 54**,** 1475-1486.

LAIRD, C., SMITH, G.C. (1962) Crack propagation in high stress fatigue. *Philosophical Magazine,* 8**,** 847-857.

LASAGNI, F., LASAGNI, A., HOLZAPFEL, C., CKLICH, F. & DEGISCHER, H. (2006) Three Dimensional Characterization of Unmodified and Sr-Modified Al-Si Eutectics by FIB and FIB EDX Tomography. *Advanced Engineering Materials,* 8**,** 719-723.

LEE, B. J. & MEAR, M. E. (1999) Stress concentration induced by an elastic spheroidal particle in a plastically deforming solid. *Journal of the Mechanics and Physics of Solids,* 47**,** 1301-1336.

LEE, F. T., MAJOR, J.F., SAMUEL, F.H. (1995) Effect of silicon particles on the fatigue crack growth characteristics of Al-12 wt pct Si-0.35 wt pct Mg-(0 to 0.02) wt pct Sr casting alloys. *Metallurgical and Materials Transactions A: Physical Metallurgy and Materials Science,* 26A**,** 1553-1570.

LEE, M. H., KIM, J. J., KIM, K. H., KIM, N. J., LEE, S. & LEE, E. W. (2003) Effects of HIPping on high-cycle fatigue properties of investment cast A356 aluminum alloys. *Materials Science and Engineering A,* 340**,** 123-129.

LI, P., LEE, P. D., LINDLEY, T. C., MAIJER, D. M., DAVIS, G. R. & ELLIOTT, J. C. (2006) X-ray microtomographic characterisation of porosity and its influence on fatigue crack growth. *Advanced Engineering Materials,* 8**,** 476-9.

LI, X.-D. & EDWARDS, L. (1996) Theoretical modelling of fatigue threshold for aluminium alloys. *Engineering Fracture Mechanics,* 54**,** 35-48.

LIAO, H., SUN, Y. & SUN, G. (2002) Correlation between mechanical properties and amount of dendritic [alpha]-Al phase in as-cast near-eutectic Al-11.6% Si

alloys modified with strontium. *Materials Science and Engineering A,* 335**,** 62-66.

LOPEZ, I. A., ZEPEDA, C. M., GONZALEZ REYES, J. G., FLORES, A. M., RODRIGUEZ, J. S. & GOMEZ, L. B. (2007) TEM microstructural characterization of melt-spun aged Al-6Si-3Cu-xMg alloys. *Materials Characterization,* 58**,** 509-518.

LUDWIG, W., BUFFIERE, J.-Y., SAVELLI, S. & CLOETENS, P. (2003) Study of the interaction of a short fatigue cracks with grain boundaries in a cast Al alloy using X-ray microtomography. *Acta Materialia,* 51**,** 585-98.

MERCEDES BENZ, (2007) The invention of the automobile, http://www.museum-mercedes-benz.com.

MOFFAT, A. J., SINCLAIR, I., PROUDHON, H. & BUFFIERE, J. Y. (2007) Interim report: *In-situ* three dimensional monitoring and modelling of small corner cracks in airframe Al-alloys., SES, University of Southampton, UK.

MONDOLFO, L. F. (1976) *Aluminium Alloys - Structure and Properties,* London, Butterworth & Co.

MORI, T. & TANAKA, K. (1973) Average stress in matrix and average elastic energy of materials with misfitting inclusions. *Acta Metallurgica,* 21**,** 571-4.

MORRIS, W. L. & JAMES, M. R. (1980) Statistical aspects of fatigue crack nucleation from particles. 11A**,** 850-851.

MYERS, M. R. & HURD, N. J. (1990) Interaction of creep and fatigue in an aluminium silicon alloy. IN BENSUSAN, P. (Ed.) *Proceedings of the MECAMAT International Seminar on High Temperature Fracture Mechanisms and Mechanics, Oct 13-15 1987.* Dourdan, Fr, MEP, London.

NEEDLEMAN, A. (1987) A continuum model for void nucleation by inclusion debonding. *Transactions of the ASME. Journal of Applied Mechanics,* 54**,** 525-31.

NOBEL FOUNDATION, (2007) The Nobel peace prize, http://nobelprize.org/nobel_prizes/peace/laureates/2007/.

OLIVER, W. C. & PHARR, G. M. (2004) Measurement of hardness and elastic modulus by instrumented indentation: Advances in understanding and refinements to methodology. *Journal of Materials Research,* 19**,** 3-20.

OROWAN, E. (1952) Fundamentals of brittle behaviour of metals. *Fatigue and Fracture of Metals***,** 139-167.

PACZ, A. (1921) Alloy, US Patent No. 1387900. USA.

PADKIN, A. J., BRERETON, M. F. & PLUMBRIDGE, W. J. (1987) Fatigue crack growth in two-phase alloys. *Materials Science and Technology,* 3**,** 217-223.

PARIS, P. C., ERDOGAN, F. (1963) A critical analysis of crack propagation laws. *Journal of Basic Engineering,* 85**,** 528-534.

PARRY, M. R., SYNGELLAKIS, S. & SINCLAIR, I. (2000) Numerical modelling of combined roughness and plasticity induced closure effects in fatigue. *Materials Science & Engineering A,* A291**,** 224-234.

PHARR, G. M., OLIVER, W. C. & BROTZEN, F. R. (1992) On the generality of the relationship among contact stiffness, contact area, and elastic modulus during indentation. *Journal of Materials Research,* 7**,** 613-617.

POLMEAR, I. J. (1989) *Light Alloys,* London, Edward Arnold.

QAMAR, S. Z., ARIF, A. F. M. & SHEIKH, A. K. (2004) Analysis of product defects in a typical aluminum extrusion facility. *Materials and Manufacturing Processes,* 19**,** 391-405.

QIN, S., CHEN, C., ZHANG, G., WANG, W. & WANG, Z. (1999) The effect of particle shape on ductility of SiCp reinforced 6061 Al matrix composites. *Materials Science and Engineering A,* 272**,** 363-370.

RAVI, M., PILLAI, U. T. S., PAI, B. C., DAMODARAN, A. D. & DWARAKADASA, E. S. (2002) The effect of mischmetal addition on the structure and mechanical properties of a cast Al-7Si-0.3Mg alloy containing excess iron (up to 0.6 pct). 2 ed. San Diego, CA, USA, Minerals, Metals, Materials Society & ASM International.

RICE, J. R. (1968) A path independent integral and the approximate analysis of strain concentrations by notches and cracks. *Journal of Applied Mechanics,* 35**,** 379-386.

ROY, N., SAMUEL, A. M. & SAMUEL, F. H. (1996) Porosity formation in Al-9 wt pct Si-3 wt pct Cu alloy systems: Metallographic observations. *Metallurgical and Materials Transactions A: Physical Metallurgy and Materials Science,* 27A**,** 415-429.

SALVO, L., CLOETENS, P., MAIRE, E., ZABLER, S., BLANDIN, J. J., BUFFIERE, J. Y., LUDWIG, W., BOLLER, E., BELLET, D. & JOSSEROND, C. (2003) X-ray micro-tomography an attractive characterisation technique in materials science. *Nuclear Instruments and Methods in Physics Research Section B: Beam Interactions with Materials and Atoms,* 200**,** 273-286.

SCOTT, P. M. & THORPE, T. W. (1981) A critical review of crack tip stress intensity factors for semi-elliptic cracks. *Fatigue of Engineering Materials and Structures,* 4**,** 291-309.

SENIW, M. E., CONLEY, J. G. & FINE, M. E. (2000) The effect of microscopic inclusion locations and silicon segregation on fatigue lifetimes of aluminum alloy A356 castings. *Materials Science and Engineering A,* 285**,** 43-48.

SHANG, J. K. & RITCHIE, R. O. (1989) Crack bridging by uncracked ligaments during fatigue-crack growth in SiC-reinforced aluminum-alloy composites. *Metallurgical Transactions A (Physical Metallurgy and Materials Science),* 20A**,** 897-908.

SHEN, H. & LISSENDEN, C. J. (2002) 3D finite element analysis of particle-reinforced aluminum. *Materials Science and Engineering A,* 338**,** 271-281.

SHIOZAWA, K., TOHDA, Y. & SUN, S.-M. (1997) Crack initiation and small fatigue crack growth behaviour of squeeze-cast Al-Si aluminum alloys. *Fatigue and Fracture of Engineering Materials & Structures,* 20**,** 237-247.

SINCLAIR, I. & GREGSON, P. J. (1997) Structural performance of discontinuous metal matrix composites. *Materials Science and Technology,* 13**,** 709-726.

SINGH, K. D., KHOR, K. H. & SINCLAIR, I. (2006) Roughness- and plasticity-induced fatigue crack closure under single overloads: Finite element modelling. *Acta Materialia,* 54**,** 4393-4403.

SMOKERS, R., BVERMEULEN, R., VAN MIEGHEM, R., GENSE, R., SKINNER, I., FERGUSSON, M., MACKAY, E., TEN BRINK, P., FONTARAS, G. & SAMARAS, Z. (2006) Review and analysis of the reduction potential and costs of technological and other measures to reduce CO2-emissions from passenger cars. TNO report under EC contract SI2.408212.

SNEDDON, I. N. (1965) The relaxation between load and penetration in axisymmetric boussinesq problem for a punch of arbitrary profile. *International Journal of Engineering Science,* 3**,** 45-57.

SRIVATSAN, T. S. & VASUDEVAN, V. K. (1998) Cyclic plastic strain response and fracture behavior of 2080 aluminum alloy metal matrix composite. *International Journal of Fatigue,* 20**,** 187-202.

STARINK, M. J. & VAN MOURIK, P. (1994) Interactions between precipitating phases in quenched Al-Cu-Si alloys. *Journal of Materials Science,* 29**,** 2835-2840.

STOKES, B., GAO, N. & REED, P. A. S. (2007) Effects of graphite nodules on crack growth behaviour of austempered ductile iron. *Materials Science and Engineering: A,* 445-446**,** 374-385.

STOLARZ, J., MADELAINE-DUPUICH, O. & MAGNIN, T. (2001) Microstructural factors of low cycle fatigue damage in two phase Al-Si alloys. *Materials Science and Engineering A,* 299**,** 275-286.

SUAREZ-PENA, B. & ASENSIO-LOZANO, J. (2006) Microstructure and mechanical property developments in Al-12Si gravity die-castings after Ti and/or Sr additions. *Materials Characterization,* 57**,** 218-226.

SURESH, S. (1998) *Fatigue of Materials,* Cambridge, Cambridge University Press.

SURESH, S. & RITCHIE, R. O. (1984) Propagation of short fatigue cracks. *International metal reviews,* 29**,** 445-76.

TABOR, D. (1951) *The Hardness of Metals*, Oxford University Press, London.

TANAKA, K. & MURA, T. (1981) A dislocation model for fatigue crack initiation. *Transactions of the ASME. Journal of Applied Mechanics,* 48**,** 97-103.

TANAKA, K. & MURA, T. (1982) Theory of fatigue crack initiation at inclusions. 13A**,** 117-123.

TODA, H., SINCLAIR, I., BUFFIERE, J. Y., MAIRE, E., KHOR, K. H., GREGSON, P. & KOBAYASHI, T. (2004) A 3D measurement procedure for internal local crack driving forces via synchrotron X-ray microtomography. *Acta Materialia,* 52**,** 1305-1317.

TODA, H., SINCLAIR, I., BUFFIERE, J. Y., MAIRE, E., KHOR, K. H., GREGSON, P. & KOBAYASHI, T. (2004b) A 3D measurement procedure for internal local crack driving forces via synchrotron X-ray microtomography. *Acta Materialia,* 52**,** 1305-1317.

UGUZ, A. & MARTIN, J. W. (1996) Plastic zone size measurement techniques for metallic materials. *Materials Characterization,* 37**,** 105-118.

UN (1998) Kyoto protocol in the United Nations framework convention on climate change, http://unfccc.int/resource/docs/convkp/kpeng.pdf.

UNDERWOOD, E. E. (1970) *Quantitative Stereology,* Reading, MA, Addison-Wesley Publishing Company.

UNDERWOOD, E. E. & STARKE, E. A., JR. (1979) Quantitative stereological methods for analyzing important microstructural features in fatigue of metals and alloys 633-682.

VASUDEVAN, A. K. & SADANANDA, K. (2001) Analysis of fatigue crack growth under compression-compression loading. *International Journal of Fatigue,* 23**,** 365-374.

VERDU, C., CERCUEIL, H., COMMUNAL, S., SAINFORT, P., FOUGERES, R. (1996) Microstructural aspects of the damage mechanisms of cast Al-7Si-Mg alloys. *Materials Science Forum: Proceedings of the 1996 5th International Conference, ICAA5. Part 3 (of 3), Jul 1-5 1996,* 217-222**,** 1449-1454.

WANG, J., HE, S., SUN, B., GUO, Q. & NISHIO, M. (2003) Grain refinement of Al-Si alloy (A356) by melt thermal treatment. *Journal of Materials Processing Technology,* 141**,** 29-34.

WANG, Q. G., APELIAN, D. & LADOS, D. A. (2001a) Fatigue behavior of A356-T6 aluminum cast alloys. Part I. Effect of casting defects. *Journal of Light Metals,* 1**,** 73-84.

WANG, Q. G., APELIAN, D. & LADOS, D. A. (2001b) Fatigue behavior of A356/357 aluminum cast alloys. Part II - Effect of microstructural constituents. *Journal of Light Metals,* 1**,** 85-97.

WARMUZEK, M. (2004) *Aluminum-silicon Casting Alloys: Atlas of Microfractographs,* Ohio, ASM International.

WATSON, I. G., LEE, P. D., DASHWOOD, R. J. & YOUNG, P. (2006) Simulation of the mechanical properties of an aluminum matrix composite using X-ray microtomography. *Metallurgical and Materials Transactions A: Physical Metallurgy and Materials Science,* 37**,** 551-558.

WELLINGTON, B. & ASMUS, A. (1995) *Diesel engines and fuel systems,* Melbourne, Australia, Longman.

WELLS, A. A. (1963) Unstable crack propagation in metals: cleavage and fast fracture. *Proceeding of the Crack Propagation Symposium.* Cranfield, UK.

WITHERS, P. J., STOBBS, W. M. & PEDERSEN, O. B. (1989) Application of the Eshelby method of internal stress determination to short fibre metal matrix composites. *Acta Metallurgica,* 37**,** 3061-3084.

WOHLER, A. (1860) Versuche uber die festigkeit der eisenbahnwagenachsen; Zeitschrift fur Bauwesen Vol.10; English summary (1867). *Engineering,* 4**,** 160-1.

YAMAMOTO, S., TODA, H., QIAN, L., OHGAKI, T., KOBAYASHI, M., KOBAYASHI, T. & UESUGI, K. (2006) Assessment of damage and fracture behaviors in a cast aluminum alloy via in-situ synchrotron microtomography. *Materials Science Forum,* 519-521**,** 1005-10.

YE, H. (2003) An overview of the development of Al-Si-alloy based material for engine applications. *Journal of Materials Engineering and Performance,* 12**,** 288-297.

YI, J. Z., GAO, Y. X., LEE, P. D., FLOWER, H. M. & LINDLEY, T. C. (2003) Scatter in fatigue life due to effects of porosity in cast A356-T6 aluminum-silicon alloys. *Metallurgical and Materials Transactions A: Physical Metallurgy and Materials Science,* 34 A**,** 1879-1890.

YI, J. Z., LEE, P. D., LINDLEY, T. C. & FUKUI, T. (2006) Statistical modelling of microstructure and defect population effects on the fatigue performance of cast A356-T6 automotive components. *Materials Science & Engineering A (Structural Materials: Properties, Microstructure and Processing),* 432**,** 59-68.

ZABLER, S., LINK, T., EPISHIN, A., HAIBEL, A., BANSAL, M. & THIBAULT, X. (2006) Synchrotron tomography of porosity in single-crystal nickel-base superalloys. *Materials Science and Engineering A (Structural Materials: Properties, Microstructure and Processing),* 425**,** 47-54.

ZHANG, B., POIRIER, D. R. & CHEN, W. (1999) Microstructural effects on high-cycle fatigue-crack initiation in A356.2 casting alloy. *Metallurgical and Materials Transactions A: Physical Metallurgy and Materials Science,* 30**,** 2659-2666.

ZHANG, D. L., ZHENG, L. H. & STJOHN, D. H. (2002) Effect of a short solution treatment time on microstructure and mechanical properties of modified Al-7wt.%Si-0.3wt.%Mg alloy. *Journal of Light Metals,* 2**,** 27-36.

Appendix A

Publications

Moffat, A.J., Mellor, B.G., Sinclair, I., Reed, P.A.S. (2007) The mechanisms of long fatigue crack growth behaviour in Al-Si casting alloys at room and elevated temperature, *Materials Science and Technology*, In press.

Moffat, A.J., Barnes, S., Mellor, B.G., Reed, P.A.S. (2006) Microstructural analysis of fatigue initiation in Al-Si casting alloys. *Materials Science Forum*, 519-521: p. 1083-1088.

Moffat, A.J., Barnes, S., Mellor, B.J., Reed, P.A.S., (2005). The effect of Si content on the long crack fatigue behaviour of Al-Si piston alloys at elevated temperature. *International Journal of Fatigue*, 27 (10-12): p. 1564-1570